UNIVERSITÉ DE STRASBOURG

ÉCOLE DOCTORALE 222

UMR 7140 – Chimie de la Matière Complexe
UPR 22 – Institut Charles Sadron

THÈSE présentée par :

Alexis BIGO--SIMON

soutenue le : **17 octobre 2023**

pour obtenir le grade de : **Docteur de l'Université de Strasbourg**

Discipline/ Spécialité : Chimie/Physique

Résolution à l'échelle moléculaire de la structure de nanofibres de peptides courts par reconstruction d'images de cryo-microscopie électronique, analyse spectrale et dynamique moléculaire

THÈSE dirigée par :

Mme. SCHURHAMMER Rachel	Professeure, Université de Strasbourg
M. JIERRY Loïc	Professeur, Université de Strasbourg

RAPPORTEURS :

M. BAADEN Marc	Directeur de recherches CNRS, Institut de Biologie Physico-Chimique, Paris
M. BOUDIER Thomas	Maître des conférences, Centrale Méditerranée, Nice

EXAMINATEURS :

M. ULRICH Sébastien	Directeur de recherches CNRS, Institut des Biomolécules Max Mousseron, Montpellier
Mme BEGIN Sylvie	Professeure, Université de Strasbourg

MEMBRES INVITES :

M. SCHMUTZ Marc	Ingénieur de recherches CNRS, Institut Charles Sadron, Strasbourg
M. CHAUMONT Alain	Maître des conférences, Université de Strasbourg
M. ESTROZI FARIAS Leandro	Chargé de recherches CNRS, Institut de Biologie Structurale, Grenoble

« Quarante-deux ! cria Loonquawl. Et c'est tout ce que t'as à nous montrer au bout de sept millions et demi d'années de boulot ?

- J'ai vérifié très soigneusement, dit l'ordinateur, et c'est incontestablement la réponse exacte. Je crois que le problème, pour être tout à fait franc avec vous, est que vous n'avez jamais vraiment bien saisi la question. »

Douglas Adam, *Le Guide du voyageur galactique*

Remerciements

En été 2020 une confiance m'a été donnée par mes deux directeurs : Rachel SCHURHAMMER et Loïc JIERRY. Je tiens à tout particulièrement les remercier puisqu'ils ont pris le pari de former un expérimentateur à la chimie computationnelle et à la reconstruction d'images. Leur bienveillance à mon égard m'ont permis de grandir et de murir dans un monde scientifique en constante évolution.

Je tiens à remercier mes encadrants de thèse : Alain CHAUMONT et Marc SCHMUTZ pour les projets qu'ils m'ont apporté ainsi que toute leur confiance tout au long de mes années de doctorat. Je tiens à les remercier particulièrement pour m'avoir donné les moyens techniques et scientifiques pour réussir tout au long de ce projet.

Ce qu'il ne faut jamais oublier dans le monde de la recherche c'est que des chercheurs ont passé une carrière entière à nous paver le chemin pour enrichir notre vie professionnelle. Pour cela je tiens à remercier Pierre SCHAAF qui m'a été d'une grande aide tout au long de mon cursus. Son aide, son esprit critique et ses remarques constructives m'ont permis de me développer scientifiquement et intellectuellement.

Je tiens à remercier Jérôme COMBET et Guillaume FLEITH spécialistes des rayons X qui m'ont permis de comprendre que les informations utiles sont effectivement bien dans l'espace des fréquences. Merci pour vos contributions à mon travail de thèse et à nos discussions régulières.

Je souhaite également remercier Etienne ENGLER qui a su régler tous nos problèmes informatiques en dynamique moléculaire et qui est toujours d'excellents conseils pour nous aider à améliorer nos performances computationnelles.

Je tiens également à remercier deux microscopistes qui m'ont guidé tout au long de mon projet de thèse : Guy SCHOEHN et Leandro ESTROZI de l'Institut de Biologie Structurale à Grenoble. Ils m'ont consacré du temps, accueilli et formé aux bonnes pratiques de la reconstruction d'images. Merci de m'avoir donné de leur temps pour mon projet de thèse et de nous avoir permis de découvrir

des résultats qui, je l'espère, sauront enthousiasmer la communauté scientifique.

Je tiens également à remercier tous mes collègues dans les deux instituts avec qui j'ai pu partager des moments de convivialité et d'échange scientifique.

Merci également à mes amis proches et à ma famille de m'avoir soutenu et épaulé tout au long de ces années de thèse.

Table des matières

Introduction

Au cours des vingt dernières années, un nombre croissant d'articles relatifs aux hydrogels supramoléculaires à base de peptides a été publié. La cohésion de ces matériaux est assurée par une architecture nanométrique (généralement un réseau nanofibreux) résultante de l'auto-assemblage de peptides. L'organisation de ces briques de base gouverne à la fois les propriétés chimiques et mécaniques de ces matériaux. En effet, l'aptitude des nanofibres de peptides à s'associer entre-elles sous la forme de microfibrilles, à s'organiser pour faire émerger des poches catalytiques performantes capable de discriminer entre différents substrats ou à interagir avec des biopolymères, comme des protéines ou des polysaccharides, dépend directement de la façon dont les peptides sont organisés spatialement au sein de la nanostructure. Ainsi la connaissance de cette organisation est cruciale pour concevoir un peptide adéquat ou optimiser les propriétés de ces matériaux qui trouvent des applications principalement dans le domaine de ces matériaux, de la catalyse et du biomédicale.

Cependant, à l'heure actuelle, il n'existe pas un outil d'analyse unique permettant d'avoir accès sans ambiguïté à l'organisation des peptides auto-assemblés au sein de la nanostructure. La combinaison de plusieurs approches analytiques est souvent nécessaire pour extraire une information structurale solide : utilisation de la diffraction des rayons X de poudres ou de monocristaux, diffusion des rayons X à différents angles, microscopie confocale à fluorescence, microscopie électronique, microscopie à force atomique, dichroïsme circulaire, spectroscopie infrarouge, etc. Dans le domaine de l'élucidation des structures biologiques à une échelle quasi-atomique, il a été développé une approche basée sur la reconstruction d'images de haute résolution obtenues par cryo microscopie électronique afin de résoudre la structure d'objets de dimensions nanométriques comme des virus, ou des agrégats amyloïdes, avec une résolution proche de l'angström. Cette approche performante a été mise à l'honneur par l'attribution du Prix Nobel de Chimie aux chercheurs pionniers dans ce domaine, en

l'occurrence à Dubochet, Frank et Henderson en 2017.

Au cours des dix dernières années, mes laboratoires d'accueil ont contribué au développement du concept d'auto-assemblage de peptides initié par des enzymes et conduisant à la formation d'hydrogels supramoléculaires (un concept communément connu sous le terme « EASA » signifiant « Enzyme-Assisted Self-Assembly » en anglais). Plus particulièrement, le tripeptide amphiphile court de séquence Fmoc-FFY (Fmoc : fluorométhoxycarbonyle, F : phénylalanine, Y : tyrosine) a été utilisé comme brique moléculaire modèle pour démontrer, entre autres, la capacité à localiser spatialement des processus d'auto-assemblage de peptides, et ainsi la formation localisée d'hydrogels supramoléculaires, grâce à l'immobilisation au préalable d'une enzyme sur une surface. Le tripeptide Fmoc-FFY peut être généré *in situ* par l'action de la phosphatase alcaline (PA) en présence du peptide précurseur Fmoc-FFpY (p : phosphate), comme illustré sur la Figure 1. **Mon projet de thèse se focalise sur les trois points suivants : (i) la compréhension des interactions qui régissent les assemblages de Fmoc-FFY à l'échelle moléculaire, (ii) la résolution de la structure des nanofibres de Fmoc-FFY auto-assemblés et l'impact de la voie de préparation (par « EASA » ou par chauffage-refroidissement), et (iii) la compréhension de l'origine de la formation de microfibrilles de Fmoc-FFY en présence d'un polysaccharide, en l'occurrence de l'acide hyaluronique, un phénomène mis en évidence par mon laboratoire de thèse.**

Mon manuscrit de thèse est divisé en cinq Chapitres 1, 2, 3, 4 et 5.

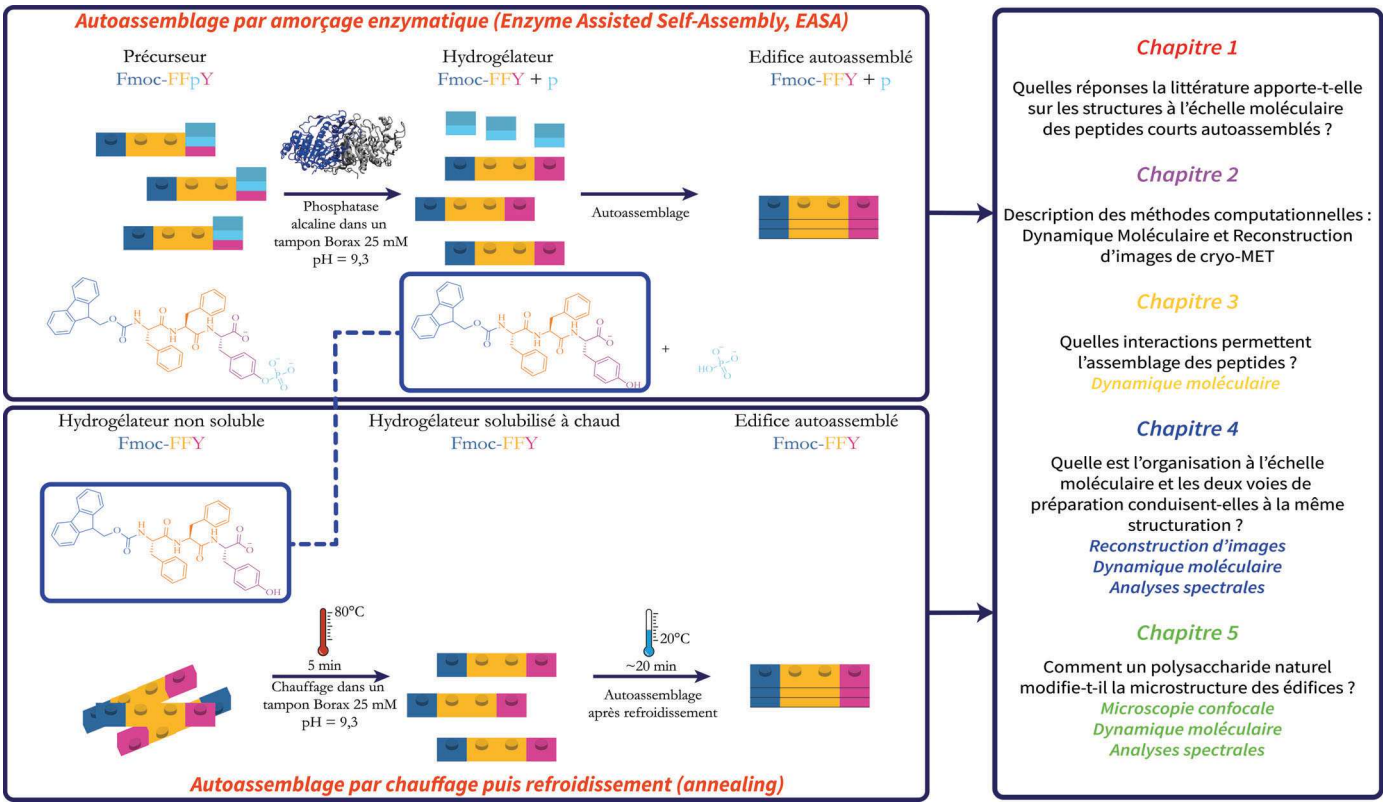

FIGURE 1 – Illustration des deux voies de préparation d'auto-assemblage du Fmoc-FFY par voie enzymatique, appelée EASA (en haut) et par voie thermique, par chauffage puis refroidissement (en bas). Les cinq chapitres de mon manuscrit et leurs objectifs associés sont présentés dans l'encadré à droite.

Le **Chapitre 1** est un état de l'art décrivant les connaissances portant sur l'organisation moléculaire de peptides courts en sein de nanostructures, quel que soit les outils analytiques utilisés. Ce chapitre couvre également la parution d'articles d'intérêt publiés pendant mon doctorat (2020-2023) et se focalisera sur le peptide Fmoc-FFY et ses analogues.

Suivra ensuite un **Chapitre 2** consacré à la description du matériel et des méthodes de deux techniques computationnelles : premièrement *la dynamique moléculaire classique* et deuxièmement *la reconstruction de la carte de projection du potentiel électrostatique à partir d'images de cryo microscopie électronique à transmission (cryo-MET)*. Les autres matériels et méthodes expérimentales se trouvent individuellement au sein de chaque chapitre expérimental concerné (en l'occurrence les **Chapitres 4 et 5**).

L'utilisation de la dynamique moléculaire a permis d'étudier les interactions qui régissent l'auto-assemblage de dimères Fmoc-FFY aux premiers instants dépend de la voie considérée. Ces résultats sont présentés dans le **Chapitre 3**.

Le **Chapitre 4** est dédié à la résolution de la nanostructure de Fmoc-FFY auto-assemblé à l'échelle quasi-atomique. Pour ce faire, il a été nécessaire de s'approprier l'approche de reconstruction d'images utilisée par les biologistes structuraux. D'autre part, la maitrise de cet outil a permis

d'étudier l'impact de la voie de préparation des assemblages de Fmoc-FFY, en l'occurrence par voie enzymatique (EASA) ou par chauffage et refroidissement, sur l'organisation interne des nanostructures de Fmoc-FFY auto-assemblés. Cette étude s'appuie sur une approche pluridisciplinaire regroupant la microscopie électronique, le traitement d'image, la dynamique moléculaire, la diffusion des rayons X et le dichroïsme circulaire.

L'interaction entre des polysaccharides et des nanostructures de peptides auto-assemblés est déjà largement décrit dans la littérature. Ces interactions conduisent généralement à la formation de microstructures organisées et parfois orientées dans l'espace dont la compréhension des mécanismes n'est pas encore clairement établie. En présence d'acide hyaluronique (HA), mes laboratoires d'accueil ont montré que les nanofibres de Fmoc-FFY formées par EASA s'organisent spontanément en microfibrilles, modifiant ainsi les propriétés mécaniques et biologiques des hydrogels supramoléculaires résultants. Le **Chapitre 5** décrit notre démarche pour comprendre l'origine de l'effet du HA sur les nanofibres de Fmoc-FFY auto-assemblées, et propose un mécanisme.

Une conclusion en fin de manuscrit rappelera les résultats obtenus au cours de ma thèse au regard des objectifs initialement fixés et décrits brièvement ci-dessus.

Mon projet de thèse est un projet pluridisciplinaire par essence. Il a impliqué de nombreuses collaborations dont les noms des personnes avec qui j'ai collaborés seront mentionnés en début de chacun des chapitres concernés. En dehors des **Chapitres 1 et 2,** le **Chapitre 3** doit donner lieu à la soumission d'un article, le **Chapitre 4** va être soumis au moment de la fin de la rédaction de manuscrit et le **Chapitre 5** a été publié dans la revue *Biomacromolecules* de l'éditeur American Chemical Society (ACS) en 2023. Par conséquent, les **Chapitres 3, 4 et 5** sont présentés sous la forme d'articles, et rédigés en anglais. Néanmoins, une introduction spécifique à chacun de ces chapitres a été ajoutée.

En annexe se trouvent deux articles dans le domaine de l'EASA auxquels j'ai participé au cours de mon doctorat mais qui n'entre pas directement dans mon projet de thèse : un premier article où j'ai participé à l'établissement de l'état de l'art sur le mécanisme et les applications du processus de EASA. [1]Un second article concerne la mise en évidence de la formation de microfibrille de Fmoc-FFY en présence de HA, et son impact sur l'adhésion cellulaire. [2]

Enfin, parce que cette thèse est pluridisciplinaire et parce que certains termes ou notions ne sont pas clairement définis, un glossaire a été établi et se trouve disponible en fin de manuscrit (page 217).

Chapitre 1 : Etat de l'art

Questions et problématiques dans le domaine de l'auto-assemblage des peptides courts

Quelle est la structure à l'échelle moléculaire ?

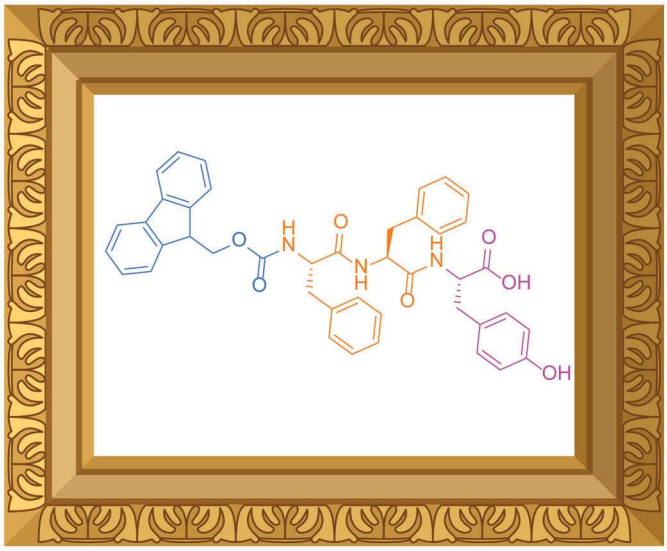

Quelles applications pour les auto-assemblages ?

Comment des peptides de séquence similaire vont-ils s'assembler ?

Quelles sont les techniques pour déterminer la structure ?

1 Introduction

Les hydrogels sont des matériaux composés d'un réseau de polymères où l'agent de gonflement est de l'eau. Ces derniers sont très étudiés en tant que matériaux mous pour des applications biomédicales. A titre d'example, ils peuvent servir de support pour de la culture cellulaire, comme matériaux pour l'ingénierie tissulaire et éventuellement comme hôte pour le relargage contrôlé de médicaments.[1-3] Les hydrogels actuellement utilisés dans cette application sont composés de polymères synthétiques biocompatibles. Le problème majeur de ces derniers est leur fin de vie dans l'hôte car le processus de dégradation peut générer des produits déclenchant une réaction immunitaire.[4, 5] De plus, l'évaluation de la toxicité des molécules issues de la dégradation du réseau peut s'avérer être une tâche complexe car il faut isoler, identifier et évaluer la toxicité des sous-produits. Ainsi, les scientifiques se sont tournés vers des biopolymères biocompatibles naturels tel que l'acide hyaluronique, la cellulose ou le chitosan qui pourraient devenir de nouvelles cibles de gels hôtes.[6-8]

Une application très prometteuse dans le monde de l'ingénierie tissulaire vise à réaliser la différenciation des cellules souches en différents types de tissus (musculaires, cardiaques, etc.) dans un seul matériau. Pour cela, il est nécessaire d'avoir plusieurs propriétés rhéologiques au sein d'un même gel. Or les polymères actuellement utilisés forment tous des matériaux homogènes ayant les propriétés identiques quelque soit la région spatiale du gel. Pour répondre à cette problématique il faudrait moduler la concentration locale en polymère. L'une des méthodes reviendrait à réaliser la polymérisation *in situ* dans l'eau. L'eau est également un produit de la polycondensation, un autre type de polymérisation, ce qui rend le solvant cinétiquement défavorable à la réaction. Les polymérisations classiques ne sont donc pas adaptées pour réaliser les matériaux souhaités. Depuis les années 1990, un nouveau type de polymérisation a vu le jour : la polymérisation supramoléculaire. Elle consiste à assembler des monomères par des interactions non-covalentes faibles telles que des liaisons hydrogène, des empilements d'orbitales π, etc. La formation du matériau peut être dirigée localement sans que l'eau soit un élément perturbateur et pourrait ainsi permettre d'accéder à des domaines rhéologiques locaux différents pour l'application souhaitée. Dans la famille des hydrogels supramoléculaires il est, depuis plus d'une vingtaine d'années, mentionné des monomères qui peuvent s'assembler pour conduire à des gels : les peptides hydrophobes. Ces derniers sont des (oligo)polymères d'acides aminés à séquence définies. Les peptides représentent des candidats de choix pour ces applications. En effet, les peptides sont constitués des mêmes briques élémentaires que les protéines ce qui diminue nettement la potentielle toxicité des produits de dégradation. De plus, certains peptides possèdent des

actions biologiques d'intérêts comme des activités antivirales ou antimicrobiennes.[9] Les chimistes se sont donc majoritairement intéressés à cette famille de molécules pour concevoir des matériaux aux propriétés désirées pour les applications biomédicales. Une méthode de formation d'hydrogel a été utilisée dans l'auto-assemblage de peptides : l'initiation de la polymérisation par une enzyme. Cette approche a été développée en 2004 par Bing Xu à partir d'un précurseur ne pouvant pas s'autoassembler, le Fmoc-pY (Fmoc : fluorénylméthoxycarbonyle, pY : tyrosine phosphate), qui en présence de phosphatase alcaline (PA) va s'hydrolyser en Fmoc-Y et conduire à la formation des nanofibres de peptides autoassemblés résultant ainsi à la gelation.[10] L'emploi d'un précurseur (Fmoc-pY) qui ne s'assemble pas et qui va conduire à un hydrogélateur (Fmoc-Y) permet de contrôler cinétiquement la formation des hydrogélateurs et ainsi de moduler la structuration.[11] Cette technique appelée Enzyme-Assisted Self-Assembly (EASA) a également permis le développement d'une variante localisée spatialement en greffant l'enzyme sur une surface, méthode appelée Localized Enzyme-Assisted Self-Assembly (LEASA)[12, 13] et qui permet de mieux répondre aux exigences de la variation locale de propriétés rhéologiques demandées dans les applications de différenciation cellulaire. En effet, il existe un gradient de concentration en nanofibres à partir de la surface de greffage de l'enzyme qui pourrait permettre la modulation des propriétés. Cependant, diriger spatialement la concentration en édifices structurés n'est pas suffisant pour avoir une modulation fine des propriétés. L'édifice à l'échelle moléculaire rentre également en compte lors de l'évaluation des propriétés car c'est cet arrangement qui constitue les propriétés mécaniques. La structuration moléculaire reste encore un des défis majeurs dans ce domaine. Les techniques de caractérisation utilisées actuellement donnent de forts indices sur l'organisation générale des peptides comme par exemple la présence de structures secondaires comme les feuillets β ou les hélices α et même parfois l'arrangement des groupements chimiques entre eux. Néanmoins, l'obtention de l'organisation moléculaire à l'échelle atomique et à l'état solvaté est, depuis les 20 dernières années, un challenge important. Il s'agit dans cet état de l'art de décrire les avancées dans le domaine de l'assemblage de peptides courts, principalement pour le motif Fmoc-FFY qui concerne cette thèse et ensuite de comprendre comment les scientifiques ont élaboré une démarche pour élaborer des hypothèses et fournir des réponses sur la structure moléculaire de peptides similaires (Figure 1). Une comparaison rapide des méthodes pour répondre à cette problématique est résumée dans le tableau 1 en fin de chapitre.

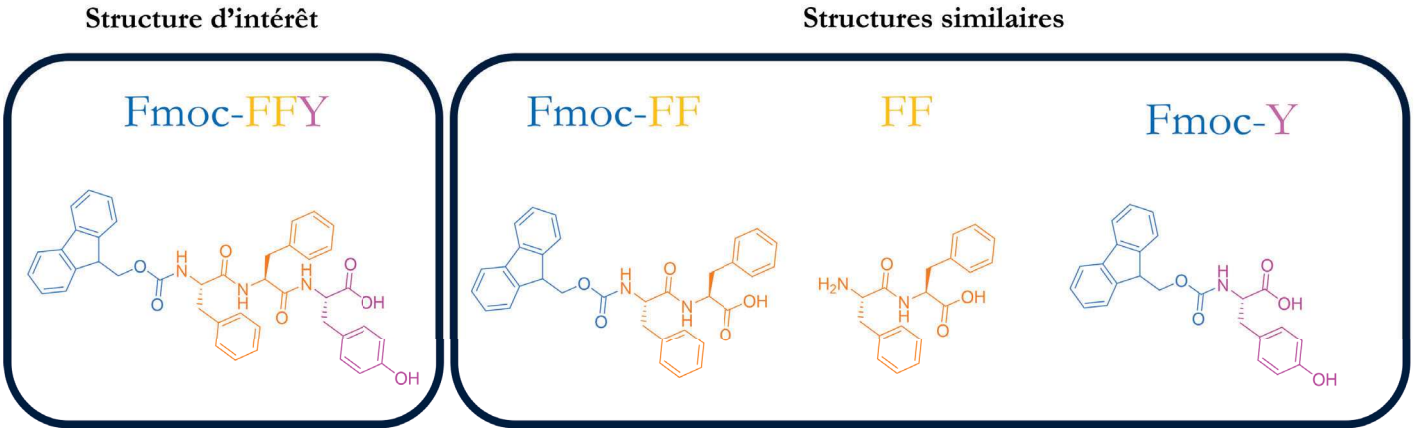

FIGURE 1 – Structures moléculaires basées sur les peptides contenant un Fmoc qui ont principalement servi de base de recherche dans le cadre de cet état de l'art.

2 Motif Fmoc-FFY

Dans cette partie nous nous intéressons à différents aspects du peptide d'intérêt, le Fmoc-FFY : (i) quelle est l'origine de la séquence et (ii) quelles sont les applications de ce dernier.

2.1 Conception du Fmoc-FFY comme hydrogélateur

Dans la littérature dédiée à l'assemblage de peptides, il existe une grande variété de séquences[14, 15] et cette diversité s'exprime principalement par des choix liés à des applications spécifiques. Parmi les peptides courts, deux articles sont pionniers. Le premier est celui de Gorbitz qui a montré en 2001 que la diphénylalanine (FF) avait la capacité de former des nanotubes, et, à forte concentration, des hydrogels.[16] L'article présente une structure cristalline, mise en évidence après l'évaporation de l'eau contenue dans le gel, où les interactions non-covalentes majoritaires sont des liaisons hydrogène entre les dipeptides. Ce dipeptide hydrophobe peut s'organiser pour former des édifices cristallins qui piègent de l'eau dans une cavité tubulaire centrale de 10 Å de diamètre. Bing Xu et ses collaborateurs ont utilisé le Fmoc-pY, décrit plus haut, pour former un hydrogelateur *in situ* via la méthode EASA.[10] La présence du Fmoc en position N-terminale de la séquence rajoute de l'hydrophobicité au peptide amphiphile ce qui accroît la capacité d'auto-assemblage. Mon équipe d'accueil à l'Institut Charles Sadron s'est appuyée sur ces deux articles pour proposer la séquence Fmoc-FFpY qui combine à la fois l'hydrophobicité des acides aminés ainsi que l'approche EASA conduisant à l'hydrogélateur Fmoc-FFY après hydrolyse de la tyrosine phosphate par la phosphatase alcaline. L'un des objectifs principaux dans mon équipe est de localiser l'auto-assemblage sur une surface et de comprendre les mécanismes régissant le processus de polymérisation supramoléculaire.[17, 18] La séquence Fmoc-FFY

n'est pas la plus décrite ou utilisée dans la littérature comparativement aux séquences Fmoc-FF ou FF qui seront présentés ultérieurement. Mis à part la littérature de mon groupe d'accueil, deux autres travaux font mention du Fmoc-FFY en tant qu'hydrogélateur et qui contiennent des informations structurales de l'assemblage peptidique résultant.

Le premier article est publié par Liang et ses collaborateurs et se focalise sur l'hydrogélation de ce tripeptide pour l'étude *in vitro* de maladies impliquant une activité anormale de la phosphatase alcaline.[19] Les auteurs se positionnent également sur l'amorçage de l'assemblage par la technique EASA. Ils étudient également la diffusion de l'eau dans le réseau autoassemblé via l'imagerie à résonnance magnétique (IRM). Dans cette étude les auteurs ont réalisé des images de cryo-MET qui permettent d'observer la nanostructure sous forme de fibres. Un modèle moléculaire est proposé comme illustré dans la Figure 2.

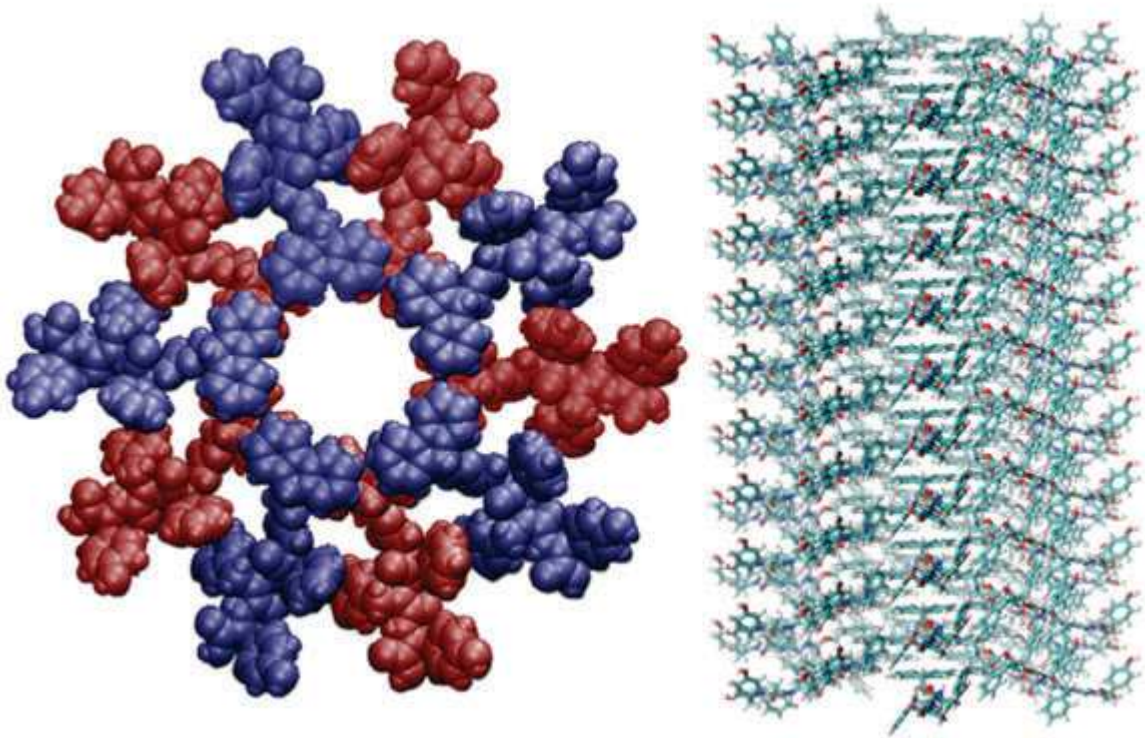

FIGURE 2 – Arrangement moléculaire pour le Fmoc-FFY auto-assemblé. A gauche, supermacrocycle de peptides auto-assemblés composé de 5 membres par couronne, chaque couronne possède une couleur différente. A droite, visualisation de la même structure moléculaire mais vue de côté. Issu de l'article de Liang et ses collaborateurs[19]. Réimprimé avec l'autorisation de Liang et ses collaborateurs. Copyright 2014 American Chemical Society.

Ce modèle s'appuie sur une couronne de 5 Fmoc-FFY placés circulairement (molécules en bleu) et laissant place à une cavité centrale. Les auteurs font l'hypothèse que la couronne suivante (ou précédente) distante de 0,4 nm est identique en conformation mais décalée d'un angle donné par rapport à la précédente (molécules en rouge). La nanofibre semble donc être formée d'une alternance de

ce motif. L'assemblage ainsi constitué contient les Fmocs au centre, viennent ensuite les phénylalanines et finalement la tyrosine, acide aminé le plus hydrophile qui serait alors en contact avec l'eau. Ce premier modèle rend également compte d'interactions d'empilement $\pi - \pi$ entre les Fmocs au centre de la structure. Cependant, cet édifice est uniquement postulé et n'est pas issu d'un processus de reconstruction d'images ou d'une analyse structurelle à l'échelle moléculaire.

Un deuxième article traite également du Fmoc-FFY. Il a été publié par Wang et ses collaborateurs en 2010 et a pour objectif d'expliquer le processus d'auto-assemblage et la modulation de la géométrie des nanofibres[20]. Le Fmoc-FFY est d'abord dissous dans du DMSO à 50 mg/mL et ensuite dilué à 10 mg/mL dans de l'eau ce qui produit l'hydrogélation du peptide. L'hydrogel est observé par Microscopie à Force Atomique (AFM) qui montre que les peptides s'assemblent en un réseau de fibres (Figure 3) de diamètre très varié.

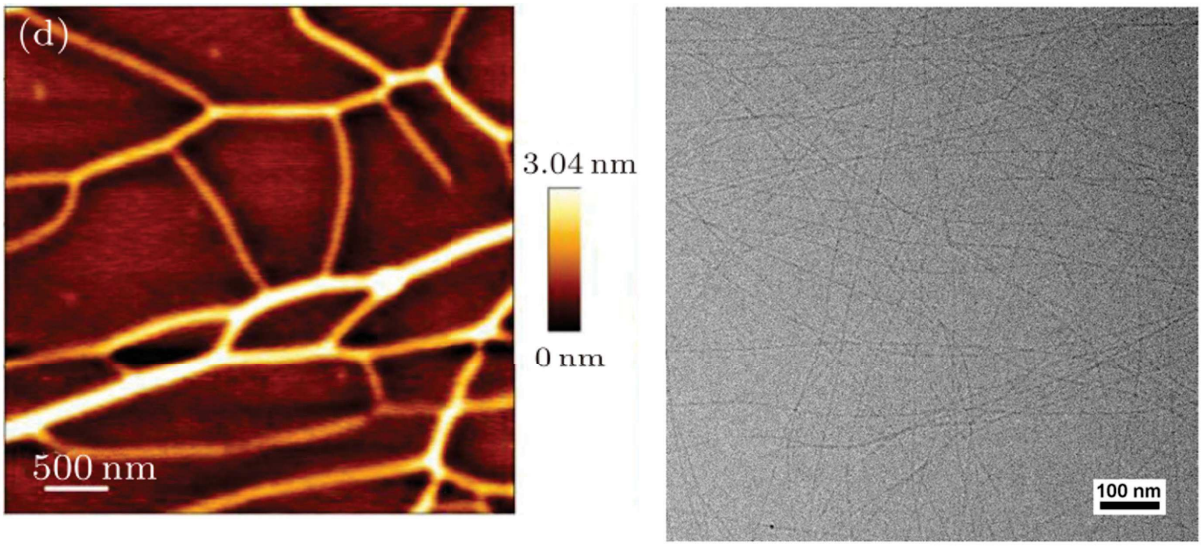

FIGURE 3 – Image de cryo-MET de Fmoc-FFY assemblé par le processus EASA avec la phosphatase alcaline, issue de la publication de Liang et ses collaborateurs [19]. Réimprimé avec la permission de Liang et ses collaborateurs. Copyright 2014 American Chemical Society.

Les fibres sont regroupées en paquets de fibres de diamètre total 100 nm, ce qui est différent de Liang et ses collaborateurs qui observent des fibres uniques de diamètre 5,3 nm. [19] L'arrangement des peptides à l'échelle moléculaire est ici étudié grâce à des mesures spectroscopiques de dichroïsme circulaire (CD) et d'analyse infrarouge (IR)). En effet, l'article mentionne une bande à 215 nm en CD qui est la marque de feuillets β, cette structure secondaire souvent observée dans les protéines et enzymes est confortée par une bande d'absorption à 1640 cm^{-1} en IR typique de l'élongation de la fonction carbonyle impliquée dans une liaison peptidique. Malgré les informations combinées à l'échelle moléculaire aucune structure atomique n'est proposée dans cet article.

Ces deux articles présentent surtout les interactions à l'échelle moléculaire tels que les empilements

$\pi - \pi$ et la présence de liaisons hydrogène tout en proposant un arrangement moléculaire hypothétique. Les informations à l'échelle moléculaire sont donc très limitées pour ce peptide.

2.2 Les travaux de mon groupe d'accueil sur le Fmoc-FFY

Mon équipe d'accueil à l'Institut Charles Sadron a publié plusieurs articles utilisant le Fmoc-FFY.[9, 21-28] L'objectif principal du Dr. Vigier-Carrière, la première doctorante de l'équipe à travailler sur ce peptide, était de déposer des enzymes à la surface d'un substrat par la méthode de couche par couche pour ensuite contrôler localement l'assemblage du peptide. [21] Après déphosphorylation et auto-assemblage, cette méthode permet de générer un gradient de densité de fibres à partir de la surface du substrat. Même si cet article ne propose pas d'hypothèse sur l'organisation moléculaire, l'analyse infrarouge de l'auto-assemblage montre la présence de liaisons hydrogène entre les peptides associée soit à un assemblage en feuillets β anti-parallèles ou à une liaison hydrogène impliquant le carbamate du Fmoc comme le montre la Figure 4.

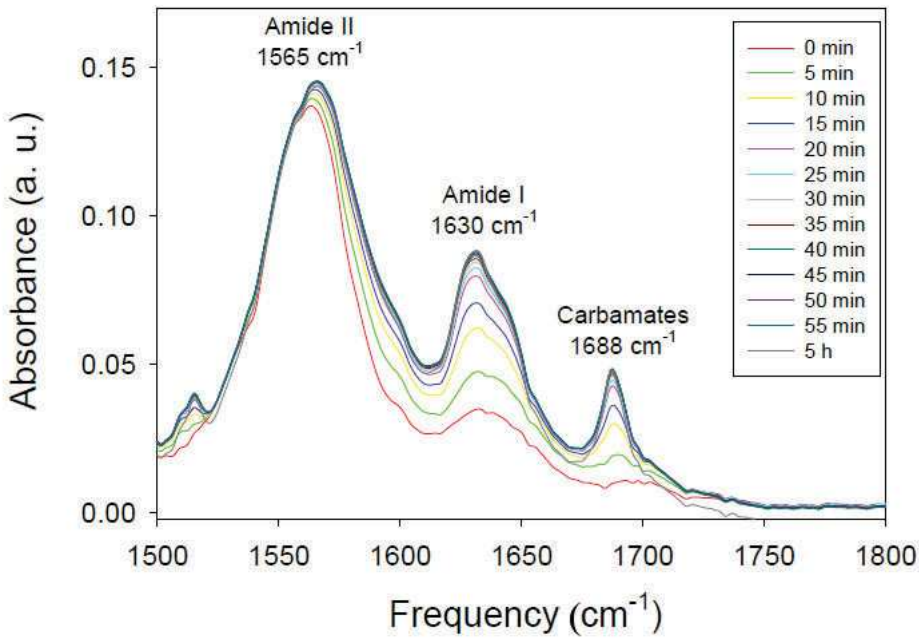

FIGURE 4 – Spectre infrarouge ATR-FTIR en fonction du temps après ajout de 0,9 mM de Fmoc-FFpY sur un film multicouche de PEI-(PSS/PAH)-ALP-(PAH/PAA-CFF-Fmoc). Issu de l'article de Jierry et ses collaborateurs[21]. Réimprimé avec permission des auteurs, Copyright 2015 John Wiley & Sons, Inc.

Un autre article a comme objectif d'utiliser les hydrogels comme hôte support pour des nanotubes de carbone et afin de permettre la libération contrôlée de doxorubicine par amorçage à l'aide d'une impulsion dans l'infrarouge proche qui résulte de la collaboration avec le Dr. MERTZ de l'IPCMS à Strasbourg[23]. La figure 5 ci-dessous montre le montage d'irradiation employée ainsi que le relarguage de doxorubicine à partir des gels chauffés par irradiation.

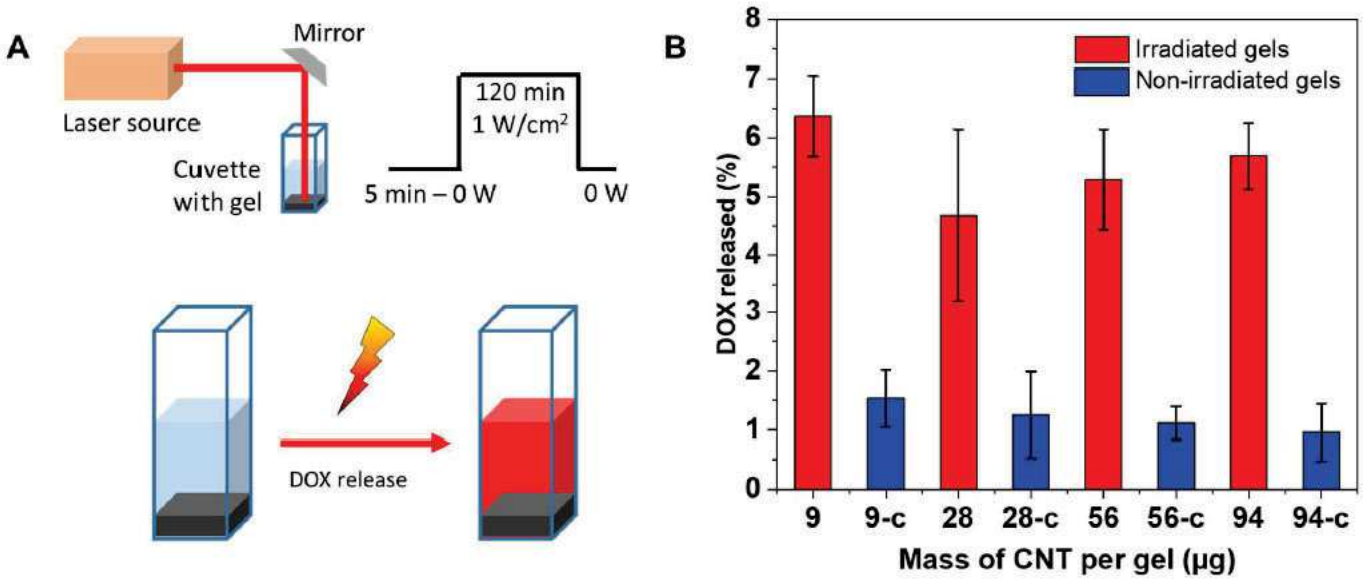

FIGURE 5 – (a) Schéma du montage pour l'irradiation dans le proche infrarouge et principe de libération de la doxorubicine sous irradiation. (b) Relarguage de doxorubicine (% par rapport à la charge initiale) après irradiation dans le proche infrarouge pendant 2h à 1 W/cm^{-2}. Issu de l'article de Mertz et ses collaborateurs[23]. Réimprimé de la publication avec la permission d'Elsevier.

Mon groupe d'accueil s'est également focalisé sur d'autres applications telles que les revêtements antimicrobiens [9] et la séparation de phase dans les hydrogels grâce à la localisation de l'enzyme sur des nanoparticules.[27]

Nous venons de voir qu'il existe un nombre limité d'articles qui traitent de la résolution de structure du Fmoc-FFY et que le recoupement des informations ne permet pas de converger vers un modèle à l'échelle moléculaire. Néanmoins, comme évoqué précédemment, la structure de ce peptide est inspirée d'une approche combinée entre l'EASA via la tyrosine phosphate (pY) et le motif Fmoc-FF. C'est cette dernière séquence, avec la variante sans Fmoc, qui a été majoritairement étudiée au cours des 20 dernières années et qui sera présentée dans la partie suivante.

Les points clef de cette section sont :

- La structure du Fmoc-FFY est une combinaison de l'approche EASA (via le motif pY) et d'une étude sur les peptides hydrophobes (FF).
- Une structure du Fmoc-FFY autoassemblé a été proposée avec 5 peptides formant une couronne. Chaque élévation de la fibre conduit à une rotation de ce motif par rapport au plan du dessous distant de 0,4 nm.
- En fonction de la méthode d'autoassemblage les fibres possèdent des diamètres différents.
- Mon groupe d'accueil a montré que la liaison hydrogène avec le carbamate du Fmoc est sûrement impliquée dans le processus d'autoassemblage.

- De nombreuses applications et de préparation de gels supramoléculaires ont été investiguées dans le domaine biomédical.

3 Motif FF, une séquence avec différentes structures

L'objectif de cette partie est de présenter quelles sont les structures supramoléculaires constituées du dipeptide FF, un motif présent dans le Fmoc-FFY.

La séquence FF est l'une des plus petites séquences peptidiques qui a la capacité de s'auto-assembler. Composée de deux phénylalanines liées par une liaison amide, le FF va, via différentes méthodes d'amorçage, s'assembler et produire des gels supramoléculaires.[29] Cependant, la structure dépend de la méthode et des conditions de l'auto-assemblage. Une présentation, non exhaustive, des nanostructures obtenues est illustrée dans la Figure 6.

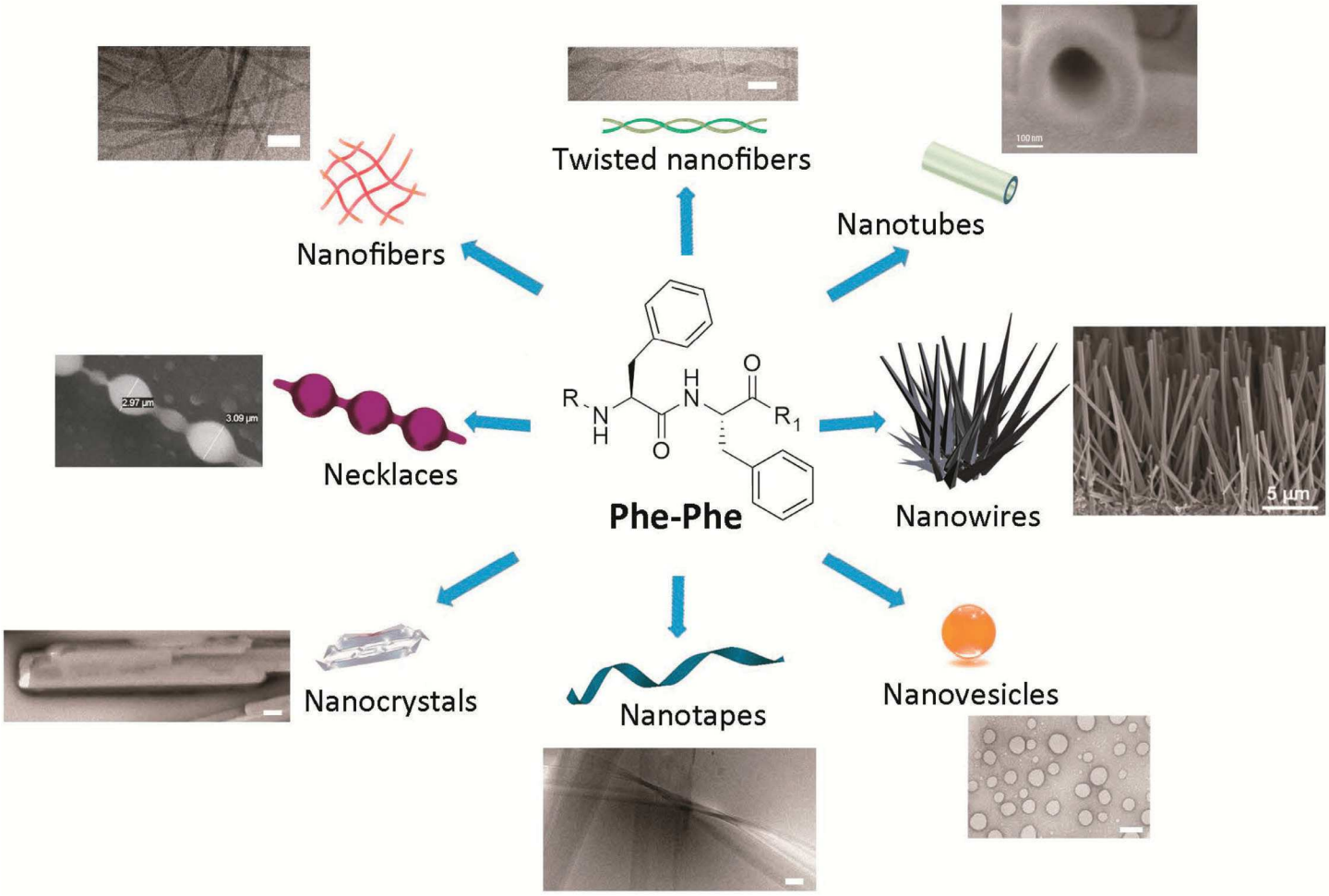

FIGURE 6 – Composés simples portant le motif Phe-Phe qui s'auto-assemblent selon différentes morphologies. Les échelles font 100 nm sauf mentionné autrement. Issue de l'article de Styan et ses collaborateurs [29]. Reproduit avec la permission de MDPI.

En dissolvant le FF dans de l'hexafluoro-2-propanol (HFP) et en le déposant sur une plaque de

verre siliconée avec de l'eau contenant des particules de Fe_3O_4, il est possible d'aligner des nanotubes à base de FF via l'application d'un champ magnétique lors de l'évaporation du solvant.[30] Cela conduit à des nanofils alignés perpendiculairement au substrat. Il est possible de réaliser un collier de perles en utilisant la même méthode d'évaporation d'HFP en rajoutant du Boc-FF ce qui va induire un co-assemblage différent de celui observé précédemment. [31] Dans le même article publié par Reches en 2012 la modulation de la structure d'assemblage est possible en variant la concentration des deux co-assembleurs. Une faible concentration en FF comparativement au Boc-FF donne lieu à une structuration en sphères. Lorsque la concentration en FF augmente les colliers de perles commencent à se former. Il a été montré également par Gazit en 2003 que des nanotubes de FF peuvent être obtenus après dilution dans l'eau d'une solution de FF à 100 mg/mL dans le HFP.[32] Cela prouve que le motif FF peut conduire à une variété de structures en fonction des conditions de préparation. On peut supposer que l'architecture à l'échelle moléculaire pourrait être également différente dans chaque assemblage.

Les méthodes principalement utilisées pour identifier les structures moléculaires et atomiques sont très majoritairement des techniques de microscopie électronique et à force atomique. De plus, la diffraction des rayons X de cristaux de peptides assemblés pour obtenir une structure atomique est également une méthode très prisée même si elle ne rend compte que de la structure cristalline non solvatée.[**2021**, 33-39] En 2010, Ihee et ses collaborateurs ont montré qu'une transition de structure à base de dipeptide FF existait en solution et que l'on pouvait passer de l'une à l'autre via une modification des conditions physico-chimiques (Figure 7)[40].

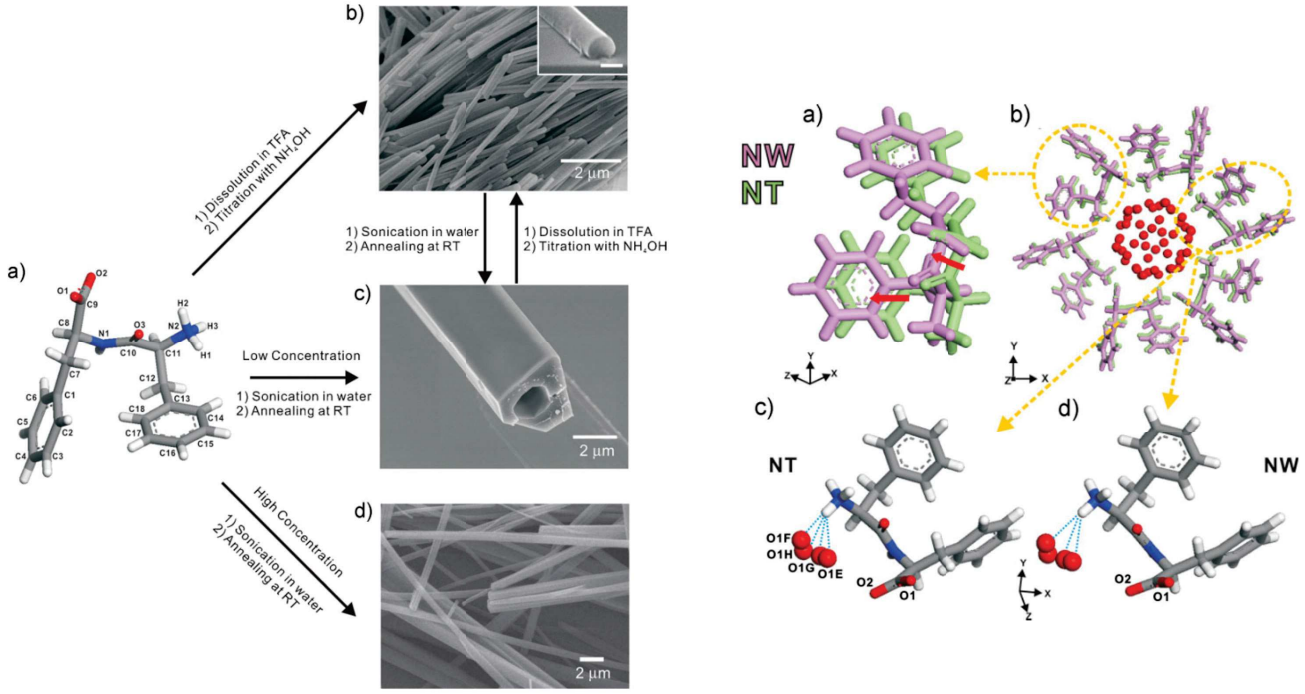

FIGURE 7 – A gauche. Préparation des nanotubes et nanofils de diphénylalanine avec leurs morphologies respectives. (a) Structure moléculaire de la diphénylalanine issue de la structure cristalline connue avec la numérotation atomique de Görbitz[16]. (b) Les nanofils sont préparés par la méthode de titration. Durant cette étape un précipité blanc s'est formé proche des conditions isoélectriques. L'échelle de la sous image est de 200 nm. (c) Nanotubes préparés à partir d'une concentration faible (< 2,5 mg/mL) de diphénylalanine par sonication et un cycle de chauffage puis refroidissement dans de l'eau neutre déionisée. (d) Nanofils préparés à partir d'une forte concentration (> 2,5 mg/mL) de diphénylalanine par sonication et un cycle de chauffage puis refroidissement dans de l'eau neutre déionisée. La limite de la concentration en diphénylalanine est atour de 2,5 mg/mL. Nanotubes et nanofils peuvent être préparés sélectivement par ajustement des conditions de réaction.

A droite. Comparaison des arrangements moléculaires de diphénylalanine dans les nanotubes (NT) et nanofils (NW) dans une maille hexagonale après l'amélioration de Rietveld. (a) Superposition de la structure molécules des nanotubes (vert) et nanofils (magenta) ; visualisation du décalage translationnel relatif (flèches rouges) des modèles moléculaires. (b) Superposition des mailles hexagonales des nanotubes et nanofils vus selon l'axe *c*. Les cercles rouges représentent les molécules d'eau centrales de taille arbitraire, les atomes d'hydrogène sont omis. (c) liaisons hydrogène intermoléculaires (ligne en pointillés bleus, autour de 2,5 Å) entre les diphénylalanines et l'eau dans les nanotubes. (d) liaisons hydrogène intermoléculaires dans les nanofils.

Issues de l'article de Ihee et ses collaborateurs [40]. Copyright 2010 John Wiley & Sons, Inc.

Les auteurs présentent des structures cristallines de nanotubes et nanofils. Il n'existe pas de différences majeures entre les deux structures mis à part le voisinage de l'eau aux alentours de l'amine terminale et un décalage spatial. Les édifices sont des structures en équilibre les unes avec les autres. Pour transitionner il est nécessaire de passer une barrière énergétique par chauffage ou de changer le pH de la solution.

L'assemblage du FF présente une variété de structure importante qui dépend des conditions de préparation de l'échantillon mais également du milieu dans lequel il est présent. Pour accentuer le caractère hydrophobe du FF, Ulijn et ses collaborateurs se sont inspirés partiellement de la structure

de Bing Xu publié en 2004 en rajoutant le fluoromethoxycarbonyle en position N-terminale conduisant au Fmoc-FF.

Les points clefs à retenir de cette section sont les suivants :

- Le dipeptide FF présente différentes structures en fonction de la méthode d'auto-assemblage.
- Il est possible de changer de nanostructure via un stimulus physique et/ou chimique.
- La détermination de la structure n'est pas triviale à obtenir et varie selon la préparation de l'édifice supramoléculaire.

4 L'ajout du Fmoc en position N-terminale

L'objectif de cette partie est de présenter des exemples de la littérature où le Fmoc a été introduit dans la séquence du peptide pour accentuer l'effet hydrophobe. Une description de la structure obtenue ainsi qu'une discussion sur la flexibilité du groupement carbamate entre le peptide et le Fmoc est également évoquée.

Il a été montré par Bing Xu en 2004 que le moteur de l'assemblage des Fmoc-Y est l'empilement $\pi - \pi$ entre les groupements aromatiques et principalement entre les Fmocs. Ainsi l'introduction du Fmoc dans la séquence permet d'accentuer cette interaction. Ulijn et ses collaborateurs ont montré en 2008 la différence dans les assemblages des peptides Fmoc-FF et Fmoc-F.[41] Le premier dipeptide a la capacité de gélifier dans l'eau alors que l'acide aminé contenant un Fmoc ne forme pas de gel dans les mêmes concentrations molaires. Ce qui permet donc, en comparant avec l'article de Xu et ses collaborateurs de 2004, de faire une hypothèse : le Fmoc-Y est un cas particulier pour les acides aminés fonctionnalisés. Néanmoins, Ulijn et ses collaborateurs ont étudié l'assemblage du Fmoc-FF et ont découvert via une analyse IR qu'il y existe des liaisons hydrogène entre les peptides composant l'hydrogel qui conduisent à la formation de feuillets β anti-parallèles grâce à l'identification des bandes d'absorption à 1630 et 1685 cm^{-1} (Figure 8). Les bandes d'absorption infrarouge ont été attribuées de manière analogue à ce qui a été découvert et interprété pour les protéines.[42] La présence de ces feuillets a été confirmée par spectroscopie fluorescence avec un décalage des bandes d'émission de 320 à 330 nm à partir d'une excitation à 280 nm, ce qui est une caractéristique de l'auto-assemblage des peptides contenant un Fmoc.

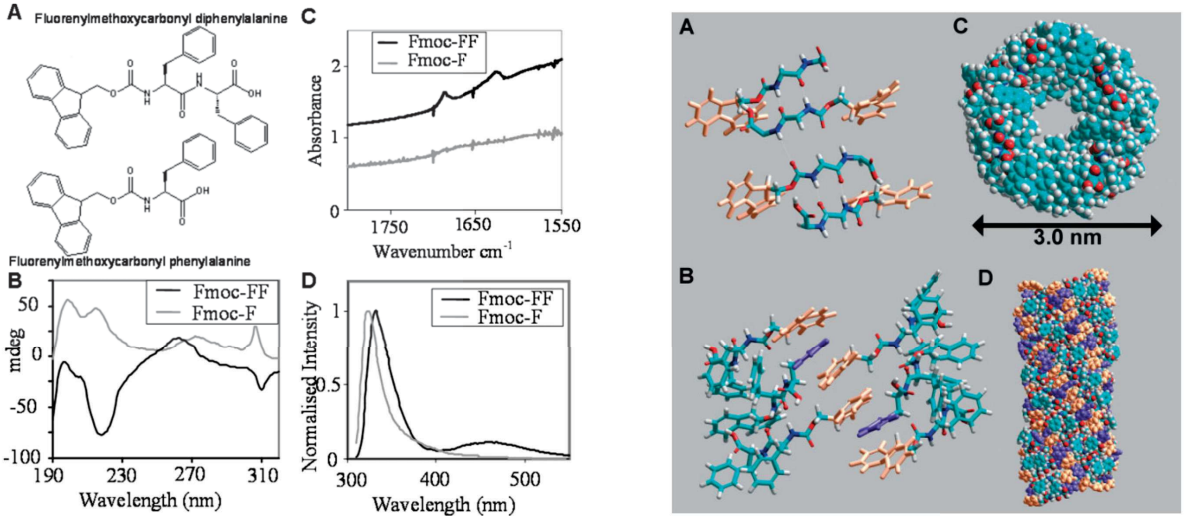

FIGURE 8 – A gauche. Structure moléculaire du Fmoc-FF et Fmoc-F (a). Dichroïsme circulaire du Fmoc-F et Fmoc-FF, le minimum à 218 nm pour le Fmoc-FF est en accord avec une structure en feuillets β (b). Spectre FTIR du Fmoc-FF dans la région de transition de l'amide I, la région du spectre présente deux pics distincs du Fmoc-FF en accord avec un feuillet β antiparallèle (c). Spectre d'émission de fluorescence du Fmoc-FF qui montre un décalage de 320 à 330 nm indicatif de la formation d'un excimer et la présence d'un nouveau pic à 460 nm est indicatif de la formation d'agrégats.
A droite. Modèle moléculaire proposé de Fmoc-FF arrangé en feuillets β anti-parallèles. (a) imbrication des groupements Fmoc issu de l'alternance de feuillets β pour créer des paires d'empilement π avec l'entrelaçage des phénylalanines (b). A cause de la rotation des feuillets β le deuxième feuillet doit être tourné de façon relative au premier pour maintenir une interaction entre les groupements fluorényles créant une structure cylindrique vue du dessus (c) de la structure et de côté (d). L'énergie de la structure a été minimisée avec le champ de force d'Amber. Dans le (a), (b) et (d) les groupements fluorényles sont colorés en orange et les groupements phényles sont colorés en violet pour illustrer la paire d'empilement π. Issu de l'article d'Ulijn et ses collaborateurs [41]. Copyright 2008 John Wiley & Sons, Inc.

En combinant toutes ces informations Ulijn et ses collaborateurs ont pu présenter une structure qui contient 28 monomères par tours, avec un diamètre de 30 Å et une cavité centrale de 7 Å. La structure obtenue est identifiée comme un nanotube. Cette hélicité présente au sein de la nanofibre est identifiée grâce au dichroïsme circulaire qui montre une bande d'absorption à 307 nm et attribuée par Bing Xu en 2004, comme étant due à l'hélicité du Fmoc assemblé. Pour autant, il n'y a pas dans l'article de description des paramètres hélicoïdaux. La composante à 218 nm en CD confirme également la présence de feuillets β. Le modèle proposé présente de l'empilement $\pi - \pi$ entre les différents groupements aromatiques incluant le Fmoc : Fmoc-Fmoc et Fmoc-Phe. L'arrangement peptidique se fait en anti-parallèle et il y a présence de liaisons hydrogènes entre les liaisons peptidiques. La cavité centrale est de diamètre presque identique à celle déjà trouvée pour le FF dans le cristal (10 Å [16]). Cela voudrait dire que le Fmoc en position terminale ajoute effectivement un aspect d'empilement $\pi - \pi$ et d'orientation des peptides en feuillets β anti-parallèles.

Dans un article publié en 2013 Ulijn et ses collaborateurs présentent l'intérêt du Fmoc dans le processus d'auto-assemblage.[43] Ils ont montré que dans le peptide Fmoc-espaceur-tyrosine-leucine

(Fmoc-espaceur-YL) la flexibilité du fluorényle en position N-terminale modulée par des espaceurs chimiques a une grande influence sur la restriction conformationnelle et ainsi les capacités du peptide à s'auto-assembler (Figure 9).

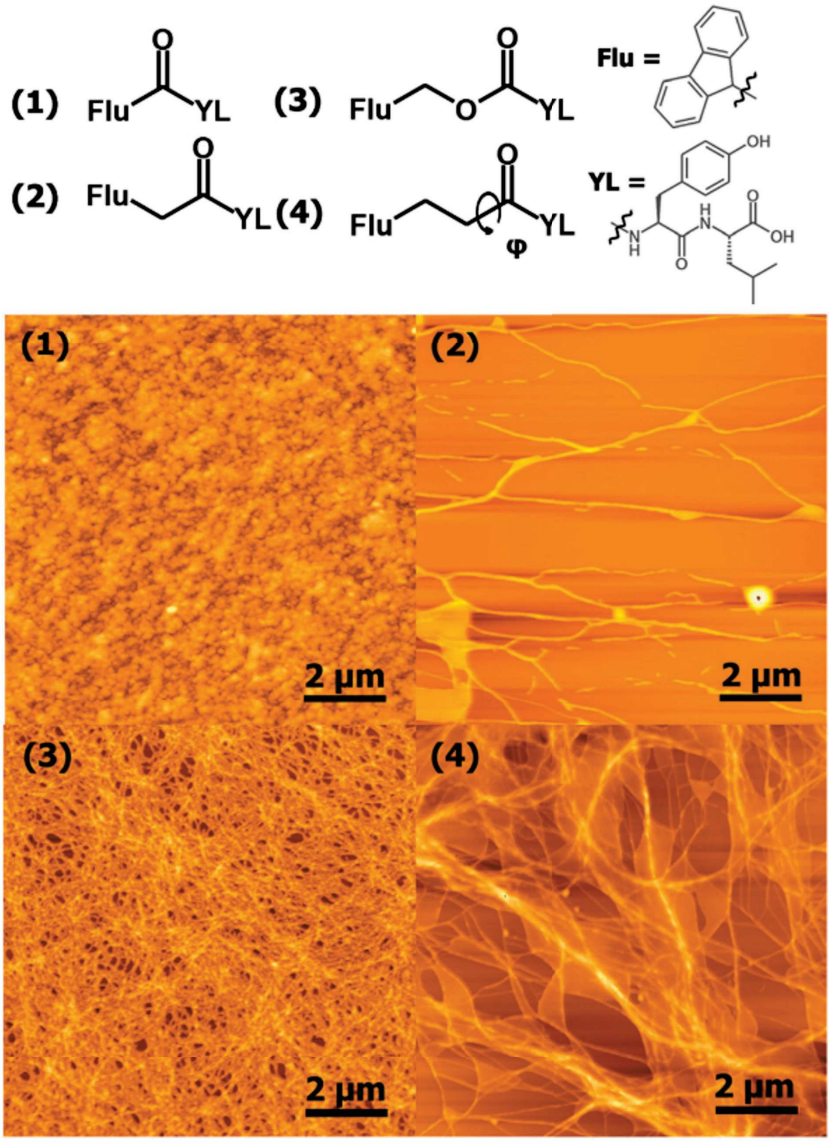

FIGURE 9 – En haut, les quatre structures de Fluorocarbonyles étudiés dans l'article avec différentes flexibilités de chaînes, allant de 1 à 4. En bas, images de microscopie à force atomique (AFM) des gels dans l'eau issus des quatre structures présentées. Reproduit de la référence [43] avec la permission de la Royal Society of Chemistry.

Les auteurs concluent qu'en fonction de la rigidité il est possible de restreindre certaines conformations et ainsi obtenir des édifices de structures différentes. Plus l'espaceur chimique entre le fluorényle et le dipeptide est rigide plus l'hydrogélation (et également l'auto-assemblage) est facilitée dans l'eau.

En 2020 Gazit et ses collaborateurs ont publié un article dans *Angewandte Chemie Int. Ed.* où ils ont modulé la structuration d'un réseau 3D de peptides en modifiant le ratio Fmoc-FF/FF. [44] Une partie de l'étude est effectuée par dynamique moléculaire gros grains. Leur résultat principal est la modulation de la structure par augmentation du ratio de Fmoc-FF/FF (Figure 10).

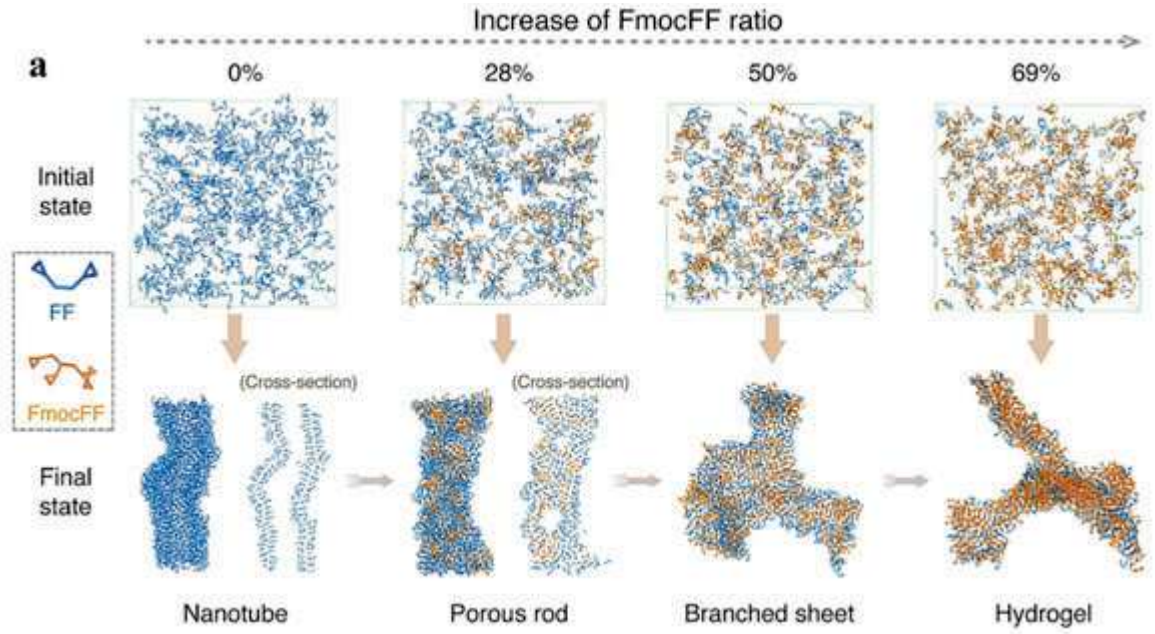

FIGURE 10 – Autoassemblages de FF et co-assemblage de FF/Fmoc-FF à différents ratios massiques de Fmoc-FF. (a) Images de la situation initiale aléatoire et des configurations après 10 μs de dynamique pour les quatre systèmes avec augmentation du ratio massique de Fmoc-FF. Issu de la publication de Gazit et ses collaborateurs [44]

Les auteurs ont montré que la dynamique moléculaire gros grains permet de bien reproduire la formation de nanotubes pour des FF dans la boîte après 1,5 µs de dynamique. La structure est modifiée par l'ajout successif de Fmoc-FF dans la boîte de simulation, et conduit à une fibre poreuse à l'état final de la simulation lorsque le ratio massique de Fmoc-FF/FF atteint 28%. En augmentant encore ce ratio à 50% la structure commence à changer vers des feuillets branchés. Lorsque le ratio atteint 69% la structuration finale est décrite comme étant celle d'un hydrogel sans autre information supplémentaire. L'un des avantages à utiliser la dynamique moléculaire comme outil d'étude est de pouvoir obtenir la structure 3D des peptides et les interactions entre les résidus (Fmoc, Phe) qui les composent (Figure 11).

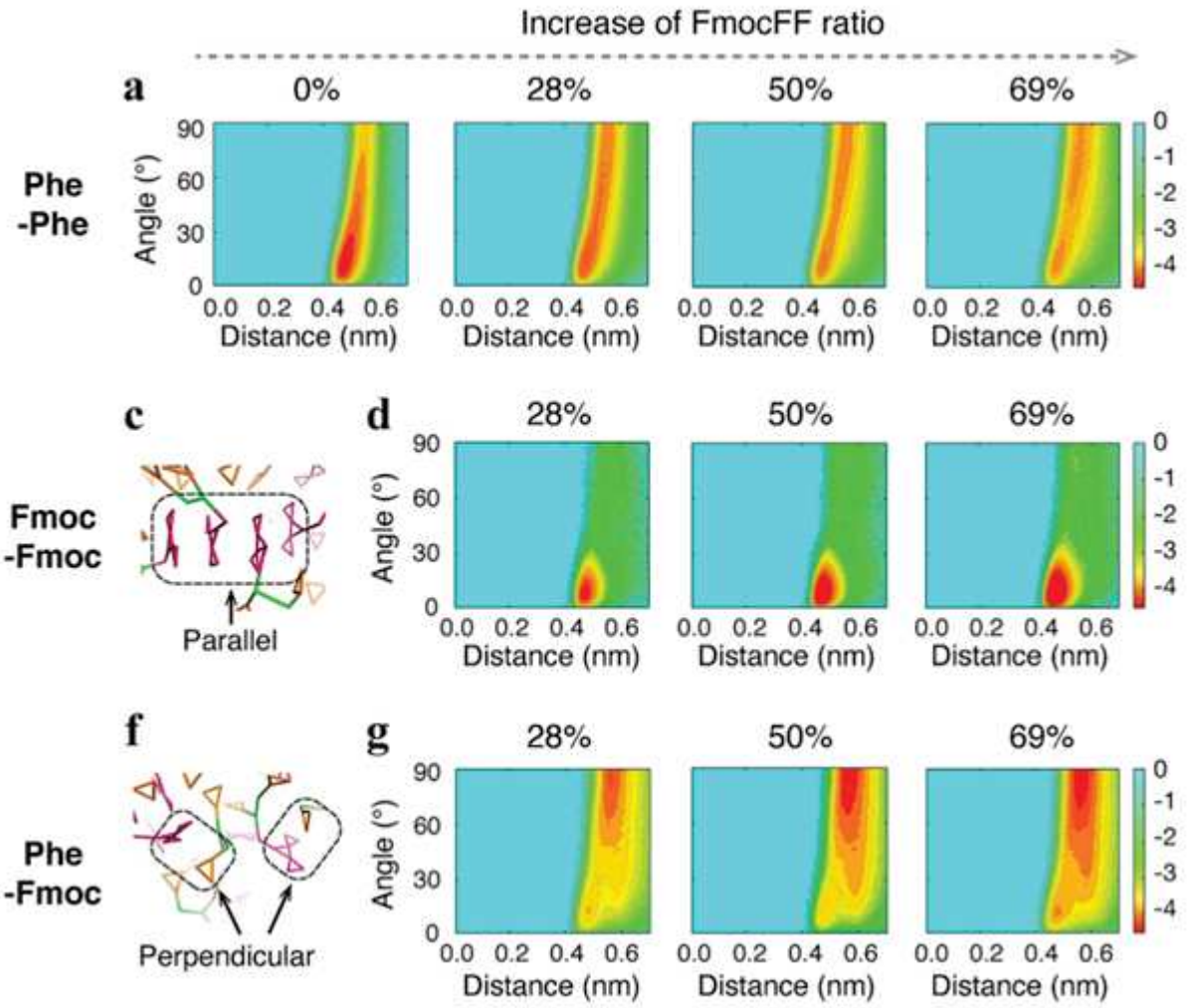

FIGURE 11 – Analyse de l'interaction via des empilements aromatiques qui dirigent la formation des nanostructures variées.(a) Surface d'énergie libre de l'empilement Phe-Phe tracée comme une fonction des centres de masse et des angles formés dans le système du FF auto-assemblé et dans les systèmes FF + Fmoc-FF coassemblés avec différents ratios massiques de Fmoc-FF. (c) Empilement parallèle des Fmoc-Fmoc et (f) empilement perpendiculaire du Fmoc-Phe. (d) identique à (a) mais pour le Fmoc-Fmoc. (g) identique à (a) mais pour la paire Phe-Fmoc. Issu de la publication de Gazit et ses collaborateurs [44]. Copyright 2020 John Wiley & Sons, Inc.

Les auteurs ont analysé les corrélations entre les angles et les distances des plans formés entre résidus. La conclusion principale est que l'arrangement Fmoc-Fmoc parallèle est l'une des causes de la formation de l'hydrogel alors que la composante Phe-Fmoc qui est un empilement $\pi - \pi$ perpendiculaire tend à diriger la structuration vers un feuillet branché. Les interactions différentes permettent de diriger l'édification de l'assemblage.

Nous venons donc de voir que le Fmoc a une importance capitale sur la structure des assemblages. Ce groupement en position N-terminale favorise les empilement $\pi - \pi$ entre peptides. La flexibilité de la chaîne entre le peptide et le Fmoc a également une influence, plus la chaîne est rigide plus le nombre de conformations diminue et plus l'hydrogélation devient favorable. Il a également été montré que dans un co-assemblage de Fmoc-FF/FF les interactions avec les Fmoc pouvaient permettre

de moduler la structuration à l'échelle moléculaire. Ainsi, le Fmoc a un double rôle : (i) favoriser l'hydrogélation via des interactions $\pi - \pi$ et (ii) moduler les structures d'auto-assemblages.

Cependant, dans toutes les méthodes présentées il n'y en a pas une seule qui permet d'avoir la structuration à l'échelle moléculaire à l'état solvaté. Il est toujours nécessaire de soit passer par un cristal soit d'obtenir uniquement des informations sur les interactions. Dans la prochaine section nous évoquerons une méthode qui permet d'accéder aux coordonnées atomiques des peptides auto-assemblés dans l'eau.

Les points clefs de cette section 4 sont les suivants :

- L'ajout du groupement fluorénylmethoxycarbonyle en position N-terminale du peptide permet de favoriser l'empilement $\pi - \pi$.
- La modification de la flexibilité de la chaîne entre le fluorényle et le peptide permet de moduler la nanostructure des assemblages.
- Une autre méthode de modulation est l'incorporation d'un co-assembleur hydrophobe tel que le FF.
- Les interactions entre groupements Fmoc sont favorisées vis-à-vis des interactions entres autres résidus hydrophobes dans la séquence peptidique (*i.e* Phe-Phe).

5 La détermination de structure à l'échelle moléculaire

L'objectif de cette section est de montrer comment la reconstruction d'images de cryo-MET permet d'obtenir le modèle moléculaire dans la nanofibre et l'arrangement spatial des peptides et de présenter des exemples de la littérature sur les peptides auto-assemblés.

Dans le monde de la détermination de structure à l'échelle moléculaire, les biologistes ont quelques années d'avances sur les chimistes. En effet, dans la discipline de la biologie structurale, il est aujourd'hui aisé d'obtenir les coordonnées atomiques des macromolécules comme les protéines, les enzymes ou d'autres complexes issus du vivant. [45-47] Avant l'apparition de la méthode de reconstruction d'images, les biologistes exploitaient massivement la diffraction des rayons X des protéines cristallisées ainsi que la spectroscopie RMN. Cependant, les données issues des expériences demandaient une longue durée de traitement. Avec l'émergence de la microscopie électronique à transmission à effet cryo dans les années 1980 les biologistes ont pu commencer à reconstruire des protéines, virus et complexes piégés dans la glace. Une deuxième révolution dans les années 2010 avec l'arrivée des cartes graphiques dans les laboratoires a permis de pallier au problème des longues durées

de traitement et d'améliorer la résolution des modèles. En 2012, Sjors Scheres au laboratoire Medical Research Council, à Cambridge, au Royaume-Uni a développé une approche bayésienne empirique pour reconstruire des macromolécules à partir d'un très grand nombre d'images.[45] Le logiciel, nommé RELION (Regularized LIkelihood OptimizatioN), a su s'implémenter rapidement dans les laboratoires du monde entier pour aider les biologistes à obtenir des cartes de projection du potentiel électrostatique de leurs complexes. Ces cartes de densités ont permis d'incorporer des modèles moléculaires des structures à résoudre et ainsi obtenir les informations tant désirées des coordonnées moléculaires. D'abord appliquées aux particules isolées depuis 2012, un travail d'un étudiant au MRC, Shaoda He, a permis d'étendre les capacités du programme aux objets hélicoïdaux en 2017.[48] Cette méthode est une technique de choix pour l'étude des systèmes peptidiques nanofibrillaires auto-assemblés dans l'eau. Nous verrons au sein de cette section quelles sont les différentes informations obtenues et comment la méthode a été appliquée pour des peptides auto-assemblés. Il est nécessaire de préciser que tous les articles présentés ci-dessous dans le domaine l'ont été durant ma thèse qui a démarré en 2020.

5.1 Les principales informations obtenues

La reconstruction d'objets vus en cryo-MET donne des informations à plusieurs échelles. La première information est l'obtention d'une image en 2D issue d'une sommation d'un grand nombre de segments de fibres par classification bayésienne. [45] Il est donc possible de voir une première structuration des édifices. Il est ensuite possible de réaliser la transformée de Fourier de l'image ce qui donne le spectre de puissance. A partir de cette étape les paramètres hélicoïdaux sont accessibles par indexation du cliché de diffraction [49] Cela permet d'avoir un premier aperçu de la structuration moléculaire dans la fibre.

La deuxième information est la carte de projection du potentiel électrostatique. Cette carte est accessible après application des orientations aux particules (des sous images de l'objet d'intérêt, ici une section de fibre, voir Glossaire page 217). Elle permet d'observer l'arrangement du peptide en 3D. Les densités représentent la moyenne des vues cumulées de l'échantillon observées en cryo-MET.

La troisième information est la structuration moléculaire à partir des densités. Il est possible de positionner un modèle moléculaire dans les densités. Après avoir un modèle qui corrèle avec les densités expérimentales il est possible pour le chimiste d'engager une démarche de réflexion sur les conformations des peptides et les interactions pouvant conduire à l'assemblage. Ce chapitre se

focalisera sur deux articles de l'auto-assemblage de peptides courts où la structure a été obtenue par reconstruction d'images cryo-MET.

5.2 Reconstruction d'objets vus en cryo-MET

La publication de Conticello et ses collaborateurs en 2021 dans le journal *Matter* a permis de montrer qu'un octapeptide, le KFE8 (Ac-FKFEFKFE, Ac : groupement acétyle, E : acide glutamique, F : phénylalanine, K : lysine) pouvait présenter deux structures via deux méthodes de préparation de l'auto-assemblage : une à température ambiante et une autre par chauffage-refroidissement (Figure 12)[50].

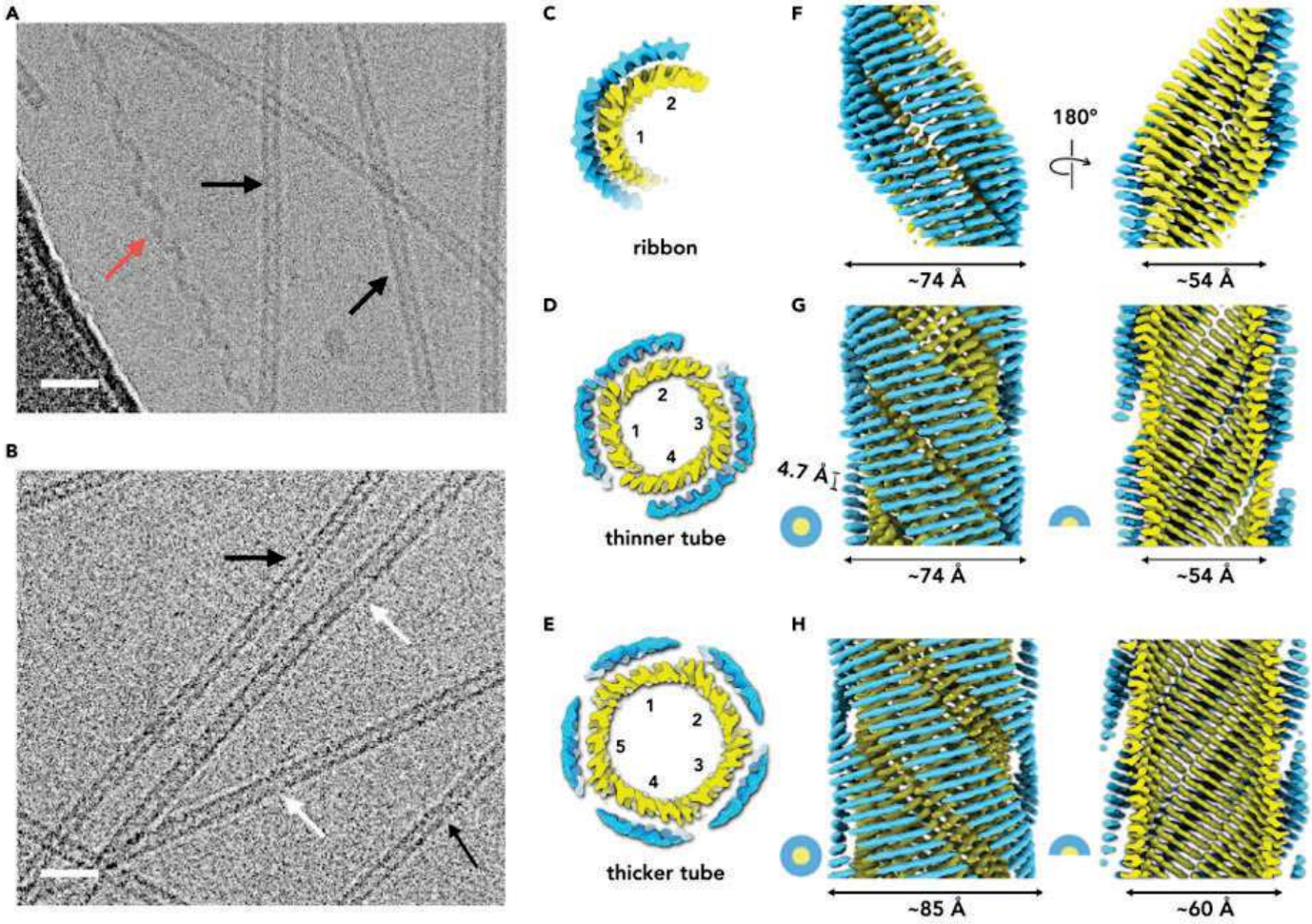

FIGURE 12 – (a) Micrographie de cryo-microscopie de tubes de KFE8 assemblés à température ambiante, l'échelle sur l'image fait 20 nm. Les flèches noires pointes vers les tubes fins et les flèches rouges pointent vers les rubans.(b) Micrographie de cryo-microscopie de tubes de KFE8 assemblés par le processus de chauffage puis refroidissement. Le peptide a été chauffé à 95°C après solubilisation puis lentement refroidi à 20°C, l'échelle sur l'image fait 20 nm. Les flèches en noir pointent vers les tubes fins and les flèches blanches vers les tubes épais. (c-e) Vue du dessus du ruban, tube fin et tube épais. (f-e) Vue de côté de la reconstruction 3D du ruban (f), tube fin (g), et du tube épais (h). La surface extérieure est représentée sur le côté gauche de chaque reconstruction alors qu'une surface coupée révèle le lumen représentée à droite. Issu de l'article de Conticello et ses collaborateurs[50]. Réimprimé avec la permission d'Elsevier.

L'article évoque principalement la structuration en hélice de ce peptide quelque soit la façon dont l'assemblage a été généré. Des différences morphologiques sont principalement observées par le nombre d'unités qui composent la fibre. Les rubans sont composés de deux unités répétitives, alors que les tubes fins en ont quatre et les tubes les plus larges en contiennent cinq. Il est également montré que cet assemblage est constitué, dans toutes les structures, de deux feuillets représentés dans la figure précédente en bleu et jaune. Les cartes de densités de résolution 3,6 Å permettent d'introduire un modèle moléculaire (Figure 13).

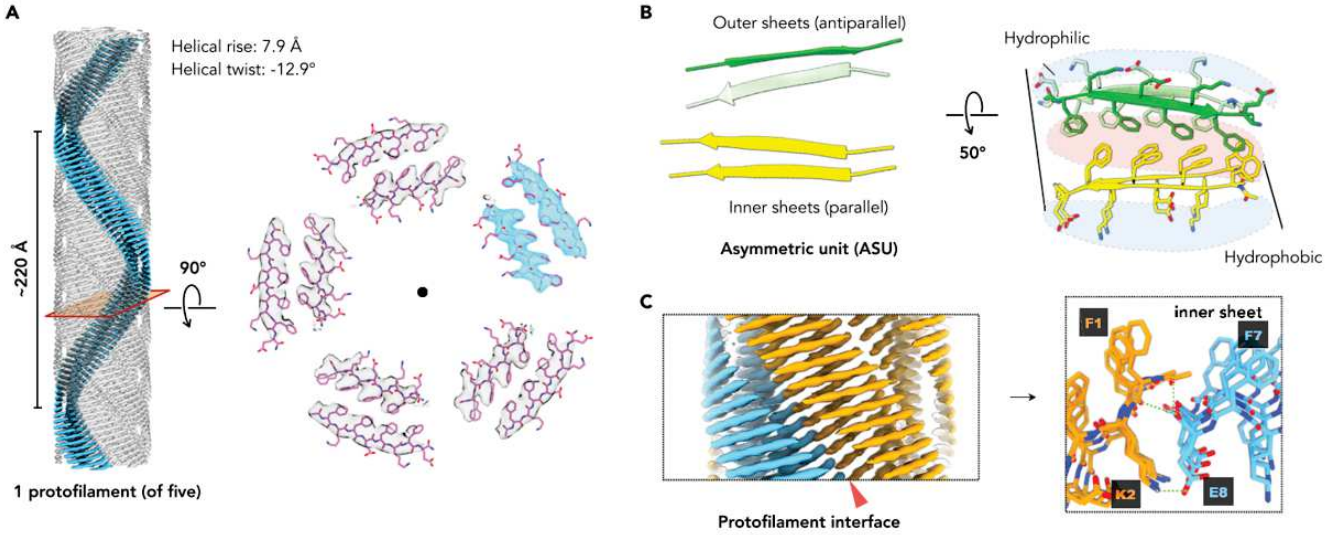

FIGURE 13 – (a) carte de densité de la nanofibre avec un seul protofilament illustré en bleu avec une coupe dans le plan à droite contenant le modèle moléculaire proposé, (b) représentation des unités asymétriques dans la fibre, les zones hydrophobes émergent des interactions entres phénylalanines, (c) interface des protofilaments qui existe uniquement dans la couche intérieure, les liaisons hydrogènes sont représentées en pointillés. Issu de l'article de Conticello et ses collaborateurs [50]. Réimprimé avec la permission d'Elsevier.

En réalisant cette opération il est maintenant possible de voir réellement la structuration et les interactions qui permettent la cohésion de l'édifice. Dans cet article il y a en premier lieu les liaisons hydrogène entre les interfaces des feuillets. Ces liaisons hydrogène ne se retrouvent cependant pas entre les différents étages de l'hélice à cause d'une distance entre plan de 7,9 Å ce qui est beaucoup trop important. Néanmoins, la cohésion est assurée entre les feuillets interne et externe. De plus, on observe des interactions hydrophobes entre les phénylalanines. En effet, une poche hydrophobe est présente à l'interface entre les feuillets qui est uniquement possible par la présence de deux symétries complémentaires de feuillets β parallèles et anti-parallèles. En effet, le feuillet interne possède tous les peptides dirigés dans le même sens ce qui donne un feuillet β parallèle alors que le feuillet extérieur a des peptides en feuillet β antiparallèle. La combinaison des deux permet donc la formation d'une poche interfaciale hydrophobe.

Un article publié dans le journal Cell Reports Physical Science en 2020 a permis de montrer

comment un quadripeptide de chiralité non naturelle, le 1-KMe_3 (Nbd-FFpYK, Nbd : nitrobenzoxadiazole, F : phénylalanine, pY : tyrosine phosphatase, K : lysine) pouvait être déphosphorylé par la phosphatase alcaline dans des cellules d'ostéosarcome qui conduit à l'assemblage du peptide Nbd-FFYK en filaments[51]. Un des résultats majeurs en lien avec les travaux dans ma thèse est la présence d'une structure moléculaire des filaments issue de la reconstruction d'image par cryo-MET pour une séquence peptidique proche de la notre (motif FFY) (Figure 14).

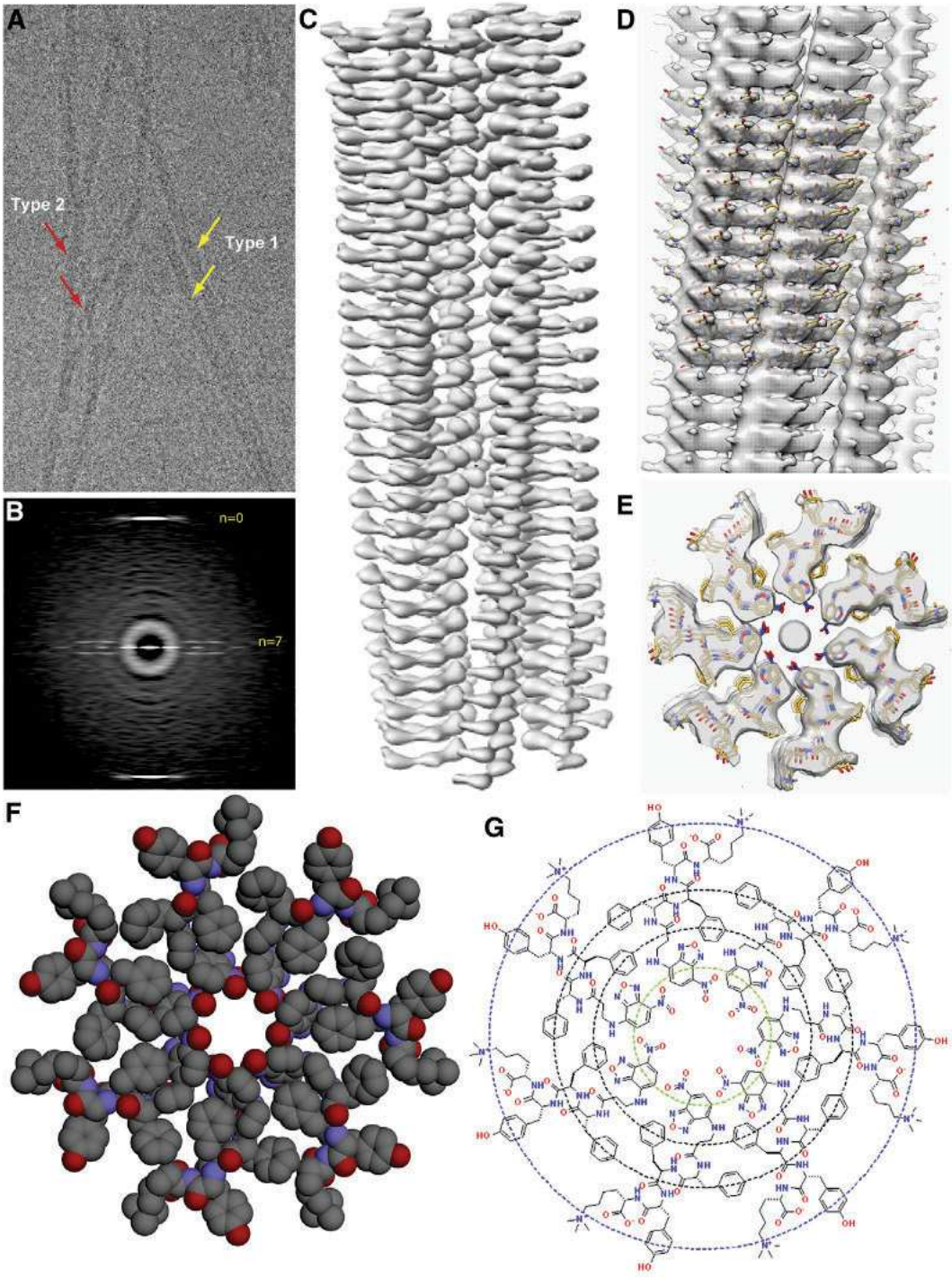

FIGURE 14 – (a) image de cryo-MET de l'échantillon avec les filaments de type 1 en flèche jaune et de type 2 en flèche rouge issu de l'assemblage du peptide 1-KMe_3. (b) spectre de puissance moyen du filament de type 1. (c) reconstruction 3D du filament de type 1 issu des images de cryo-MET. (d) Modèle atomique de la fibre de type 1 avec des feuillets β croisés. (e) vue du dessus de la coupe de la carte de densité du filament de type 1 avec la représentation en bâtons des peptides. (f et g) modèle CPK et structure chimique d'une couche de filament à la coupe (e). Issu de l'article de Xu et ses collaborateurs [51]. Réimprimé avec la permission d'Elsevier.

La symétrie entre les deux types de filaments est différente. En effet, le filament de type 1 possède une symmétrie C_7 et le type 2 a une symmétrie C_2. Le filament de type 1 a une élévation de 4,9 Å et un pas angulaire de 2,3° alors que le type deux a la même élévation mais un pas angulaire de 2,9°. Les résolutions de densité éléctronique sont d'environ 4,3 Å pour le filament de type 1 et aux alentours

de 5 à 6 Å pour le type 2. La résolution de la carte permet d'intégrer un modèle moléculaire et d'interpréter l'arrangement des peptides. La structuration va du N-terminal au C-terminal du centre jusqu'à l'extérieur du filament, le plus hydrophobe au centre (Nbd) et le plus hydrohile à l'extérieur (lysine). L'intérieur du filament possède une densité centrale non attribuée au peptide. Selon les auteurs il serait possible que ce soit de l'eau qui est directement incluse dans le filament. Cependant, ayant imposé une symmétrie C_7 l'interprétation de cette densité n'est plus possible. Pour investiguer ce qui peut être inclus à l'intérieur de la fibre les auteurs ont réalisé la dynamique moléculaire de leurs fibres (Figure 15).

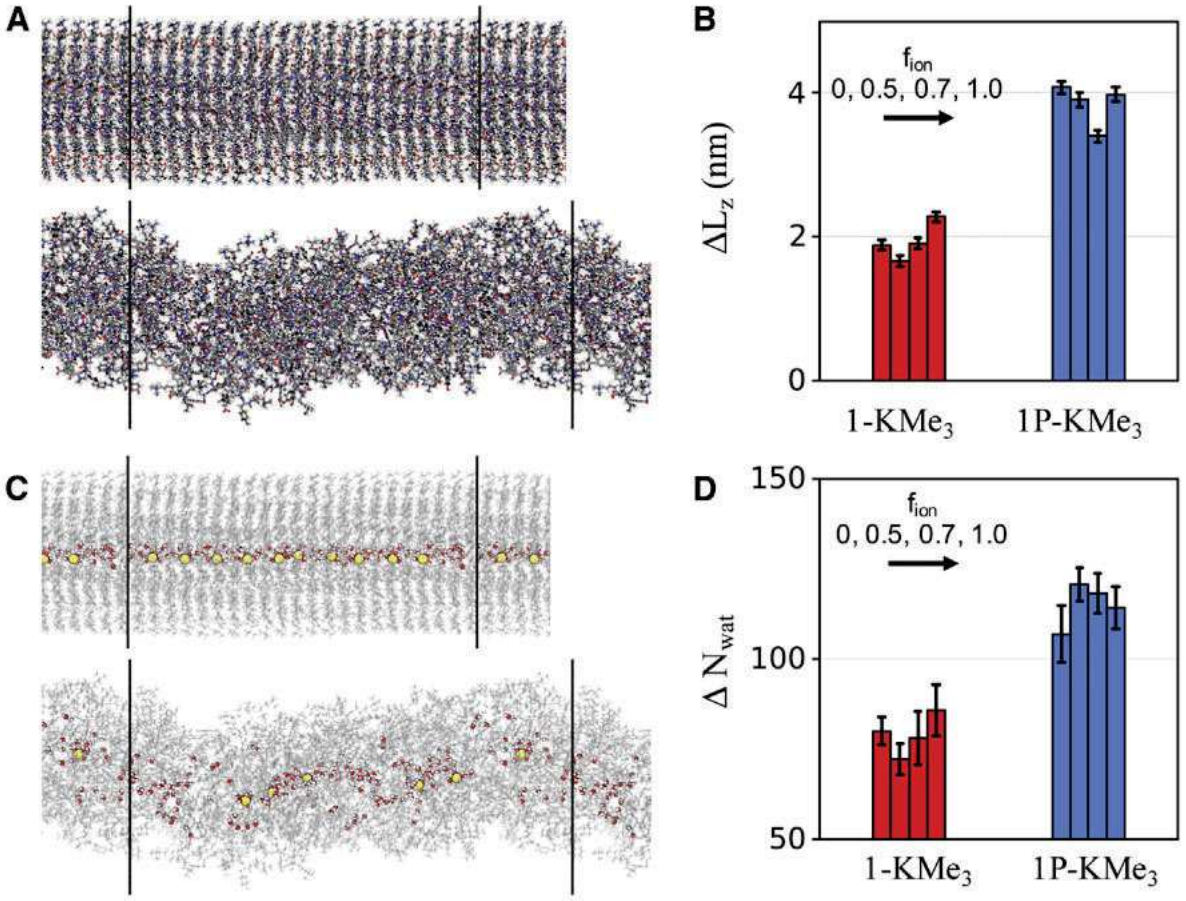

FIGURE 15 – (a) Structure initiale ainsi qu'une image après 50 ns de dynamique du peptide 1-KMe$_3$ avec une fraction en ions de 0,5. Cette fraction donne le nombre d'ions par paire de couche de peptides placés orthogonalement à l'axe du filament. Les ions et l'eau ne sont pas affichés par soucis de clarté, les barres noires représentent les conditions périodiques. (b) longueur d'élongation du filament après 120 ns de dynamique moléculaire pour différents systèmes (1-KMe$_3$ et 1P-KMe$_3$ avec différents nombre d'ions placés au coeur du filament). Les barres d'erreur représentent la déviation standard. (c) distribution d'eau (en rouge) et de cations (en jaune) dans le filament (en gris) dans la structure initiale et après 50 ns de simulation avec le filament de 1-KMe$_3$ avec une fraction en ions de 0,5. (d) nombre de molécules d'eau qui sont maintenues dans le filament après 120 ns de dynamique pour différents systèmes. Les barres d'erreur représentent la déviation standard. Les bares d'erreurs dans le (b) et (d) sont obtenues en utilisant les 10 dernières ns de trois simulations indépendantes de 120 ns chacune. Issu de l'article de Xu et ses collaborateurs [51]. Réimprimé avec la permission d'Elsevier.

La dynamique moléculaire montre que les peptides interagissent majoritairement par des interactions de type van der Waals entre peptides d'un étage à un autre du filament.De plus, la présence d'ions phosphates augmente la longueur d'élongation du filament. Cela destabilise le filament à cause de la répulsion électrostatique des phosphates présents sur la tyrosine. Grâce à la dynamique moléculaire les auteurs ont pu montrer que la cavité centrale peut accueillir des molécules d'eau et du sel. Ce qui laisse supposer que la densité non attribuée dans la cavité pourrait appartenir au solvant.

Ainsi les auteurs ont réussi à reconstruire un modèle moléculaire du 1-KMe_3 grâce à la méthode de reconstructions en cryo-EM. Leur objectif initial était d'analyser l'effet de ces filaments artificiels dans une cellule d'ostérosarcome. La méthode de reconstruction s'applique donc dans un contexte de bio-intégration de filaments synthétiques *in vitro*.

Dans une des reviews publié par Conticello et ses collaborateurs sur les polymères hélicoïdaux il est mentionné un paragraphe sur les peptides courts de moins de cinq amino-acides[17]. La première partie évoque une forme d'interrogation sur le choix des peptides courts. Ces derniers n'ont en effet pas de structure secondaire à cause du trop petit nombre d'acides aminés dans la séquence ce qui empêche par exemple le repliement de la chaîne sur elle-même. Ainsi, par quelles interactions et mécanismes les peptides vont-ils s'auto-assembler ? C'est à cette question que nous nous efforcerons de répondre tout au cours de mon travail de thèse grâce à différentes approches telles que la reconstruction d'images en microscopie électronique à transmission, la dynamique moléculaire classique ainsi que différentes techniques de spectroscopie (CD et diffusion des rayons X). Ceci sera présenté dans le chapitre 4.

Les points clefs de cette partie sont les suivants :

- Il est possible d'obtenir la structuration à l'échelle moléculaire pour des peptides autoassemblés grâce à la reconstruction d'images.
- Certains peptides présentent plusieurs structures distinctes en fonction du mode d'initiation de l'assemblage.
- Des nanofibres de peptides peuvent accueillir un canal interne contenant de l'eau et des ions.
- Les peptides de moins de 5 acides aminés n'ont pas de structure secondaire, ainsi leur mécanisme d'autoassemblage reste encore à être déterminé.

6 Conclusion sur l'état de l'art

Depuis un peu plus d'une vingtaine d'années, les chercheurs s'interrogent sur la structure moléculaire à l'état solvaté des peptides courts auto-assemblés. Depuis quelques années cela est possible

via l'utilisation de la reconstruction d'images en cryo-microscopie électronique à transmission. Les informations d'abord hypothétisées sont maintenant vérifiables et il y a en effet, de l'empilement $\pi - \pi$ entre les groupements aromatiques ainsi que la présence de liaisons hydrogène. La connaissance de la structure à l'échelle moléculaire devient de plus en plus complète. Même si certains points sont encore à identifier, l'augmentation de l'utilisation de la reconstruction et de la combinaison avec des techniques d'analyse spectrales et de dynamique moléculaire devient de plus en plus courante. L'article de Xu et ses collaborateurs publié durant ma thèse traite du peptide proche avec la séquence commune du FFY. En guise de conclusion générale sur les informations obtenues la Figure 16 récapitule les points principaux de chaque structure recherchée dans la bibliographie et le tableau 1 donne un aperçu des avantages et inconvénients de chaque méthode qui a été trouvée dans les articles discutés précedemment.

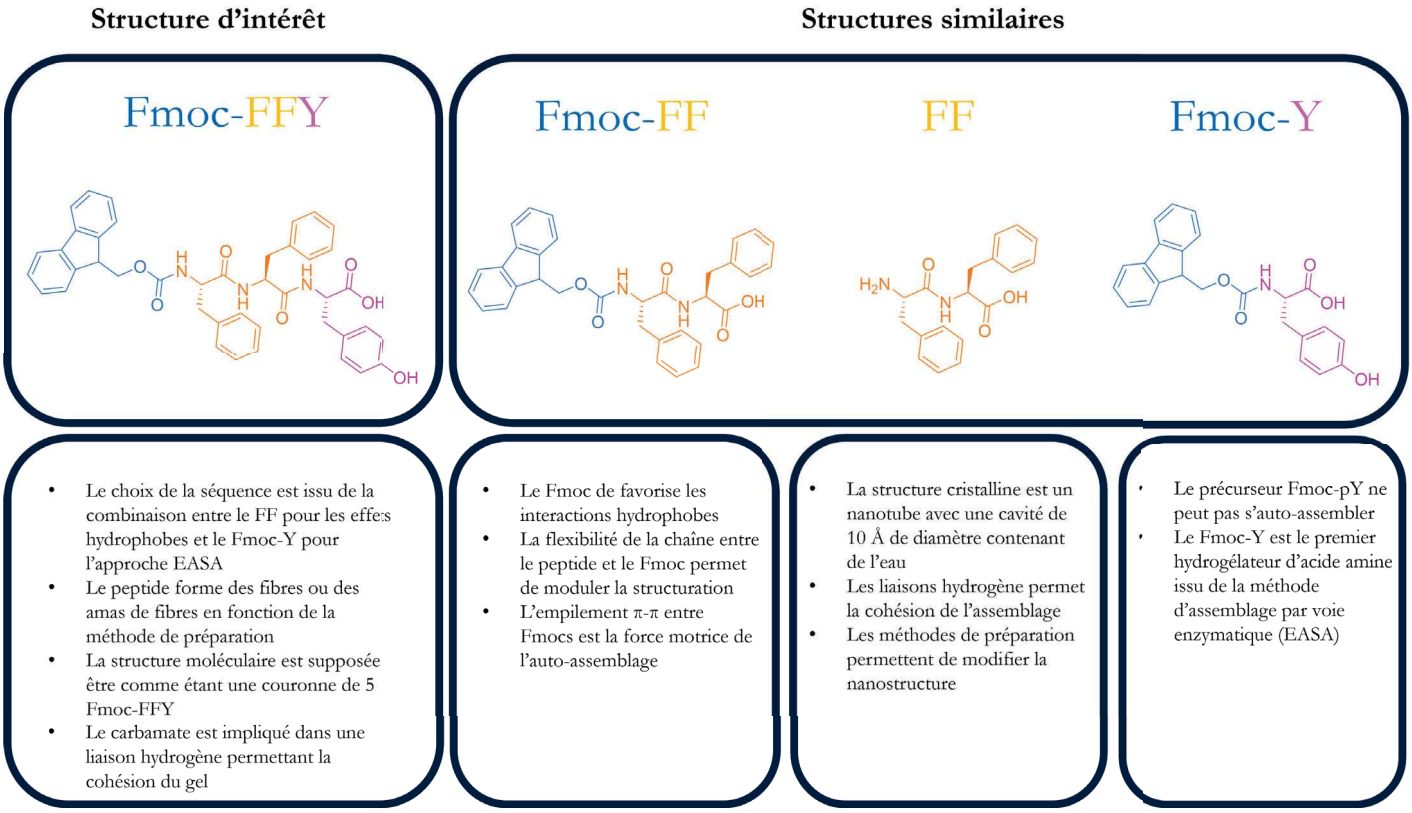

FIGURE 16 – Résumé des informations structurales obtenues pour chaque séquence d'acides aminés étudiés dans la bibliographie.

Tableau 1 – Résumé des méthodes trouvées dans la recherche bibliographique. Les avantages et inconvénients ne sont pas tous présentés dans les articles et ont nécessité des recherches supplémentaires hors du cadre de la bibliographie des peptides auto-assemblés.

Méthodes	**Avantages**	**Inconvénients**
Diffraction des rayons X	Structure cristalline et positions atomiques	Structure non solvatée
Dichroïsme circulaire	Structures secondaires et groupements interagissant entre eux	Informations uniquement sur les interactions et les groupements, pas d'informations sur les coordonnées moléculaires
Infrarouge	Description des liaisons hydrogène impliquées dans l'auto-assemblage et structures secondaires ainsi que les groupements interagissant entre eux	Pas d'informations sur l'organisation moléculaire
Microscopie (confocale, électronique, AFM)	Visualisation des micro- et nano-structures	Informations moléculaires compliquées à obtenir
Dynamique moléculaire	Dynamique des assemblages, de leur formation et des interactions	Possibilité de tomber dans un minima local différent de la structure réelle, échelle de temps restreinte à la microseconde
Reconstruction d'images de cryo-MET	Obtention de l'édifice à l'échelle moléculaire	Structure statique moyennée sur l'observation de centaines de milliers d'images nécessitant un placement manuel du modèle moléculaire avec parfois une limitation en résolution

Dans les chapitres 3, 4 et 5 nous verrons comment nous avons pu déterminer la structure du Fmoc-FFY aux premiers instants de l'assemblage grâce à la dynamique moléculaire (chapitre 3) ainsi que la structure à l'échelle moléculaire grâce à la reconstruction d'images (chapitre 4) et l'évolution de la microstructure par l'ajout d'acide hyaluronique (chapitre 5).

Bibliographie

(1) Matson, J. B.; Zha, R. H.; Stupp, S. I. *Current Opinion in Solid State and Materials Science* **2011**, *15*, 225-235.

(2) Gelain, F.; Luo, Z.; Rioult, M.; Zhang, S. *npj Regenerative Medicine* **2021**, *6*, 1-8.

(3) Guilbaud-Chéreau, C.; Dinesh, B.; Schurhammer, R.; Collin, D.; Bianco, A.; Ménard-Moyon, C. *ACS Applied Materials and Interfaces* **2019**, *11*, 13147-13157.

(4) Palmer, B. C.; DeLouise, L. A. *Molecules* **2016**, *21*, 7-9.

(5) Han, T. S.; Hur, K.; Choi, B.; Lee, J. Y.; Byeon, S. J.; Min, J.; Yu, J.; Cho, J. K.; Hong, J.; Lee, H. J.; Kong, S. H.; Kim, W. H.; Yanagihara, K.; Song, S. C.; Yang, H. K. *Oncotarget* **2017**, *8*, 108848-108858.

(6) Ciolacu, D. E.; Nicu, R.; Ciolacu, F. *Materials* **2020**, *13*, 1-37.

(7) Yaghoubi, A.; Ghojazadeh, M.; Abolhasani, S.; Alikhah, H.; Khaki-Khatibi, F. *Journal of Cardiovascular and Thoracic Research* **2015**, *7*, 113-117.

(8) Huang, G.; Huang, H. *Drug Delivery* **2018**, *25*, 766-772.

(9) Criado-Gonzalez, M.; Iqbal, M. H.; Carvalho, A.; Schmutz, M.; Jierry, L.; Schaaf, P.; Boulmedais, F. *Frontiers in Bioengineering and Biotechnology* **2020**, *8*, 1-9.

(10) Yang, Z.; Gu, H.; Fu, D.; Gao, P.; Lam, J. K.; Xu, B. *Advanced Materials* **2004**, *16*, 1440-1444.

(11) Wang, Z.; Liang, C.; Shang, Y.; He, S.; Wang, L.; Yang, Z. *Chemical Communications* **2018**, *54*, 2751-2754.

(12) Vigier-Carrière, C.; Wagner, D.; Chaumont, A.; Durr, B.; Lupattelli, P.; Lambour, C.; Schmutz, M.; Hemmerlé, J.; Senger, B.; Schaaf, P.; Boulmedais, F.; Jierry, L. *Langmuir* **2017**, *33*, 8267-8276.

(13) Muller, C.; Ontani, A.; Bigo-Simon, A.; Schaaf, P.; Jierry, L. *Advances in Colloid and Interface Science* **2022**, *304*, 102660.

(14) Frederix, P. W.; Ulijn, R. V.; Hunt, N. T.; Tuttle, T. *Journal of Physical Chemistry Letters* **2011**, *2*, 2380-2384.

(15) Frederix, P. W.; Scott, G. G.; Abul-Haija, Y. M.; Kalafatovic, D.; Pappas, C. G.; Javid, N.; Hunt, N. T.; Ulijn, R. V.; Tuttle, T. *Nature Chemistry* **2015**, *7*, 30-37.

(16) Görbitz, C. H. *Chemistry - A European Journal* **2001**, *7*, 5153-5159.

(17) Miller, J. G.; Hughes, S. A.; Modlin, C.; Conticello, V. P. *Quarterly Reviews of Biophysics* **2022**, *55*, e2.

(18) Du, X.; Zhou, J.; Shi, J.; Xu, B. *Chemical Reviews* **2015**, *115*, 13165-13307.

(19) Wang, W.; Qian, J.; Tang, A.; An, L.; Zhong, K.; Liang, G. *Analytical Chemistry* **2014**, *86*, 5955-5961.

(20) Tie, Z. X.; Qin, M.; Zou, D. W.; Cao, Y.; Wang, W. *Chinese Physics Letters* **2011**, *28*, 028702.

(21) Vigier-Carrière, C.; Garnier, T.; Wagner, D.; Lavalle, P.; Rabineau, M.; Hemmerlé, J.; Senger, B.; Schaaf, P.; Boulmedais, F.; Jierry, L. *Angewandte Chemie - International Edition* **2015**, *54*, 10198-10201.

(22) Criado-Gonzalez, M.; Wagner, D.; Iqbal, M. H.; Ontani, A.; Carvalho, A.; Schmutz, M.; Schlenoff, J. B.; Schaaf, P.; Jierry, L.; Boulmedais, F. *Journal of Colloid and Interface Science* **2021**, *588*, 580-588.

(23) Li, B.; Adam, A.; Criado-Gonzalez, M.; Jierry, L.; Bizeau, J.; Chaumont, A.; Harlepp, S.; Mélart, C.; Begin-Colin, S.; Begin, D.; Mertz, D. *Materialia* **2022**, *22*, 101414.

(24) Runser, J. Y.; Criado-Gonzalez, M.; Fneich, F.; Rabineau, M.; Senger, B.; Weiss, P.; Jierry, L.; Schaaf, P. *Journal of Colloid and Interface Science* **2022**, *620*, 234-241.

(25) Vigier-Carrière, C.; Boulmedais, F.; Schaaf, P.; Jierry, L. *Angewandte Chemie - International Edition* **2018**, *57*, 1448-1456.

(26) Criado-Gonzalez, M.; Rodon Fores, J.; Wagner, D.; Schröder, A. P.; Carvalho, A.; Schmutz, M.; Harth, E.; Schaaf, P.; Jierry, L.; Boulmedais, F. *Chemical Communications* **2019**, *55*, 1156-1159.

(27) Criado-Gonzalez, M.; Fores, J. R.; Carvalho, A.; Blanck, C.; Schmutz, M.; Kocgozlu, L.; Schaaf, P.; Jierry, L.; Boulmedais, F. *Langmuir* **2019**, *35*, 10838-10845.

(28) Criado-gonzalez, M. et al. **2020**.

(29) Marchesan, S.; Vargiu, A. V.; Styan, K. E. *Molecules* **2015**, *20*, 19775-19788.

(30) Reches, M.; Gazit, E. *Nature Nanotechnology* **2006**, *1*, 195-200.

(31) Yuran, S.; Razvag, Y.; Reches, M. *ACS Nano* **2012**, *6*, 9559-9566.

(32) Reches, M.; Gazit, E. *Science* **2003**, *300*, 625-627.

(33) Chakraborty, P.; Bera, S.; Mickel, P.; Paul, A.; Shimon, L. J.; Arnon, Z. A.; Segal, D.; Král, P.; Gazit, E. *Angewandte Chemie - International Edition* **2022**, *61*, DOI : 10.1002/anie.202113845.

(34) Arnon, Z. A.; Kreiser, T.; Yakimov, B.; Brown, N.; Aizen, R.; Shaham-Niv, S.; Makam, P.; Qaisrani, M. N.; Poli, E.; Ruggiero, A.; Slutsky, I.; Hassanali, A.; Shirshin, E.; Levy, D.; Gazit, E. *iScience* **2021**, *24*, 102695.

(35) Bera, S.; Mondal, S.; Xue, B.; Shimon, L. J.; Cao, Y.; Gazit, E. *Nature Materials* **2019**, *18*, 503-509.

(36) Adler-Abramovich, L.; Arnon, Z. A.; Sui, X. M.; Azuri, I.; Cohen, H.; Hod, O.; Kronik, L.; Shimon, L. J.; Wagner, H. D.; Gazit, E. *Advanced Materials* **2018**, *30*, DOI : 10.1002/adma.201704551.

(37) Bera, S.; Xue, B.; Rehak, P.; Jacoby, G.; Ji, W.; Shimon, L. J.; Beck, R.; Král, P.; Cao, Y.; Gazit, E. *ACS Nano* **2020**, *14*, 1694-1706.

(38) Pellach, M.; Mondal, S.; Shimon, L. J.; Adler-Abramovich, L.; Buzhansky, L.; Gazit, E. *Chemistry of Materials* **2016**, *28*, 4341-4348.

(39) Mason, T. O.; Chirgadze, D. Y.; Levin, A.; Adler-Abramovich, L.; Gazit, E.; Knowles, T. P.; Buell, A. K. *ACS Nano* **2014**, *8*, 1243-1253.

(40) Kim, J.; Han, T. H.; Kim, Y.-I.; Park, J. S.; Choi, J.; Churchill, D. G.; Kim, S. O.; Ihee, H. *Advanced Materials* **2010**, *22*, 583-587.

(41) Smith, A. M.; Williams, R. J.; Tang, C.; Coppo, P.; Collins, R. F.; Turner, M. L.; Saiani, A.; Ulijn, R. V. *Advanced Materials* **2008**, *20*, 37-41.

(42) Kong, J.; Yu, S. *Acta Biochimica et Biophysica Sinica* **2007**, *39*, 549-559.

(43) Fleming, S.; Sisir, D.; Frederix, P. W.; Tuttle, T.; Ulijn, R. V. *Chemical Communications* **2013**, *49*, 10587-10589.

(44) Chakraborty, P.; Tang, Y.; Guterman, T.; Arnon, Z. A.; Yao, Y.; Wei, G.; Gazit, E. *Angewandte Chemie - International Edition* **2020**, *59*, 23731-23739.

(45) Scheres, S. H. *Journal of Structural Biology* **2012**, *180*, 519-530.

(46) Scheres, S. H. *Acta Crystallographica Section D : Structural Biology* **2020**, *76*, 94-101.

(47) Lövestam, S.; Scheres, S. H. *Faraday Discussions* **2022**, *240*, 243-260.

(48) He, S.; Scheres, S. H. *Journal of Structural Biology* **2017**, *198*, 163-176.

(49) Diaz, R.; Rice, W. J.; Stokes, D. L. in *Methods in Enzymology*; C; Academic Press Inc. : 2010; t. 482, p. 131-165.

(50) Wang, F.; Gnewou, O.; Wang, S.; Osinski, T.; Zuo, X.; Egelman, E. H.; Conticello, V. P. *Matter* **2021**, *4*, 3217-3231.

(51) Feng, Z.; Wang, H.; Wang, F.; Oh, Y.; Berciu, C.; Cui, Q.; Egelman, E. H.; Xu, B. *Cell Reports Physical Science* **2020**, *1*, 100085.

Chapitre 2 : Matériel et Méthodes

Dynamique moléculaire

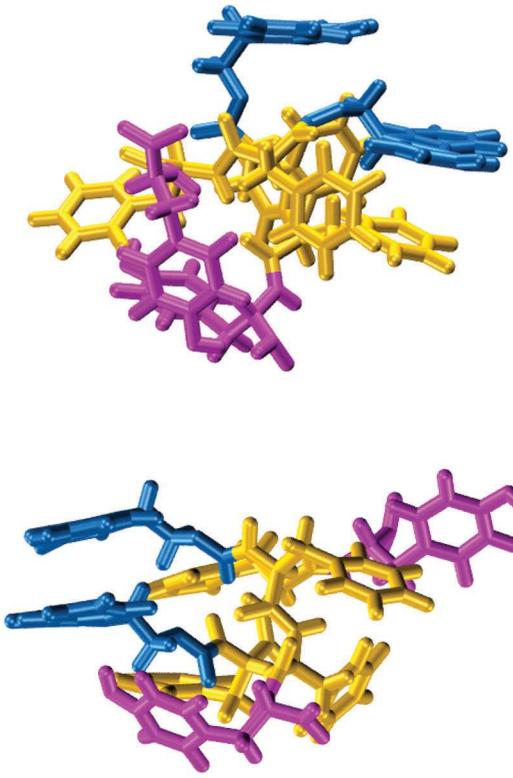

Reconstruction de l'image

1 Dynamique moléculaire

La dynamique moléculaire (DM) utilisée dans cette thèse se base sur une approche dite "classique". Les molécules sont représentées comme des atomes sous formes de sphères liées entre elles par des ressorts. Les interactions non-covalentes sont représentées par des fonctions d'énergie potentielles électrostatiques et de Lennard-Jones. Dans ce type de représentation les charges sont ponctuelles et les électrons ne sont pas explicitement inclus. La formation et rupture de liaison covalente n'est pas possible.

1.1 Champ de force

Les calculs de dynamique moléculaire sont réalisés avec le logiciel AMBER[1, 2], qui se base sur la représentation d'une énergie potentielle décrite empiriquement par la formule suivante (équation 3.1) :

$$U = \sum_{bonds} k_b(r-r_0)^2 + \sum_{angles} k_\theta(\theta-\theta_0)^2 + \sum_{dihedrals}\sum_{n} V_n(1+cos(n\varphi-\gamma)) + \sum_{i<j}[\frac{q_i q_j}{R_{ij}} - 2\epsilon_{ij}(\frac{R^*_{ij}}{R_{ij}})^6 + \epsilon_{ij}(\frac{R^*_{ij}}{R_{ij}})^{12}] \quad (3.1)$$

Cette équation peut être décomposée en interactions intra et intermoléculaires comme le montre le schéma suivant (Figure 1).

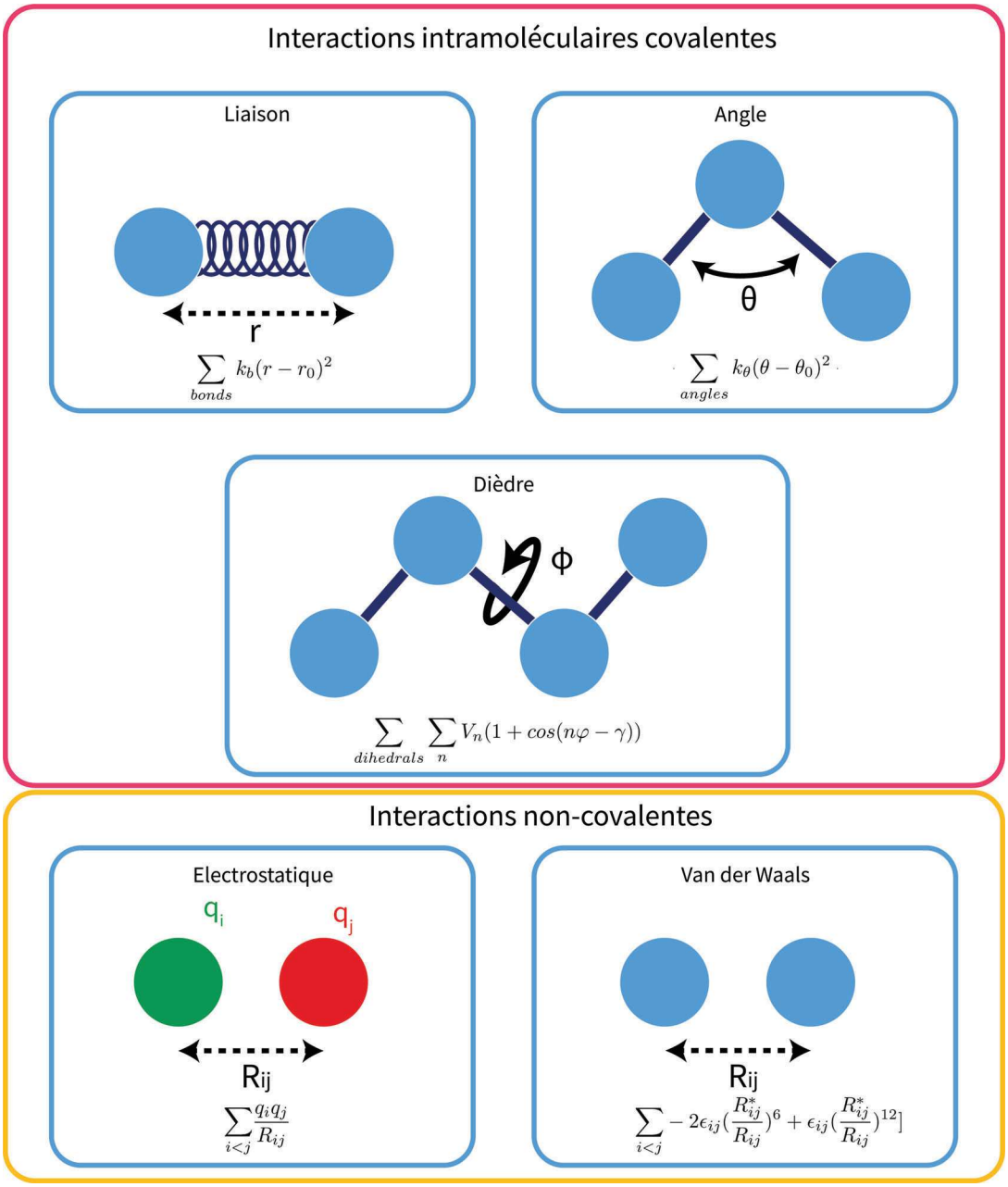

FIGURE 1 – Composantes intra et intermoléculaires présentes dans le calcul d'énergie potentielle dans le logiciel AMBER

La composante d'énergie intramoléculaire est constituée de la somme des énergies de : (1) déformation des liaisons, les paramètres associés à cette énergie sont la constante de raideur du ressort k_b ainsi que la position d'équilibre r_0. (2) La composante intramoléculaire de l'énergie liée à la déformation des angles entre trois atomes, les paramètres associés sont la constante de raideur de l'angle k_θ ainsi que l'angle d'équilibre θ_0. (3) En dernière composante il y a l'énergie associée à la déformation des dièdres des paramètres de l'énergie de barrière du dièdre V_n à l'ordre n ainsi que l'angle ϕ associé au dièdre mentionné et la phase γ.

Les composantes d'énergies intermoléculaires sont constituées de deux termes, la première est l'intraction électrostatique qui prend en compte les charges q_i des atomes ainsi que la distance entre

ces dernières R_{ij}. La seconde est le potentiel de Lennard-Jones utilisant les paramètres de l'énergie au puits de potentiel du couple ij nommé ϵ_{ij} ainsi que la distance associée au puits R^*_{ij}.

Il est nécessaire de préciser que les paramètres ϵ_{ij} ainsi que R^*_{ij} sont calculés à partir des composantes des atomes et de règles de mélange de Lorentz-Berthelot tel que : $\epsilon_{ij} = \sqrt{\epsilon_{ii} \times \epsilon_{jj}}$ et $R^*_{ij} = \frac{R^*_{ii}+R^*_{jj}}{2}$.

Au cours de cette thèse le champ de force ff14SB a été utilisé.[3] Ce dernier est régulièrement employé pour l'étude de la conformation de protéines dans l'eau, il paraît donc être de prime abord un bon candidat pour étudier l'assemblage de peptides courts.

1.2 Dynamique moléculaire classique : fonctionnement

En dynamique moléculaire classique la force $\overrightarrow{F_i}$ est calculée à partir des masses des atomes et de leurs accélérations $\overrightarrow{a_i}$ comme décrit dans l'équation suivante (équation 3.2) :

$$\overrightarrow{F_i} = m_i \times \overrightarrow{a_i} \tag{3.2}$$

Pour résoudre cette équation pour tous les atomes en fonction du temps le logiciel AMBER utilise une variante de l'algorithme de Verlet tel que présentée par l'équation (équation 3.3) :

$$\begin{aligned} v(t + \frac{1}{2}\Delta t) &= v(t - \frac{\Delta t}{2}) + a(t)\Delta t + O(\Delta t^3) \\ r(t + \Delta t) &= r(t) + v(t + \frac{\Delta t}{2})\Delta t \end{aligned} \tag{3.3}$$

Ainsi les vitesses v de $t + \Delta t$ sont calculées à partir des vitesses trouvées à $t - \frac{1}{2}\Delta t$ et les positions des atomes r de $t + \Delta t$ sont calculées à partir de $t + \frac{1}{2}\Delta t$. Les vitesses initiales v_0 sont générées aléatoirement selon une distribution de Maxwell-Boltzmann.

Chaque ensemble de vitesse composant le système est associé à une température. Pour calculer la température totale du système il est possible d'utiliser l'équation de Clausius qui se base sur la théorie de l'équipartition de l'énergie des gaz parfaits (équation 3.4) :

$$E_c = \sum_{i=1}^{N} \frac{1}{2} m_i v_i^2(t) = \frac{1}{2} N_{dl} k_B T(t) \tag{3.4}$$

Avec N_{dl} le nombre de degrés de liberté du système, k_B la constante de Boltzmann et v_i la vitesse associée à l'atome i de masse m_i. Dans le cadre de nos simulations le pas d'intégration a été réglé à 1 fs.

1.3 Paramètres de simulation

Toutes les simulations qui ont été analysées durant l'étape de production dans ma thèse ont été effectuées dans un ensemble canonique N,V,T ce qui signifie que le nombre de particules, le volume et la température du système sont maintenues constants tout au long de la simulation. Il est possible de fixer facilement le nombre de particules et le volume cependant, il est nécessaire d'ajuster la température via un thermostat externe. Les paramètres de simulations sont inscrits dans un fichier d'entrée via une liste de "flags", qui seront, pour chaque partie mentionnés en italique. Il s'agira également dans cette partie de discuter des autres méthodes pour le calcul des interactions et des restraintes tout au long des simulations.

1.3.1 Contrôle de la température

La méthode employée pour contrôler la température a été dévéloppée par Berendsen et ses collaborateurs en 1984[4]. La méthode à couplage faible permet d'introduire un bain thermique qui va permettre un échange d'énergie sans échange de matière avec le système. L'équation présentée par les auteurs, et utilisée dans AMBER via le flag *ntt = 1*, est la suivante (équation 3.5) :

$$\frac{dT(t)}{dt} = \frac{1}{\tau_T}[T_0 - T(t)] \tag{3.5}$$

L'algorithme de contrôle de la température demande deux paramètres : τ_T le temps de relaxation de la température (flag *tautp=1*) ici de 1 ps ainsi que la température de référence T_0 (flag *temp0=298.15*) ici égale à 298.15 K. La température du système étant associée directement aux vitesses le contrôle thermique se fait sur un "scaling" (multiplication par un facteur) des vitesses des atomes.

1.3.2 Conditions aux limites périodiques 3D

Les conditions aux limites périodiques sont utilisées en dynamique moléculaire pour permettre de simuler des systèmes homogènes où le nombre de particules reste constant. L'utilisation de cette méthode se base sur la réplication miroir du système au temps t dans les trois directions de l'espace (x,y et z en coordonnées cartésiennes). Ainsi, une molécule en bord de boîte peut intéragir avec la molécule du bord opposé de la boîte. Pour des conditions périodiques à volume constant il faut utiliser le flag *ntb=1*. Dans ma thèse, nous avons utilisé une boîte cubique (Figure 2).

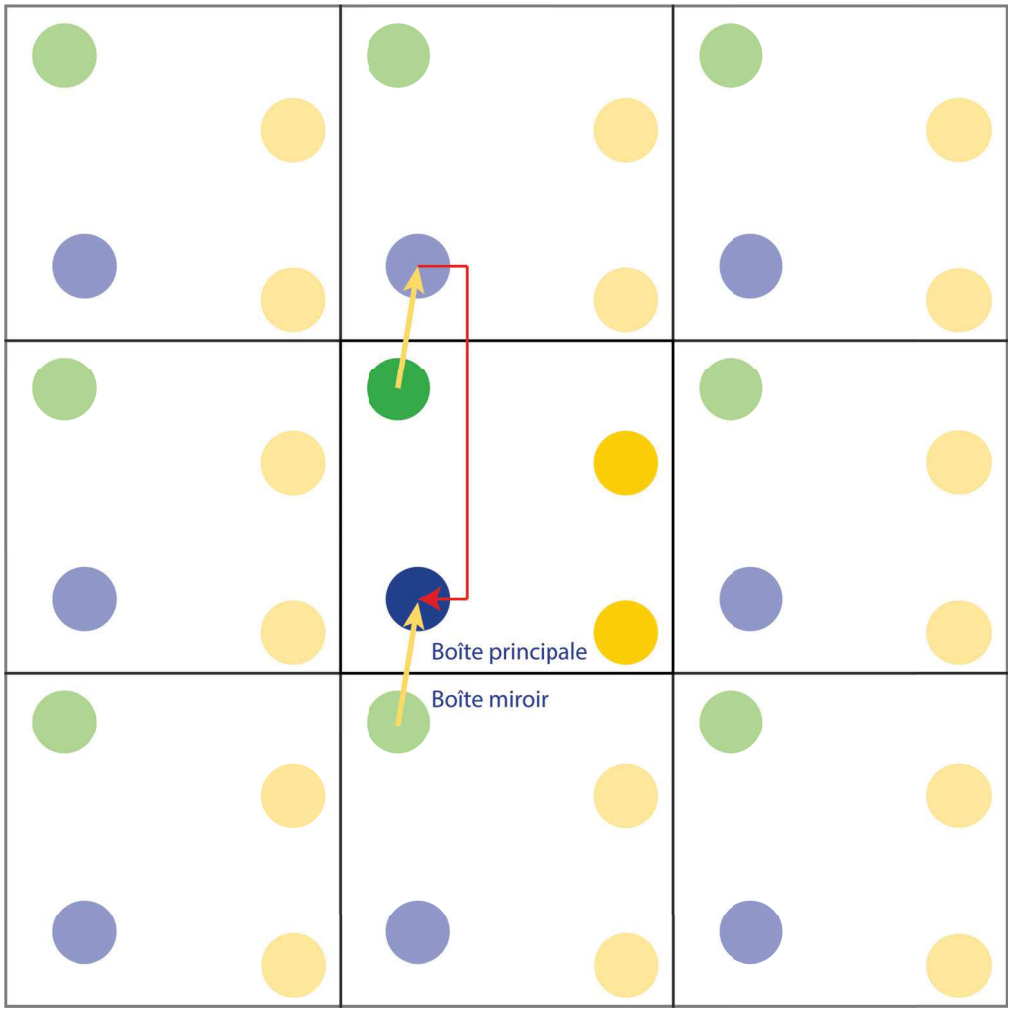

FIGURE 2 – Illustration des conditions limites périodiques. Le déplacement d'une particule (verte) dans la boîte principale est représenté par une flèche jaune. Cette dernière va rentrer à nouveau dans la boîte par l'autre côté, cette nouvelle position est représentée en bleu. Les particules inchangées sont en jaune. Adapté de Wikipédia [5]

1.3.3 Interactions à longues distances et cut-off

Les interactions non-covalentes (Van der Waals et électrostatiques)dépendent, toutes les deux, de la distance interatomique (R_{ij}). Les interactions sont calculées pour toutes les paires d'atomes qui existent dans le système. Calculer toutes les paires (même distances de plus d'une dizaine voir centaine d'angstrom) peut s'avérer couteux en temps de calcul. Pour réduire ce temps de calcul, les logiciels de dynamique utilisent une valeur de cut-off pour toutes les interactions non-covalentes. Cela signifie que pour les interactions de Van der Waals les énergies sont calculées directement jusqu'à cette valeur pour les distances R_{ij}. Les interactions électrostatiques sont également calculées pour les distances R_{ij} inférieures au cut-off et au delà la méthode de sommation d'Ewald est employée. Dans mon travail de thèse la valeur par défaut est de 12 Å (*cutoff=12*).

1.3.4 Algorithme SHAKE

L'algorithme SHAKE permet de restreindre les fréquence de vibration dûes aux liaisons impliquant, dans notre cas, un hydrogène. En limitant ces dernières il est possible d'appliquer un pas d'intégration plus grand et ainsi de diminuer le temps de calcul. Le flag associé est *ntc=2*.

1.3.5 Application de restrictions sur les positions

Il a été vu que les positions peuvent être restraintes dans certains cas via, par exemple, l'algorithme SHAKE. Dans certaines situations il est parfois nécessaire de restraindre les positions cartésiennes de certains atomes ou fragments de molécules. La situation à laquelle s'applique cette restriction se trouve dans le premier chapitre expérimental qui implique la dynamique moléculaire de la fibre reconstruite. La restriction se fait grâce à l'application d'une contrainte de position sous la forme $k(\Delta x)^2$ avec k la constante de force en kcal.mol^{-1}Å^{-2}. Le flag associé est *ntr=1* avec la contrainte sous le flag *restraint_wt=5*.

1.4 Paramétrisation création du système

En ce qui concerne le tripeptide Fmoc-FFY, deux étapes de paramétrisations sont nécessaires :(i) le fragment FFY a été paramétrisé grâce à xLeap, un logiciel présent dans la suite d'AMBER, et les paramètres appliqués sont ceux du champ de force ff14SB en considérant la tyrosine comme un amino-acide terminal chargé négativement au niveau du carboxylate. La première phénylalanine est considérée comme un amino-acide qui peut réaliser une liaison avec un autre fragment (comme le Fmoc par exemple). (ii) Pour le fragment Fmoc, les paramètres appliqués sont ceux du champ de force ff14SB et les charges ont été calculées avec la méthode RESP (Figure 3) [6].

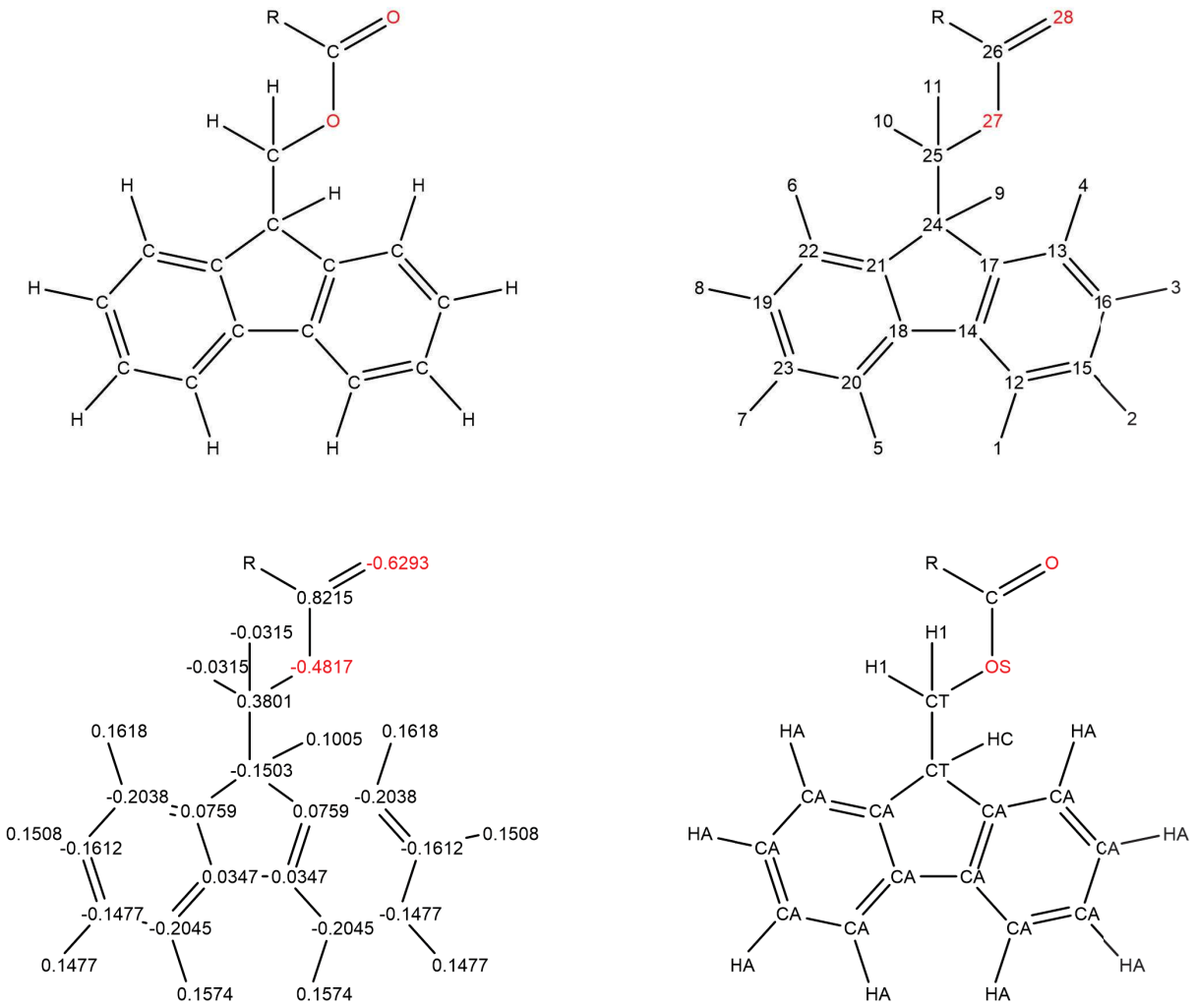

FIGURE 3 – Paramètres appliqués au Fmoc avec en haut à gauche la formule topologique, en haut à droite les numéros d'atomes, en bas à gauche les charges calculées grâce à la méthode RESP et en bas à droite les types d'atomes du champ de force ff14SB.

Pour ce qui est des ions, les paramètres sont issus de la publication de Joung et Cheatham[7] et dépendant du modèle d'eau utilisé. Les peptides et les ions, dont les concentrations pour chaque systèmes sont disponibles dans le tableau 3.1 suivant, sont ensuite placés aléatoirement dans une boîte cubique de dimension finie. Le solvant est également introduit grâce à la superposition d'une boîte d'eau déjà équilibrée qui ne chevauche pas à moins de 2 Å une molécule de soluté. Sauf mention contraire le modèle d'eau mentionné est le TIP3P [8]. Le système étant crée il faut ensuite passer à une étape d'équilibration.

1.5 Equilibration

Le processus d'équilibration en dynamique moléculaire comprend, dans notre cas, trois étapes distinctes : (i) la minimisation de l'énergie, (ii) le chauffage à la température désirée et (iii) l'ajustement de la pression pour obtenir la bonne densité.

1.5.1 Minimisation

Cette étape a pour objectif de diminuer les forces internes qui peuvent résulter de la création du système. Cela permet d'éviter la superposition d'atomes et de molécules qui pourrait conduire à des problèmes de divergence de l'énergie. Le procédé de minimisation de l'énergie est réalisé avec un calcul dit "single point energy" puis un gradient stochastique descendant sur les positions d'atomes avec un minimum de 2500 cycles d'optimisation, d'itération maximale de 5000 cycles.

1.5.2 Ajustement de la température

Ce premier ajustement de la température va permettre d'introduire des vitesses initiales de manière aléatoires. La température initiale est de 0K et le système va être progressivement chauffé à 298.15K en passant par des paliers de 100 et 200K grâce à un thermostat de Berendsen. L'augmentation de la température est réalisée par un scaling de la vitesse des atomes.

1.5.3 Ajustement de la densité

Quand la température a atteint la valeur souhaitée il est nécessaire d'ajuster la densité via un contrôle en pression. En effet, l'étape de production de la trajectoire est dans l'ensemble canonique NVT ce qui signifie que le système est à volume constant. Or, pendant le chauffage la boîte a pu légèrement s'agrandir et avoir un volume plus grand ce qui induit une densité différente de celle attendue, il est ainsi nécessaire de l'ajuster. Le contrôle se fait avec un barostat de Monte-Carlo et une pression de référence de 1 bar. Pour arriver à la pression choisie le barostat va modifier isotropiquement la taille de la boîte . Une fois la densité désirée atteinte il est possible de passer à l'étape de production de la dynamique.

1.6 Production de la dynamique

La production de la dynamique consiste à générer les trajectoires qui vont servir à la visualisation et l'analyse de phénomènes physico-chimiques. Cette dernière a été réalisée dans un ensemble NVT avec les paramètres mentionnés ci-dessus. Les calculs ont été réalisés avec des cartes graphiques NVIDIA GTX 1080.

1.7 Analyse de la trajectoire

Le logiciel CPPTRAJ [9] est utilisé pour générer un fichier de coordonnées global (en netCDF) où les résidus d'intérêts sont placés au centre de la boite. La dynamique est ensuite observée et analysée via l'application VMD [10].

1.7.1 Liaisons hydrogène

Les liaisons hydrogène sont analysées via le programme CPPTRAJ[9]. Le critère d'angle et de distances sont respectivement de 135° et 3 Å maximum. L'analyse concernant la carte de chaleur des couples donneurs - accepteurs a été réalisée manuellement en deux étapes : (i) pour chaque couple la somme du nombre de frames est réalisé pour toutes les paires, (ii) chaque valeur est divisée par la plus grande valeur trouvée pour tous les couples. La carte est normalisée entre 0 et 1.

1.7.2 Analyse de corrélation angles - distances

L'analyse de corrélation revient à produire une liste d'angles entre les plans et les distances associées entre ces derniers pour chaque paire de résidus. Ensuite, un comptage est opéré sur un critère de sélection entre deux angles et deux distances. La liste suivante est crée (Tableau 3.1) :

Tableau 3.1 – Matrice de fréquences de corrélations observées pour une paire considérée. Les exposants des fréquences sont relatifs à l'intervalle de distance et l'indice à l'intervalle d'angle.

		Distances			
		0-1 Å	1-2 Å	2-3 Å	a-b Å
Angles	0-5°	f_{0-5}^{0-1}	f_{0-5}^{1-2}	f_{0-5}^{2-3}	f_{0-5}^{a-b}
	5-10°	f_{5-10}^{0-1}	f_{5-10}^{1-2}	f_{5-10}^{2-3}	f_{5-10}^{a-b}
	10-15°	f_{10-15}^{0-1}	f_{10-15}^{1-2}	f_{10-15}^{2-3}	f_{10-15}^{a-b}
	c-d°	f_{c-d}^{0-1}	f_{c-d}^{1-2}	f_{c-d}^{2-3}	f_{c-d}^{a-b}

La liste comprend les fréquences pour chaque couple d'angle - distance pour chaque paire considérée (Fmoc-Fmoc, Fmoc-Phe1, etc.). Ensuite, la représentation en carte de chaleur comprenant les fréquences est normalisée par le volume d'un cercle entre les deux distances considérées dans l'intervalle comme le montre l'équation suivante (équation 3.6) :

$$f_{c-d}^{a-b} = \frac{f_{c-d}^{a-b}}{\frac{4}{3}\pi\left(\frac{d_b}{2}^3 - \frac{d_a}{2}^3\right)} \tag{3.6}$$

Avec f_{c-d}^{a-b} la fréquence entre les distances a et b considérées, sachant que $b > a$.

Chaque groupement de graphiques est ensuite normalisé selon la fréquence la plus haute parmi toutes. Cela crée une densité de fréquences normalisées avec 1 étant la plus haute fréquence rencontrée pour une série d'angles $c - d$ à une certaine distance $a - b$ et 0 étant une fréquence nulle non observée.

2 Reconstruction des édifices auto-assemblés via RELION

Le logiciel **RE**gularised **LI**kelihood **O**ptimisatio**N**, RELION[11], est un outil permettant de reconstruire en 3D des objets de taille nanoscopique observés en cryo-microscropie électronique à transmission (Cryo-MET). L'utilité de cette technique de préparation d'échantillons est que les analytes sont préservés dans leur état natif, *i.e* hydratés.

La technique de préparation de l'échantillon, couplée à la microscopie électronique à transmission (MET), permet d'observer des édifices macromoléculaires à haute résolution. En effet, la MET a accès à des résolutions spatiales de l'ordre de l'angstroem. Il est donc possible d'obtenir, avec un traitement d'images adéquat, des informations de cette dimension. Une des approches du traitement de l'image développée en 2012 par Scheres avec une approche bayésienne a permis d'obtenir des cartes de projection du potentiel électrostatique de macromolécules biologiques en solution grâce à un très grand nombre d'images[11]. L'article présentant un nouveau logiciel, nommé RELION et distribué librement, a permis à la communauté des microscopistes d'obtenir les cartes de densité électroniques de particules isolées. En 2017, la méthode a été étendue aux hélices[12]. C'est grâce à ce module que RELION a pu être utilisé comme moyen de reconstruire en 3D les nanofibres de peptides auto-assemblés et de déterminer leur structure à l'échelle moléculaire. Le logiciel suit plusieurs étapes pour arriver à une carte de densité de la projection du potentiel électrostatique de la fibre. Les deux systèmes (initiés par chauffage refroidissement et par l'action de l'enzyme) ont pu être étudiés. Les auto-assemblages sont préparés dans du Borax 25 mM à pH=9,3 en régime dilué à $1,6 \times 10^{-4}$ mol/L.

2.1 Workflow général

RELION est un logiciel qui présente différents outils pour permettre de passer des images jusqu'à une carte de densité. Le processus complet, appelé également "Workflow", sera présenté en partie avec un accent principalement sur les étapes qui ont nécessité un travail et une réflexion supplémentaire pour reconstruire des objets non biologiques de diamètre ou taille de l'ordre de dizaine ou de la centaine de nanomètres. Le processus de reconstruction se déroule en 15 étapes comme présentées dans la Figure 4.

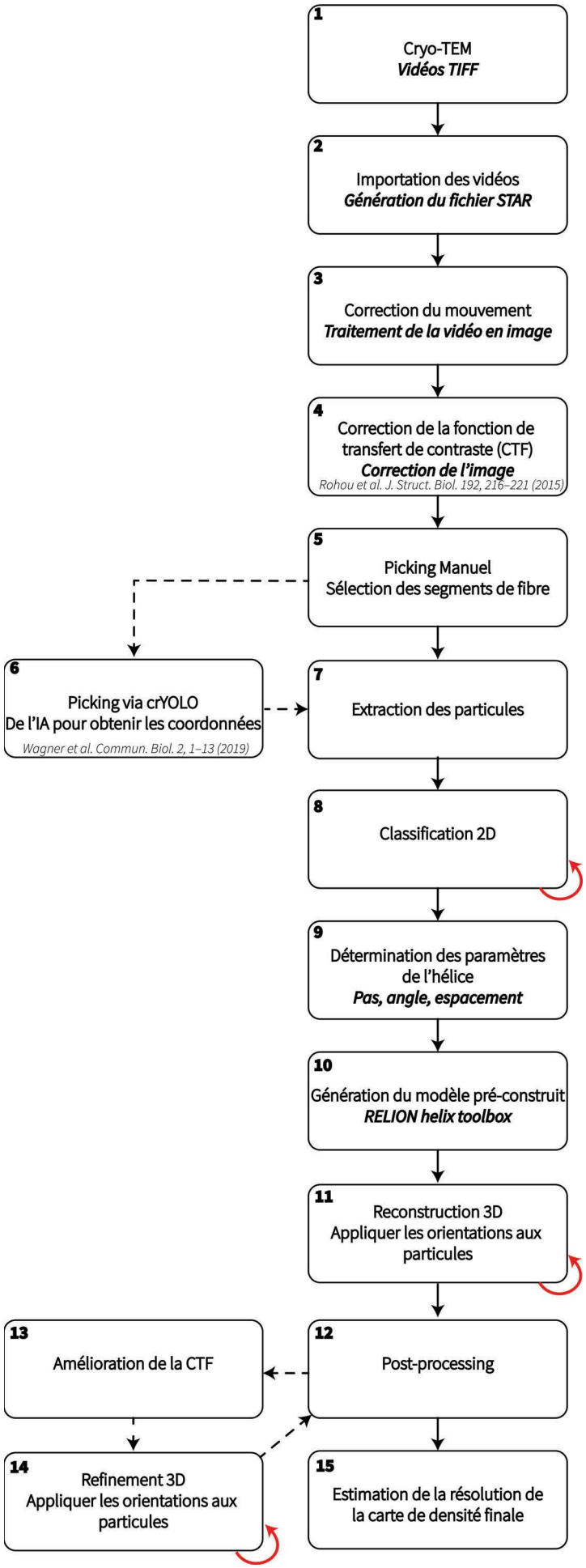

FIGURE 4 – Workflow RELION 3.1.2 avec ses 15 étapes permettant de passer de l'image à la carte de densité en 3D. Les processus avec des flèches rouges sont itératifs. Les chemins en pointillés sont facultatifs mais peuvent permettre dans certains cas d'améliorer la résolution.

Dans la suite de ce chapitre, des sections du processus de reconstruction seront illustrés avec certains résultats obtenus au cours de ma thèse sur le Fmoc-FFY ayant subi un assemblage par chauffage à 80°C puis refroidissement à température ambiante.

2.2 Sélection des particules étapes 5 et 6

Dans le traitement de l'image il y a un certain nombre de facteurs limitant la résolution de la carte de densité électronique que l'on va calculer. Le nombre de particules est un de ces derniers car le rapport signal sur bruit est directement proportionnel au nombre de particules. Une particule est définie, dans ce contexte, comme étant un objet d'intérêt (segment de fibre dans cette situation) avec de la glace dans son environnement proche. Les particules sont placées dans des boîtes carrées extraites d'une partie de l'image. Une image peut donc contenir plusieurs particules qui peuvent, ou non, avoir un espace de recouvrement. A la différence des particules isolées (*single particules*, en anglais) les particules de fibres contenant des segments ont un recouvrement le plus souvent définit par un autre paramètre qui est la distance interboîte et ayant pour équation la relation suivante (équation 3.7) :

$$\text{Distance interboîte} = \text{nombre d'unités asymétriques} \times \text{élévation de l'hélice} \tag{3.7}$$

A l'heure actuelle il n'y a pas encore de recommandations claires sur le nombre de particules nécessaires pour obtenir une carte de densité interprétable. Néanmoins, le nombre de particules moyen retrouvé dans les publications est au delà de 100 000 particules par objet à reconstruire.

Pour sélectionner des particules il existe à ce jour trois méthodes : (i) la sélection manuelle, (ii) l'utilisation d'Intelligence Artificielle et (iii) la sélection automatique basée sur une approche statistique. Dans le contexte de mon travail nous n'avons utilisé que les deux premières approches et ce sont celles que je présenterai dans la suite de cette section. Ce choix d'exclure directement la sélection via l'approche statistique se base sur des tests internes au projet qui montrent qu'un grand nombre de faux positifs (une contamination considérée comme un segment de fibre) sont présents avec cette technique ce qui impose un plus grand nombre de particules nécessaires pour avoir la même qualité de reconstruction que les deux autres méthodes.

2.2.1 Sélection manuelle, étape 5

La sélection manuelle consiste à choisir les objets d'intérêt sur les images à l'aide de la souris. Cette approche possède deux intérêts : (i) identifier un ou plusieurs objets visuellement et (ii) sélectionner spécifiquement les objets ce qui permet d'éviter les contaminations de la sélection. Néanmoins, malgré l'efficacité de cette méthode qui a fait ses preuves dans le monde de la biologie structurale elle présente un inconvénient : la sélection demande beaucoup de temps. Pour obtenir un nombre de particules suffisant il est parfois nécessaire de passer plusieurs semaines à sélectionner ses objets. En effet, pour arriver à 500 000 particules extraites, dont les paramètres d'extraction se trouvent dans le tableau en fin de chapitre, il a fallu environ une semaine complète de sélection manuelle.

Pour palier à cela, il existe des méthodes de sélection de particules toutes aussi performantes que la sélection manuelle tel que l'utilisation de l'Intelligence Artificielle avec la méthode YOLO.

2.2.2 Sélection via un réseau de neurones : Méthode YOLO, étape 6

Pour aider dans cette étape nous avons eu recours au logiciel crYOLO qui permet de sélectionner les segments après entrainement d'un réseau de neurones [13]. La méthode You Only Look Once (YOLO) est une méthode de détection d'objets sur des images à l'aide d'un réseau de neurones convolutionnel (CNN, Convolutionnal Neural Network, Figure 5). L'utilité de ce réseau est de préserver le lien qui existe entre les pixels. En effet, l'objet désiré est, quelque soit sa rotation angulaire, une suite de pixels ordonnée qui représente un sens physique. Le réseau de neurones convolutionnel permet de préserver cette information et donc améliorer les performances de la sélection par IA. Dans l'article original de Redmon sur la méthode YOLO [14] l'un des inconvénients cité est la mauvaise position des objets dans l'image lors de la prédiction (sélection par l'IA sur un jeu de données désiré). Ceci, ne pose qu'un problème mineur tant que la proportion d'erreur reste minoritaire car les particules qui ne sont pas centrées correctement peuvent être enlevées automatiquement en classification 2D. L'avantage de la méthode YOLO est donc sa rapidité d'entrainement. De plus, le réseau permet de réaliser des prédictions sur plusieurs jeux de données similaires.

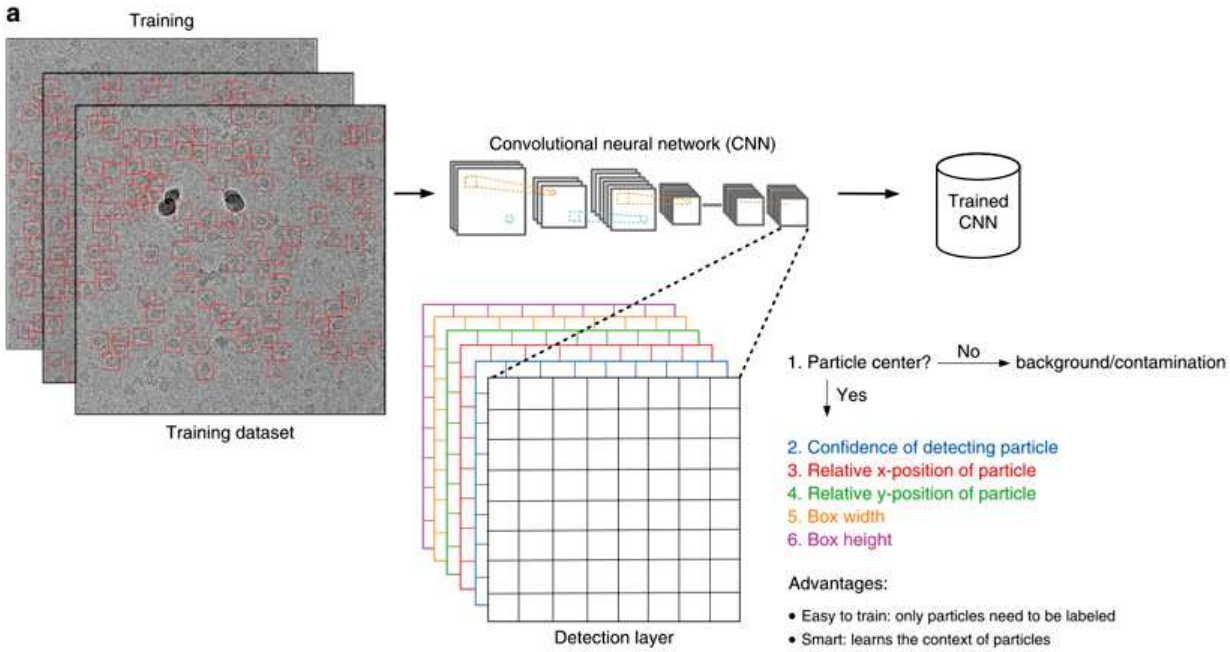

FIGURE 5 – Réseau de neurones convolutionnels (CNN) utilisé par crYOLO et développé par Wagner et ses collaborateurs.[13]. Reproduit avec l'autorisation de Springer.

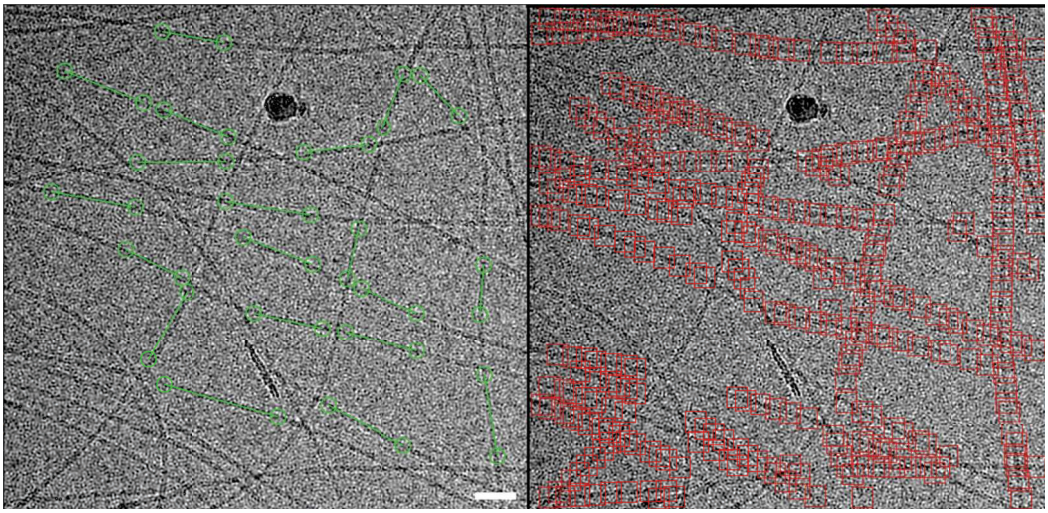

FIGURE 6 – Comparaison entre la sélection manuelle à gauche et la prédiction du réseau de neurones après entrainement à droite. La barre d'échelle représente 100 Å. Les deux micrographiques sont identiques, seule la sélection diffère.

L'utilisation de crYOLO se fait en deux étapes : (1) l'entrainement du réseau de neurones, le modèle, avec des particules caractéristiques de l'échantillon puis (2) la prédiction, c'est à dire l'application du modèle, sur le jeu de données dont l'utilisateur souhaite obtenir les coordonnées des segments de fibre (Figure 6).

Le jeu de données d'entrainement du réseau de neurones contient 779 images dont le mouvement a été préalablement corrigé avec l'implémentation de RELION. Les segments de fibres ont été sélectionnés à la main sur 335 images parmi les 779 à une résolution de 0,5925 Å/pixel et un binning de 2. Il y a eu 20 714 segments espacés chacun de 20 pixels donnant lieu à 345 680 particules au total. Le réseau

de neurones, d'architecture PhosphorusNet, a été entrainé avec 284 images et validé avec 71 images. Il y a eu en tout 48 cycles itératifs d'entrainement (epoch) pour entrainer le modèle.

L'étape de prédiction est réalisé sur un autre ensemble d'images à une résolution de 0,88 Å/pixel contenant 2183 micrographies qui sera utilisée plus tard dans la reconstruction du peptide auto-assemblé. Cette étape a permis de créer des fichiers en .box qui sont utilisés ensuite dans RELION pour segmenter et extraire les particules.

2.3 Extraction des particules, étape 7

RELION va ensuite réaliser tous les processus de reconstruction sur des particules. Une particule est définie comme étant une sous-partie d'une image contenant la totalité ou une fraction de l'objet d'intérêt entouré de glace. Après avoir obtenu les coordonnées il est nécessaire d'extraire les particules. Le choix de la méthode de sélection des segments de fibre qui a été retenu est via l'utilisation de crYOLO. Le réseau de neurones donne accès au début et à la fin de chaque segment de fibre ce qui permet d'extraire les particules selon un espacement de $9 \times 1,6258 = 14,6322$ Å pour la distance interboîte (équation 3.7).

2.4 Classification 2D, étape 8

Cette étape est nécessaire pour permettre de regrouper les particules (segments de fibres) qui sont identiques. Cela permet également de séparer les faux positifs du jeu de données de particules. En effet, même après avoir extrait des particules il est possible de retrouver des segments non désirés, tel que des croisements de fibres par exemple. La classification bayésienne permet de comparer les particules entre elles et de les regrouper en classes. La procédure de classification emploie un masque circulaire. Ce dernier est défini comme étant une frontière entre l'objet et la glace. En effet, lors de l'application d'un masque seuls les pixels à l'intérieur de ce dernier sont considérés dans la classification. Cette étape de regroupement de particules est utile dans le cadre de l'indexation de l'hélice car il est nécessaire d'obtenir une image mieux résolue qu'une particule uniquement extraite de l'image. La classification repose donc sur des similitudes entre les objets observés après détermination de la rotation dans et hors du plan. Les classes présentées ci-dessous (Figure 7) sont celles qui ont été retenues pour la suite du processus de reconstruction.

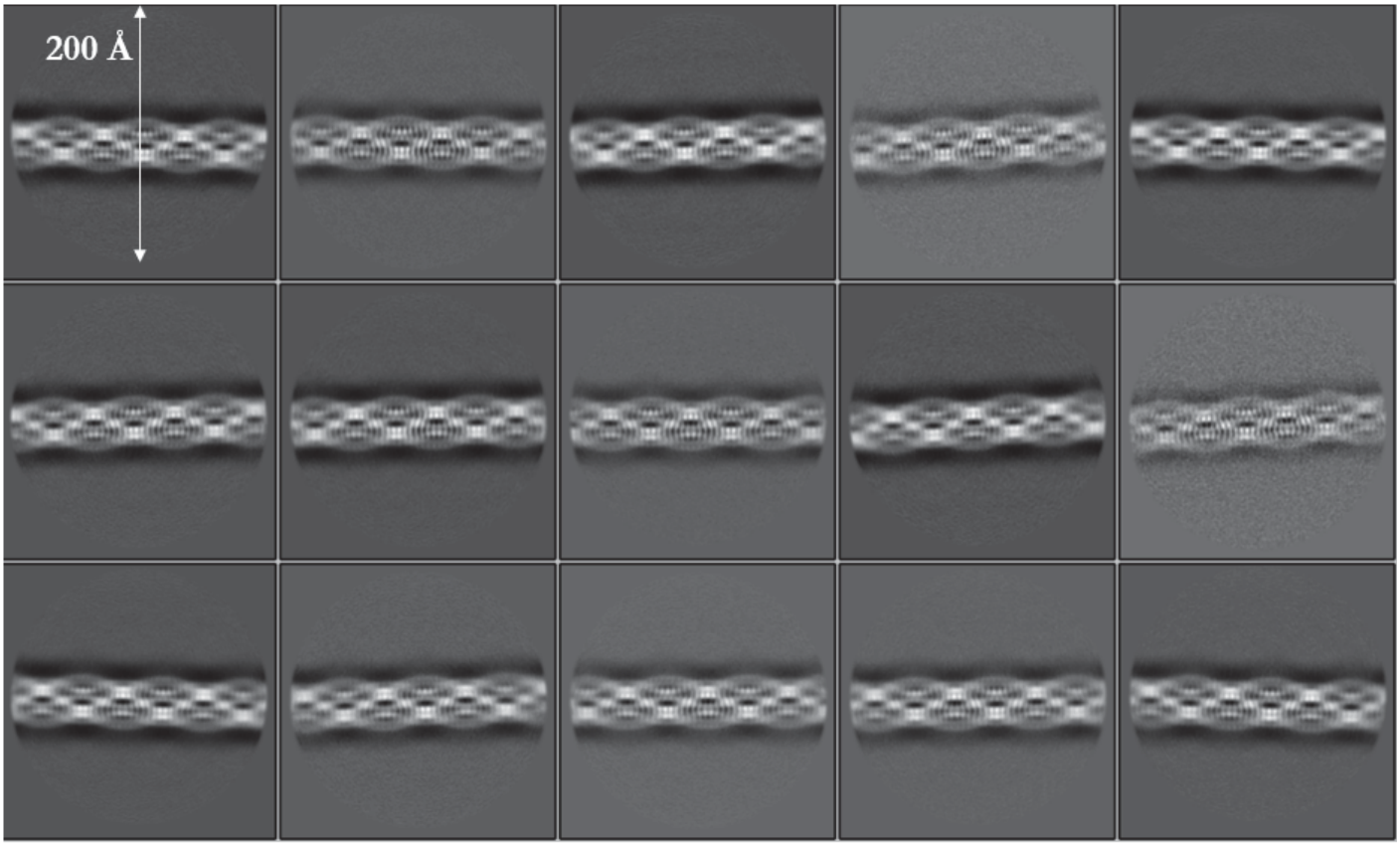

FIGURE 7 – Classes 2D retenues pour la reconstruction de la nanofibre. Le masque employé fait 200 Å de diamètre.

Au départ, 50 classes ont été demandées et seules 20 sont retenues pour la phase de reconstruction suivante. La seule différence entre ces classes est la rotation de la fibre qui n'est pas toujours horizontale dans le plan ou encore le début de la particule qui ne commence pas à la même localisation. Avec les classes qui sont similaires et représentent le même objet il est possible d'affirmer que parmi les 650 000 particules sélectionnées après la classification toutes appartiennent à un seul objet.

2.5 Obtention des paramètres hélicoïdaux, étape 9

En passant dans l'espace réciproque, aussi appelé espace des fréquences, il est possible d'analyser la périodicité d'un objet. Pour se faire, une classe 2D peut être utilisée pour calculer et indéxer le cliché de diffraction. Le spectre de puissance de la classe 2D a été obtenu à l'aide du site HELIXPLORER (`https://rico.ibs.fr/helixplorer/helixplorer/`, Figure 8) crée par Leandro F. Estrozi, Ambroise Desfosses et Guy Schoehn à l'Institut de Biologie Structurale, Grenoble, France.

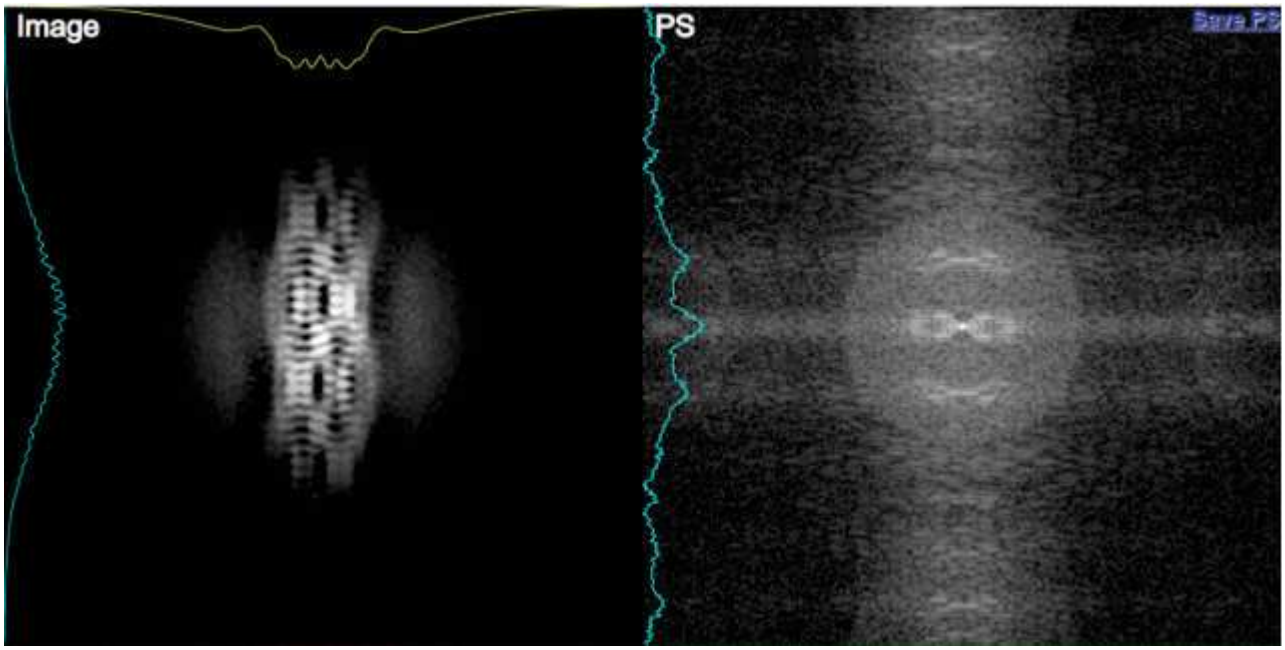

FIGURE 8 – A gauche, une classe 2D avec un diamètre de fibre d'environ 45 Å et à droite, le spectre de puissance associée à cette classe. Les tracés en bleu correspondent au profil d'intensité de l'image selon l'axe vertical et le tracé en jaune correspond au profil selon l'axe horizontal.

L'indexation du cliché de diffraction donne les paramètres suivants, avec leurs équivalents anglais entre parenthèses :

- Élévation (rise) : 1,6258 Å
- Angle (twist) : 122,685°
- Tour complet (pitch) : 4,8774 Å

Ces paramètres sont ensuite introduits dans RELION pour la reconstruction 3D.

2.6 Modèle 3D initial, étape 10

Pour la reconstruction d'objets hélicoïdaux il est possible de partir d'un modèle initial simple tel qu'un cylindre à un diamètre défini. Ce diamètre devrait être le plus proche de l'objet vu sur les micrographies. Ce cylindre servira de modèle de référence qui sera ensuite utilisé dans le calcul de la distribution des angles associés à chaque particule. Cependant, cette approche ne fonctionne pas pour tous les objets. En effet, pour des polypeptides qui forment des fibres amyloïdes la distance entre deux unités successive étant petite, proche de 5 Å, l'utilisation d'un cylindre ne peut pas toujours permettre d'arriver à une carte où les unités polypeptidiques sont bien espacées. Pour palier à ce problème, S. Scheres, a crée une méthode qui permet, à partir d'une classe 2D de générer un modèle initial le plus proche possible de la réalité expérimentale[15]. En appliquant la méthode de Scheres la carte initiale passe d'un cylindre à une carte plus proche de celle observée dans les classes 2D de la

section précédente.

La première commande permet de générer un cylindre de diamètre 60 Å avec une taille de boite cubique de 250 pixels de côté. La flèche rouge dans le code indique uniquement la continuité de la commande. La carte correspondante est présente dans la Figure 3.9 ci-dessous, en gris, à gauche.

```
$ relion_helix_toolbox --cylinder --o ref.mrc --boxdim 250 --cyl_outer_diameter 60 --
    ↪ angpix 0.88
```

Cette méthode a été utilisée dans de nombreuses reconstructions publiées par le MRC[16-19]. Les commandes qui permettent de réaliser la projection d'une classe 2D sont décrites ci-dessous. La flèche rouge dans le code indique uniquement la continuité de la commande. La carte correspondante est la présente dans la Figure 3.9, en jaune, à droite.

```
$ relion_image_handler --i 5@Class2D/job006/run_ct35_it050_classes.mrcs --o bigclass.mrc
$ relion_star_loopheader rlnReferenceImage > bigclass.star
$ echo "bigclass.mrc" >> bigclass.star
$ mkdir IniModel
$ relion_helix_inimodel2d --i bigclass.star --iter 1 --sym 1 --crossover_distance
    ↪ 101.910571923743501 --angpix 0.88 --o IniModel/bigclass.mrc --mask_diameter 250
```

FIGURE 9 – A gauche, un cylindre de diamètre externe de 60 Å obtenu comme décrit ci-dessus (premier encart) et à droite, une projection 3D d'une classe 2D générée grâce à la deuxième série de commandes ci-dessus (deuxième encart).

2.7 Reconstruction 3D, étape 11

La reconstruction 3D est l'étape de calcul de la distribution de probabilité des orientations des particules par rapport à un modèle de référence. Elle permet donc de reconstruire l'objet en 3D. Dans la reconstruction il est possible d'appliquer la symétrie hélicoïdale via le rise et le twist trouvés précédemment et d'utiliser les groupes de symétrie (C,C_n,D_n, etc.) pour réduire le nombre d'orientations nécessaires à la reconstruction. Dans le cas de nos objets qui présentent un twist de 122.8° il n'est pas possible d'appliquer cette méthode. Notre nanofibre présente ainsi la symétrie la plus simple possible : C_1.

La carte de densité obtenue est composée de la projection du potentiel électrostatique des molécules composant l'objet. Cependant, une hypothèse est faire lors de l'utilisation de la méthode bayésienne : le potentiel électrostatique possède une variation locale continue qui n'est pas brutale. En effet, il n'y a pas de coupure de densité dans les liaisons chimiques. De ce fait, les cartes de densité obtenues sont bien les densités expérimentales mais moins marquées. Il est donc nécessaire, pour un aspect visuel, de réaliser une étape dite de "sharpening" et qui est comprise dans le module de post-processing de RELION. Une comparaison des cartes avant et après post-processing sera illustrée dans la partie suivante.

2.8 Post-processing, étape 12

Cette modification de la carte se fait en deux étapes : (1) il est nécessaire de créer un masque de la densité électronique de la carte et (2) réaliser le sharpening (voir Figure 10). Le masquage (1) se fait à l'aide d'une valeur de densité seuil de la carte issue de la reconstruction pour laquelle il n'y a pas de pixel de bruit autour de la fibre. Ensuite, un filtrage à une certaines résolution peut également être appliqué, tout comme un rajout de densité de masque ou un lissage via une fonction sinusoïdale. Ce qu'il faut retenir de cette étape c'est que le masque permet d'enlever les densités de bruit et de focaliser le sharpening aux densités propres à l'objet d'intérêt. La deuxième étape (2) est le sharpening qui permet de mieux représenter les densités à l'échelle moléculaire et donne accès à une carte dans laquelle il est possible d'introduire un modèle moléculaire.

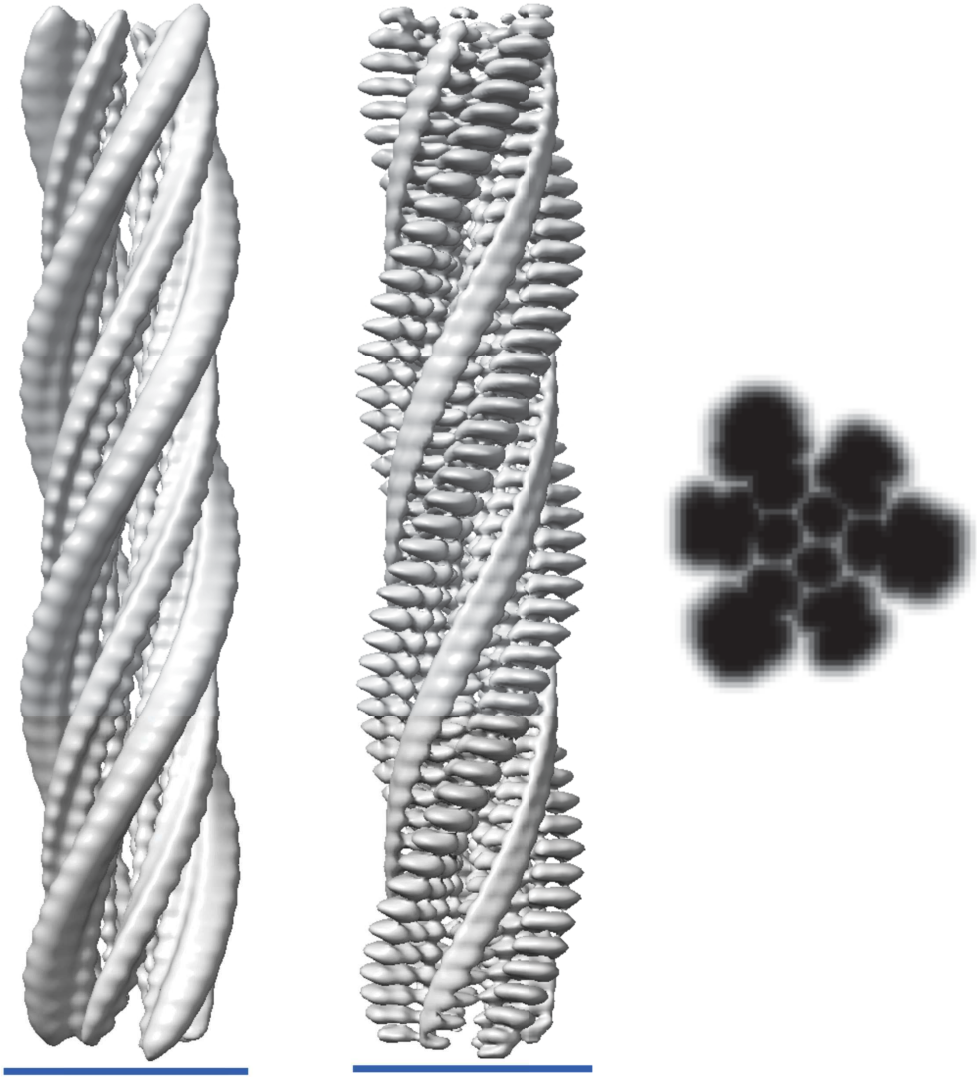

FIGURE 10 – A gauche, la carte de densité juste après la reconstruction 3D, au milieu la même carte mais avec le sharpening et à droite, le masque de la coupe centrale de la carte. Pour le masque les densités ont subi une inversion de contraste pour plus de visibilité. Les deux échelles en bleu représentent une longueur de 50 Å.

Les étapes 13 et 14 peuvent être réalisées pour obtenir une meilleure résolution de la carte en permettant la correction de l'anisotropie de l'image ainsi que le recalcul des paramètres de la CTF après reconstruction. Cependant, dans notre situation ces étapes n'ont pas aidé à améliorer la résolution.

2.9 Estimation de la résolution, étape 15

Toute carte obtenue grâce à la reconstruction possède une résolution. Cette dernière étant définie comme une valeur en angström qui donne la plus petite taille distinguable sans ambiguïté. La résolution dans ce cas est exprimée comme étant un critère de qualité. Pour illustrer la notion de résolution à l'échelle moléculaire il est possible de simuler les densités avec ChimeraX (Figure 11).

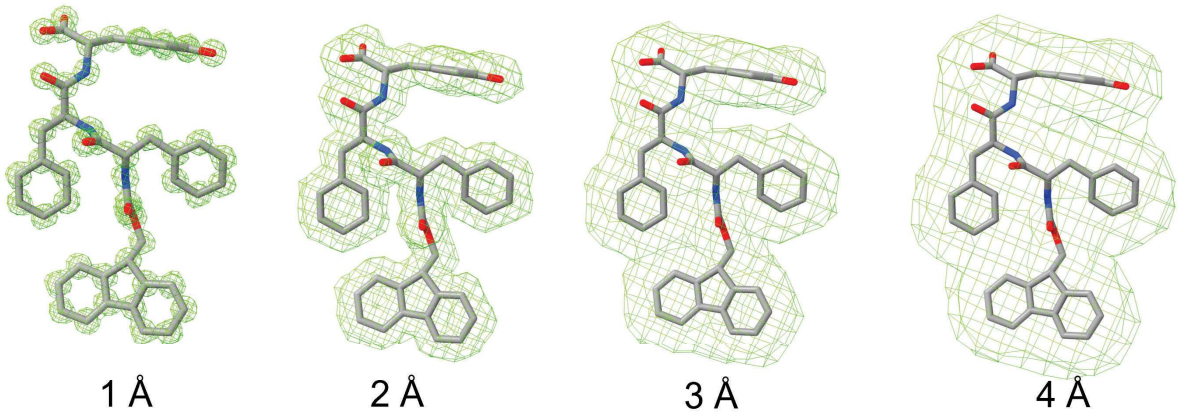

FIGURE 11 – Echelle de résolution de cartes de densité simulées pour le Fmoc-FFY à partir de des densités atomiques pour des résolutions allant de 1 à 4 Å. Les densités sont issues de la commande molmap de ChimeraX et les hydrogènes n'ont pas été pris en compte.

Cette figure illustre uniquement une échelle de résolution théorique. Même si certains microscopes ont des caméras qui arrivent à aller à la résolution de 1 Å la caméra K2 du Glacios permet d'arriver à une résolution d'environ 2 Å. Cependant, pour notre carte il a été possible de descendre uniquement à 3,8 Å. Comme le montre le schéma (Figure 11) il est tout de même possible de placer un peptide dans une densité sans pour autant avoir accès à la chiralité de l'hélice via le backbone.

Dans le cas de la FSC cette dernière présente un plateau proche de 1 dans les basses fréquences (longues distances) ce qui indique une bonne qualité de la reconstruction effectuée. La courbe diminue ensuite pour tendre vers 0 pour les hautes fréquences (courtes distances). Pour évaluer cette résolution il faut trouver la valeur en $Å^{-1}$ qui correspond à une FSC de 0,143. Cette valeur arbitraire de FSC a été déterminée par Rosenthal et Henderson en 2003[20].

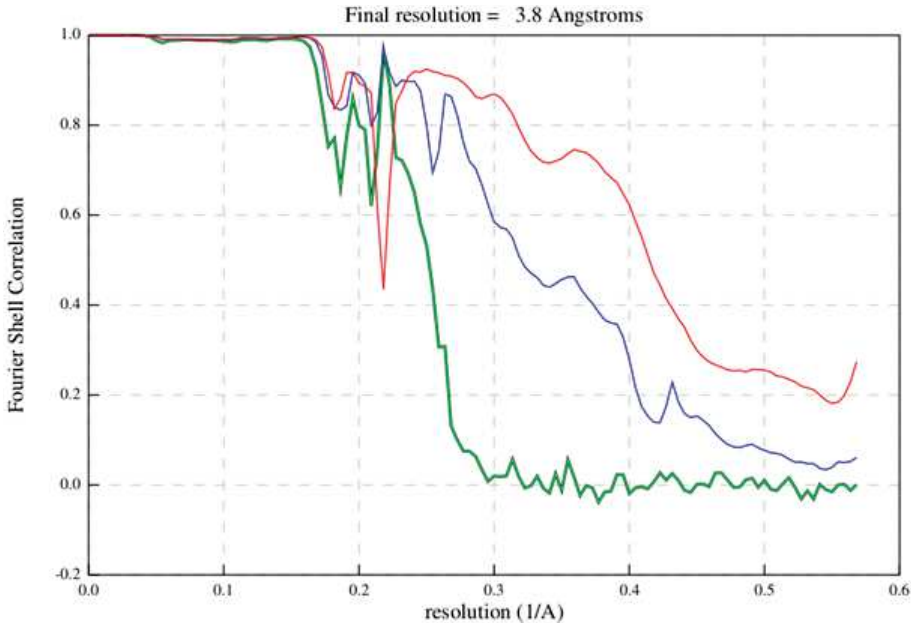

FIGURE 12 – Fourier Shell Correlation (FSC) de la carte de densité présentée plus haut avec en noir (superposée à la courbe verte) la FSC de la carte corrigée, en vert la FSC de la carte non masquée, en bleu la FSC de la carte masquée et en rouge la FSC de la carte masquée avec les phases aléatoires.

2.10 Placement du modèle moléculaire dans la carte de densité

Cette section traite du passage de la carte de densité jusqu'au modèle moléculaire. Cela permet de fournir une interprétation chimique aux densités expérimentales observées. Pour se faire, le peptide est issu du fichier au format PDB généré pour la dynamique moléculaire et est importé dans ChimeraX[21, 22]. La carte de densité, en format .mrc[23, 24], est également importée dans le logiciel. Il s'agit ensuite de déplacer le peptide dans la carte, de faire tourner certaines liaisons et de voir si la molécule rentre dans les densités. Pour vérifier si le modèle est à la bonne place il est possible de calculer un coefficient de corrélation dans ChimeraX. Il est à préciser que ce facteur de corrélation ne tient compte que des densités atomiques et non des densités de liaisons ou de groupements chimiques. Il a été nécessaire de symmétriser le modèle moléculaire via les paramètres trouvés dans l'étape 11 après reconstruction.

2.11 Paramètres utilisés en reconstruction

Ci-dessous le tableau 3.2 présente tous les paramètres utilisés pour les étapes de reconstruction.

Tableau 3.2 – Liste des paramètres utilisés dans RELION. Les valeurs où plusieurs itérations successives ont été effectuées sont séparées par des barres transversales

Paramètres	**Fmoc-FFY**	**Fmoc-FFpY + PA**
Acquisition des images		
Microscope	Glacios	
Caméra	K2	
Tension (kV)	200	
Abbération sphérique C_s (mm)	2,7	
Type de données	Vidéos de 40 stacks en format TIFF	
Taille du pixel (Å/pix)	0.88	
Nombre de vidéos	2182	2709
Correction du mouvement		
Nombre de stacks à corriger/Nombre total considéré	40/40	
Présence d'image de référence	Oui, en fichier .mrc	
Patch (X,Y)	5 x 5	
Facteur de binning	1	
Logiciel de correction	Implémentation de RELION	
Correction de la fonction de transfert de contrast (CTF)		
Estimation du décalage de phase	Non	
Valeur de l'astigmatisme (Å)	100	
Logiciel de correction	CTFFIND 4.1 [25]	
Taille pour le FFT (pix)	512	
Résolution maximale/minimale (Å)	30/5	
Valeur du défocus maximal/minimal (Å)	5 000/50 000	
Pas de recherche de la valeur du défocus (Å)	500	
Extraction de particules		
Taille de la boîte (pix)	250	
Normalisation des particules	Oui	
Redimensionnement des segments	Non	
Diamètre du tube (Å)	60	80
Coupe des tubes en segments	Oui / $9 \times 1,6258$ Å	
Nombre de particules obtenues	1,4 millions	1 million

Paramètres	Fmoc-FFY	Fmoc-FFpY + PA
Classification 2D		
Algorithme utilisé	EM	
Correction de la CTF	Oui	
Nombre de classes demandées	50	
Paramètre de régularisation	2 / 4 / 4	
Nombre d'itérations	25 / 35 / 50	
Sous sets rapides	Non	
Diamètre du masque (Å)	200	
Masquer les particules individuelles par des zéros	Oui	
Alignement des images	Oui	
Echantillonnage angulaire dans le plan (pix)	1	
Décalage de l'intervalle de recherche angulaire (pix)	5 / 2 / 0,5	
Décalage du pas de recherche angulaire (pix)	2 / 1 / 0,5	
Autoriser un échantillonnage plus grossier	Non	
Diamètre du tube (Å)	60	80
Recherche des angles bimodaux	Oui	
Intervalle de recherche angulaire ψ (deg)	6 / 3 / 1	
Restriction du pas de l'hélice	Oui / 1,6258 Å	
Nombre de particules en pool	16	
Nombre de particules retenues	≈650 000	≈500 000
Reconstruction 3D		
Filtrage de la carte de référence (Å)	30	
Correction de la CTF (carte + référence)	Oui et Oui	
Diamètre du masque (Å)	200	
Sampling angulaire initial (°)	7,5	
Décalage de l'intervalle de recherche angulaire (pix)	5	
Décalage du pas de recherche angulaire (pix)	1	
Diamètre du tube (Å)	60	80
Symmétrie hélicoïdale	Oui, $9 \times 1,6258$	
Angle de rotation de l'hélice initial (deg)	122,685	
Pourcentage de la valeur centrale Z	30	
Recherche de la symmétrie localement	Oui	
Recherche de l'angle de rotation Min-Max-Pas (deg)	122 - 123 - 0,01	
Recherche de l'élévation de l'hélice Min-Max-Pas (Å)	1,6 - 1,7 - 0,01	

Paramètres	Fmoc-FFY	Fmoc-FFpY + PA
Création du masque		
Filtre passe-bas (Å)	0	
Seuil pour la binarisation	0,0038	
Extension du masque (pix)	0	
Lissage de la densité externe (pix)	6	
Masquage de l'hélice	Non	
Post-processing		
Estimation du facteur B automatiquement	Oui	
Plus basse résolution pour la régression du facteur B (Å)	10	

2.12 Capacité de calculs

La reconstruction a été effectuée sur deux systèmes informatiques. Le premier est un ordinateur local Dell Precision avec deux CPU Intel Xeon Gold 5218R (20 Coeurs, 2.1-4.0GHz Turbo, 22Mo cache, 125W). Lors de l'utilisation de l'accélération grâce au GPU [26] une carte NVIDIA RTX 4000 (8 Go de RAM) a été utilisée. La machine contient également 96 Go de RAM ECC. Le disque de calcul est un disque SSD NVMe de 2 To.

Le deuxième système est l'infrastructure de l'HPC de l'Université de Strasbourg qui a pu fournir une capacité de calcul suffisante grâce à l'obtention d'un grant (projet PeptoStruct accepté pour l'année universitaire 2022-2023).

Bibliographie

(1) Case, D. A.; Aktulga, H. M.; Belfon, K.; Ben-Shalom, I.; Brozell, S.; Cerutti, D. Amber 2021, 2021.

(2) Cornell, W. D.; Cieplak, P.; Bayly, C. I.; Gould, I. R.; Merz, K. M.; Ferguson, D. M.; Spellmeyer, D. C.; Fox, T.; Caldwell, J. W.; Kollman, P. A. *Journal of the American Chemical Society* **1995**, *117*, 5179-5197.

(3) Maier, J. A.; Martinez, C.; Kasavajhala, K.; Wickstrom, L.; Hauser, K. E.; Simmerling, C. *Journal of Chemical Theory and Computation* **2015**, *11*, 3696-3713.

(4) Berendsen, H. J.; Postma, J. P.; Van Gunsteren, W. F.; Dinola, A.; Haak, J. R. *The Journal of Chemical Physics* **1984**, *81*, 3684-3690.

(5) Osborne, A. R. Periodic boundary conditions. Physics, data analysis, data assimilation, and modeling, 2010.

(6) Sigfridsson, E.; Ryde, U. *Journal of Computational Chemistry* **1998**, *19*, 377-395.

(7) Joung, I. S.; Cheatham, T. E. *Journal of Physical Chemistry B* **2008**, *112*, 9020-9041.

(8) Jorgensen, W. L.; Chandrasekhar, J.; Madura, J. D.; Impey, R. W.; Klein, M. L. *The Journal of Chemical Physics* **1983**, *79*, 926-935.

(9) Roe, D. R.; Cheatham, T. E. *Journal of Chemical Theory and Computation* **2013**, *9*, 3084-3095.

(10) Humphrey, W.; Dalke, A.; Schulten, K. *Journal of Molecular Graphics* **1996**, *14*, 33-38.

(11) Scheres, S. H. *Journal of Structural Biology* **2012**, *180*, 519-530.

(12) He, S.; Scheres, S. H. *Journal of Structural Biology* **2017**, *198*, 163-176.

(13) Wagner, T. et al. *Communications Biology* **2019**, *2*, 1-13.

(14) Redmon, J.; Divvala, S.; Girshick, R.; Farhadi, A. *Proceedings of the IEEE Computer Society Conference on Computer Vision and Pattern Recognition* **2016**, *2016-Decem*, 779-788.

(15) Scheres, S. H. *Acta Crystallographica Section D : Structural Biology* **2020**, *76*, 94-101.

(16) Falcon, B.; Zhang, W.; Murzin, A. G.; Murshudov, G.; Garringer, H. J.; Vidal, R.; Crowther, R. A.; Ghetti, B.; Scheres, S. H.; Goedert, M. *Nature* **2018**, *561*, 137-140.

(17) Zhang, W.; Falcon, B.; Murzin, A. G.; Fan, J.; Crowther, R. A.; Goedert, M.; Scheres, S. H. *eLife* **2019**, *8*, 1-24.

(18) Falcon, B.; Zhang, W.; Schweighauser, M.; Murzin, A. G.; Vidal, R.; Garringer, H. J.; Ghetti, B.; Scheres, S. H.; Goedert, M. *Acta Neuropathologica* **2018**, *136*, 699-708.

(19) Falcon, B.; Zivanov, J.; Zhang, W.; Murzin, A. G.; Garringer, H. J.; Vidal, R.; Crowther, R. A.; Newell, K. L.; Ghetti, B.; Goedert, M.; Scheres, S. H. *Nature* **2019**, *568*, 420-423.

(20) Rosenthal, P. B.; Henderson, R. *Journal of Molecular Biology* **2003**, *333*, 721-745.

(21) Pettersen, E. F.; Goddard, T. D.; Huang, C. C.; Meng, E. C.; Couch, G. S.; Croll, T. I.; Morris, J. H.; Ferrin, T. E. *Protein Science* **2021**, *30*, 70-82.

(22) Goddard, T. D.; Huang, C. C.; Meng, E. C.; Pettersen, E. F.; Couch, G. S.; Morris, J. H.; Ferrin, T. E. *Protein Science* **2018**, *27*, 14-25.

(23) Crowther, R. A.; Henderson, R.; Smith, J. M. *Journal of Structural Biology* **1996**, *116*, 9-16.

(24) Cheng, A.; Henderson, R.; Mastronarde, D.; Ludtke, S. J.; Schoenmakers, R. H.; Short, J.; Marabini, R.; Dallakyan, S.; Agard, D.; Winn, M. *Journal of Structural Biology* **2015**, *192*, 146-150.

(25) Rohou, A.; Grigorieff, N. *Journal of Structural Biology* **2015**, *192*, 216-221.

(26) Kimanius, D.; Forsberg, B. O.; Scheres, S. H.; Lindahl, E. *eLife* **2016**, *5*, 1-21.

Chapitre 3 : Molecular Dynamics study of early stages of short peptide's self-assembly

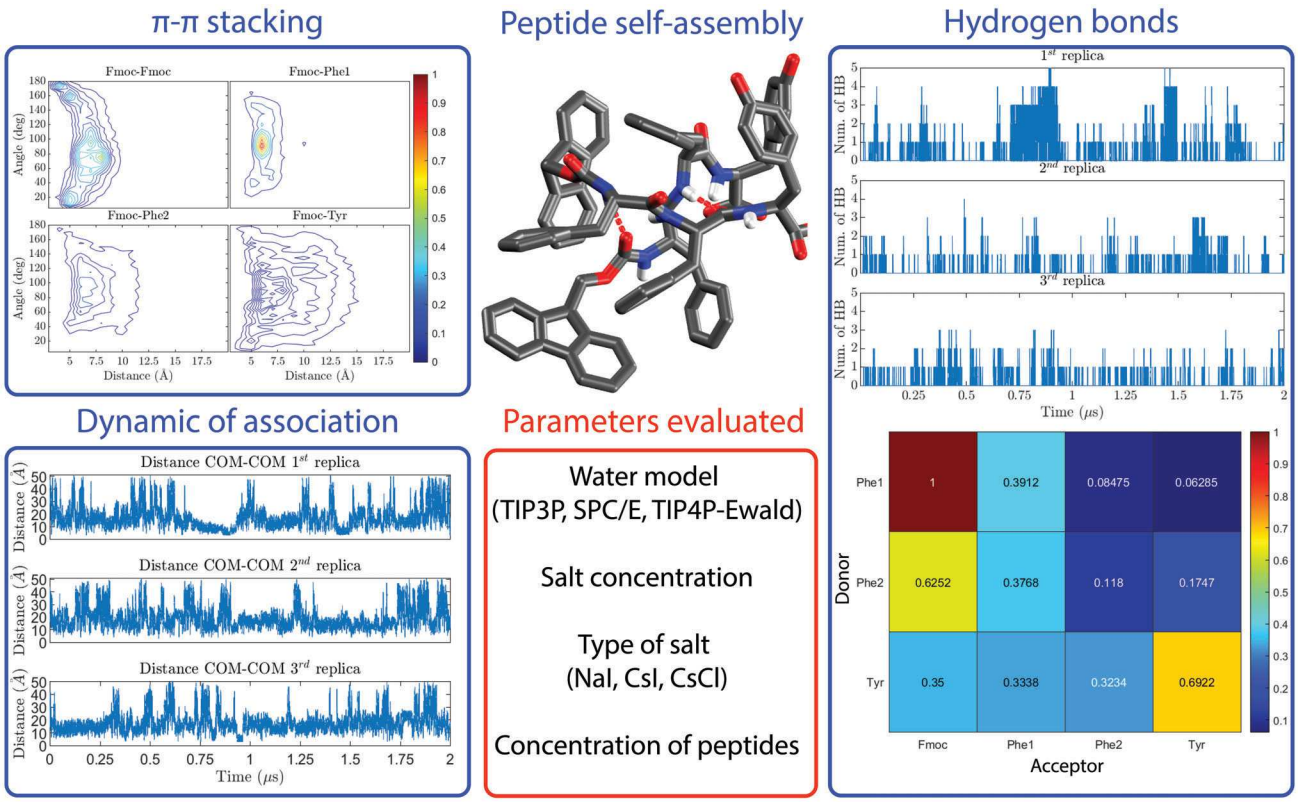

1 Contexte

Ce chapitre 3 est le premier chapitre de résultats obtenu durant ma thèse. Il s'agit ici d'étudier l'assemblage de peptides aux premiers instants (aux alentours de la centaine de nanoseconde) lorsque les premiers Fmoc-FFY produits par voie enzymatique (enzyme omise dans les simulations) rentrent en interaction. Comment ces derniers vont-ils interagir ? La littérature du chapitre 1 nous a montré que les interactions les plus favorables sont l'empilement π des groupements aromatiques et les liaisons hydrogène. Une autre question sera évoquée dans ce chapitre sur comment la structure des peptides vont rentrer en interation ?

Pour répondre à ces deux questions majeures nous avons utilisé des outils de chimie computationnelle : la dynamique moléculaire et l'optimisation de la géométrie de molécules en mécanique quantique. Ces deux méthodes vont mettre en lumière à la fois les interactions, la structure mais également la dynamique d'interaction et d'association. Puisque ce chapitre est dédié intégralement à des méthodes computationnelles il sera également question de valider le champ de force utilisé en dynamique moléculaire (ff14SB) ainsi que le modèle d'eau. Enfin, une approche physico-chimique nous permettra d'analyser en détail comment les peptides s'assemblent et comment ces paramètres vont influencer, ou non, les conformations finales des peptides. Ce chapitre est entièrement rédigé en anglais.

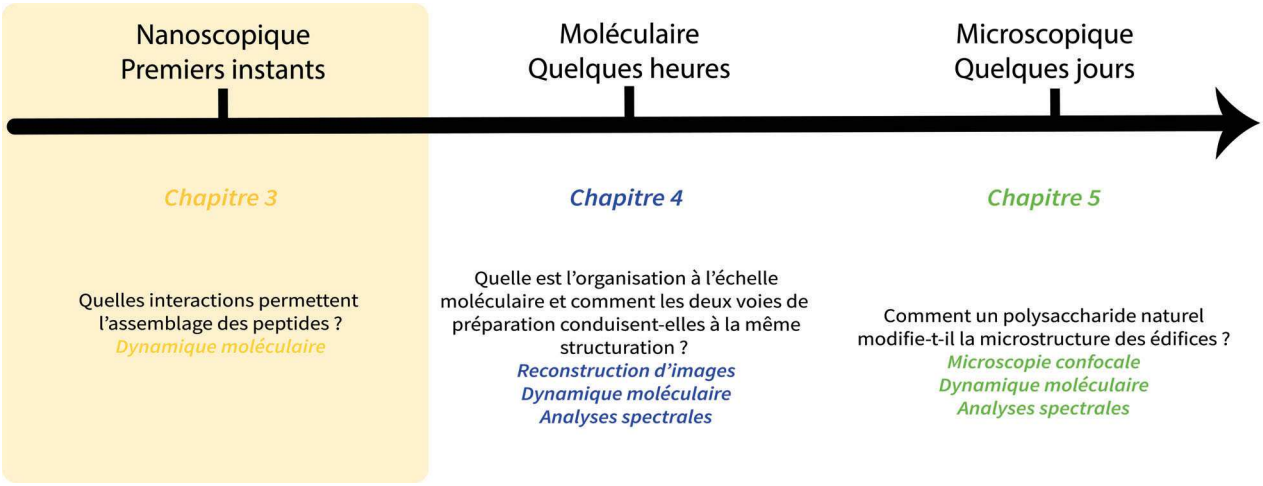

2 Introduction

Self-assembly of short peptides has been vastly studied in the last two decades[1-20]. Their main characteristic is their capability to organize themselves in a 3D network when self-assembled. The chemical nature of these peptides are mostly hydrophobic by essence as they are used in aqueous conditions and have the capacity to trap water within the network. The main motifs found in the literature, described in Chapter 1, contain a fluorenylmethoxycarbonyl modification on the N-terminal side of the peptide chain that increases hydrophobicity hence self-assembling properties. In the case of this thesis, we are currently investigating the Fmoc-FFY, that self-assemble in borax buffer in basic conditions. There are two domains of concentrations that are currently of interest : the diluted system where the concentration of peptide is around 10^{-4} mol/L and the concentrated system that does produce a hydrogel around 10^{-2} mol/L. The main common part of these two concentrations is the early states of self-assembly : there is always a time, kinetically dependent on the concentration, where the first peptides will come in contact and interact. It is experimentally challenging in getting information about this stage regarding the fast time scale in motion here (around nano- or micro-second time scale). The information that need the chemist are in the structural domain such as the type of conformer obtained and the type of interactions involved in the mechanism of self-assembly. However as they are not yet experimentally accessible the scientist have to study self-assembly with computational methods such as molecular dynamics. The tool is allowing to gain access to the desired timescale to give both structural information and type of interactions. The literature already presented molecular dynamics simulations of self-assembled peptides in water media[21-24]. Their main result is the presence of both $\pi - \pi$ stacking between aromatic moieties and hydrogen bonds between backbones of the peptides. However, one major part of these studies mainly focus on dozens or hundred peptides [21, 22, 24]. In these articles there is only few discussions about the structure of the early stages of self-assembly. This is the key information we want to address to the scientific community with this chapter. Probing early stages will be done with an all atomic molecular dynamics simulations of Fmoc-FFY in water. The goal is to identify three main components : (i) what are the type of non-covalent interactions between peptides and their implication in self-assembly, (ii) what are the structural conformations that emerge from peptides' self-assembly and (iii) what is the dynamic of aggregation ? We first start with QM geometry optimization of the dimers and some residues to identify the enthalpy of association of chosen conformations in order to identify the interactions between peptides. In this chapter our goal will also to do methodological tests about

the water model (TIP3P, SPC/E and TIP4P-Ewald) in order to try to validate the most fitted one regarding literature and experimental data. Three important physico-chemical parameters are also included in this study such as the peptide concentration, the type of added salt and its concentration. The concentration of peptides investigated is between the gel state and diluted system (1.5×10^{-2} mol/L and 4.8×10^{-3} mol/L). The type of salt will also be studied in order to chemically reproduce the borax buffer that has not been yet parametrized and is hypothesized as chaotropic. Chaotropic salts such as NaI, CsI and CsCl will be used. The salt concentration (NaCl) will be varied to study its effect on self-assembly processes (from 2.5×10^{-3} to 2.4 mol/L). The focus of this chapter will aim to link the variation of the parameters to the three key components described above. Firstly, we will describe the results in a dedicated section. Secondly, we will discuss these results and their impact on self-assembly. At the end a conclusion will summarize all the information we get regarding these systems and how they can be applied to bigger systems.

3 Material and methods

3.1 Systems studied

TABLE 1 – Summarize of all the simulated systems from this chapter

System	Number of peptides (P) [Concentration ($\times 10^{-3}$mol/L)]	Number of monovalent cations [Concentration ($\times 10^{-3}$mol/L)]	Number of monovalent anions [Concentration ($\times 10^{-3}$mol/L)]	Water model and number of molecules	Box dimensions (Å)	Simulation time (ns)
2P	2 [15.4]	2 Na [15.4]	0 Cl [0]	7000 TIP3P	60x60x60	2000 ; 2000 ; 2000
2P-SPCE	2 [15.4]	2 Na [15.4]	0 Cl [0]	7000 SPCE	60x60x60	2000 ; 2000 ; 2000
2P-TIP4P-E	2 [15.4]	2 Na [15.4]	0 Cl [0]	7000 TIP4P-E	60x60x60	2000 ; 2000 ; 2000
2P-NaCl	2 [15.4]	314 Na [2430]	312 Cl [2430]	7000 TIP3P	60x60x60	2000 ; 2000 ; 2000
5P-TIP3P	5 [4.8]	15 Na [14.4]	10 Cl [9.6]	56 000 TIP3P	120x120x120	250 ; 250 ; 250
5P-SPCE	5 [4.8]	15 Na [14.4]	10 Cl [9.6]	56 000 SPC/E	120x120x120	250 ; 250 ; 250
5P-TIP4P-E	5 [4.8]	15 Na [14.4]	10 Cl [9.6]	56 000 TIP4P-E	120x120x120	250 ; 250 ; 250
5P-NaI	5 [4.8]	15 Na [14.4]	10 I [9.6]	56 000 TIP3P	120x120x120	250 ; 250 ; 250
5P-CsI	5 [4.8]	15 Cs [14.4]	10 I [9.6]	56 000 TIP3P	120x120x120	250 ; 250 ; 250
5P-CsCl	5 [4.8]	15 Cs [14.4]	10 Cl [9.6]	56 000 TIP3P	120x120x120	250 ; 250 ; 250
5P-1000NaCl	5 [4.8]	1005 Na [966]	1000 Cl [961]	56 000 TIP3P	120x120x120	250 ; 250 ; 250

All the Material and Methods are presented in the Chapter 2 page 46. For the 2P systems the window of analysis of correlation maps and RDF is the complete 2000 ns of trajectory. For the 5P systems the window is reduced to the last 25 ns of the trajectory out of 250 ns.

3.2 Determination of conformation with hydrogen bonds analysis

This part is explaining how the structuration of the peptides is determined through hydrogen bonds analysis.

Firstly, heatmap analysis is done through the computation of all the hydrogen bonds that fall into the hydrogen bond description given by CPPTRAJ [25]. Then, pair analysis is done by dividing all donor-acceptor pairs between residues from the highest value found in all of these pairs (12 pairs in total). Secondly, structural analysis is done by identifying the most observed pairs. If the peptide adopt a particular conformation such as N- to C-terminal then certain type of donor-acceptor pairs are more present during the trajectory. The Scheme 1 describes the arrangement of the peptides and Scheme 2 the interpretation of hydrogen bonds analysis.

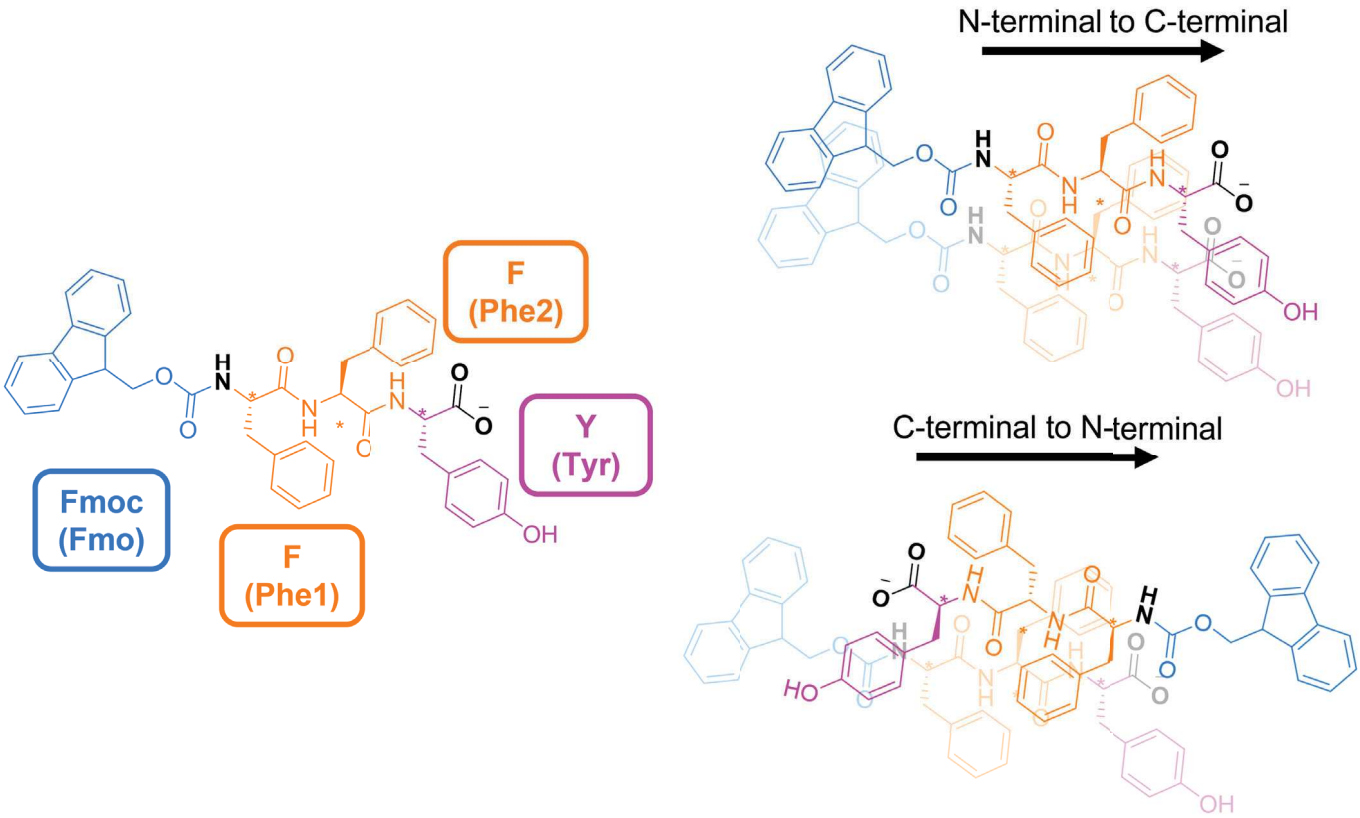

Scheme 1 – Fmoc-FFY peptide (L-amino acids) simulated in this work. The acronym given in this work is framed along wiht the letter code dedicated for amino-acids. The description of the N-terminal to C-terminal conformation and C-terminal to N-terminal conformation are described by the dimer of Fmoc-FFY on top of each other.

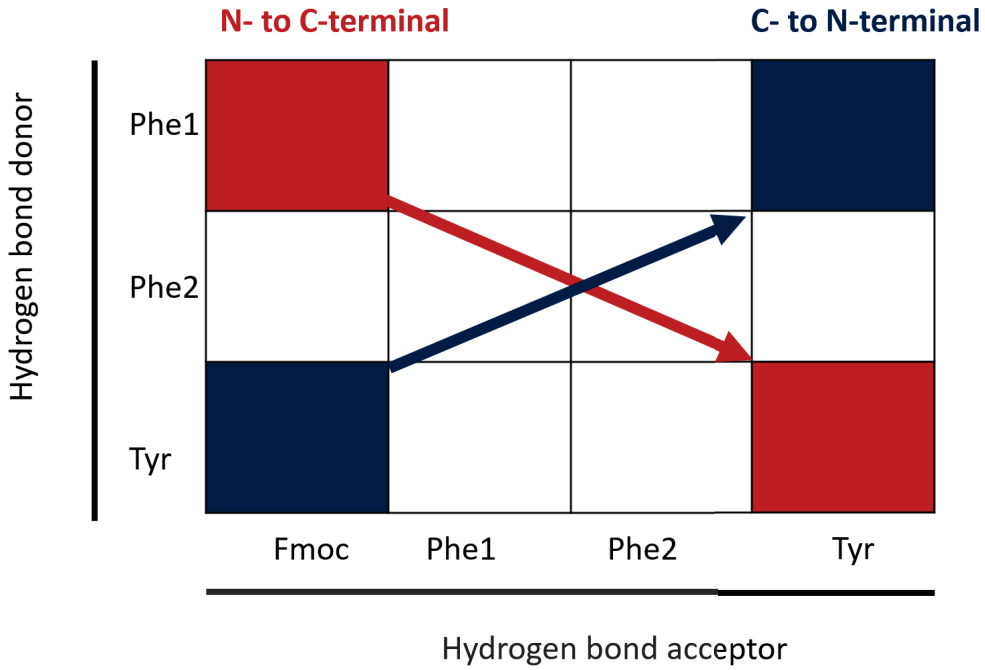

SCHEME 2 – Illustration of the hydrogen bond heatmap and how the N- to C-terminal (or the opposite) structuration are determined. If the highest values of the heatmap are in the two red regions then structuration is from N- to C-terminal, if they are in the blue regions then structuration is from C- to N terminal.

The N- to C-terminal conformation mean that, on the average of the trajectory, the peptides are on top of each other in the direction of the backbone. In that way the first phenylalanine would only be hydrogen bonded to the Fmoc (red square in scheme 2 on the top left corner). That particular phenylalanine would not interact with the tyrosine in the end of the chain (Scheme 1 top). In addition, the tyrosine would only interact with its corresponding self (red square in the bottom right corner). By combining these two information the N- to C-terminal conformation is the only possible. However, it has to be taken into account that the heatmap is a trend to describe if one structure emerges from the lot. If it does not converge on one conformation, multiple high values can be found for opposite pairs (blue and red regions) and then analysis would be the sign of multiple conformers co-existing during the trajectory.

The C- to N-terminal conformation is, by analogy, the opposite that was previously discussed. The squared regions are symmetrical from the diagonal of the matrix of the heatmap.

3.3 QM optimization

DFT calculations are done using Gaussian 09 software[26]. The functional used is the ωB97X-D [27] and the def2TZVP[28] basis set. Optimization is done with SFC tight grid and maximum 500 cycles of optimization. Initial structures have been extracted from the 2P simulations with the atomic

xyz coordinates from the trajectory. Extraction of coordinates is done with VMD.[29] Hydrogen atom is added to the carboxylate in order to have a neutral compound. When water solvation is used the solvation model is PCM. The enthalpy of association is calculated with the following equation 4.1 :

$$\Delta Association = (Dimer\,energy) - (2 \times monomer\,energy) \tag{4.1}$$

The monomer energy is calculated with the same basis set and functional and is an average of 10 different conformations (from MD simulations of 1 peptide) in order to avoid falling in a pitfall of energy that may not be representative of the overall conformations.

4 Results

4.1 QM optimization of the dimer

Dimer structures of Fmoc-FFY have been studied through QM geometry optimization. The optimization has been run on four dimers that have various initial conformations. The final structures (Table 2) show the presence of $\pi - \pi$ stacking between aromatic moieties. Nevertheless, no specific aromatic pair (Fmoc-Fmoc, Fmoc-Phe, Phe-Tyr, etc.) is favored. In addition, the difference of energy between dimers is up to 16.1 kcal/mol compared to the most stable conformer (number 1 table 2). However, between the three remaining structures (number 2 ; 3 and 4 table 2) the difference of energy is lower than 3 kcal/mol. In addition, enthalpy of self-association in the dimer can be computed and is reported in table 2. All of the energies of association are negative meaning that association in dimer form is preferred regarding peptides apart in solution. The enthalpy of association are evaluated here in gas phase and water (model with PCM model). They are between -35.41 and -51.49 kcal/mol for the gas phase and from -30.00 to -45.61 kcal/mol for the PCM water solvation. One other criteria of self-assembly is the interaction between the Fmocs. It is indeed proved that the Fmoc is a hydrophobic residue that will favor self-association in water media. In that sense, the distances between the Fmoc and the angles formed from the aromatic planes can be evaluated from the structures (table 2). They display both parallel and perpendicular stacking. There is, however, no direct link between distances from the two Fmocs regarding the enthalpy of association (table 2). Same conclusion can be drawn with the angles between the Fmocs and enthalpy of association.

Table 2 – QM geometry optimization of Fmoc-FFY dimers from molecular dynamic simulation. ωB97X-D / def2TZVP optimization in gas and water (PCM).

Dimer number	Snapshot of the optimized structure	Energy (Ha) gas/water	ΔE (kcal/mol) from most stable	Angle between Fmocs (deg)	Distance between Fmocs (Å)	Enthalpy of association (kcal/mol)
1	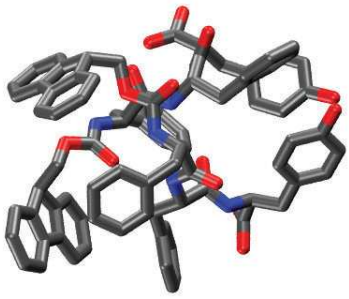	-4630.13085621 / -4630.18359657	0 / 0	82.51 / 84	6.6 / 6.8	-51.49 / -45.61
2	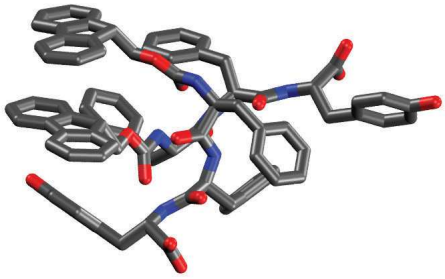	-4630.11107386 / -4630.16654280	12.4 / 10.7	7.4 / 7.7	4.6 / 4.8	-39.07 / -34.91
3	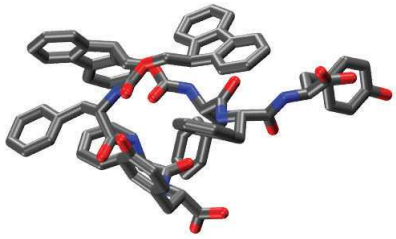	-4630.10648576 / -4630.15871837	15.3 / 15.6	60.7 / 67.5	8.6 / 9.0	-36.2 / -30.00
4	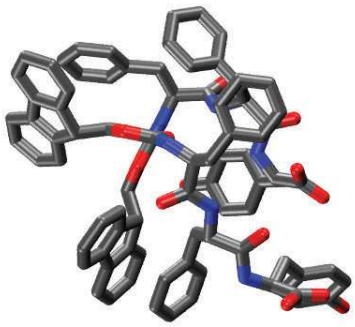	-4630.10522727 / -4630.16876527	16.1 / 9.3	84.4 / 84.4	6.8 / 7.5	-35.41 / -36.31

QM geometry optimization can also be achieved between the pairs of residues (Fmoc-Fmoc, Fmoc-Phe, Phe-Phe, etc.). The informations arising from these optimizations is the enthalpy of association between residues. The results are presented in table 3.

Table 3 – Enthalpy of association for some pairs of residues found in the tripeptide

Pair	**Enthalpy of association (kcal/mol)**
Fmoc-Fmoc	-13.03
Fmoc-Tyr	-11.76
Fmoc-Phe	-8.81
Tyr-Tyr	-7.00
Phe-Phe	-6.39

As reported in this table the most energetic association is between the Fmocs. This result highlight the fact already presented in the literature that Fmoc-Fmoc interaction is the driving force of self-assembly[30]. Nevertheless, other pairs presenting $\pi - \pi$ stacking are implicated in the enthalpy of association of the peptides. There is an order of magnitude 2 in energy between the lowest pair (Phe-Phe) and the highest energetic pair (Fmoc-Fmoc). When sorting the pairs by their energy, it emerges that when the Fmoc is part of the interaction the energy are in the upper median of the values. In that sense, Fmoc is in fact a driving force of self-assembly.

4.2 MD of Fmoc-FFY dimer assembly

System simulated : 2P.

The trajectory of 2P system display two oligopeptides that come closer and dynamically interact (Figure 1.a) through multiple non-covalent interactions. The first one is a hydrogen bond between the backbones of the peptides (mainly N-H $\cdots$ O=C), and the second is $\pi - \pi$ stacking between aromatic moieties. The statistic of self-assembly can be analyzed by plotting the distance between the two centers of mass (COM) of the peptides for each of the three MD runs (Figure 1.b). It is seen that both Fmoc-FFY come in close contact (below 10 Å) during the dynamic. As the peptides are not always in the dimer form, it can be hypothesized that the energetic landscape found in QM optimization can be achieved through MD but does not lead to a static and irreversible association which is in accordance with the IUPAC definition[31]. The statistic of association shows that during the 2000 ns of dynamic the peptides are in contact for 180 ns which is 9% of the time of the trajectory. In diluted systems self-assembly is, in this case, not a regular phenomenon, however, its presence would suggest that aggregation can be studied by MD simulations.

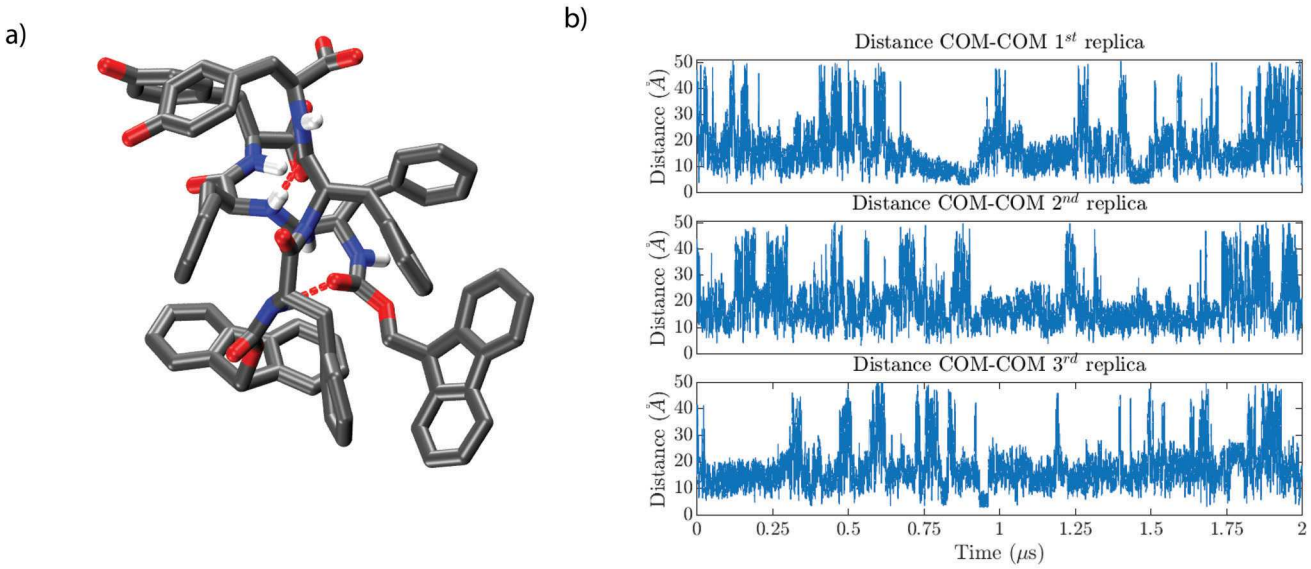

FIGURE 1 – (a) Snapshot of the association for the 2P system (Table 1), hydrogen bonds are shown in dotted red. (b) Distance between the two centers of mass (COM) of the peptides along the trajectory for the three replicas.

To study the structuration of the self-assembly, correlations between angles and distances of aromatic moeties can be calculated (Figure 2.a). The correlation helps to define the directionality of $\pi - \pi$ stacking between aromatic rings. This analysis is, in this case, focused between the Fmoc and the other aromatic groups, the attention drawned to the Fmoc is justified by literature that suggests a strong influence of this residue in self-assembly. Normalized correlation maps, have already been used in previous articles of other groups to understand the molecular organization in self-assembly[21]. For the 2P system the highest correlation found is between the Fmoc and the first phenylalanine (Phe1, Scheme S1.a) forming an angle of 90° at a distance of 6 Å (Figure 2.a). This interaction is in accordance with perpendicular $\pi - \pi$ stacking already seen by Gazit and colleagues [21]. It also exists a correlation between the two Fmoc, that arrange in nearly perpendicular T-shaped $\pi - \pi$ stacking (from 50 to 110°) at 7 Å along with parallel stacking (10, 155 and 170°) at 4 Å. These observed conformations are almost half in propensity compared to the perpendicular stacking between the Fmoc and the phenylalanine. In addition the Fmoc moieties do not have the same structuration for $\pi - \pi$ stacking with the first and second phenylalanine. This result means that the Fmoc have a specific interaction with one of the two phenylalanines (Figure 2.a). Correlation maps for the three independent replicas can be found in Figure S2 and display the same overall trend.

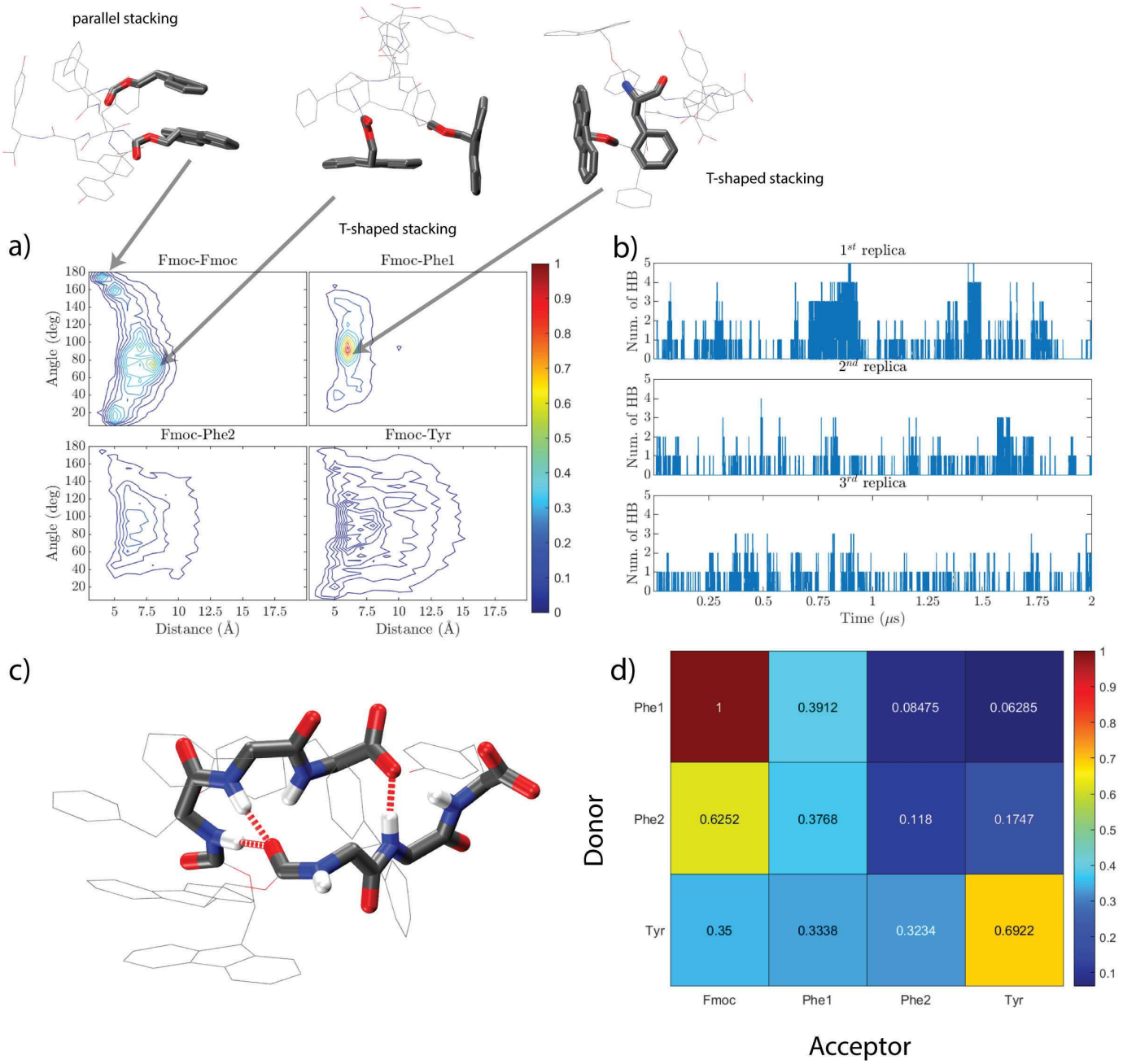

FIGURE 2 – (a) Correlation map for the 2P system with the Fmoc moieties with all peptides are from the N- to the C-terminal conformation, (b) Number of H-bonds (for the three replicas), (c) Snapshot of H-bonds in dotted red between the backbones, (d) Heatmap of hydrogen bond analysis between donor and acceptor residues.

Radial Distribution Functions (RDF) can also be calculated for the same pairs (Figure S3) and display the same conclusions as the correlation maps. All three replicas have the same RDF profile which means that interactions of all systems are similar and independently found. Nevertheless, the angles formed between the Fmoc residues for each replica are not identical and this is the gain of information not seen in RDF and brought by correlation analysis. Hydrogen bonds are considered spatially restricted non-covalent interactions due to the limit in the angle (135°) and distance (3 Å) formed between the donor and acceptor atoms. The analysis of hydrogen bonds gives the amount

of bonds formed during the trajectory and also the details by residue of each donor and acceptors. By combining these two information, it is possible to monitor hydrogen bonding of the backbone of the peptide and evaluate structuration of the peptide through this interaction. For the dimeric system (2P, Table 1) the number of simultaneous hydrogen bonds can go up to 5 bonds at the same time between the two backbones (Figure 2.b). Donors can only be amino-acids as the Fmoc does not possess any hydrogen donor. However, all residues can be considered as acceptors. The graphical pair analysis is done using a heatmap (Figure 2.d). In the case of the dimer the amid group of the two phenylalanines will mostly give hydrogen bonds to the Fmoc as depicted in the snapshot in the Figure 2.c. This analysis is an indicator of the underlying structure of the dimer and hence improve description of self-assembly. Combined with the angle-distance correlation it is possible to highlight that both peptides will organize themselves from N- to C-terminal conformation (Schemes 1 and 2). In addition, the tyrosine is associated mainly with its corresponding self in the other peptide, revealing that this end chain residue has to be stacked on top of each other for this specific hydrogen bonding to happen along with the $\pi - \pi$ stacking of the Fmocs described above.

4.3 Influence of the concentration of peptides

System simulated : 5P-TIP3P.

We now propose to study self-assembly with a higher concentration of peptides (five peptides in a bigger simulation box, 4.8×10^{-3} mol/L) to see if aggregation can occur and lead to an organized structure. The box is extended to 120x120x120 Å and then, as previously, peptides are put in random positions. The trajectory show full aggregation after starting at 225 ns until the end of the trajectory. The peptides form a pentamer for the three replicas (Figure 3.a), the individual trends can be found in Figure S4.

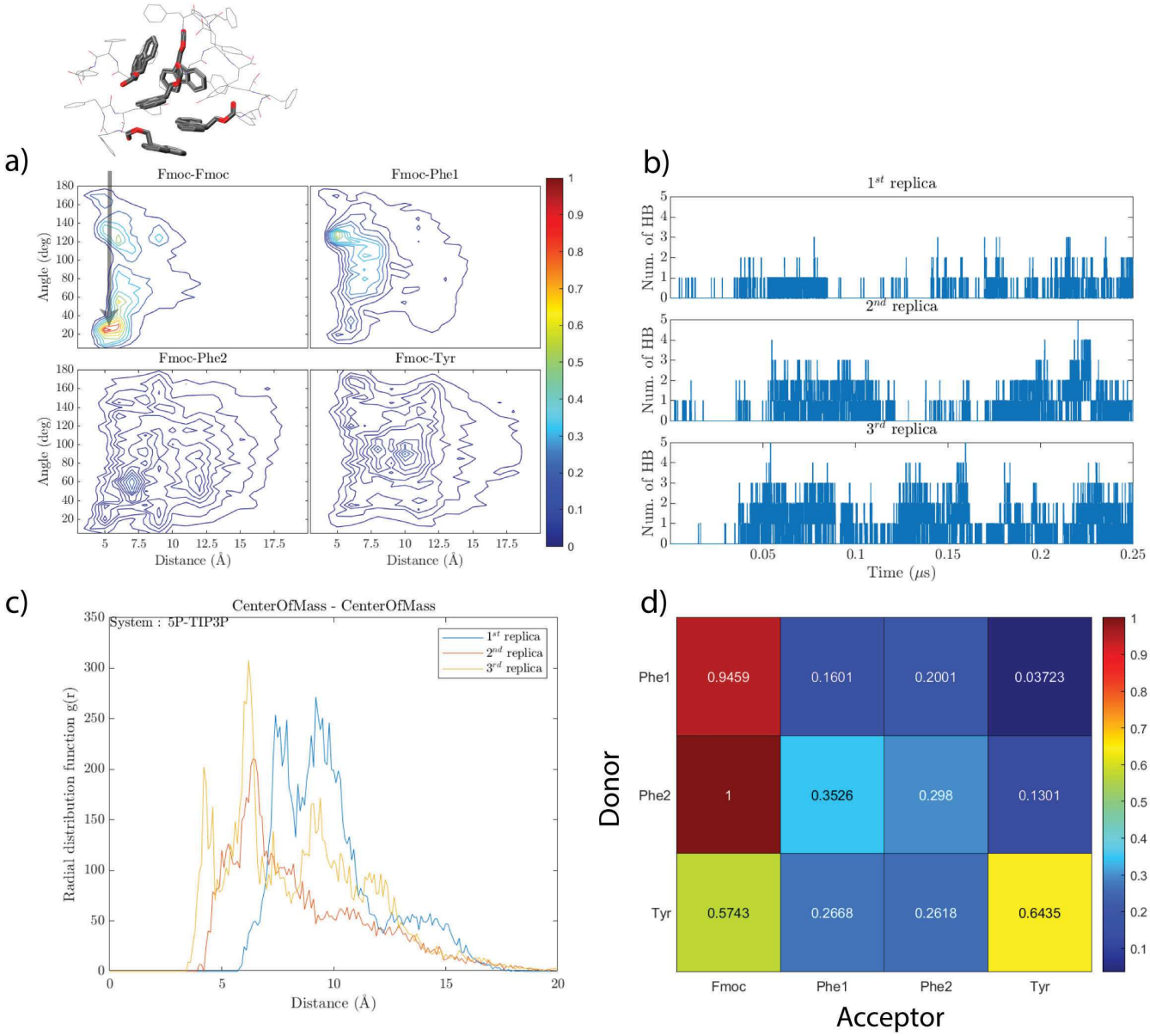

FIGURE 3 – (a) Correlation map for the 5P-TIP3P system for all the correlations possible with the Fmoc moieties, (b) Number of hydrogen bonds regarding time of MD for all three replicas, (c) Radial Distribution Function (RDF) of the COM-COM for the three replicas, (d) Heatmap of hydrogen bond analysis between donor and acceptor residues. Full description of the three replicas for the correlation maps and hydrogen bonds heatmap can be found in figure S4.

One way to define self-assembly is to observe if a clear repeating pattern can be found when peptides are aggregating. By the only means of observation of the trajectory, no clear motif is found. Nevertheless, structuration can be found through structural analysis. Correlations of the angles and distances between the Fmocs display a peak of structuration at 5 Å for an angle at nearly 30° (Figure 3.a). The snapshot in the same figure display this spatial organization of the Fmoc moieties and highlight a parallel displaced $\pi - \pi$ stacking. As presented in the Figure 3.c, RDF between COMs of peptides display at least two peaks for two replicas meaning that aggregation is occurring. Hydrogen bonds can be monitored during the trajectory and its average number throughout is 0.53 (Figure 3.b and Table S1). The Figure 3.d displays a similar pattern than the 2P system for the structural

analysis, the main difference is the higher value of donor/acceptor pairs (Phe1-Fmoc ; Phe2-Fmoc ; Tyr-Tyr) with increasing peptide concentration. In that case the conclusions over the structure of the 5P system are identical to those of the 2P : the peptides are on top of each other mainly with N- to C-terminal conformation (Scheme 1 and 2) during the trajectory.

4.4 Influence of the water model

Systems simulated : 2P, 2P-SPCE, 2P-TIP4E, 5P-TIP3P, 5P-SPCE, 5P-TIP4P-E.

Water is a complex solvent to model with all its properties fitting experimental data. Hence, computational chemists invented various water models depending on the application and the desired properties of interest. We wanted to analyze if the water model could have an influence over the self-assembly of peptides. We thus checked the effect of the water model (TIP3P, SPC/E and TIP4P-Ewald) with both 2 and 5 peptides in the simulation box.

For the dimeric systems, no major effect has been encountered for the cumulated aggregation time that is 180 ; 230 and 130 ns for TIP3P, SPC/E and TIP4P-Ewald water models for an overall of 2000 ns. As seen in the 2P system with TIP3P, there is the appearance of a peak of structuration between the Fmoc and the first phenylalanine (Phe1) which is not predominant for the 2P-SPCE and 2P-TIP4P-E simulations (Figure 4, correlation maps).

This is seen in the correlation maps of the three systems (Figure 4, correlation maps) that indicate three peaks at different angles/distances pairs. The Fmoc-Fmoc are structured at [6 Å, 110°] for SPC/E and both [5 Å, 10°] and [5 Å, 150°] for TIP4P-Ewald water models. It means that peptides are not aggregating in the same conformation in different water models. This can also be analyzed through the hydrogen bond heatmap (Figure 4, heatmaps below correlation maps) that are different for the TIP4P-Ewald water model. It reflects more structuration in both C- to N-terminal and N- to C-terminal conformations. In addition the percentage of aggregation time is 9 ; 11 and 6 % respectively for the TIP3P, SPC/E and TIP4P-Ewald water models regarding the full 2000 ns of trajectory.

In that sense, more concentrated systems at 5 Fmoc-FFY have been investigated with the three water models to observe if the structures are concentration dependant with various water models.

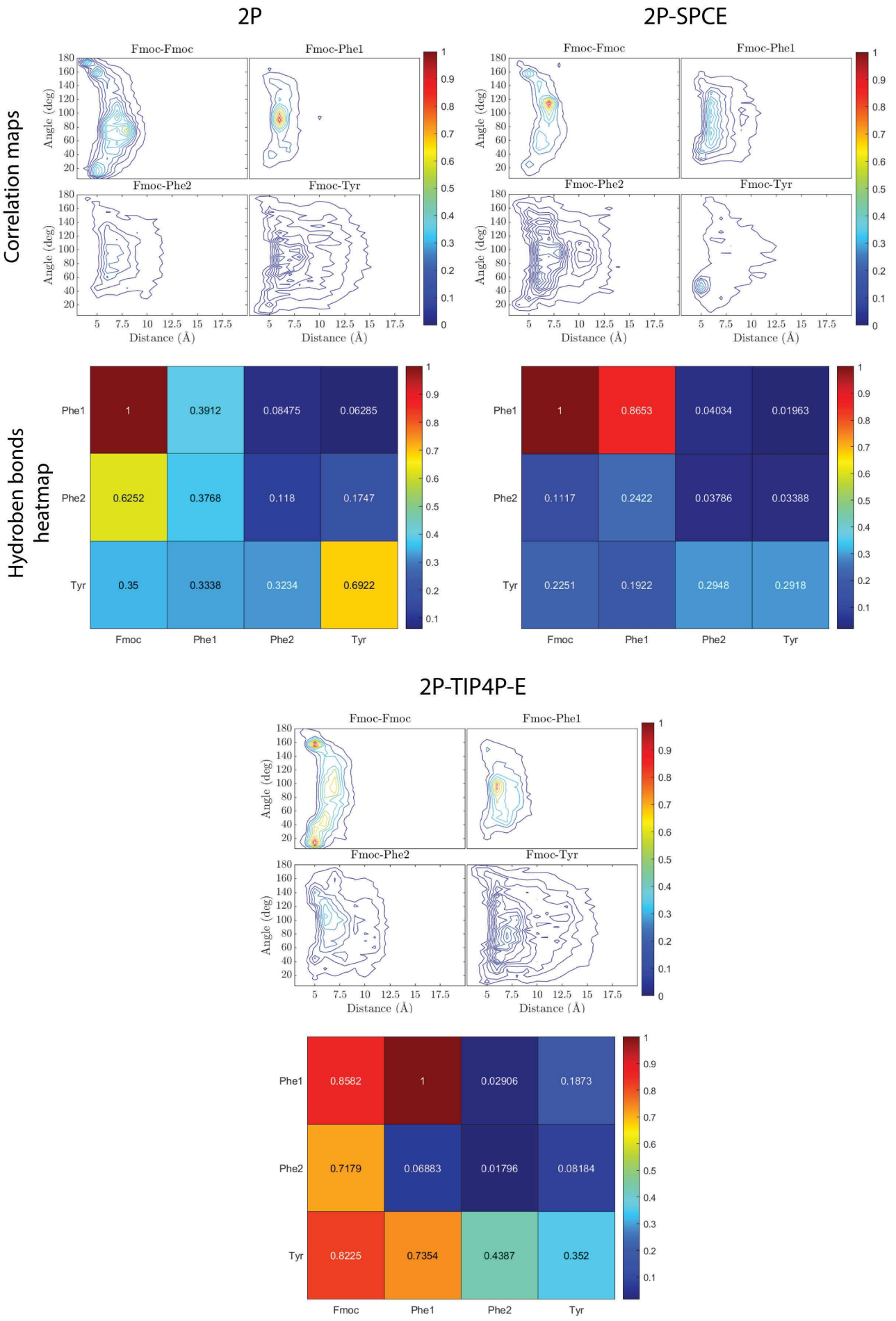

FIGURE 4 – Correlation maps and hydrogen bonds heatmap for 2P system with the three water models (TIP3P, SPC/E, TIP4P-Ewald)

For the pentameric systems with the SPC/E water model the observation that is made over the replicas is that self-assembly is rarely presenting full aggregation of the peptides meaning that pentamers are not often seen (Figure 5, snapshots). However, the structure of aggregates is in a narrower region of the correlation map for the Fmoc-Fmoc (Figure 5, 5P-SPCE system, correlation maps) regarding other simulations. The Fmoc-Fmoc interaction for the 5P-SPCE display a sharp peak at 5 Å forming an angle of 160°, in addition to another area of correlation found between 5 and 9 Å with a wider angle range from 40 to 80°. These regions of correlations are not connected and may be the result of two structures coexisting in different clusters. In Fmoc-Tyr correlation, the map displays a strong correlation which is visible at 7 Å with two angles at 60 and 110°.

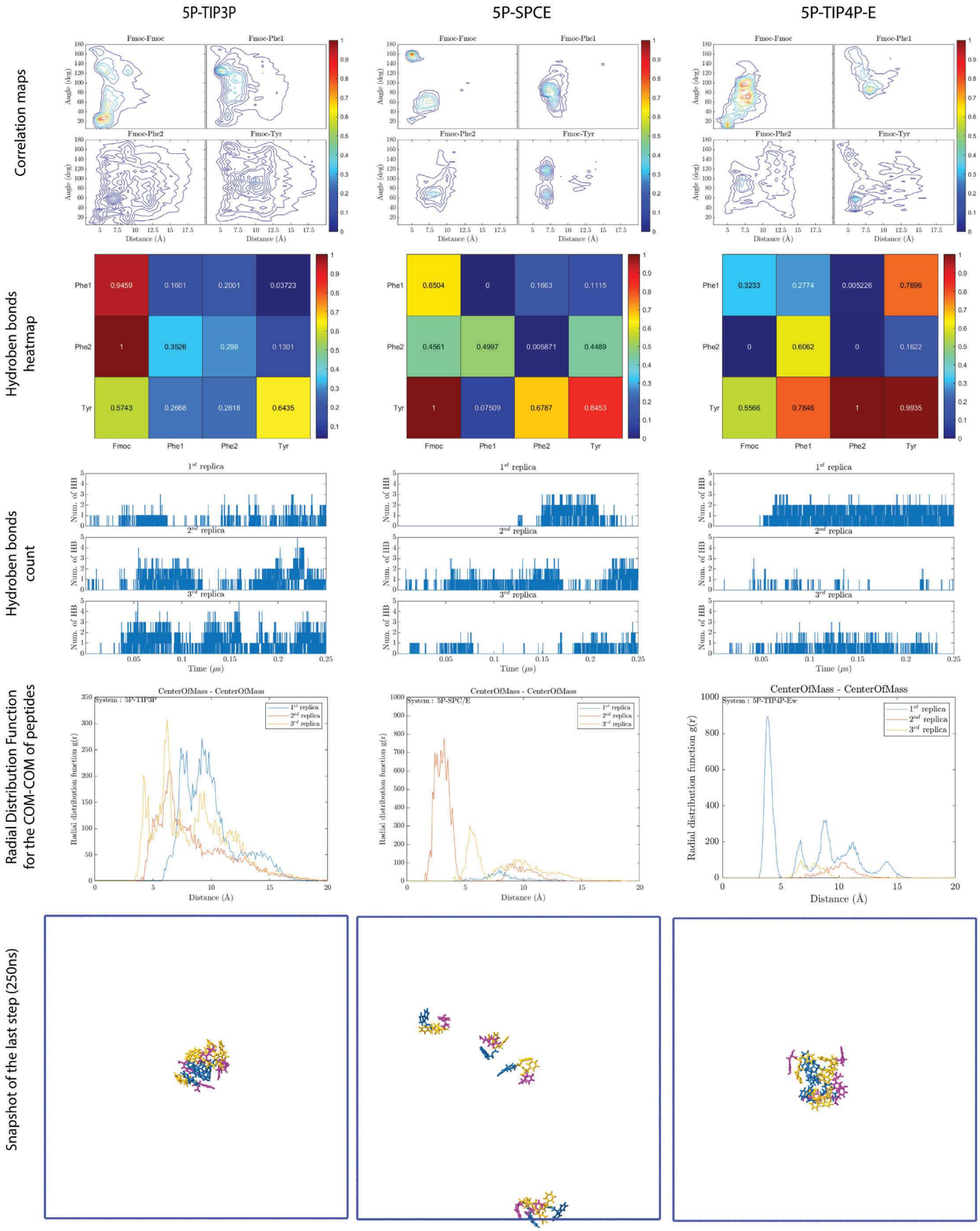

FIGURE 5 – Correlations maps, hydrogen bonds heatmap and couting, RDF of COM-COM of peptides and final snapshot after 250 ns for 5P-TIP3P, 5P-SPCE and 5P-TIP4P-E systems all analysis presented, except snapshots, take into account the three replicas done for each system. Colors of each residue can be found in Scheme 1.

When analyzing both RDF and hydrogen bonds of the three replicas of 5P-SPCE only the second one display higher aggregation (Figure 5, 5P-SPCE hydrogen bonds and RDF). The detail of hydrogen bonds is quite different as previously seen with the TIP3P model (5P-TIP3P system, section 3.3, Figure 3) mainly because now the tyrosine residue is the main hydrogen bond donor with the Fmoc. This result may be the explanation of two aggregates that have different structures. The conclusion over that system is that SPC/E is not a suitable candidate for studying self-assembly because aggregation is never fully reached (formation of pentamers) for a majority of replicas. In addition the hydrogen bond heatmap reveal that self-assembly is structured in both N- to C-terminal and C- to N-terminal conformations.

One other water model that can be of interest is the TIP4P-Ewald model that uses an additional virtual point in space in the water molecule and is also adapted for the use of Ewald summation. The observation made for the replicas of this system is that pentamer is observed during the trajectory of only one replica. In terms of correlation maps (Figure 5) there is a wide area of peaks for the Fmoc-Fmoc association in the range of 5 to 8 Å and from 40 to 120°. In that case dynamic of the analysis of the systems may be in cause due to two replicas that does not display full aggregation but are still contributing in the analysis. Still, Fmoc-Fmoc interaction present a specific structuration at 5 Å forming an angle of 10° which is near parallel stacking, other correlations are found with an angle range from 50 to 110° in the 6 to 8 Å area. It may be a sign of some peptides that adopt close structuration. One other strong correlation of the Fmoc is with the first phenylalanine (Phe1) at 8 Å forming a perpendicular stacking. However, it has to be noted that 8 Å is quite in the end of the range of $\pi - \pi$ stacking and may not be as energetic as the others that are closer. RDF of COMs of peptides in the first replica exhibits 5 peaks that are structured at 3.9 ; 6.7 ; 8.8 ; 11.2 and 14 Å each (Figure 5, RDF of the 5P-TIP4P-E). It may be the result of a structuration with different layers of peptides. However, analysis of the structures by the use of COM does not reveal the molecular interactions in RDF peaks. With TIP4P-Ewald, hydrogen bonds are found mainly in two replicas and the details give however different information compared to TIP3P and SPC/E. The most hydrogen bond found is the Tyr-Phe2 and the second highest normalized propensity is Tyr-Tyr interaction. In this TIP4P-Ewald model the tyrosines are more in interactions than with the previous water models. When adding the correlation map to the overall analysis, the structure revealed is the C-to N-terminal with N- to C-terminal. So, even if the TIP4P-Ewald does not always aggregates in full propensities it is still possible to obtain a structure from statistical analysis.

For the structuration of the higher concentration of peptides with the three water models it is

found that only the 5P-TIP3P is presenting the N- to C-terminal conformer. The two other models (SPC/E and TIP4P-Ewald) present a co-existence of the two conformers. To conclude the TIP3P is the model that will be used for the influence of the chaotropic salt due to observation of the formation of pentamers in all replicas. However, further discussion about the impact of the water model is held in the dedicated "Discussion" section (page 100).

4.5 Influence of the salt concentration in self-assembly

System simulated : 2P-NaCl.

The salt and its concentration are physico-chemical parameters that are also experimentally studied. In our systems we want to observe how a high concentration of salt (2.4 mol/L which is way above the experimental concentration of 2.5 $\times 10^{-3}$ mol/L) can affect self-assembly and structures of the dimer. Analysis of distances between the COMs for the three replicas states that aggregation (distance below 10 Å) is in fact happening more often (180 ns versus 810 ns without and with salt respectively) than in pure water(Figure 6.b).

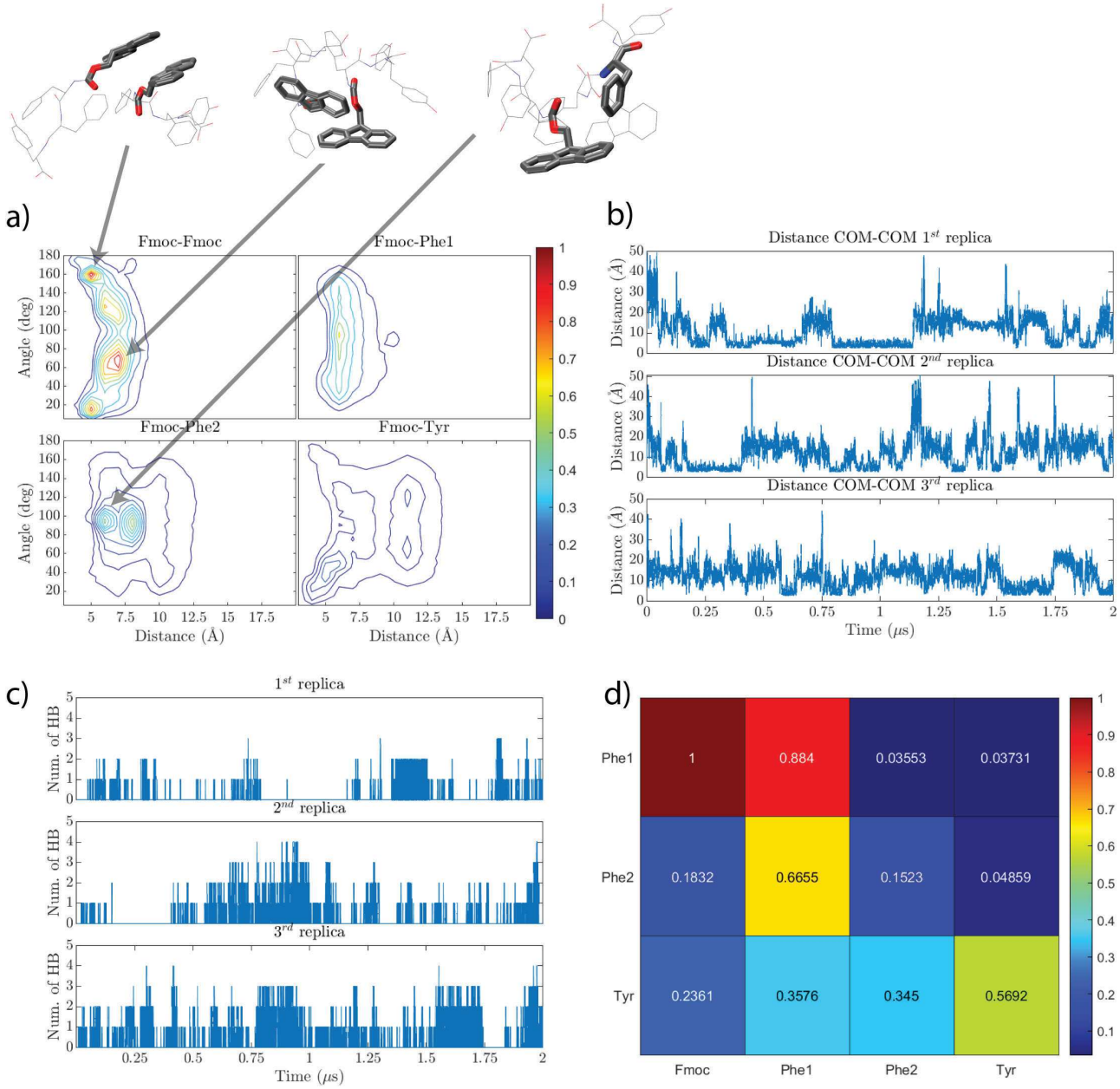

FIGURE 6 – (a) Correlation map for the 2P-NaCl system for all the correlations possible with the Fmoc moieties, (b) Distance between COM of peptides in presence of salt in the simulation box for the three replicas, (c) Hydrogen bond counting regarding time of MD for all three replicas, (d) Heatmap of hydrogen bond analysis between donor and acceptor residues.

The aggregation occurs via a different pattern of the correlation map (Figure 3.a). The Fmoc-Fmoc structuration is now higher than the Fmoc-Phe1 and $\pi - \pi$ stacking become wider in the angle distribution (from 40 to 150°) for a distance of 6 Å. Salted water media increase in addition the aggregation of the Fmoc-Phe2. That pair structuration is now 90° for 6 Å in T-shape compared with similar systems in pure water. However, $\pi - \pi$ stacking is not the only non-covalent bonding that is affected by the presence of an electrolyte. The details of the analysis of the hydrogen bonds for the 2P-NaCl is similar to the 2P system. The main difference is that the second phenylalanine is less hydrogen bonded to the Fmoc and more to Phe1. The structure is, in this system also an N- to

C-terminal conformer as also previous seen for the 2P system. The salt is not affecting the conformers, only the dynamic of association.

In addition, RDF between COM of peptides and Na^+ are of identical shape for the 2P and 2P-NaCl. The only difference lies in the g(r) value of the first peak at 2.3 Å which are 1.3 and 7 respectively for 2P and 2P-NaCl which is in accordance with the increase of salt's concentration. When analyzing the RDF between water and Na^+ to see if solvation of the cations could lead to the depletion of water near the peptides, the number of molecules of water in the second shell of solvation of sodium is the same and equal to 22 for both 2P-NaCl and 2P systems. When analyzing the RDF between the Fmoc and the water molecules in the first and second solvation shell, there is almost identical values for the first (4.9 ; 4.5) and second (49.7 ; 46.0) solvation shells for 2P and 2P-NaCl respectively. The sodium ions are placed on top of the Fmoc during some frames of the trajectory. Which can be associated as cation-π stacking. In addition, some sodium ions interact with carboxylate to compensate the negative charge.

4.6 Chaotropic effect of salt

Systems simulated : 5P-NaI, 5P-CsI, 5P-CsCl.

The first salt studied is NaI (ten sodium iodide pairs in presence with five Fmoc-FFY, Table 1). The observation of the trajectory present that association is reversible : when pentamers are formed they are often dissociating in smaller clusters as illustrated by Figure 7. Nevertheless, correlation maps give a structuration at 4 Å and an angle of 170° for the Fmoc-Fmoc interaction. This is typical of a parallel $\pi - \pi$ stacking. A correlation is also found between Fmoc and Phe1 in the region from 5 to 7.5 Å displaying an angle between 110 and 140°. For the rest of the association with the Fmoc, Phe2 and Tyr have only few interactions compared to the Fmoc-Fmoc regarding the correlation maps.

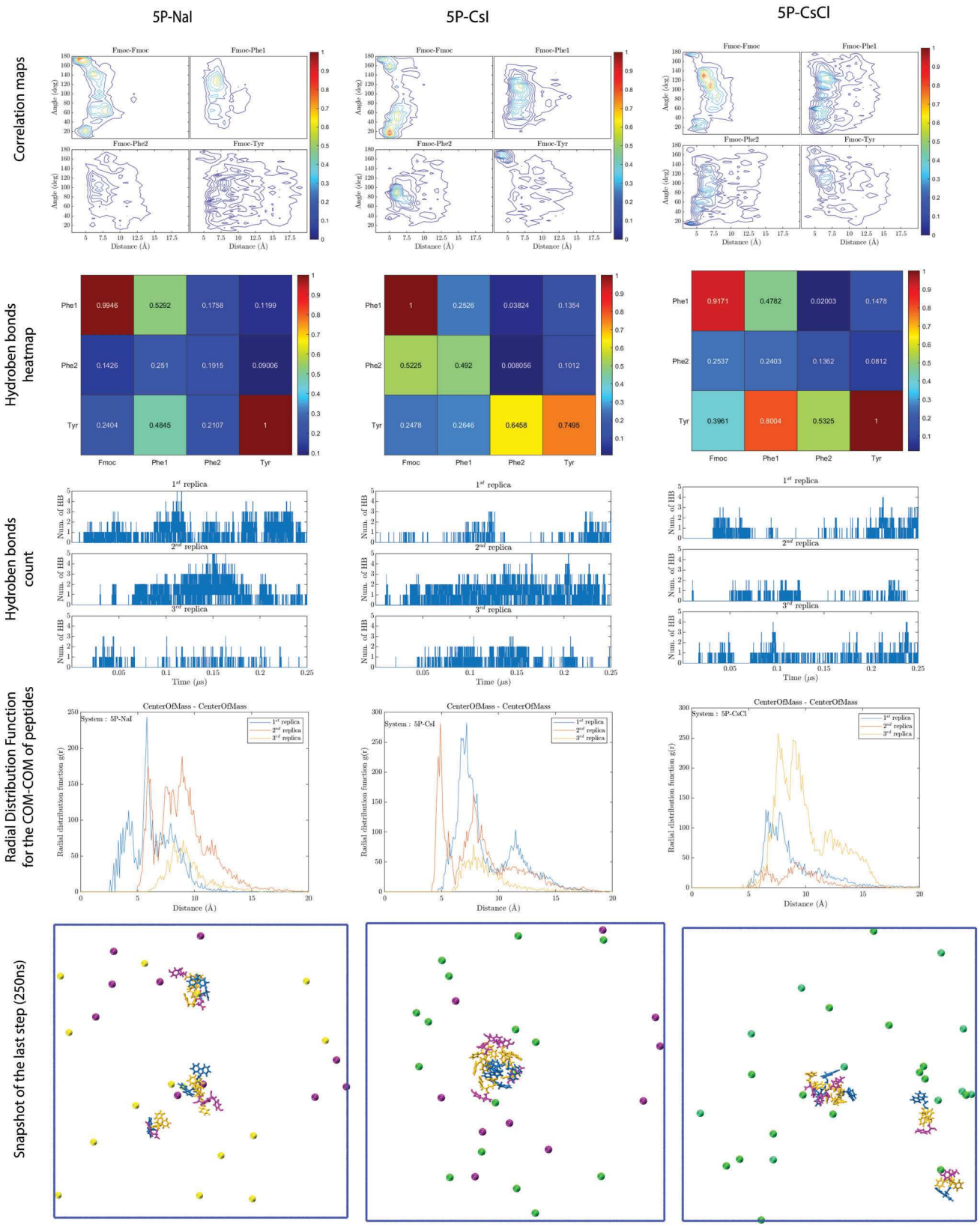

FIGURE 7 – Correlations maps, hydrogen bonds counting and heatmaps, RDF of COM-COM of peptides and final snapshot after 25 ns for 5P-NaI, 5P-CsI and 5P-CsCl systems all analysis presented, except snapshots, take into account the three replicas done for each system. Colors of each residue can be found in Scheme 1. Sodium is in yellow, chloride in green, iodine in purple and cesium in cyan. Ionic radius are not represented with the right scale.

In addition COM-COM RDF's of peptides display structuration in the three replicas and are, in

this case, the average of all the small clusters found during the trajectory. With NaI, hydrogen bonds propensities, are the same as with NaCl, (Figures 7 and 5) the average amount of hydrogen bonds is 0.51 versus 0.53 for the overall dynamics with NaI (5P-NaI) and NaCl (5P-TIP3P) respectively (see Table S1). However, what is quite different is how peptides self-assemble and which backbone's residue is going to interact. Phe1 is hydrogen bonded the Fmoc and, the tyrosine is also a donor to it corresponding self on another peptide. The combination of this previous analysis with the angle-distance correlation helps to make assumptions about the N- to C-terminal assembly and also parallel displaced Fmoc-Fmoc $\pi - \pi$ stacking because the only possibility to have hydrogen bonds between Phe1 and Fmoc is for one them to be on top of each other and make a small translation in order to form the hydrogen bond.

When replacing sodium by cesium the outcome of the structure of self-assembly is the equivalent as before. The RDF of COM-COM display a broad peak and the aggregation propensity is higher and goes up to the formation of the pentamer. The CsI salt also helps to favor $\pi - \pi$ stacking with the Fmoc for other residues (Fmoc-Phe and Fmoc-Tyr) as illustrated by Figure 7. The only new data is the correlation of Fmoc-Tyr at 5 Å forming an angle of 170° and Fmoc-Fmoc correlation at the same distance and an angle of 10° which is new compared to previous results. Phe1 interacts with the Fmoc via H-bonds and the tyrosine, it is not possible to have both in the same time, it indicates that there are two conformers. In addition, aggregation is not observed at full propensities, meaning that several clusters can have different structurations.

The cesium chloride however present a different pattern of structuring : Fmoc-Fmoc interaction is at 6 and 7 Å with 130 and 110° respectively. In addition, correlations maps with other residues highlight that Fmoc is also stacked in a wide range of angles with both Phe1 and Phe2. Then, RDF of the COM of peptides with the CsCl salt is displaying an aggregation pattern for two out of three dynamics (1st and 2nd replicas). The hydrogen bonds, however, are quite lower than with the other salts. One other hydrogen bond type emerges from the analysis which is the tyrosine that acts as a hydrogen bond donor with the first phenylalanine. The interpretation also falls in the same hypothesis that multiple conformers exist simultaneously even though the trend displays a majority of N- to C-terminal conformation.

The RDF's integration between ions and peptides are not different with the three types of salts. However, there is a high variation of water around the Fmoc for the three systems : in the 5P-TIP3P system, the Fmoc has 30 surrounding water molecules at 8 Å, with NaI, CsI or CsCl there are 45 ; 47 ; 24 water molecules respectively. When analyzing water around each ion the result is that all ions

do have the same amount of water in their solvation shell.

4.7 Higher concentration of peptides and NaCl

System studied : 5P-1000NaCl.

We saw that different types of salt can have an effect over the peptides self-assembly and even its structure. Nevertheless, one question remains about the concentration of salt : what are the structures when the concentration of buffer or salt is even higher ? In the simulations presented in this paragraph salt were from 9.6 x 10^{-3} mol/L up to 2.4 mol/L (see Table 1 and Figure 8). The increase of the salt concentration led to a quicker aggregation time : it does need in average 110 ns to reach the formation of the pentamer versus 225 ns for 5P-TIP3P.

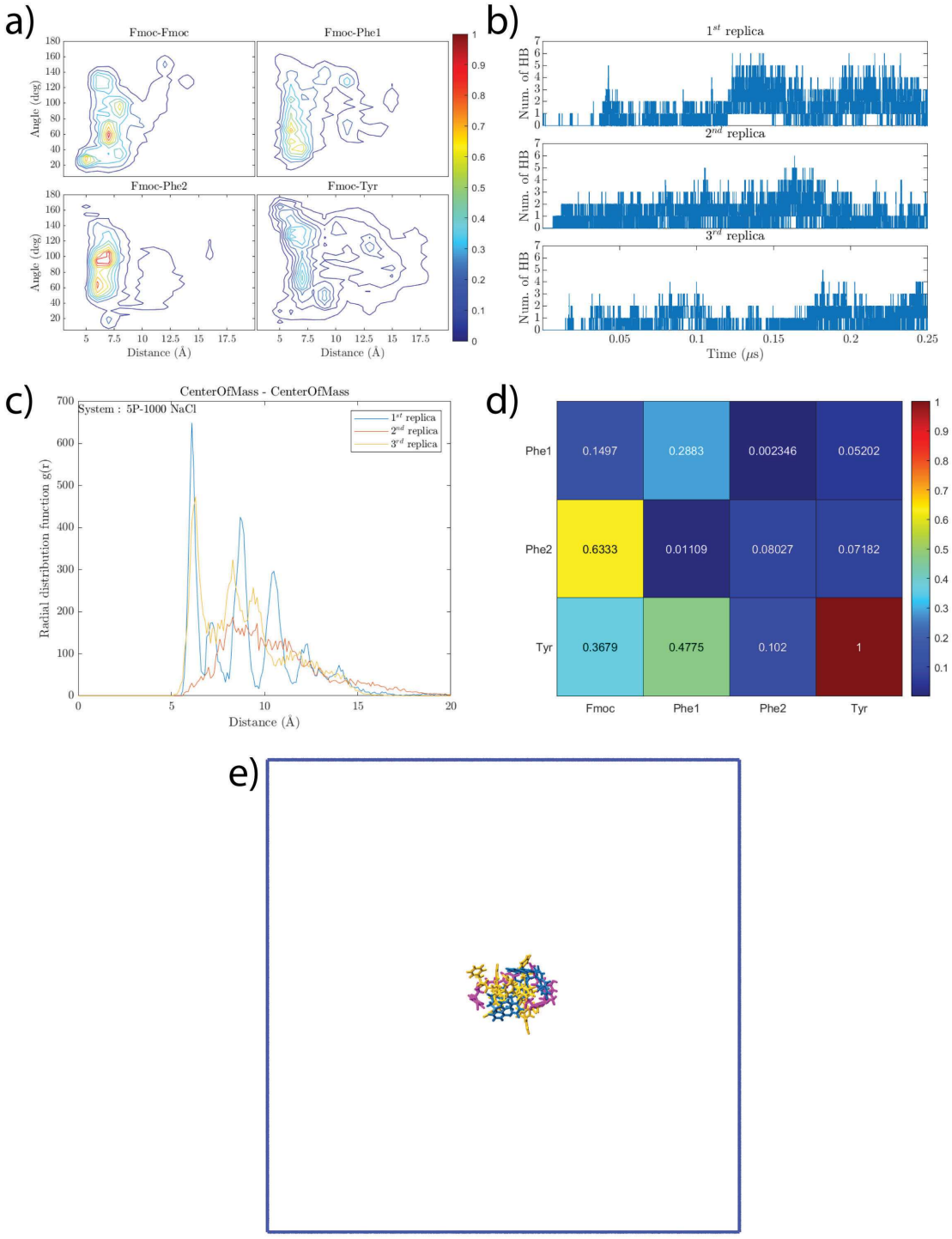

FIGURE 8 – (a) Correlation maps, (b) numbering of hydrogen bonds, (c) RDF between the COMs, (d) hydrogen bond structural heatmap and (e) snapshot of the box after 250ns of 5P-1000NaCl system

The structuration is almost equivalent for the Fmoc-Fmoc and Fmoc-Phe2, they both present a correlation at 6 Å however the angle is 50 and 90° respectively (Figure 8.a). There is also a small contribution for the Fmoc-Fmoc at 5 Å with an angle of 30°. The Fmoc-Phe1 also presents a correlation, yet it is broader in the distance and angle region. The COM-COM's RDF (Figure 8.c) of peptides during the last 25 ns of dynamic presents various peaks that indicate a structuration of peptides as seen in the 5P-TIP4P-E system. For the hydrogen bonds of the 5P-1000NaCl the influence

of salted media has been mentioned above and a change of hydrogen bonds have been observed here. For the pentamer simulation, the mean number of hydrogen bonds is higher than for the 5P-TIP3P system that acts as a reference 1.01 versus 0.53 respectively (Figure 8.b and Table S1). The analysis of the detail of hydrogen bonds shows hydrogen bonding between the tyrosines. The second most populated hydrogen bonding concern the second phenylalanine that acts as hydrogen bond donor for the Fmoc (Figure 8.d). Peptides present the higher state of aggregation with the formation of pentamers that is reached at 250 ns of MD simulation (Figure 8.e). In that dynamic the peptides also adopt a conformation in the N- to C-terminal as seen with the 5P-TIP3P.

5 Discussion

This part is dedicated to the interpretation of the results decribed above. The goal here is to develop the two following points : (i) evaluation of the force field to reproduce self-assembly, (ii) evaluation of the effect of MD and physico-chemical parameters such as (A) the type of non-covalent interactions, (B) the structural conformations and (C) the dynamic of aggregation.

5.1 Evaluation of the force field

The ff14SB force field used in this study has been designed to simulate proteins and peptides in solution[32]. On paper, this choice is the best one available as our molecule is a tri-peptide with one organic ligand covalently bonded to the N-terminal side. However, in peptides and proteins the parameters such as dihedral angles of amino acids are fitted to reproduce secondary structures such as α-helices and β-sheets. In short peptides there is no such secondary structures, then the question of the accuracy of the forcefield is legitimate. We thus need to identify the following key points : (i) self-assembly must be observed in the range of concentration of peptides, (ii) interactions described in the literature must be seen. For the first point, in the majority of the reference systems (2P, 5P-TIP3P) self-assembly occurs at the highest propensity. Even if there are only two peptides inside the simulation box in the 2P system and they only associate 9% of the time, aggregation is occurring. That low value of association is not seen here as a default of the forcefield, the definition of self-assembly by IUPAC implies reversible state. Systems that presents higher concentration of salt (2P-NaCl) is also displaying a higher propensity of aggregation (around 40% of the time) which leads to conclude that self-assembly is even occurring when the concentration of salt is very high (around 1 mol/L). For the 5P system aggregation is also present during the dynamic it is firstly seen

by the presence of dimers, trimers, etc. but mostly by the fact that full aggregation (formation of pentamers) is seen for the last 25 ns of trajectory and do not lead to dissociation in smaller clusters. The time to achieve full aggregation is proportional to the number of peptides. In conclusion of that first point, yes, the force field is able to reproduce self-assembly in solution.

For the second point the interactions expected from the literature are $\pi - \pi$ stacking and hydrogen bonding. They are both found in all systems no matter the parameters used. As there are no experimental datas to support the structural early stages of self-assembly we will assume that the ff14SB seems accurate, compared to the analogy of structures in the nanofiber at longer times (which is N- to C-terminal and presented in the following chapter).

Comparison between QM optimization and MD highlight that indeed the Fmoc-Fmoc interaction by $\pi - \pi$ stacking is represented and is present in the majority of correlation maps of the systems. The sorting of residue-residue energy in QM has proven to be observed with correlation maps in MD simulations.

In summary the ff14SB is accurately representing self-assembly as aggregation is observed, and both hypothesized non-covalent interactions from literature and QM geometry optimization were found.

5.2 Concentration of peptides

The concentration of the peptides used in the simulations are in the range between gel state and diluted system. In our simulations the highest concentration (closer to the gel state) is the dimeric system (1.5×10^{-2} mol/L), the pentameric system (closer to diluted state) which contains more peptides is less concentrated (4.8×10^{-3} mol/L). We will discuss here the evolution of the number of peptides in the simulation box instead of the increasing concentration.

The modification of the number of peptides has an influence on the most frequent $\pi - \pi$ stacked pair that shift from Fmoc-Phe1 for the 2P to Fmoc-Fmoc in the 5P-TIP3P. It does arise the question about the driving force of self-assembly, is it $\pi - \pi$ stacking in general or stacking of a specific pair ? As it is quite difficult to answer directly, some clues lie down in the correlation maps. When comparing the two Fmoc-Fmoc and Fmoc-Phe1 pairs for both systems, it appears that normalized observed propensities are almost inverted. Indeed, the highest one (1 in the scale) is the Fmoc-Phe1 for 2P and Fmoc-Fmoc for the 5P-TIP3P but the second highest propensities of Fmoc-Fmoc for 2P and Fmoc-Phe1 for 5P-TIP3P are almost identical at a value of 0.6. So, when adding more peptides

there is a complete turnout of observed correlations. The addition of peptides will then tend to favor the Fmoc-Fmoc pair instead of Fmoc-Phe1. This has also been observed with the Fmoc-FF/FF co-assembly studied by Gazit and colleagues.[21] This structural change in interactions does not lead to different conformer, they are both from N- to C-terminal. The average number of hydrogen bonds are here scaled by the number of peptides. Indeed it increases from 0.19 to 0.53 hydrogen bonds in average for 2P and 5P-TIP3P respectively and related to the number of peptides and not to their concentration in the simulation box.

The structural conformers determined with the hydrogen bond heatmap show that both systems are in the N- to C-terminal conformation. Peptides are on top of each other and interact through hydrogen bonds and, as described above, $\pi - \pi$ stacking. There is, however, no clue on what type of interaction will drive self-assembly. Nevertheless, in terms of energy some articles stated that hydrogen bonds in peptides and $\pi - \pi$ stacking also in water are energetically close, around 1.5-3 kcal/mol [33, 34]. There is then, no high predominance from one type of interaction, the mechanism seems in this case concerted.

5.3 Choice of the water model

It exists in the literature various water models. In this chapter we focused our attention to some of the main used models in simulations such as TIP3P, SPC/E and TIP4P-Ewald. We will discuss here what are the results regarding self-assembly of Fmoc-FFY and the key justifications to use one particular model.

The comparison between water models can be achieved through observation of aggregation. There is always association for the 2P system disregarding the water model. The percentages of association are relatively the same (between 6 and 11%). The dynamic of self-assembly is then similar, nevertheless the conformational analysis give different results. Indeed, except for the SPC/E the two other water models display N- to C-terminal conformation. SPC/E model lead to a mix between N- to C-terminal and C- to N-terminal. As there are only two peptides, these two structures co-exist during the whole trajectory even though they are not observed at the same time.

The conformational analysis from the hydrogen bonds seems to lead toward two co-existing structures for the 5P systems. Self-assembly in SPC/E is occurring, even if the formation of a pentamer is not reached, and aggregates have different conformations. Their dynamic nature is highly complex to observe experimentally in the early stages of self-assembly then we cannot be sure if we

have te capability to coroborate experimentally how the peptides are in early stages. Nevertheless, regarding experimental work previously done with that peptide in the same range of concentration it is sure that aggregation is observed, which is not the case computationally with SPC/E water model. In summary, SPC/E is not the right water model to study self-assembly regarding the statistic of self-assembly itself.

The two other models are both inducing the formation of pentamers during the trajectory, mainly during the last 25 ns. The non-covalent interactions, $\pi - \pi$ stacking and hydrogen bonds are still found during the trajectory, the two water models do not impact their propensity. However the structurations are different. Indeed, the Fmoc-Fmoc stacking changes from parallel to perpendicular when modifying the model from TIP3P to TIP4P-Ewald. The RDF of TIP4P-Ewald display a stronger structuration pattern regarding TIP3P. This organization, by layers of peptides, is only seen for one replica and visualization does not help identifying the underlying pattern. Nevertheless, the hydrogen bond heatmaps do indicates the conformational behavior of peptides inside the aggregate. The difference lies in the presence of the N- to C-terminal conformation for the TIP3P and both conformers (N- to C-terminal and C- to N-terminal) for the TIP4P-Ewald. Experimental data suggest that hydrogen bond with the carbamate is involved[35] and molecular organization of self-assembly in the following chapter will give the answer that N- to C-terminal conformation is the one found in the nanofiber.

For further investigations we will retain TIP3P water model for various reasons : (i) self-assembly is observed at full propensities, (ii) the two non-covalent interactions types are found during the trajectory and (iii) the conformational structuration is the one found in the nanofiber. This last point is, however, from a strong assumption that structuration at the early stage is identical that the one found in the nanofiber.

5.4 Influence of NaCl concentration

In this section we will discuss the influence of NaCl salt on self-assembly structuration. We found for the 2P and 2P-NaCl system that the dynamic of self-assembly is quite different. Indeed, the average percentage of association time is 9 and 40% for 2P and 2P-NaCl systems. As decribed in the result section, RDF did not differ between the two systems. The hypothesis of water depletion near the peptides and salt cannot be justified here. Then how peptides would be more drawn together when the salt is present at high concentration ? One article suggests that cation-π interactions may lead to

increased self-assembly[36]. Indeed, in our simulations there are more sodium ions near the peptides due to the presence of high concentration of NaCl, some sodium ions are indeed in interaction with the Fmoc during the dynamic. This hypothesis is, for the moment, the only explanation that we could draw regarding the analysis that have been done. It is also supported by the fact that water molecules are in the same propensity around the peptides regardless the salt concentration.

For the interaction types both $\pi - \pi$ stacking and hydrogen bonds are present. There is a change in the most seen stacked pair in the correlation maps upon addition of the salt. The Fmoc-Fmoc pair is now more favored in the same angles and distances than before. The salt is exalting the stacking of the Fmoc. The number of hydrogen bonds are almost identical to the systtem without salt.

In the structural domain both simulations present a N- to C-terminal conformation. It does highlight that the concentration of salt is not influencing structuration through hydrogen bonds but is increasing $\pi - \pi$ stacking.

5.5 Effect of chaotropic salt

The simulations of self-assembly with chaotropic salt present different signs of aggregation. Only the simulation with CsI displays formation of pentamer. Indeed, when aggregates started to form they quickly dissociated after few nanoseconds. The behavior with CsI is quite handy to explain, however, some comparisons with the other systems can be drawn and hypothesis carried out. First, the hydrogen bonds are not involved in the process because with NaI there are as much hydrogen bonds as with the CsI and the system does not display a stable formation of pentamer. Secondly, $\pi - \pi$ stacking exist and are present, always in majority between the Fmocs, hence it is not affected by the presence of different salts. Thirdly, there is an odd inexplicable behavior regarding the solvation of the Fmoc by water molecules for the systems. As for the NaI and CsI, there is more water around the Fmoc than with the use of CsCl where there is a little bit less water regarding the 5P-TIP3P system as a reference. This solvation of ions cannot be explained by the salt effect over water because all ions do have the same number of water around their shell. It is surprising that self-assembly is not affected by the number of water molecules around the Fmoc. Indeed, with CsI salt, where pentamers are formed there is the same amount of water as with NaI where assembly is reverting to non-aggregated state. It has been reported in the literature that peptides with chaotropic salts will have fewer propensities of self-assembly which is in accordance with the majority of the salts that we simulated [37].

Concerning the type of interactions, there is also $\pi - \pi$ stacking in near parallel conformation between the Fmoc except when CsCl salt is used. For the hydrogen bonds, the propensities are lower than with NaCl in the 5P-NaCl mostly for the CsCl salt (Table S1). As chaotropic salts are known to disrupt hydrogen bonds between water and to cause more chaos, it should also be the same for peptides.

In the structural point of view, there is not much change with the reference system (with NaCl). The conformation is, when peptides aggregate, always N- to C-terminal even if the slight difference is that with CsCl where there is also a strong contribution of the Tyr-Phe1 hydrogen bonding pair.

The goal of the use of chaotropic salt is to mimic borax buffer. However, we just saw that self-assembly is not always occurring within these conditions. However, experimentally with sodium tetraborate we do have self-assembly and hydrogel formation. Then we may consider two points (i) the hypothesis of chaotropic from borax buffer is wrong or (ii) the choice of NaI and CsCl do not reflect the chaotropic behavior of sodium tetraborate. This needs further investigation.

5.6 Increase of both salt and peptide concentration

We have discussed the two topics about the increase of concentration of salt and peptides previously but what happens when both parameters are brought together ? In terms of dynamics of the self-assembly, the formation of the pentamer is a lot faster : around 110 ns for the 5P-1000NaCl and around 225 ns for 5P-TIP3P.

The peptides here are structured in the same conformation but with new higher interactions. In the correlation maps there is now a strong interaction between the Fmoc and Phe2 in a perpendicular fashion, this behavior have already been seen for the 5P-NaI system. As for hydrogen bonds, they are in more propensities than the system with lower salt concentration (5P-TIP3P), around the double. More NaCl pairs does not impact and create a competition in hydrogen bonds. Then conclusions seem to converge in the same way as before.

For the structuration, there is however a new phenomenon when the salt concentration is increasing : the presence of peaks of structures in the RDF. Two out of three replicas does highlight this trend. The system simulated with TIP4P-Ewald water model also present these peaks. However, they are not directly visible in the pentamer. Nevertheless, the structural conformation from N- to C-terminal is still the same as before.

The increase of salt and peptides are exalting the structuration of the self-assembly. It combines

both conclusions drawned for the referenced systems with high concentration of peptides (5P-TIP3P) and high NaCl concentration (2P-NaCl). In addition the higher number of hydrogen bonds should be an additional result regarding the hypothesis of cation-π presented above. The salt is also here structuring peptides. It may be said that the concentration of the salt is only increasing the effect of the previous discussed interactions.

6 Conclusion

In this chapter we used molecular dynamics and quantum mechanics to study early stages of peptides' aggregation. We first used QM geometry optimization to minimize dimers and calculate the enthalpy of association. The aggregation process is spontaneous in both gas and water phase. The step of residues' optimization allowed to prove that indeed Fmoc-Fmoc interaction is the $\pi - \pi$ most favored. Then molecular dynamics helped us to understand the dynamic of the system. We saw that with two peptides in solution the propensity of association is low, around 10% of the trajectory, but the phenomenon of self-assembly is still occurring through hydrogen bonding and $\pi - \pi$ stacking. Analysis showed that peptides are stacked on top of each other and non-covalent interactions are directed towards specific residues mainly with the Fmoc involved. The study of the conformations helped to understand how parameters could impact the self-assembly. The summary of the conformations found for each system are in the figure 9.

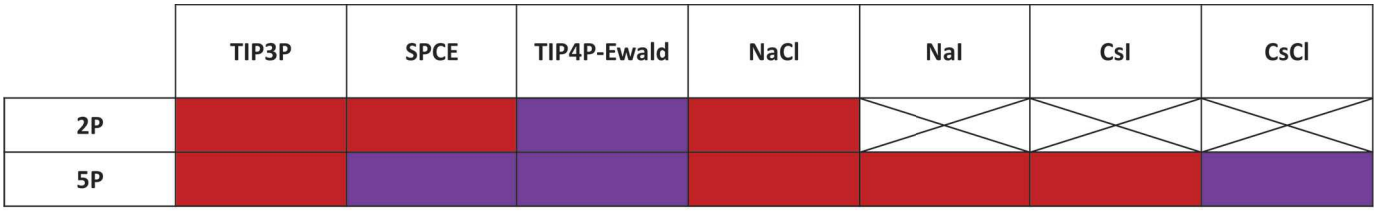

FIGURE 9 – Summary of all the conformations found in the dynamic. In red are the N- to C-terminal conformers and in purple color mean that two conformers can be found. Crossed cell mean that the system has not been simulated.

With the combination of all simulations we are able to confirm that ff14SB forcefield can be used for the overall simulations and that it is accurate enough to observe self-assembly. The study of the evolution of concentration of peptides concluded that self-assembly is also occurring with a partial shift in the structures of $\pi - \pi$ stacking with the Fmoc involved. A key point of our methodological tests about the water models is to qualify the one to use in the following simulations. Our choice was mainly driven by the fact that self-assembly has to occur and structuration must be in accordance with experimental data. As of today, the most suited water model is the TIP3P. The study of the

physico-chemical parameters showed that self-assembly is a spontaneous process and the type of salt and its concentration can impact the interactions. The use of chaotropic salts to replace the borax buffer showed that self-assembly is, when NaI and CsCl are used, not always occurring leading to uncertainty about the hypothesis about chaotropic effect from sodium tetraborate (borax). The increase of salt concentration (NaCl) allow a faster kinetic of self-assembly and an increase of $\pi - \pi$ stacking propensities. In the following section, we will describe the perspectives of all atoms molecular dynamics for the self-assembly of bigger systems.

7 Perspectives

Molecular Dynamics can also be used to simulate larger systems. The goal is to start from a random situation with a high number of peptides and observe at which concentration and if nanofibers can be observed.

First, we wanted to see how an increase number of Fmoc-FFY in the simulation box would impact the structure. Our experiment was done on five systems that contains respectively 10 ; 25 ; 50 ; 100 and 200 peptides. Simulation have been run with the same parameters as described above the only difference is the number of water molecules (56 000), of sodium cations to compensate the charge and the number of peptides. The box size is here 120 x 120 x 120 Å. The end of trajectory snapshots can be found in Figure 10. We present here first results on these larger systems.

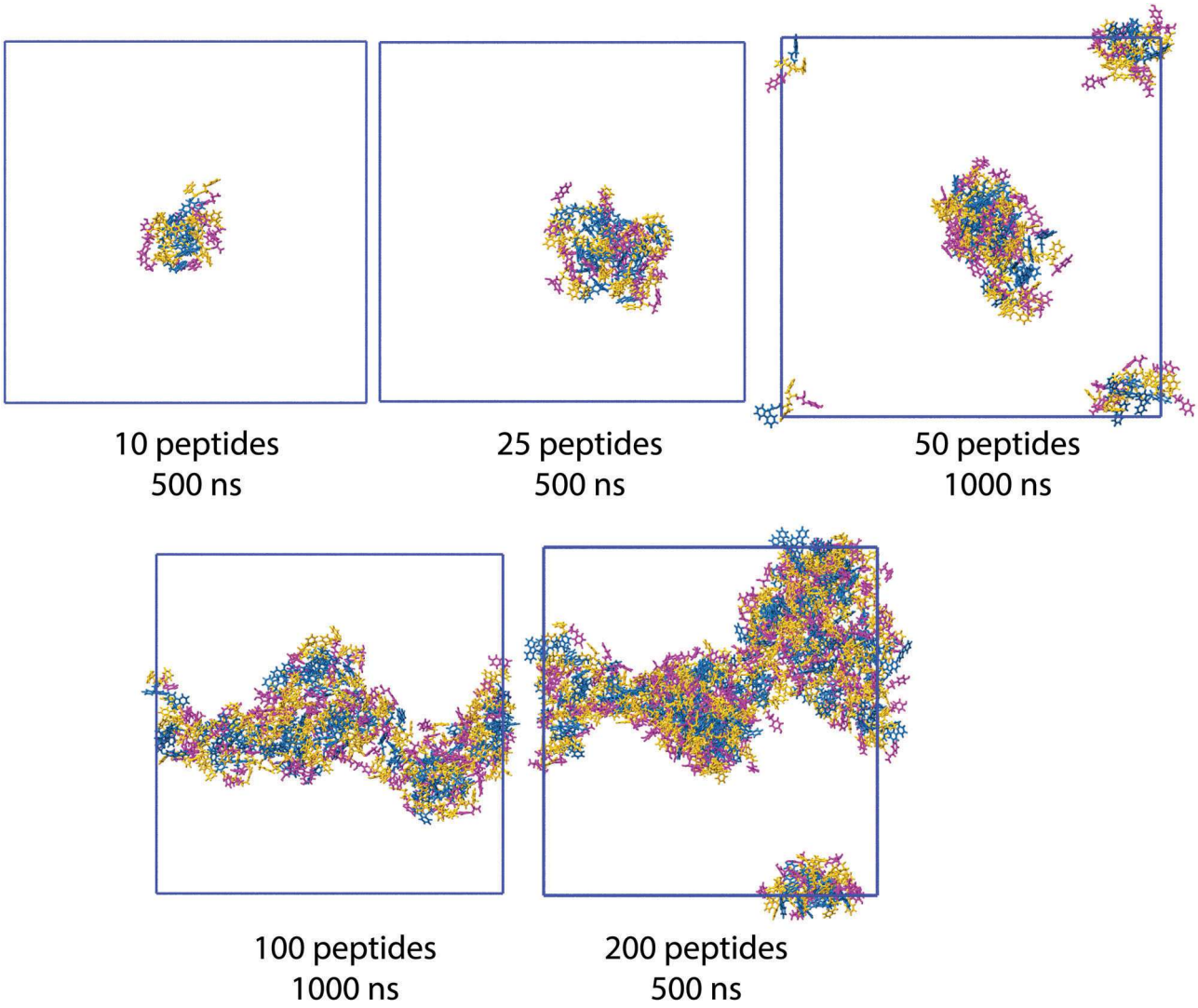

FIGURE 10 – Snapshots of the last frame of the simulations when the number of peptides is 10 ; 25 ; 50 ; 100 and 200 peptides respectively.

The snapshots give us precious information about the state of self-assembly. For example, all systems except the 50 peptides are all aggregated at the end of the dynamics. The 50 Fmoc-FFY system present a full aggregation at 1000 ns. The size of aggregates in the center of the box of the 50 peptides sytems is close to the one at 25 peptides. We may hypothesize here a critical concentration of self-assembly. This hypothesis has been studied already experimentally in peptide self-assembly.[38] However it would imply that before self-assembly there is aggregation only and no structuration. The fact the 100 and 200 peptides presents structures that are connected through the periodic conditions of the box is an indicator that 50 peptides in that box size may be near the critical concentration. It may be noted that experimentally it is difficult to quantify critical concentration with nanofibers. Indeed, the critical concentration is in general in the millimolar domain and the DLS technique (diffusion light scattering) can only be applied to spherical shapes and not nanofibers.

One major result is the presence of near nanofibers structures for both 100 and 200 peptides systems. It does show that molecular dynamics can represent the nanostructures even if it is, however, less ordered that the resolved structure presented in the next chapter. In addition the nanofiber here is not straight and present no internal structuration. However, the time scales involved are certainly in cause. The simulations have been done for a maximum of 1000 ns, then the reach of straight nanofibers may be due to a reorganization of Fmoc-FFY afterwards. What we see here though is maybe the second stage of nanofiber formation prior the reorganization.

The information that can be extracted from the dynamics is the structuration of peptides. We will only focus here in the Fmoc-Fmoc interactions as we know that it is the driving force of self-assembly. The correlation analysis between the angles and the distances of the Fmoc-Fmoc planes have been carried out for all systems (Figure 11).

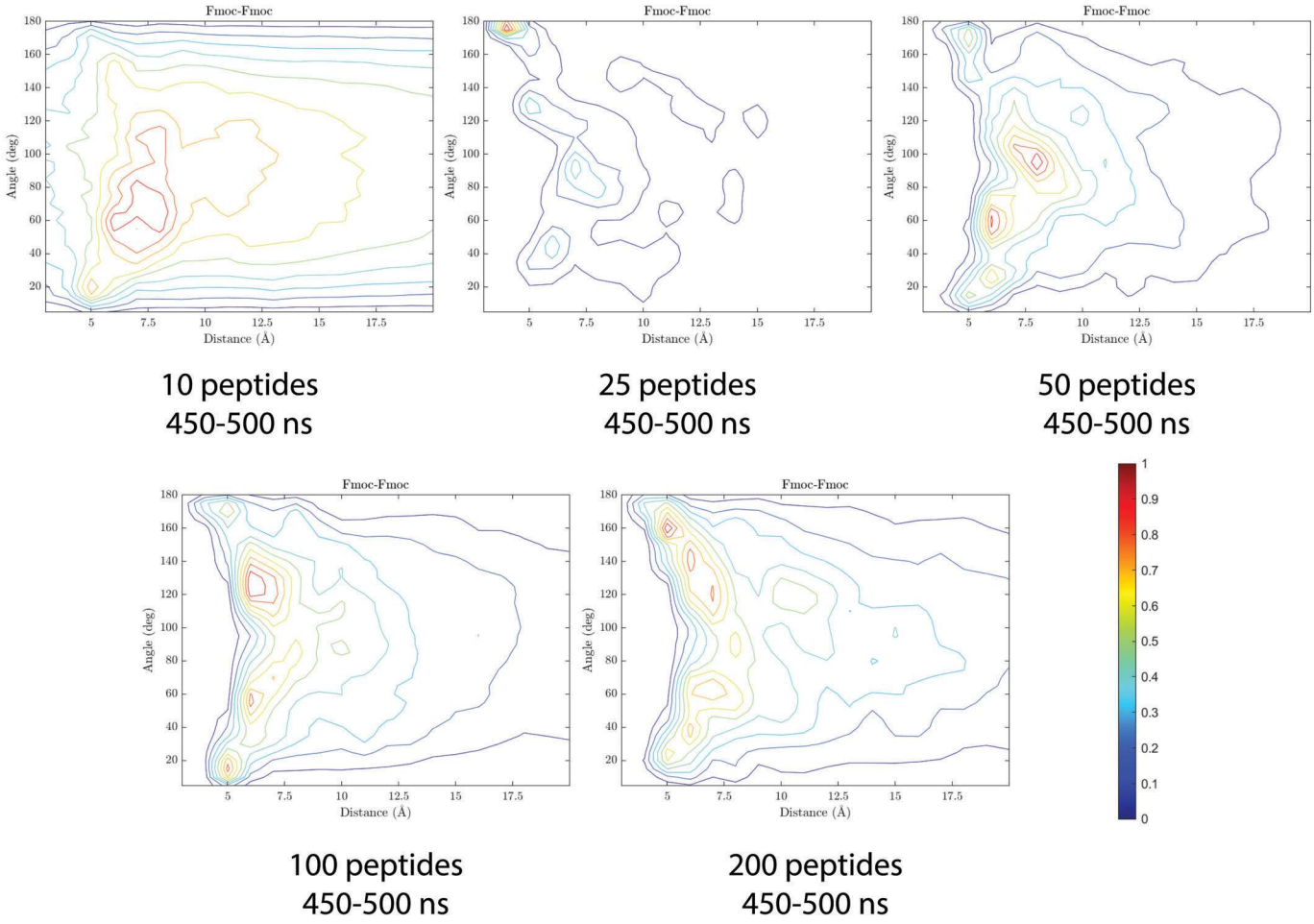

FIGURE 11 – Correlation analysis between angles and distances of Fmoc-Fmoc planes for the systems that contain 10 ; 25 ; 50 ; 100 and 200 peptides respectively. The scale is from 0 to 1 with 1 equal to the highest correlation found. All windows of analysis displayed below the name of the system are done when the peptides are aggregated and the system does not evolve anymore.

One major result that emerges from the analysis is the presence of a strong correlation for the 25 peptides systems with the Fmocs forming a parallel packing throughout the dynamic at a distance of 4.5 Å. This correlation is handy to be extracted from the snapshots of the aggregates, however, it does highlight that the so called "aggregate" is, in this system, a self-assembled structure. Then, the hypothesis described above that, below critical concentration there is only aggregation, which is a disorganized state, is false in our system. However with the 25 peptides system, it does not reach the conventional observation of nanotubes, nanofibers, etc. it may be a nucleus of the formation of fibers. Nevertheless, when increasing the concentration, the 50 peptides system does not present the same ordered behavior and correlations are seen at higher distances (6-8 Å). Indeed, the correlation is in the overall angle-distance space. The strongest correlations are in the perpendicular domain that is opposite of the previous discussed system. When increasing even more the concentration, the angles between the Fmocs tend to shift more and more toward near parallel packing. Indeed, there is a shift from 120° at 6.5 Å for 100 peptides to 160° at 5.5 Å for 200 peptides. This type of trend has already been observed by Gazit and al in their article where they used co-assembly of FF and Fmoc-FF. [21] The addition of Fmoc-FF lead to an increase of Fmoc-Fmoc correlation.

In these perspectives we just saw that increasing the number of peptides can shift towards higher sized structures and even lead to the appearance of nanofiber. The correlations maps display here the behaviour between the Fmocs and that an increase of peptides push the peptides towards a more parallel structure.

Last two perspectives for a future work are about the sampling of the system and the forcefield. Firstly, we could use Temperature Replica Exchange Molecular Dynamics (T-REMD) that would increase the sampling of the system using replicated systems at different temperatures. The exchange of coordinates would improve the conformational sampling. [39-44] Secondly, we could use the MARTINI forcefield [45] that have been widely employed for our type of systems. [46-48] One of the major result found in literature is the use of the forcefield for sampling nanostructure.[21] The article of Gazit and colleagues. presented in the Chapter 1 displayed the right nanostructures depending on the co-assemble proportion between FF and Fmoc-FF.

References

(1) Yuran, S.; Razvag, Y.; Reches, M. *ACS Nano* **2012**, *6*, 9559-9566.

(2) Ryu, J.; Park, C. B. *Advanced Materials* **2008**, *20*, 3754-3758.

(3) Arnon, Z. A.; Kreiser, T.; Yakimov, B.; Brown, N.; Aizen, R.; Shaham-Niv, S.; Makam, P.; Qaisrani, M. N.; Poli, E.; Ruggiero, A.; Slutsky, I.; Hassanali, A.; Shirshin, E.; Levy, D.; Gazit, E. *iScience* **2021**, *24*, 102695.

(4) Adler-Abramovich, L.; Arnon, Z. A.; Sui, X. M.; Azuri, I.; Cohen, H.; Hod, O.; Kronik, L.; Shimon, L. J.; Wagner, H. D.; Gazit, E. *Advanced Materials* **2018**, *30*, 1-6.

(5) Görbitz, C. H. *Chemistry - A European Journal* **2001**, *7*, 5153-5159.

(6) Reches, M.; Gazit, E. *Nature Nanotechnology* **2006**, *1*, 195-200.

(7) Kralj, S.; Bellotto, O.; Parisi, E.; Garcia, A. M.; Iglesias, D.; Semeraro, S.; Deganutti, C.; D'Andrea, P.; Vargiu, A. V.; Geremia, S.; De Zorzi, R.; Marchesan, S. *ACS Nano* **2020**, *14*, 16951-16961.

(8) Görbitz, C. H. *Chemistry - A European Journal* **2007**, *13*, 1022-1031.

(9) Adhikari, B.; Nanda, J.; Banerjee, A. *Soft Matter* **2011**, *7*, 8913-8922.

(10) Görbitz, C. H. *Chemical Communications* **2006**, 2332-2334.

(11) Hai, Z.; Li, J.; Wu, J.; Xu, J.; Liang, G. *Journal of the American Chemical Society* **2017**, *139*, 1041-1044.

(12) Castelletto, V.; Hamley, I. W.; Cenker, C.; Olsson, U. *Journal of Physical Chemistry B* **2010**, *114*, 8002-8008.

(13) Williams, R. J.; Smith, A. M.; Collins, R.; Hodson, N.; Das, A. K.; Ulijn, R. V. *Nature Nanotechnology* **2009**, *4*, 19-24.

(14) Fores, J. R.; Bigo-Simon, A.; Wagner, D.; Payrastre, M.; Damestoy, C.; Blandin, L.; Boulmedais, F.; Kelber, J.; Schmutz, M.; Rabineau, M.; Criado-Gonzalez, M.; Schaaf, P.; Jierry, L. *Polymers* **2021**, *13*, 1793.

(15) Williams, R. J.; Hall, T. E.; Glattauer, V.; White, J.; Pasic, P. J.; Sorensen, A. B.; Waddington, L.; McLean, K. M.; Currie, P. D.; Hartley, P. G. *Biomaterials* **2011**, *32*, 5304-5310.

(16) Fleming, S.; Frederix, P. W.; Ramos Sasselli, I.; Hunt, N. T.; Ulijn, R. V.; Tuttle, T. *Langmuir* **2013**, *29*, 9510-9515.

(17) Tamamis, P.; Adler-Abramovich, L.; Reches, M.; Marshall, K.; Sikorski, P.; Serpell, L.; Gazit, E.; Archontis, G. *Biophysical Journal* **2009**, *96*, 5020-5029.

(18) Castelletto, V.; Moulton, C. M.; Cheng, G.; Hamley, I. W.; Hicks, M. R.; Rodger, A.; López-Pérez, D. E.; Revilla-López, G.; Alemán, C. *Soft Matter* **2011**, *7*, 11405-11415.

(19) Yu, F.; Deng, G.; Wang, Z.; Gong, S.; Xu, X.; Zhou, Y. *Journal of Molecular Liquids* **2019**, *280*, 205-211.

(20) Kadeeja, A.; Joseph, S.; Abraham, J. N. *Soft Matter* **2020**, *16*, 6294-6303.

(21) Chakraborty, P.; Tang, Y.; Guterman, T.; Arnon, Z. A.; Yao, Y.; Wei, G.; Gazit, E. *Angewandte Chemie - International Edition* **2020**, *59*, 23731-23739.

(22) Wang, Y.; An, Y.; Shmidov, Y.; Bitton, R.; Deshmukh, S. A.; Matson, J. B. *Materials Chemistry Frontiers* **2020**, *4*, 3022-3031.

(23) Frederix, P. W.; Scott, G. G.; Abul-Haija, Y. M.; Kalafatovic, D.; Pappas, C. G.; Javid, N.; Hunt, N. T.; Ulijn, R. V.; Tuttle, T. *Nature Chemistry* **2015**, *7*, 30-37.

(24) Sasselli, I. R.; Moreira, I. P.; Ulijn, R. V.; Tuttle, T. *Organic and Biomolecular Chemistry* **2017**, *15*, 6541-6547.

(25) Roe, D. R.; Cheatham, T. E. *Journal of Chemical Theory and Computation* **2013**, *9*, 3084-3095.

(26) Frisch, M. J. et al. Gaussian-09 Revision D.01.

(27) Chai, J. D.; Head-Gordon, M. *Physical Chemistry Chemical Physics* **2008**, *10*, 6615-6620.

(28) Weigend, F.; Ahlrichs, R. *Physical Chemistry Chemical Physics* **2005**, *7*, 3297-3305.

(29) Humphrey, W.; Dalke, A.; Schulten, K. *Journal of Molecular Graphics* **1996**, *14*, 33-38.

(30) Smith, A. M.; Williams, R. J.; Tang, C.; Coppo, P.; Collins, R. F.; Turner, M. L.; Saiani, A.; Ulijn, R. V. *Advanced Materials* **2008**, *20*, 37-41.

(31) Jones, R. G.; Ober, C. K.; Hodge, P.; Kratochvíl, P.; Moad, G.; Vert, M. *Pure and Applied Chemistry* **2013**, *85*, 463-492.

(32) Maier, J. A.; Martinez, C.; Kasavajhala, K.; Wickstrom, L.; Hauser, K. E.; Simmerling, C. *Journal of Chemical Theory and Computation* **2015**, *11*, 3696-3713.

(33) Lee, H.; Dehez, F.; Chipot, C.; Lim, H. K.; Kim, H. *Journal of Chemical Theory and Computation* **2019**, *15*, 1538-1545.

(34) Sheu, S. Y.; Yang, D. Y.; Selzle, H. L.; Schlag, E. W. *Proceedings of the National Academy of Sciences of the United States of America* **2003**, *100*, 12683-12687.

(35) Vigier-Carrière, C.; Garnier, T.; Wagner, D.; Lavalle, P.; Rabineau, M.; Hemmerlé, J.; Senger, B.; Schaaf, P.; Boulmedais, F.; Jierry, L. *Angewandte Chemie - International Edition* **2015**, *54*, 10198-10201.

(36) Chen, S.; Li, Z.; Zhang, C.; Wu, X.; Wang, W.; Huang, Q.; Chen, W.; Shi, J.; Yuan, D. *Small* **2023**, *19*, 1-7.

(37) Roy, S.; Javid, N.; Frederix, P. W.; Lamprou, D. A.; Urquhart, A. J.; Hunt, N. T.; Halling, P. J.; Ulijn, R. V. *Chemistry - A European Journal* **2012**, *18*, 11723-11731.

(38) Hong, Y.; Lau, L. S.; Legge, R. L.; Chen, P. *Journal of Adhesion* **2004**, *80*, 913-931.

(39) Nymeyer, H.; Gnanakaran, S.; García, A. E. *Methods in Enzymology* **2004**, *383*, 119-149.

(40) Periole, X.; Mark, A. E. *Journal of Chemical Physics* **2007**, *126*, DOI : 10.1063/1.2404954.

(41) Buchete, N. V.; Hummer, G. *Physical Review E - Statistical, Nonlinear, and Soft Matter Physics* **2008**, *77*, DOI : 10.1103/PhysRevE.77.030902.

(42) Cheng, X.; Cui, G.; Hornak, V.; Simmerling, C. *Journal of Physical Chemistry B* **2005**, *109*, 8220-8230.

(43) Gee, J.; Shell, M. S. *Journal of Chemical Physics* **2011**, *134*, DOI : 10.1063/1.3551576.

(44) Sugita, Y.; Okamoto, Y. *Chemical Physics Letters* **1999**, *314*, 141-151.

(45) Marrink, S. J.; Risselada, H. J.; Yefimov, S.; Tieleman, D. P.; De Vries, A. H. *Journal of Physical Chemistry B* **2007**, *111*, 7812-7824.

(46) Thota, N.; Ma, Y.; Jiang, J. *RSC Advances* **2014**, *4*, 60741-60748.

(47) Szała, B.; Molski, A. *Biophysical Chemistry* **2019**, *253*, 106219.

(48) Jain, A.; Globisch, C.; Verma, S.; Peter, C. *Journal of Chemical Theory and Computation* **2019**, *15*, 1453-1462.

8 Supporting information

Table S1 – Average number of hydrogen bonds during the full trajectory

System	Average number of hydrogen bond
2P	0.19
2P-SPCE	0.29
2P-TIP4P-E	0.19
2P-NaCl	0.24
5P-TIP3P	0.53
5P-SPCE	0.27
5P-TIP4P-E	0.33
5P-NaI	0.51
5P-CsI	0.47
5P-CsCl	0.24
5P-1000NaCl	1.01

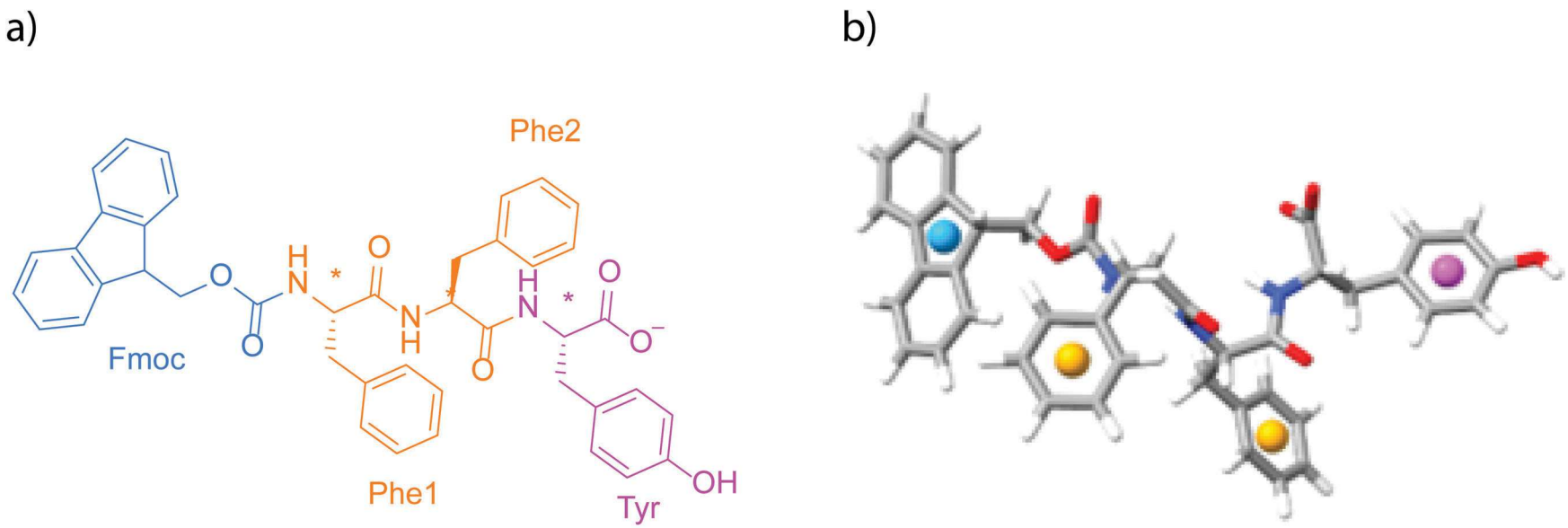

Scheme S1 – (a) Residue description of Fmoc-FFY used in MD simulations and (b) definition of the centroids used for analysis

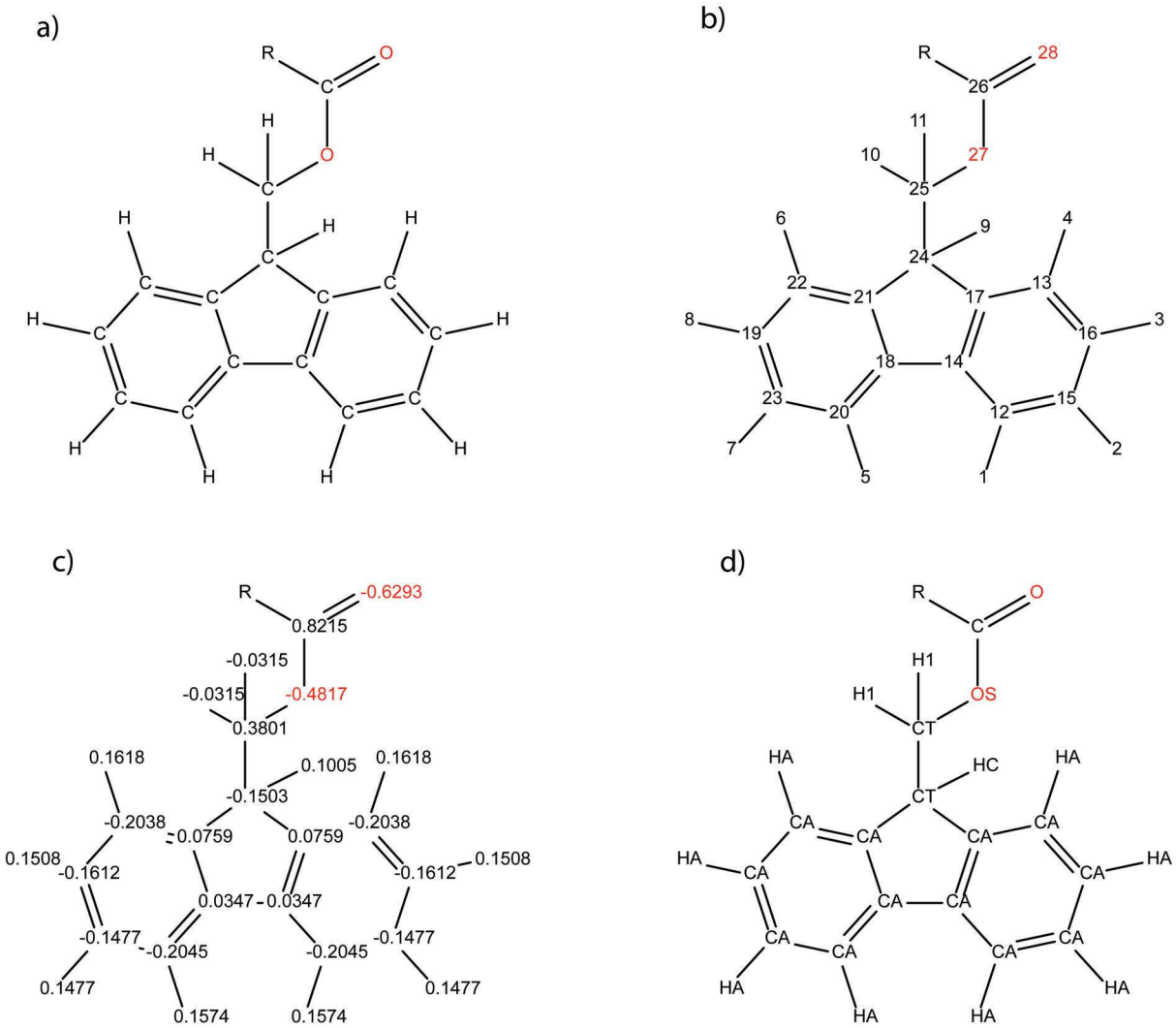

FIGURE S1 – (a) Developped structure of the Fmoc residue, (b) numbering of the atoms used in the residue, (c) atomic charges fitted with the RESP procedure, (d) ff14SB numbering for the Fmoc.

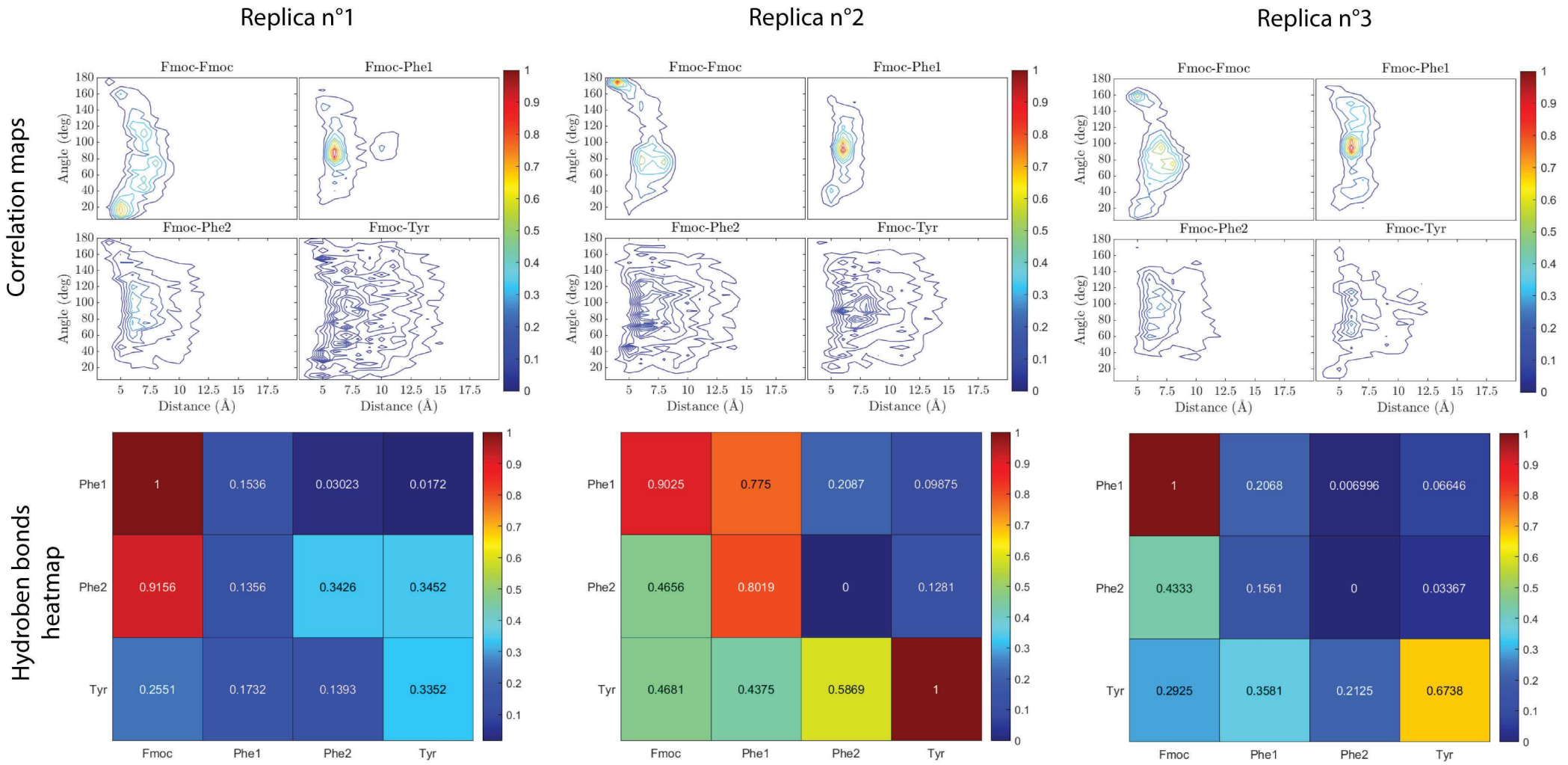

FIGURE S2 – Correlation maps and hydrogen bonds heatmaps for each replica of the 2P system

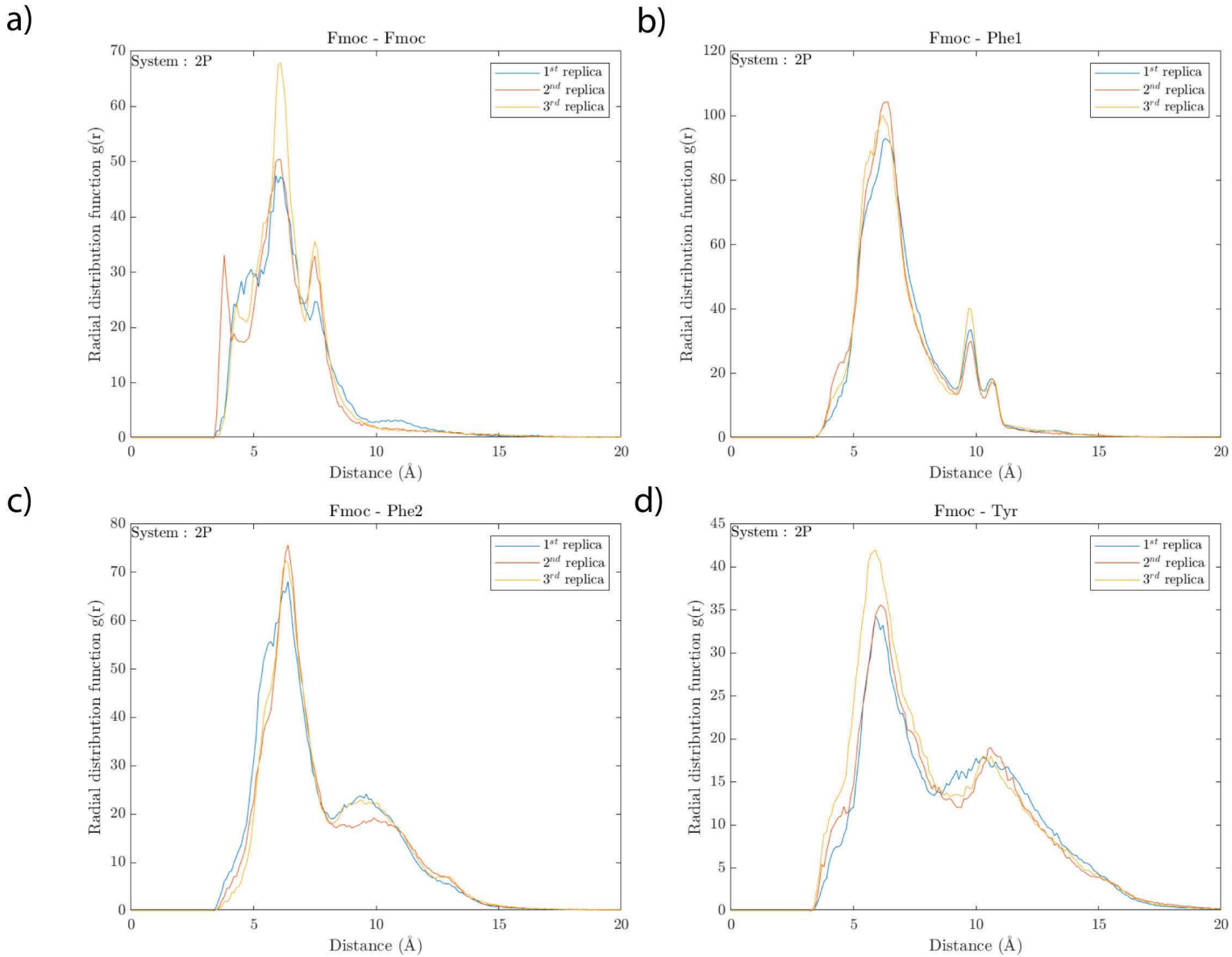

FIGURE S3 – Radial Distribution Function of Fmoc with all residues for the three replicas of the 2P system. RDF have been calculated for the overall trajectory.

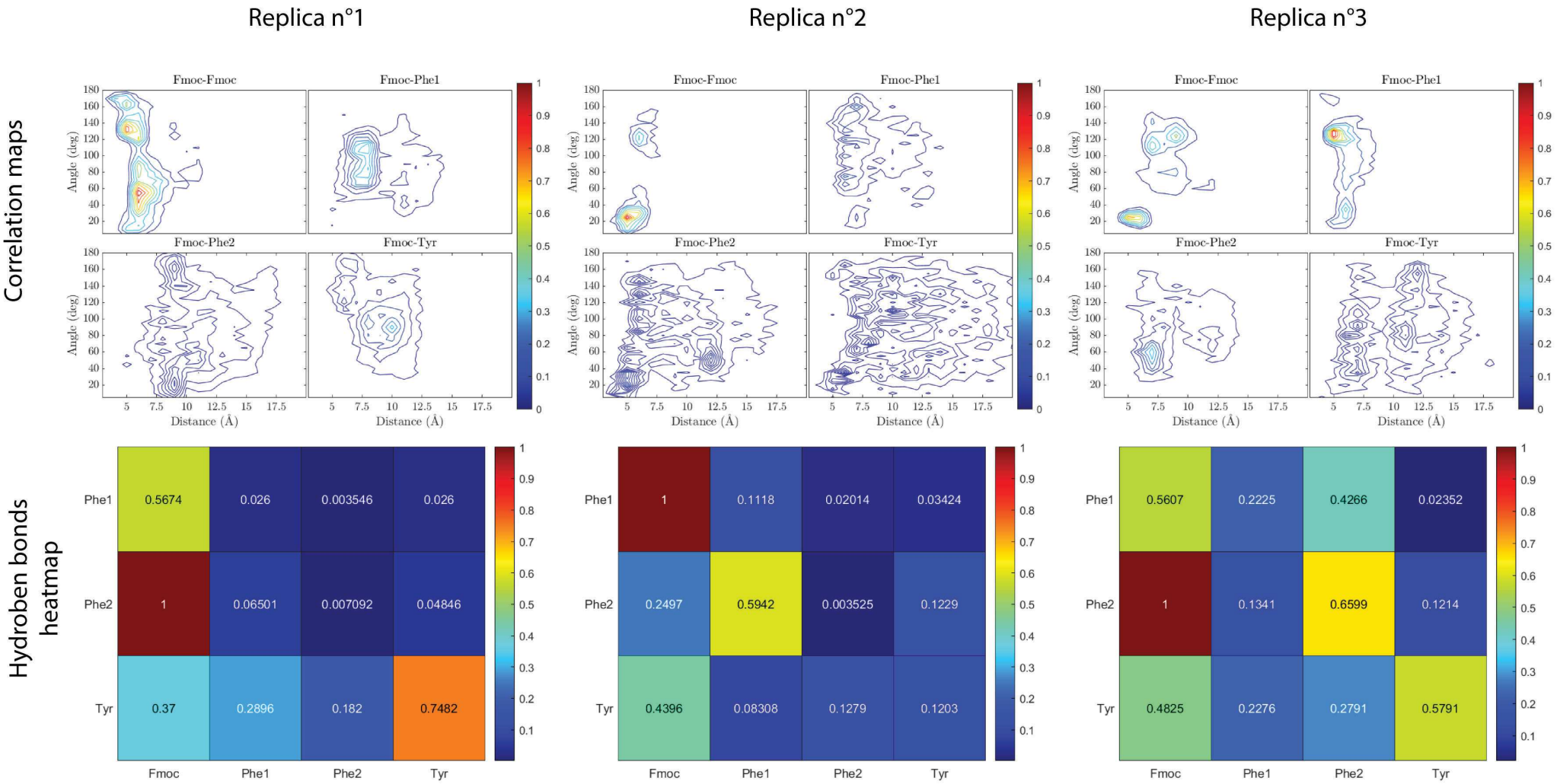

FIGURE S4 – Correlation maps and hydrogen bonds heatmaps for each replica of the 5P-TIP3P system

Chapitre 4 : Near-atomic resolution of tripeptide self-assembled nanofibers from cryo-electronic microscopy images.

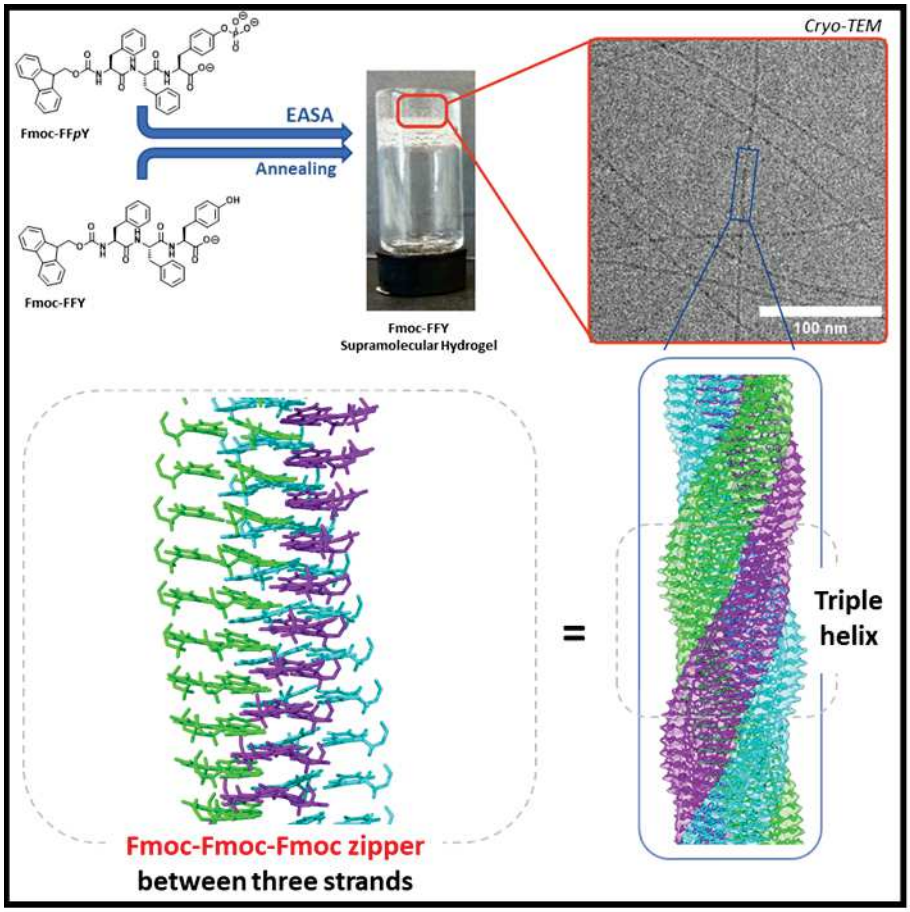

1 Contexte

Le chapitre précédent évoquait les interactions et structures entre peptides lors des premiers instants de l'auto-assemblage et nous avons conclu que les paramètres de dynamique moléculaire comme le modèle d'eau pouvait fortement influencer la structuration. Dans ce chapitre 4 nous proposons de nous focaliser principalement sur l'ordre à l'échelle moléculaire des peptides lorsqu'ils sont dans la nanofibre. Il y a deux questions auxquelles nous souhaitons répondre : (i) comment les peptides vont-ils s'agencer à l'échelle moléculaire et (ii) existe-t-il une différence d'assemblage entre l'initiation par voie enzymatique et par voie thermique ?

Pour répondre à ces questions nous nous appuyons ici sur une méthode déjà bien connue dans la biologie structurale : la reconstruction d'objets observés en cryo-MET. Cette technique récomposée par un prix Nobel en 2017 partagé entre Dubochet, Frank et Henderson apparait maintenant dans le domaine de la chimie et principalement dans les matériaux mous. Ce chapitre vise donc entièrement à décrire la fibre à l'échelle moléculaire et l'arrangement afférent. Les résultats trouvés en reconstruction sont soutenus par des mesures de diffusion de rayons X des gels supramoléculaires et de la dynamique moléculaire de la fibre reconstruite.

Ce chapitre fait parti d'une collaboration avec l'Institut de Biologie Structurale (IBS) de Grenoble avec les chercheurs Leandro FARIAS ESTROZI et Guy SCHOEHN. Ce chapitre a également pour vocation à être publié dans un journal et il est intégralement rédigé en anglais.

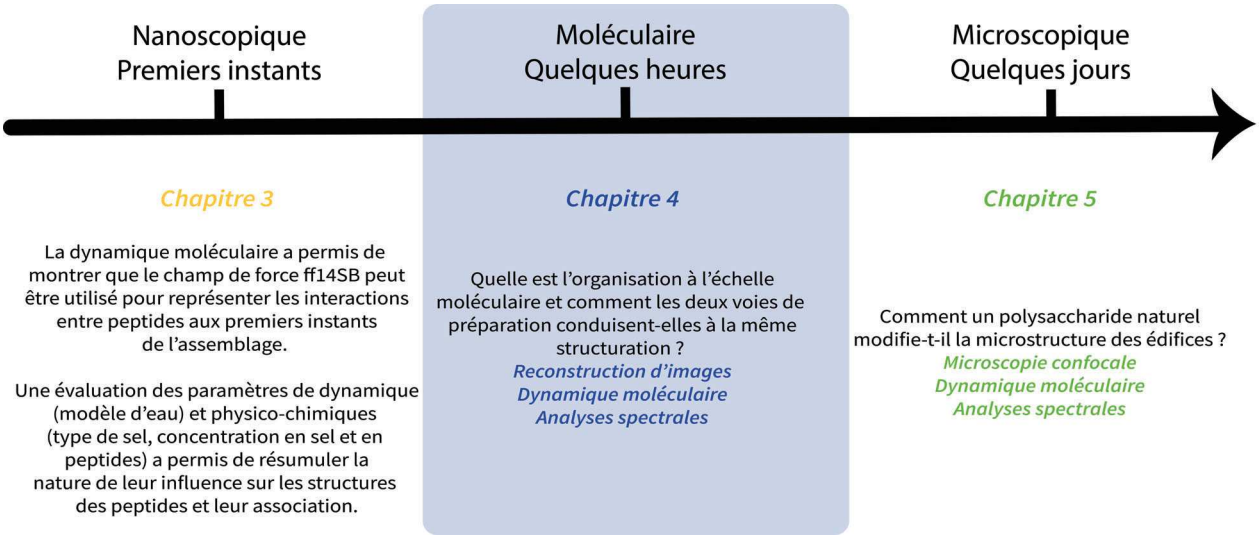

2 Highlights

- Near-atomic resolution (3.8 Å) of a tripeptide nanofiber (41 Å diameter) is established.
- Amphiphilic N-Fmoc tripeptide nanofiber is organized in a triple helix composed of three identical strands as revealed by high resolution cryo-EM reconstruction.
- The structural cohesion is mainly ensured by helix-helix lateral interaction between the amphiphilic strands.
- An original Fmoc-Fmoc-Fmoc zipper motif within the nanofiber is highlighted.
- Enzyme-assisted self-assembly leads to a different peptide organization than through annealing.

Peptide-based supramolecular hydrogel results from the spontaneous generation of a nanofibrous self-assembled network within water. Using high resolution cryo-EM image reconstruction, we succeeded to get a 3D electronic map density from a nanofibre having 41 Å diameter with a 3.8 Å near-atomic resolution. Fitting this map with the tripeptide structure and using dynamic simulation revealed a triple helix organization based on a Fmoc-Fmoc-Fmoc zipper motif between the three composing amphiphilic strands. Using the same hydrogelator peptide, enzyme-assisted self-assembly process lead to more order molecular organization than by thermal annealing.

3 Summary

In the last two decades, short peptide-based supramolecular hydrogels have been shown as highly interesting materials for applications in many fields such as medical, biomaterial, regenerative medicine, catalysis or bioengineering. The optimization of their properties relies mainly on the design of a suitable hydrogelator through an empirical trial-and-error strategy based on the synthesis of many various kind of peptides. This serendipity-based approach is due to the lack of precise insights and understanding about the molecular scale organization of the peptide self-assembled nanofibrous network. Because the 3D molecular architecture of peptides within nanofibers is directly involved in their ability to interact with entities present in their surrounding environment such as catalytic substrates, proteins, cells, inorganic nanoparticles or polymers, and thus guiding the features of the hydrogel, the lack of knowledge about it considerably limits further development. Herein, using Fmoc-FFY peptide as a model amphiphilic hydrogelator and cryo-EM reconstruction approach, we succeeded to establish a 3.8 Å near-atomic resolution of self-assembled nanofibers having a diameter of 4.1 nm. The elucidation of the spatial organization of so small nanoobjects addresses fundamental

questions about the way that amphiphilic N-Fmoc peptides, lacking secondary structure because of their low number of amino acid residues, i.e. three in case of Fmoc-FFY, can self-assemble and ensure the cohesion of the resulting nanostructure. We thus revealed a triple helix organization leading to a core-shell structure with an asymmetric unit composed from two Fmoc-FFY peptides. Three identical and amphiphilic strands are maintained together through lateral interaction coming from an original "Fmoc-Fmoc-Fmoc zipper" motif. This structural organization allows to suggest a mechanism of Fmoc-FFY nanostructure formation. The hydrophobic core is constituted by six Fmoc groups per propeller turn, surrounded by twelve phenyl groups from phenylalanine residues, non-planar with the Fmoc groups. Polar and charged tyrosine residues at C-term position constitute the shell part and are thus exposed all around the nanofiber in a continuous helical pattern. This fibre appears hollow with a very tiny internal diameter of 2.4 Å that must be a water-inaccessible environment. Dynamic molecular simulations highlight van der Waals and hydrogen bonds between peptides placed one above the other. We show that the way the self-assembly of Fmoc-FFY is led, by thermal annealing or induced through the action of a phosphatase on the phosphorylated precursor Fmoc-FFpY, results in roughly 70% similarities between the respective resolved structures. However, the molecular order is higher in the case of enzyme-assisted self-assembly process compared to the annealing way.

4 The bigger picture

The architecture of supramolecular material is ensured by a nanofibrous network which entrap water leading thus to a hydrogel. Due to their short peptide sequence, amphiphilic N-Fmoc tripeptides, such as Fmoc-FFY, do not self-assemble through secondary structures but still results in 41 Å self-assembled nanofibers underpinning hydrogels. Morphological features of a peptide nanofiber can be determined from cryo-electronic microscopy (cryo-EM) image analysis, but its internal molecular organisation remains hidden. Using high resolution cryo-EM reconstruction tools, our work highlights the strength of such an approach leading to a near-atomic 3.8 Å resolution of the tripeptide Fmoc-FFY self-assembly revealing thus a triple helical structure with a core-shell organization and a tiny central hollow of roughly 2.4 Å. The internal strong hydrophobic core is based on six Fmoc moieties and twelve phenyl groups per propeller turn, maintained through van der Waals, hydrogen bonds and an original Fmoc-Fmoc-Fmoc zipper motif. The understanding of the relationship between the nanostructure cohesion and the molecular peptide sequence is crucial for designing adequate peptides for a targeted application. Strikingly, the way to prepare the Fmoc-FFY self-assembled nanostructure impacts the

near-atomic organisation since the peptide assembly obtained from enzyme-assisted self-assembly approach seems different than the one prepared by thermal annealing.

5 Introduction

Enzyme-Assisted Self-Assembly (EASA) is a versatile strategy to spatially control the resulting self-assembly through the localization of the enzymatic trigger.[1] Temporal control can also easily be done by tuning the enzymatic activity and/or the self-assembling building blocks concentration[2] or by using out-of-equilibrium systems.[3] Based on these specific features, EASA has appeared as a powerful tool for bottom up strategies and thus was applied to many investigations in the last two decades.[4] Among the various self-assembling building blocks reported, peptide derivatives are of prime importance because of their ability to assemble in well-ordered secondary structures.[5] Thus, EASA of peptides relies on the enzymatic transformation of precursor resulting in the *in situ* production of a low molecular weight hydrogelators (LMWH) which self-assemble in a nanofibrous network underpinning what is commonly called a supramolecular hydrogel.[6] Despite remaining issues still not yet addressed about their mechanism formation,[7] peptide-based hydrogels triggered by enzymes have found great developments in the biomedical field since self-assembled peptide nanostructures used to interact with proteins or biopolymers leading to biomaterials showing biological features of interest.[8] Second, since enzymes are naturally present in living systems, they were used as endogenous trigger to induce the peptide self-assembly on cells, tissues or microorganisms. In this field, phosphatases were enzymes particularly targeted resulting in spectacular achievements for pericellular, intracellular and subcellular imaging, minimizing drug resistance, immunological applications and selective cancer cell lines downregulation and inhibition.[9] On the other hand, while isolated peptides have no catalytic activity, this feature can rise from the peptide assembly.[10] Confinement effects emerge from the resulting self-assembled nanostructure such as the shift of pKa values or specific spatial pockets formation for substrate selectivity or metal ions coordination. Thus, catalytic Diels-Alder[11] or azide-alkyne click reactions,[12] enantioselective aldolization[13] or kinetic resolution of non-activated esters using peptide-based nanostructures or catalytically-active supramolecular hydrogels were recently reported.[14] These investigations appear also highly valuable for the design of out-of-equilibrium chemical systems showing catalytic and autocatalytic features[15] or for investigations about mechanisms at the origin of life.[16]

All these successful achievements might suggest that the supramolecular hydrogel field based on

peptides is now sufficiently mature to allow a rapid transfer to industrial research and development departments. But, this assessment is misleading because it deliberately omits an important aspect, perhaps crucial in the study and development of self-assembled peptides : the molecular-scale organisation of peptides assembly within the nanostructure remains quite unknown. Of course, a combination of various characterisations can highlight the presence of many structural elements but do not allow to fully resolve the structure. Because of this kind of "black box", first, the design of suitable peptide derivatives having an optimal molecular structure for a given application is unfeasible, condemning the community to a time-consuming empirical structure-property approach as akin to serendipity. In addition, the self-assembled peptide organization is not always the same : slight variation occurs leading to a mixture of various nanostructures called polymorphism. This is a common feature in the self-assembled peptides field, but still almost impossible to predict. Because small fluctuations (sometimes uncontrolled) in the hydrogelation conditions result in a variability in the polymorph composition despite using the same peptide hydrogelator, reproducibility problems are frequently encountered.[17] Therefore, without insights about the relationship between the hydrogelator molecular structure and the way they are organized within the resulting nanostructure at the near-atomic scale, the anticipation of properties and the optimization of the material features are impossible.

Near-atomic resolutions of peptide assembly have been reported using single crystal diffraction or solid state nuclear magnetic resonance.[18] However, these analytical tools provide information about the peptide structure at the solid state. In supramolecular hydrogels, peptide assembled nanofibers are in a solvated state and intrinsically flexible which can be differently organized than in the crystallized or dried state. Cryogenic electronic microscopy (cryo-EM) image reconstruction approach address this point because the peptide assembly is first froozen before the structural analysis is realized, keeping thus its native organization. This method has revolutionized the determination of near atomic biomacromolecular structure[19]. First applied to the elucidation of protein assemblies, spectacular structural determination of self-assembled peptides was achieved as well in the last five years.[20] Now, one next challenge to tackle concerns the very short peptide sequence assemblies, which are those mainly encountered in the EASA approach using amphiphilic peptide sequence and including less than five amino acid residues. Indeed, from so short peptide sequence raises two problems for the resolution of their resulting self-assembled nanostructure : (i) the diameter of such nanoobject used to be less than 5 nm which thus requires high level of resolution to establish the spatial molecular organization and (ii) a so few numbers of amino acids in the peptide sequence do not lead to any

persistent secondary structures. This absence complicates the fitting steps between the resolved electron map density and the most suitable peptide molecular conformation. This is also an exciting challenge since this last point highlights the lack of complete knowledge about how the cohesion of such amphiphilic short peptides assembly in complex nanostructures in ensured. Besides providing insights into these fundamental issues, short peptide sequences have the great advantage to be easily synthesized at a preparative-scale and with high purity, representing thus interesting building blocks for supramolecular hydrogel applications.

Very recently, Conticello and coworkers succeeded to resolve the nanotube assembly of a short peptide, i.e. an octapeptide having the sequence Ac-FKFEFKFE-NH_2 through cryo-EM analysis (Ac = acetyl group ; F = Phenylalanine ; K = lysine ; E = glutamic acid)[21]. Specifically, they observed that the conditions used, at room temperature or annealed at 90°C, lead to a bilayer nanotube constituted of four or five beta-sheets protofilaments, respectively. This work suggested that the self-assembly process is thus kinetically controlled. In 2020, Cui, Egelman and Xu resolved for the first time a self-assembled peptide nanostructure induced by an EASA process, using a cryo-EM approach.[22] This supramolecular hydrogel is based on tetrapeptide nanostructures having the following sequence : NBD-^{D}F^{D}FpYK_{me3} (NBD = nitrobenzoxadiazole ; pY = D-phosphotyrosine ; ^{D}F = D-phenylalanine ; K_{me3} = trimethyl-lysine). Despite a low resolution (5-6 Å) in the case of some polymorph nanotubes, cryo-EM investigations result also in a 4.3 Å resolution of one self-assembled nanotube. This later shows a helical organization of seven peptide per propeller turn, with peptide backbone extended radially outward with the respect of the helical axis of the nanotube. This conformation was unexpected since it was previously shown from crystal structure analyses that the diphenylalanine motif adopts preferentially a helical conformation in dried nanostructures[23]. This investigation confirms that the structural information coming from dry or crystal state cannot directly be translated to the self-assembled state in solvated conditions.

Based on the cryo-EM resolution structure approach, we succeeded to resolve 4.1 nm diameter nanofibers constituted by the assembly of tripeptides Fmoc-FFY. A 3.8 Å density map resolution is obtained and then combined to dynamic molecular simulations of Fmoc-FFY resulting in a near-atomic scale determination of the peptide assembly. These investigations showed a nanostructuration based on a triple helix organization ensured by an original Fmoc-Fmoc-Fmoc zipper motif. A mechanism pathway of the Fmoc-FFY nanofiber formation from the EASA way is herein proposed. A comparison between the molecular assembly of Fmoc-FFY nanofibers get by annealing and the one from an EASA process shows a non-similar organization at the molecular scale which is discussed.

6 Results and discussion

6.1 Context and challenges

Different set protocols allow to get supramolecular hydrogels from LMWH, mainly by annealing, dissolution of the hydrogelator into an organic solvent and then addition of water, pH switch, addition of metallic ions or combination of them.[4] The use of an enzyme to initiate the hydrogelation differs from the other ways listed above by the requirement of a precursor compounds sensitive to the enzymatic action (which is thus not yet the hydrogelator) transformed by the enzyme to provide *in situ* the hydrogelator self-assembling in a nanofibrous network.[6] No heating, addition of other components or any physical treatments are needed. The choice of the preparation way and the respect of the different steps are not trivial since the physical properties of the resulting hydrogel vary accordingly.[24] This can be explained by the morphological variability of the resulting nanostructure network according to the preparation protocol used. Indeed, polymorphism is often observed in the field of peptide self-assembly but very difficult to anticipate. In the case of the hydrogelator Fmoc-FFY (0.16 mmol/L, pH 9.3, buffered with Borax 25 mM), high resolution cryo-TEM images of the Fmoc-FFY self-assembled nanofiber obtained from an annealing process are fully identical to those obtained when the phosphorylated precursor Fmoc-FFpY (0.16 mmol/L) is brought in contact with alkaline phosphatase (AP, 31 nmol/L, pH 9.3, buffered with Borax 25 mM) leading to Fmoc-FFY generated *in situ* at 20°C. In both cases, several hundred micrometre long nanofibers having roughly 4.9 nm diameter are observed (Figure 1). It is interesting to note that the nanofibrous network is only based on an entanglement of these nanofibers because no branching or no crosslinking of the nanofibers have been observed with this Fmoc-FFY peptide, suggesting a self-assembly growth only in one dimension. Experimental details concerning the Fmoc-FFY hydrogel preparation ways are given in the Supporting Information (SI, Part 1). But what about the internal spatial organization, at the solvated state, within the nanofiber in these two cases ? Do they lead to two distinguish polymorphs or are the Fmoc-FFY tripeptides assembled exactly in the same way ? The impact of the enzymatic trigger on the peptides self-assembled structure, compared to annealing, has never been explored so far.

Impressive and substantial works about Fmoc-Y, FF and Fmoc-FF dipeptides self-assembly at the dry or the crystal state have been previously reported, showing the formation of nanotubes of roughly 100 nm diameter.[25, 26] Concerning the self-assembled Fmoc-Y, Fmoc-FF and more particularly

Fmoc-FFY peptide nanostructures underpinning supramolecular hydrogels, structural insights rising from infrared and fluorescence spectroscopies, circular dichroism or SAXS measurements were reported.[6, 23, 27-29] The parallel or the antiparallel orientation of Fmoc groups, their "superhelicity" organization, the parallel or antiparallel dipeptides orientation (from N_t to C_t), the involvement of the carbamate group in the hydrogen bonding network, the hollow (i.e. nanotube) or solid nanostructure (i.e. nanofiber), the number of peptides involved in one propeller turn, a helical or non-helical organization and so on, are some questions still under debate. The ambiguities about an entire and clear near-atomic structure determination arising from all these previous works (including those from our own group) are not to blame because they only do demonstrate the limitations of exploiting data acquired by the current analytical tools available to address these questions. Based on the recent development in the cryo-EM resolution approaches to get near-atomic structure determination, first we have analysed the nanostructure of the Fmoc-FFY self-assembly before to compare it with the one obtained from the EASA process from Fmoc-FFpY and AP. Even if the cryo-EM resolution methods became more popular since the dedicated Nobel prize 2017 awarded the contribution of Dubochet, Frank and Henderson, a short description of the scientific and technical pathway is first briefly described below.

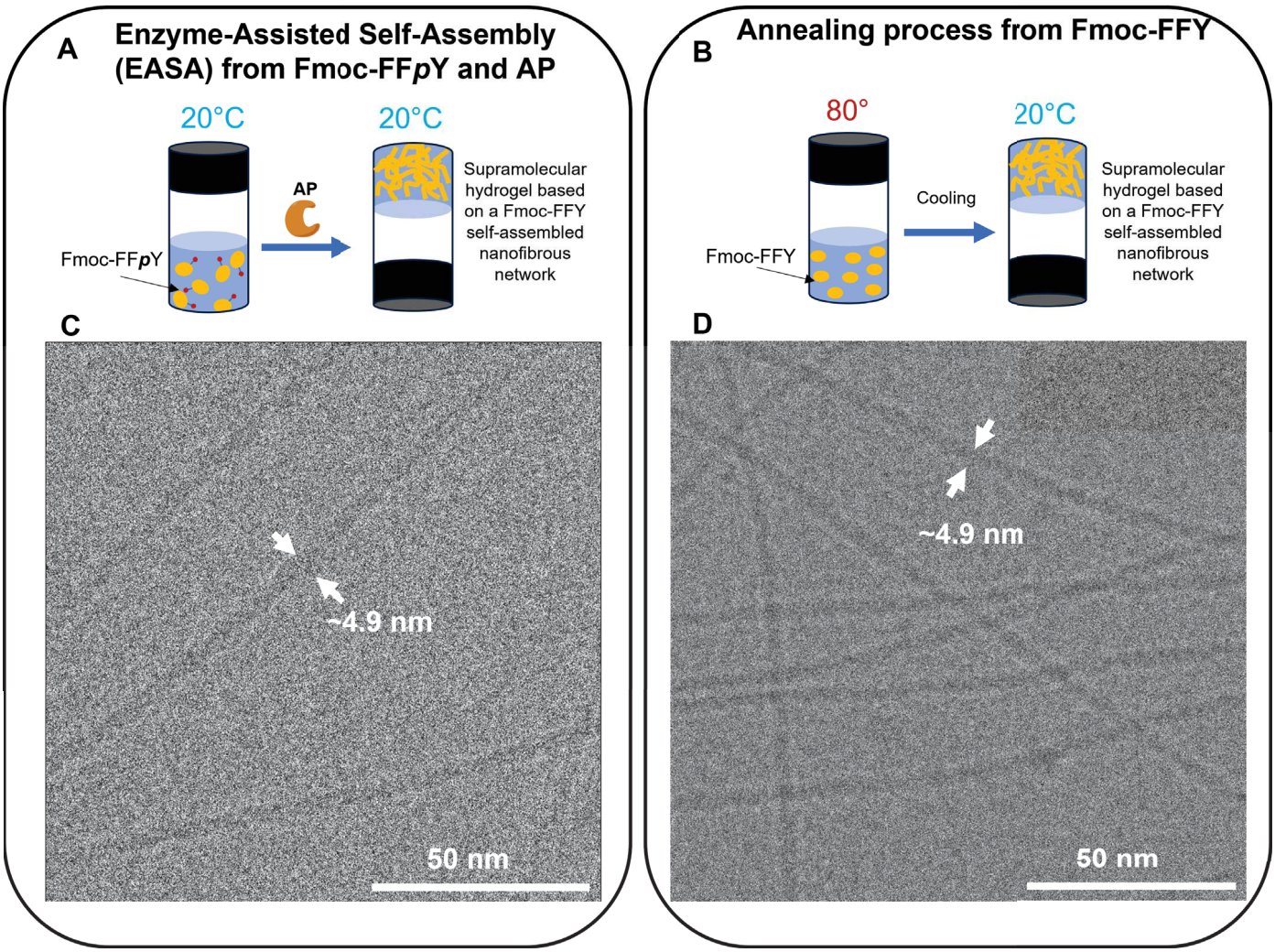

FIGURE 1 – **Schematics of the Fmoc-FFY self-assembled nanofibers preparation ways, EASA or by annealing, and their resulting typical cryo-TEM images.**
(A) The self-assembled nanofiber is obtained through the EASA way : Fmoc-FFpY is dissolved in water in presence of AP at 20°C, resulting in supramolecular hydrogel. (B) Fmoc-FFY is dispersed in water and then heated at 80°C during 10 min and then cooling to 20°C to get a supramolecular hydrogel. (C), (D) Typical cryo-TEM images of the resulting self-assembled Fmoc-FFY nanostructure formed from the EASA preparation way at 20°C and from Fmoc-FFY annealed at 90°C, respectively.

6.2 Brief description of the reconstruction process

The following 13-steps workflow used to resolve the Fmoc-FFY nanofiber structure was adapted from methods used for helical protein assembly's resolution[30] (Figure 2, from step 1 to 13). Here we describe briefly the approach and all experimental details are given in Supporting Information (SI Part 1 to 5). The dataset for the Fmoc-FFY prepared by annealing is composed of 2183 movies of 40 frames, recorded from a high resolution cryo-transmission electron microscope with a CMOS detector having 0.88 Å/pix resolution (step 1). All data have been processed with RELION 3.1.2 and 4.0.1[30, 31], a software developed by S. Scheres and colleagues (Medical Research Council, Cambridge) to reconstruct the electrostatic potential of the nanofiber (step 2). At this step, the microscope

specifications are taken into account such as the voltage, spherical aberrations and pixel size of the camera (0.88 Å/pix here). All the movies are then processed to correct the motion resulting to 2183 micrographs (step 3). This correction helps to correct the potential drift due to the electron beam interacting with our samples. The value of the contrast transfer function (CTF) is thus established to evaluate the defocus and astigmatism of each image (step 4)using CTTFIND4.1.[32] Then, a manual picking was done from an independent dataset in order to train an artificial intelligence (AI) model able to do this task quickly and efficiently over a huge number of micrographs (step 5) : the AI must be able to detect nanofibers on cryo-TEM images and to select start and end coordinates of non-crossing nanofibers. This work called autopicking was done by using the AI called crYOLO, which has been developed specifically for the treatments of high-quality cryo-TEM images (step 6)[33, 34]. The coordinates of the cylindrical nanofibers have been imported back to RELION and then extracted with an interbox distance of 14.63 Å. The segments are then called 'particles' including both the nanofiber and a part of the surrounding amorphous ice (step 7). Thus, 1.4 million particles were classified in 2D (step 8). This step involves a circular masking of 200 Å, a tube diameter of 60 Å and 50 initial classes. The first 25 iterations gave rise of populated classes that are then refined for another 25 iterations to optimize the in-plane and rotational sampling of each particle. 2D classes that does match the best our nanofibre are then selected, particles contained in these classes are saved for further processing. One of the classes has been randomly selected to serve for helical indexing in HELIXPLORER (step 9).[35] Thus, the helical feature of the nanofiber structure is determined from the diffraction pattern. This step aims to determine the rise and the twist of the helix. An initial 3D model is then generated with one 2D class as described in the literature[36] (step 10). This model acts as a first 3D reference that will be further refined. Then all the particles previously selected through 2D classification have been 3D refined (step 11). In this step, parameters of the helix found in step 9 are used in order to do helical reconstruction. Orientations of the particles are calculated through a Bayesian process. The refinement will provide a reconstructed 3D object. However, this density map has to be post-processed in order to be fitted manually with the Fmoc-FFY peptide (step 12). In addition, this post-process step will permit the evaluation of the map resolution (step 13). This will be done by applying a density mask through a threshold and calculation of the Fourier Shell Correlation (FSC). The determination of the resolution is done with the FSC criteria of 0.143 given by Rosenthal and Henderson in 2003[37]. In both dataset, from the annealing or the EASA way, resolution of the map is 3.8 Å. By the end of the reconstruction process, the density map can be analysed though observation and manual fitting of the tripeptide.

An identical approach has been used for the resolution of the Fmoc-FFY self-assembly prepared from EASA (details are given in SI Part 4). It must be noted that for both preparation way, an accurate class analysis reveals the presence of a single polymorph (steps 9 and 10), suggesting so no obvious differences between the two kind of peptide assemblies.

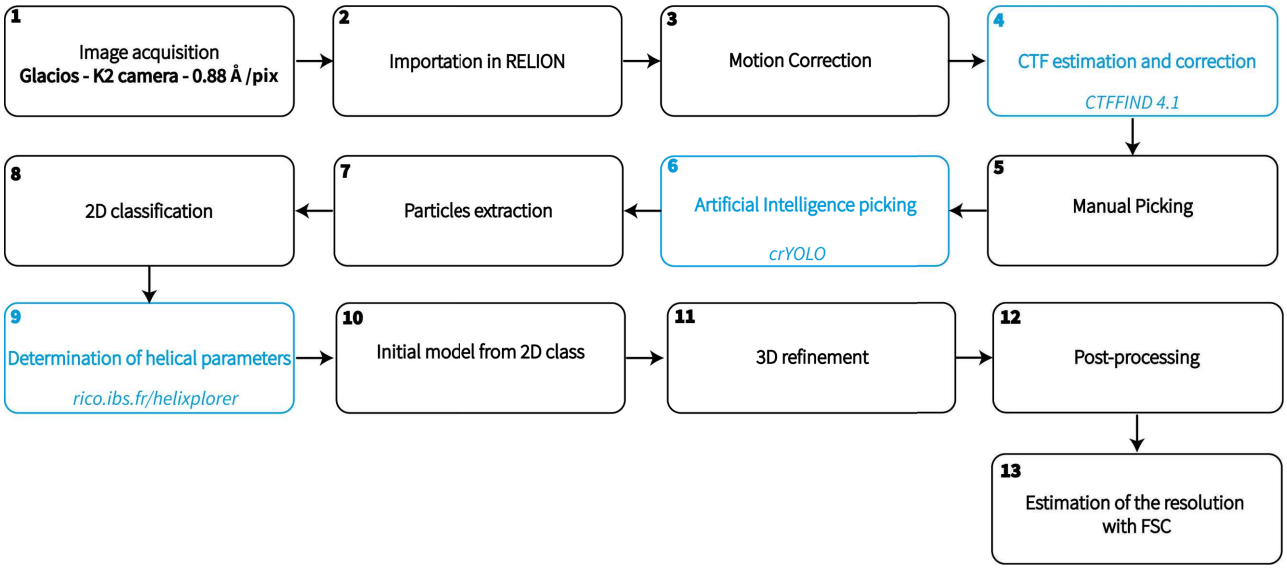

FIGURE 2 – **A 13 steps synthetic pathway of the image reconstruction task to resolve the structure of the Fmoc-FFY self-assembled nanofibers at the near-atomic scale from a dataset of cryo-TEM high quality images. This approach was applied to both Fmoc-FFY self-assembled nanofibers obtained by annealing and for those obtained the EASA strategy.**

6.3 Map density and 3D reconstructed Fmoc-FFY nanostructure prepared by annealing

First, the application of this workflow has resulted to the resolution map density of the Fmoc-FFY self-assembled nanofibers prepared by annealing at 80°C for 10 min resulting in a supramolecular self-assembly when the sample is cooled at 20°C (Figure 3A). This map reveals a helical nanostructure with a rise of 1.61 Å, a twist of 122.8° along the longitudinal z axis and 4.77 Å pitch (Figure 3B). It must be reminded that even if a right-handed supramolecular enantiomorph is shown in the whole Figure 3, the real chirality of the helix remains unknown because the 2D projection images obtained from cryo-EM analysis loses this information (Figure 2, step 8). The diameter of the 3D reconstructed nanostructure is 41 Å, shorter than the 49 Å nanofiber diameter measured directly from cryo-EM image (Figure 1). This difference is due to the high signal over noise ratio (S/N) in the images inducing biases in the direct measurement. But the most remarkable point rising from this 3D map density is the presence of grooves coming from the entanglement of several strands : in our case, we distinguish three strands, coloured differently in Figure 3C, constituting so a triple helix structure.

A cross-section view of the nanostructure shows the map density in a 2D plan organized in three moieties constituted of two asymmetric units (AU) being two distinct conformations of Fmoc-FFY peptide positioned differently in the helical structure (Figure 3D). Thanks to the 3.8 Å resolution of the map, it was possible to distinguish where the larger electron density is located, i.e. the Fmoc groups, and thus to fit the map with optimized molecular model conformations of Fmoc-FFY. Thus, the peptide backbone and the aromatic lateral groups have been assigned unambiguously, revealing so the molecular organization of the Fmoc-FFY peptides within the nanostructure. All tripeptides adopt an quasi-elongated conformation, from the N-term to the C-term direction when going from the centre outwards the nanostructure. In such spatial arrangement, all aromatic groups gathered at the centre forming a hydrophobic core. At the crystalline state, the FF dipeptide motif and PFF tripeptide (P = proline) have been reported to induce a local helical conformation rather than an extended one.[38] This is also the case for β^3-homotripeptide (β^3-homoLeu, β^3-homoIle and β^3-homoAla) analysed by X-ray diffraction.[39] The bulky aromatic Fmoc group located at the N-term position of the tripeptide Fmoc-FFY is probably at the origin of its quasi-elongated conformation in the nanostructure. This was also previously observed by Egelmann and Xu in the N-protected NBD tetrapeptide self-assembled structure resolved through a cryo-EM reconstruction approach.[22]

Because of the triple helix organisation and the presence of grooves, the resulting nanostructure is not perfectly cylindrical (Figures C and D). The 2D cross-section view shows that the mass centre of the Fmoc groups from each six Fmoc-FFY peptides are forming an equilateral triangle with three peptides positioned at each top and three others located at the middle of each triangle side. Those three last peptides forming a smaller equilateral triangle included in the first one (Figure E). Six Fmoc-FFY tripeptides are counted per propeller turn. Twelve phenyl groups from the phenylalanine residues are forming such kind of crown surrounding the six central Fmoc groups since they are tilted and thus not coplanar with the Fmoc groups (Figure S1). In this spatial structuration, the diphenyl motif of each peptide belongs to the hydrophobic core including the six central Fmoc groups. The C-terminal carboxylic acids and the six phenol groups from the tyrosine residues are constituting a hydrophilic shell. We noticed that the electron density of the phenol group appeared spatially quite expanded compared to Fmoc and phenyl groups, suggesting that these lateral groups are less sterically constrained and have more flexibility. Two different kinds of tyrosine residues are thus in interaction with the surrounding aqueous environment : those in the grooves and those outer (at the top of the triangle). A total of six Fmoc-FFY peptides are thus involved in a propeller revolution leading to an observable empty inner central cavity of roughly 2.4 Å diameter resulting in such a

very small channel that should lacking water molecules (Figure G). Because of this very small lumen diameter, the resulting structure will be not called nanotube but rather nanofiber. To understand of the cohesion interactions involved in this self-assembled Fmoc-FFY nanotube, molecular dynamic simulations have been carried out.

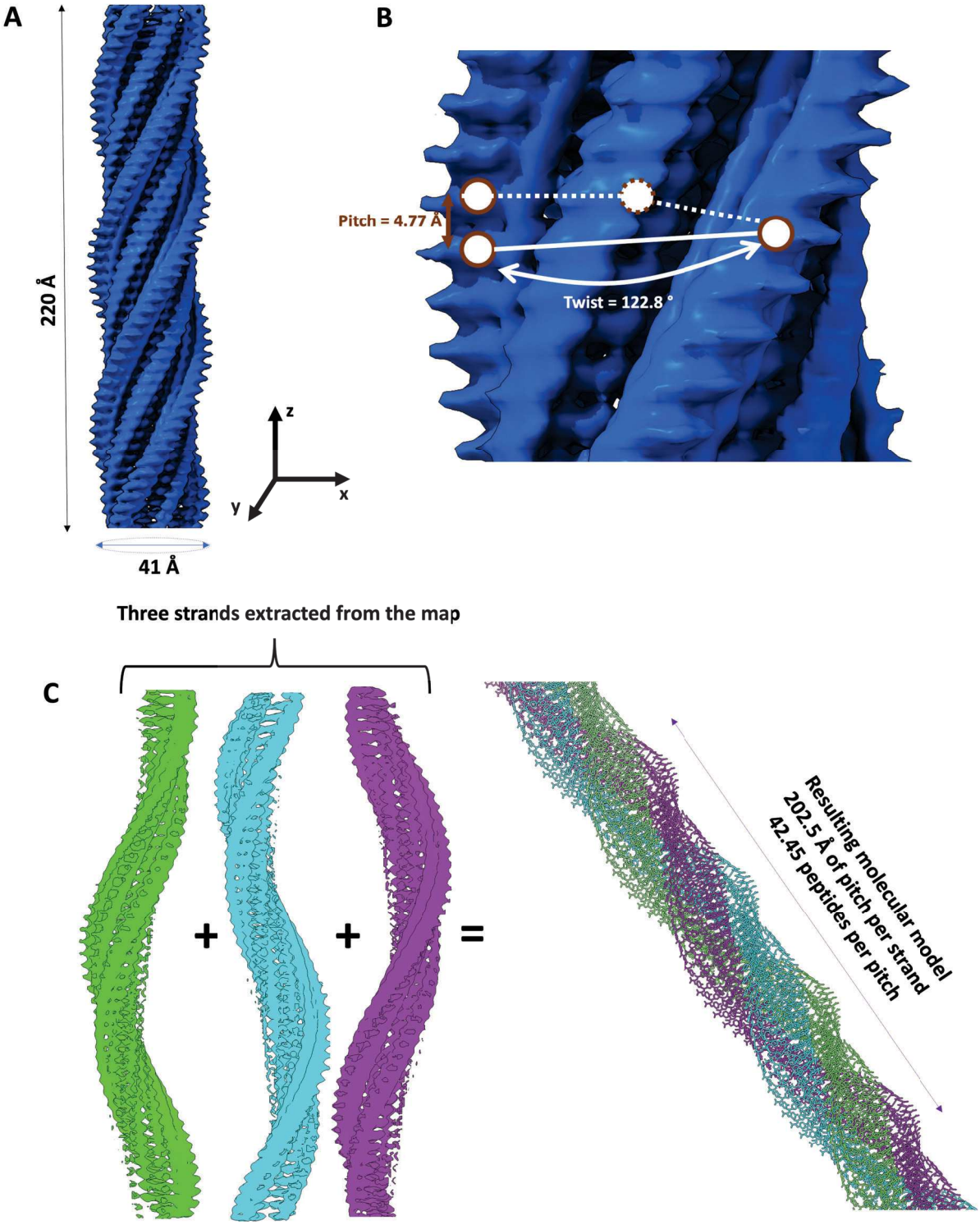

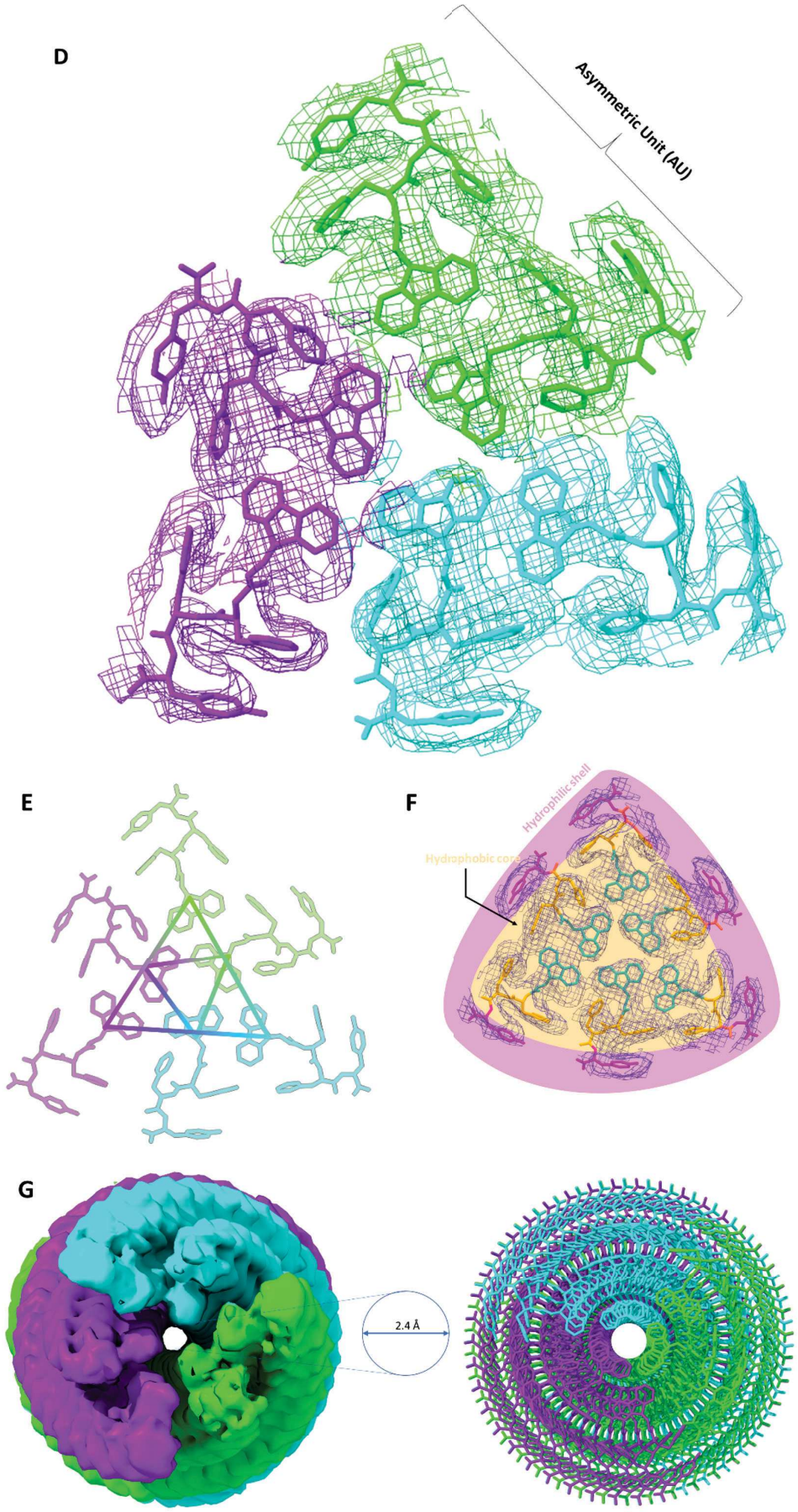
D
Asymmetric Unit (AU)
E
F
Hydrophilic shell
Hydrophobic core
G
2.4 Å

Figure 3 *(previous page)* – **Self-assembled Fmoc-FFY nanostructure prepared by annealing. Lateral and cross-sectional views from the 3D map resolution from cryo-EM image reconstruction and corresponding atomic model.**
(A) 3D map density resolution and (B) magnification showing the helical features of the self-assembled Fmoc-FFY nanostructure. The dotted line indicates a position in the background (C) Decomposition of the map in the three distinct and coloured strands (green, cyan and violet), and the resulting molecular model of the three strands entangled together. (D) Cross-section view showing the map density fitting with the most suitable Fmoc-FFY conformation. (E) Spatial arrangement in a triangular shape of one propeller turn containing six Fmoc-FFY peptides. (F) Core-shell organization of the internal nanostructure highlighting the hydrophobic (pink) and the hydrophilic (yellow) zones. (G) Map density (left) and corresponding atomic model (right) showing the presence of a tiny lumen in the self-assembled Fmoc-FFY nanostructure.

6.4 Molecular dynamic simulations of the Fmoc-FFY self-assembled nanofiber

Despite a 3.8 Å resolution, the explanation about how the cohesion between the three strands are associated together in the nanostructure is not obvious. More specifically, the six Fmoc groups seems slightly 'interwoven' according to the density map resolved (Figure 3). To address this point about the Fmoc groups organization, which is essential in the cohesion of the resulting Fmoc-FFY nanostructure, molecular dynamic simulations were investigated through the build-up of the assembly of 114 Fmoc-FFY in the optimized conformation fitting with the resolved map density (see Part 6 for computational details). This simulated supramolecular big structure is thus constituted by 19 propeller turns which represent almost a half pitch of roughly 100 Å height (Figure 4A). In addition, sodium cations are added to compensate the negative charge of the peptide coming from the C-terminal carboxylate, and TIP3P water model[40] is used as solvent, to be as close as possible to the real experimental conditions for hydrogelation. This chemical system has been run for 0.5 μs with 5 $kcal.mol^{-1}$Å^{-2}restraints over the cartesian position of the Fmoc groups. It is important to note that this restriction do not prevent conformational equilibration of the Fmoc groups over the fixed positions between the two consecutive steps of 5 ns each.

As mentioned above, the AU is composed of two amphiphilic Fmoc-FFY peptides perpendicular to the helical axis. Because of the quasi-elongated conformation of Fmoc-FFY peptides and their N-terminal to C-terminal orientation from the centre outwards of the nanostructure, it results in an amphiphilic strand due to the separation between the hydrophobic and the hydrophilic parts on opposite sides of the strand. As expected, the internal cohesion within the strand is mainly due to hydrogen bonds and $\pi - \pi$ stacking between the layers of AU. Indeed, phenylalanine residues adopt a quasi-single conformation because of their restricted spatial confinement by the upper and lower

layer within the strand. The phenyl groups are thus stacked on top of each other and form a narrow distribution of angles around 20° at a distance of roughly 5 Å between themselves (Figure 4C). The resulting $\pi - \pi$ interaction between these aromatic rings are not fully parallel because the twist of 8.5° between one layer and the following. The tyrosine residues in the hydrophilic shell has more conformational flexibility shown by the higher root-mean-square deviation (RMSD) values of the atomic position calculated for this amino acid. Tyrosines are also subject to $\pi - \pi$ stacking interaction with identical residues from above and below (Figure S2). During the trajectory of 500 ns, we observe that $\pi - \pi$ stacking interaction are present all along the helical z axis between the aromatic residues F and Y, and the Fmoc groups as well. This study also showed that intermolecular hydrogen bonds are formed during the trajectory between the amide groups but also between the carbamate and the surrounded amide groups, in agreement with reported experimental infrared measurements (Figures 4D and 4E) :[28, 29] roughly 70 ± 10 dynamic hydrogen bonds are co-existing between the simulated 114 self-assembled Fmoc-FFY nanostructures (Figure 4E). It must be said that the formation of this hydrogen bonding networks requires that the Fmoc-FFY peptides are conformationally flexible indicating that the whole peptide nanostructure is far away from a crystal structure displaying fixed position for each atom.

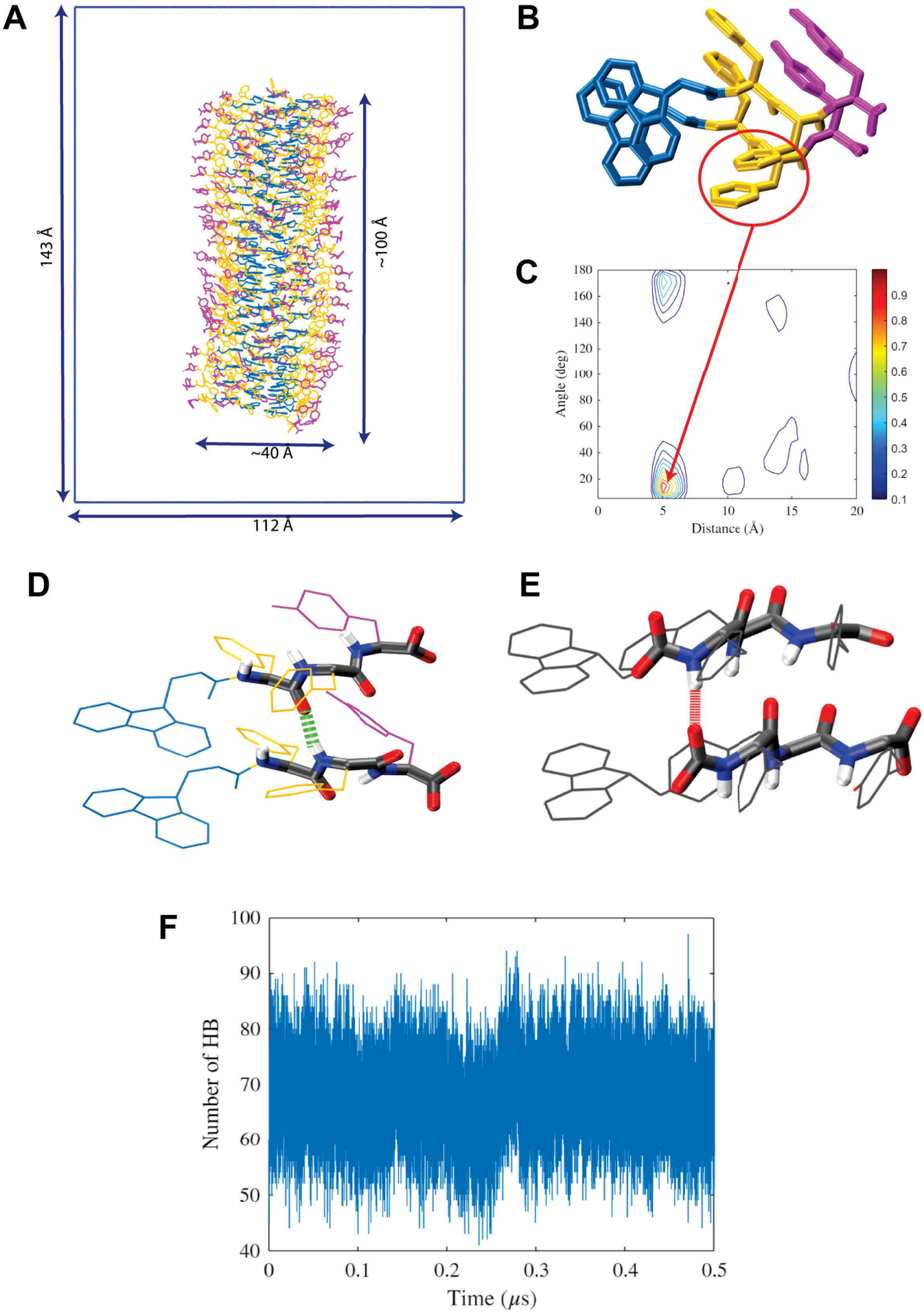
A
143 Å
~100 Å
~40 Å
112 Å
B
C
Angle (deg)
Distance (Å)
D
E
F
Number of HB
Time (μs)

Figure 4 *(previous page)* – **Molecular dynamics simulation of 114 Fmoc-FFY (19 propeller turns) assembled according to the resolved map density and equilibrated.**
(A) Equilibrated supramolecular assembly of 114 Fmoc-FFY tripeptides according to the resolved map density in its simulation box 112 x 143 Å (B) Spatial organization of two Fmoc-FFY tripeptide stacked on top of each other within the equilibrated nanostructure. (C) Variation of the distance between the centre of mass of two consecutive phenyl group along the helical z axis according to the angle between the aromatic ring. The probability of each conformation is normalized (colour gradient scale). (D), (E) Typical hydrogen bonds observed between Fmoc-FFY peptide neighbours along the helical z axis involving amide bonds or carbamate groups, respectively. (F) Number of hydrogen bonds (HB) detected between the simulated 114 Fmoc-FFY structure over the 500 ns of trajectory.

The hydrophobic part of each strand, due to the presence of both the FF dipeptide motif and the N-Fmoc group, represents a large water inaccessible area. We can thus expect that because of hydrophobic effects, the strands are thus kept together, leading to the triple helix formation. Such behaviour is close to the one explaining the formation of amyloid-like fibrils based on the spontaneous interaction between hydrophobic areas of proteins, and responsible of some neurodegenerative diseases.[41] Our molecular dynamics simulation study reveals also that the six Fmoc groups are not coplanar (actually, they cannot just be planar because of steric constraints coming from the limited space available) but rather slightly tilted (Figure 5A). More strikingly, from a lateral view showing only the six or the three central Fmoc groups, it appears that the three strands are interdigitated through the overlapping of the Fmoc groups in an organization mimicking the one observed for FF dipeptide zipper. Indeed, as shown in Figure 5B, the Fmoc groups in the core of the nanostructure seems organized in such an original zipper-like structural motif that we can called Fmoc-Fmoc-Fmoc zipper (or "Fmoc^3 zipper"). In Figure 5C emphasizes the Fmoc-Fmoc-Fmoc zipper motif at the electronic density interface between each strand on a cross-sectional view. A lateral view is given in Figure S3.

Since the structure of the Fmoc-FFY assembly is now established at the near-atomic resolution scale, let's suggest a mechanistic pathway leading to the whole self-assembled Fmoc-FFY nanostructure. Fmoc-FFY is an amphiphilic tripeptide due to its molecular peptide sequence. Because of that, and also its chiral nature, Fmoc-FFY can self-assemble into an amphiphilic helical strand. As shown before, this strand results from the stacking of asymmetric unit (AU) layers, on top of each other. Of course, it is difficult to imagine the formation of micrometre-long strand in water that would then entangle with two other strands and leading thus to the triple helix. This scenario is impossible because of the important hydrophobic area of the strand rendering it unstable. But we can expect that only few layers of AU can play the role of a building block, amphiphilic enough to interact with other building blocks through the Fmoc-Fmoc-Fmoc zipper association and leading thus to a slice of the nanofiber.

Then, the stacking of several slices drives to the resulting nanofiber. This hypothetical mechanism (Figure 6) is attractive since it could explained why the nanofibers of self-assembled Fmoc-FFY are never crosslinked together or split in two or more nanofibers, as branched nanostructures.

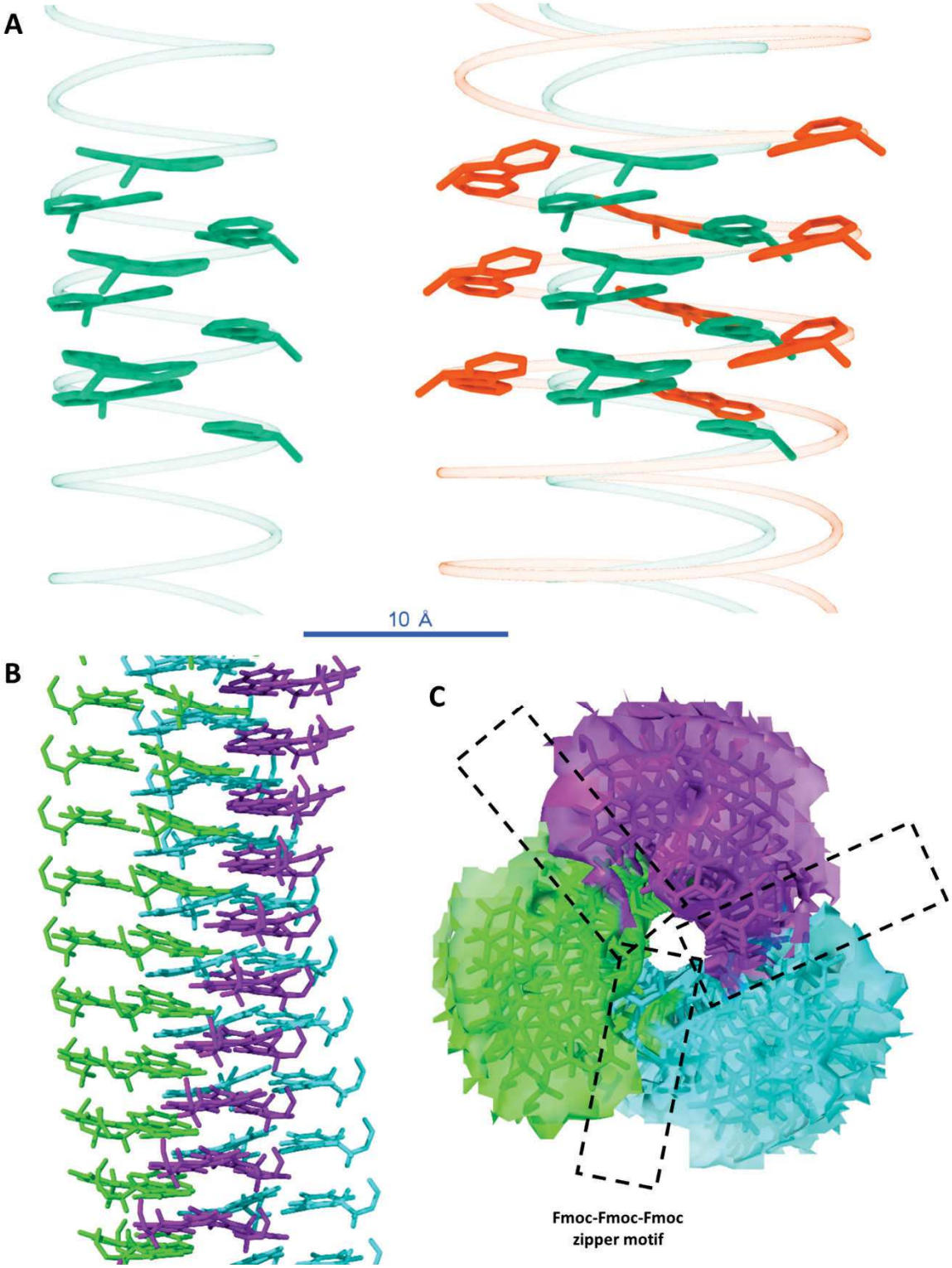

Figure 5 *(previous page)* – **Fmoc groups position in the hydrophobic core of the Fmoc-FFY nanostructure revealed by dynamic molecular simulation according to the resolved map density.**

(A) (left) Tilted conformation of the three Fmoc groups (green) around the lumen of the Fmoc-FFY self-assembled nanostructure and (right) with the three others Fmoc groups (red). (B) Entanglement of the Fmoc groups from the three strands coloured in green, violet and cyan, highlighting a Fmoc-Fmoc-Fmoc zipper motif. (C) Map density and corresponding molecular fit in a cross-sectional view showing the overlap region between the Fmoc groups of the three strands. Hydrogen atoms have been removed for sake of clarity except for Figure 5B

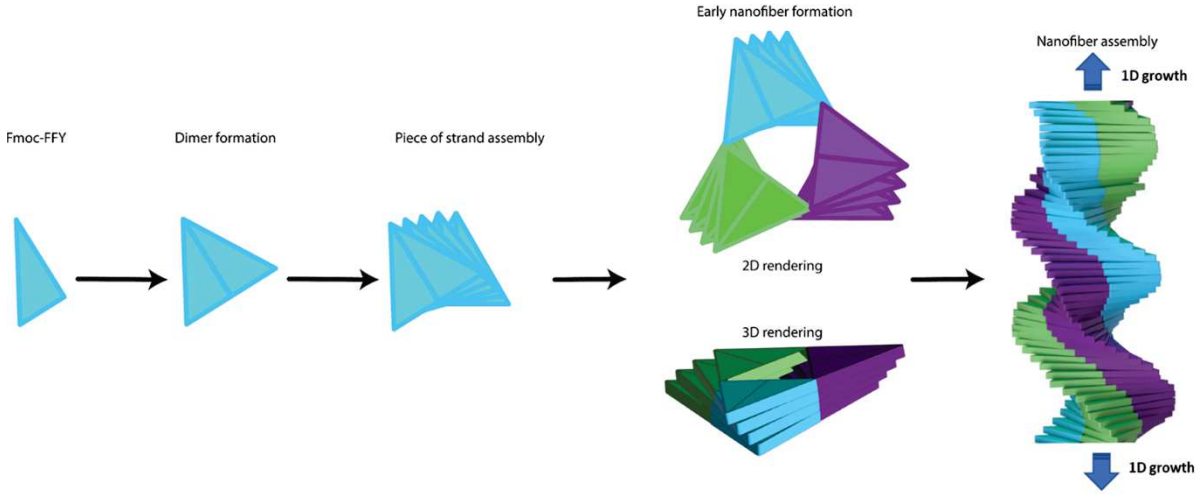

FIGURE 6 – **Hypothetical mechanism of the self-assembly of the Fmoc-FFY nanofiber prepared from the annealing way.**

6.5 Confirmation of the near-atomic resolution of self-assembled Fmoc-FFY nanostructure by SAXS and WAXS measurements.

The self-assembled Fmoc-FFY nanostructure was analysed by small-angle and wide-angle X-ray scattering (SAXS and WAXS, respectively, see Part 7 in SI for more details) in the gel state (Figure 6). SAXS measurements ($0.010 < q < 0.30$ Å^{-1}) allow the determination of the form factor of these self-assemblies. The intensity can be fitted with a model of infinite cylinder of radius R $\approx$ 24 Å that clearly reproduces the maximum at 0.2 Å^{-1} (first oscillation of the form factor). For q values in the wide-angle window ($0.30 < q < 1.00$ Å^{-1}), smaller distances are probed. A broad maximum is found around 0.43 Å^{-1}. It is related to the internal structure of the self-assembly and reveals a particular molecular packing of the peptides in the nanofibers (characteristic distance $\approx$ 14.6 Å). In addition, several Bragg peaks with low intensity are measurement at 4.6, 4.3, 4.1 and 3.8 Å . The first peak at 4.6 Å, as the molecular packing of the Fmoc scan be attributed to the distance between two consecutive layers (pitch in helical parameters). The others non-yet assigned peaks are still under investigations.

The simulated Fmoc-FFY self-assembly established from the resolved map density, described above, can be used to get theoretical SAXS-WAXS spectra with a high level of accuracy sing adequate software[42] (see SI Part 8 for fitting procedure). Comparison between the theoretical spectra with the experimental one constitutes an excellent test to evaluate the validity of our near-atomic resolution of the Fmoc-FFY nanostructure. Figure 6 shows the experimental and the theoretical spectra of the self-assembled Fmoc-FFY nanostructure. It clearly appears that both spectra are quasi-perfectly overlapped in the SAXS and WAXS region reinforcing our confidence in the resolved near-atomic resolution structure.

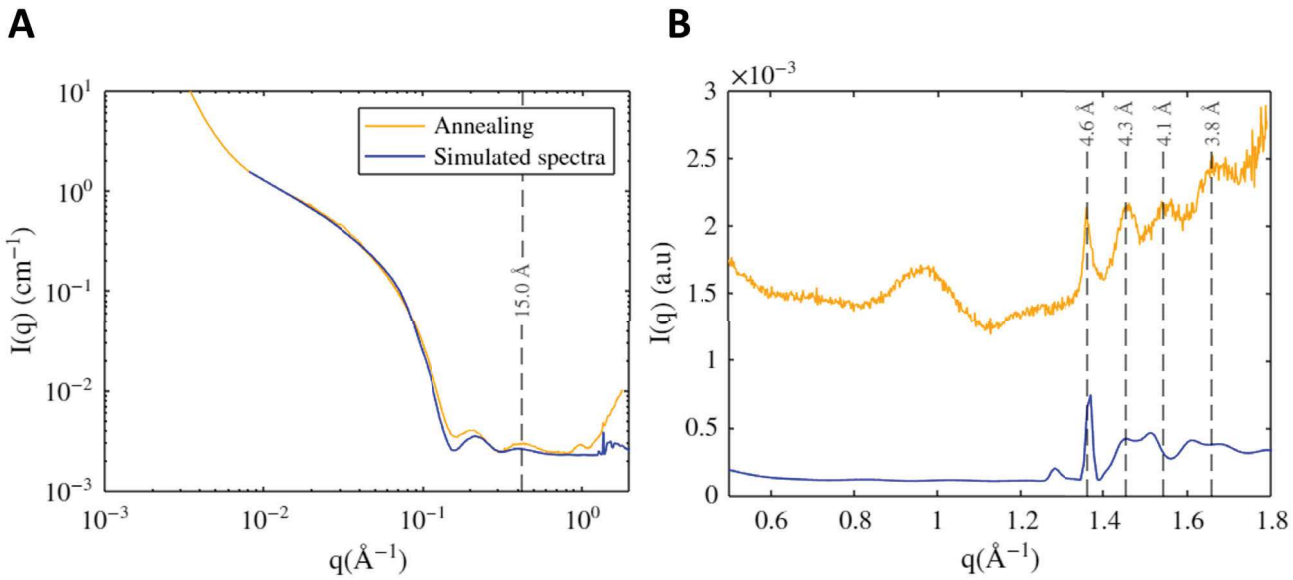

FIGURE 7 – **Experimental and theoretical SAXS-WAXS spectra of self-assembled Fmoc-FFY nanostructure measured from the gel state (orange) and calculated from the resolved near-atomic structure (blue).**
(A) Diffusion curve of simulated and experimental spectra of the annealed system at 18 mg/mL. The region displayed is between 0.01 to 0.5 Å^{-1}. The principal found peaks are represented by a dashed line and corresponding values in the real space are given. (B) Diffusion curve of simulated and experimental spectra of the annealed system at 18 mg/mL. The region displayed is between 1 and 2 Å^{-1}. The Braggs peaks are represented by a dashed line with the corresponding values in real space.

6.6 Near-atomic resolution of Fmoc-FFY nanostructure prepared through EASA way

The same cryo-EM approach based on the 13-steps workflow described above (Figure 2) was used to resolve the Fmoc-FFY nanostructure prepared by EASA. Through this preparation way, the peptide nanofibers are obtained from the dephosphorylation of the phosphorylated tyrosine residue of Fmoc-FFpY tripeptide precursor, generating *in situ* the corresponding hydrogelator Fmoc-FFY which then self-assembles. Does the enzymatic action, impact the peptide assembly within the nanostructure,

compared to a simple annealing way ? As shown in Figure 1, the morphology of the resulting nanofibers formed by annealing or through the EASA way are identical. But what about the Fmoc-FFY structure at the near-atomic resolution ? This question makes sense since Egelman, Conticello and coworkers have shown in a pioneer work in 2021, that small differences in the nucleation and the folding events of an octapeptide lead to equivalent nanofibers when observed by cryo-TEM but results in different secondary structure and organization at the near-atomic scale. [21]

The resulting map density of self-assembled Fmoc-FFY nanostructure is obtained with the same 3.8 Å resolution as shown in Figures 5A and 5B. Both the longitudinal view and its 2D cross-section of the resolved structure appear quite identical to those obtained previously from a self-assembly generated by annealing. The degree of similarity between the two maps can be estimated through the map densities correlation which lead to a value of 70% (see SI Part 5). The optimized fits of the Fmoc-FFY molecular structure with the map density obtained from EASA or annealing process are both overlapped in Figure 5C. Once again, a strong correlation between them appears and the 3.8 Å resolution do not allow to discuss the small differences observed. In addition, SAXS-WAXS measurements of Fmoc-FFY hydrogel prepared by EASA lead to the almost same spectra than the one obtained by annealing (Figure S4).

Thus, we might conclude that the self-assembled Fmoc-FFY nanostructure is equivalent whatever the way to get it, by annealing or through EASA. This would be true without taking into account the two following points : (i) first, the map density resolution obtained from the Fmoc-FFY nanostructure prepared through the EASA way results in the same 3.8 Å resolution than the one obtained by annealing but with roughly 30% less cryo-TEM images. This is not expected since less data should converge to a lower level of resolution. For instance, using 30% less data to resolve the Fmoc-FFY nanostructure prepared by annealing results to 4.1 Å resolution. This observation can be explained by a higher order in the molecular architecture of the self-assembled Fmoc-FFY nanostructure obtained from EASA than by annealing. (ii) Another argument in this direction is the evolution monitoring of the Fourier Shell Correlation (FSC) of both density map (Figure S5). It is observed that FSC drop is in higher frequencies for the EASA maps, a feature in agreement with a higher order in the molecular packing when the EASA way is involved. Finally, because the increase number of data is a crucial aspect to get a better resolution, the two sets of cryo-TEM images coming from the annealing and the EASA ways were merged together and used through the approach showed in Figure 2. Despite our best efforts, we never succeeded to get a better resolution than the 3.8 Å obtained with each dataset separately, but worse, we only get a poorer one value of 4.8 Å. Therefore, we can expect that

small differences should exist between the nanostructures prepared by these two different ways, but these differences seems not accessible from our current resolution.

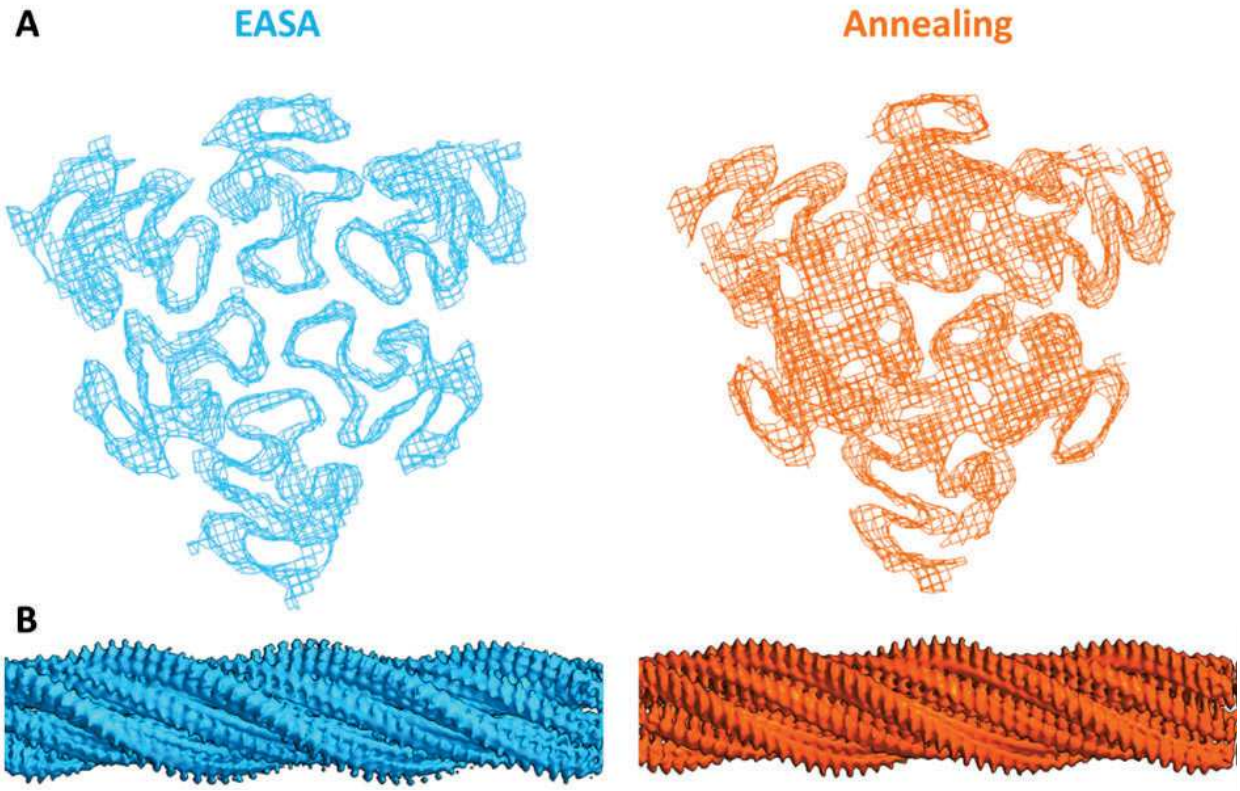

FIGURE 8 – **Longitudinal and cross-sectional views of the near-atomic resolution of the self-assembled Fmoc-FFY nanostructure when prepared by annealing or by EASA.**
(A) Cross-sectional and (B) longitudinal views of the map density of Fmoc-FFY nanostructure obtained through the EASA process (blue colour) or from an annealing way (orange colour).

7 Summary

Cryo-EM methods have revolutionized the structural analysis of peptide assemblies. When short peptide sequences are involved, the resolution is not obvious because of the absence of secondary structures. Through the structure determination of the tripeptide Fmoc-FFY assembly, we have illustrated the potential of this approach constituting the third article published in this field since the two first papers from Egelmann and Xu in 2020 and 2023. We have thus highlighted an original helical organization based on a Fmoc zipper motif participating to the cohesion of the nanostructure. Finally, despite a 3.8 Å resolution, we observed that the way to get the Fmoc-FFY assembled nanofibers impacts the molecular-scale organization of the peptides at the near-atomic scale. Indeed, when AP is used in presence of the phosphorylated precursors Fmoc-FFpY, the resolved structure is not fully identical to the one obtained by annealing. However, our current 3.8 Å resolution avoid to distinguish

the differences between the two kind of Fmoc-FFY structures.

8 Acknowledgements

The authors would like to acknowledge the Datacenter of the University of Strasbourg for the acceptation of a grant allowing GPU and CPU computation for the project. This work was also supported by the French Infrastructure for Integrated Structural Biology (FRISBI) ANR-10-INBS-0005.

References

(1) Williams, R. J.; Smith, A. M.; Collins, R.; Hodson, N.; Das, A. K.; Ulijn, R. V. *Nature Nanotechnology* **2009**, *4*, 19-24.

(2) Vigier-Carrière, C.; Wagner, D.; Chaumont, A.; Durr, B.; Lupattelli, P.; Lambour, C.; Schmutz, M.; Hemmerlé, J.; Senger, B.; Schaaf, P.; Boulmedais, F.; Jierry, L. *Langmuir* **2017**, *33*, 8267-8276.

(3) Debnath, S.; Roy, S.; Ulijn, R. V. *Journal of the American Chemical Society* **2013**, *135*, 16789-16792.

(4) Du, X.; Zhou, J.; Shi, J.; Xu, B. *Chemical Reviews* **2015**, *115*, 13165-13307.

(5) Conticello, V. P. *Current Opinion in Solid State and Materials Science* **2023**, *27*, 101066.

(6) Yang, Z.; Gu, H.; Fu, D.; Gao, P.; Lam, J. K.; Xu, B. *Advanced Materials* **2004**, *16*, 1440-1444.

(7) Muller, C.; Ontani, A.; Bigo-Simon, A.; Schaaf, P.; Jierry, L. *Advances in Colloid and Interface Science* **2022**, *304*, 102660.

(8) Zhou, J.; Du, X.; Wang, J.; Yamagata, N.; Xu, B. *Frontiers of Chemical Science and Engineering* **2017**, *11*, 509-515.

(9) Liu, S.; Zhang, Q.; Shy, A. N.; Yi, M.; He, H.; Lu, S.; Xu, B. *Journal of the American Chemical Society* **2021**, *143*, 15852-15862.

(10) Zozulia, O.; Dolan, M. A.; Korendovych, I. V. *Chemical Society Reviews* **2018**, *47*, 3621-3639.

(11) Bélières, M.; Chouini-Lalanne, N.; Déjugnat, C. *RSC Advances* **2015**, *5*, 35830-35842.

(12) Khalily, M. A.; Gulseren, G.; Tekinay, A. B.; Guler, M. O. *Bioconjugate Chemistry* **2015**, *26*, 2371-2375.

(13) Singh, N.; Zhang, K.; Angulo-Pachón, C. A.; Mendes, E.; Van Esch, J. H.; Escuder, B. *Chemical Science* **2016**, *7*, 5568-5572.

(14) Rodon Fores, J.; Criado-Gonzalez, M.; Chaumont, A.; Carvalho, A.; Blanck, C.; Schmutz, M.; Serra, C. A.; Boulmedais, F.; Schaaf, P.; Jierry, L. *Angewandte Chemie - International Edition* **2019**, *58*, 18817-18822.

(15) Rodon Fores, J.; Criado-Gonzalez, M.; Chaumont, A.; Carvalho, A.; Blanck, C.; Schmutz, M.; Boulmedais, F.; Schaaf, P.; Jierry, L. *Angewandte Chemie - International Edition* **2020**, *59*, 14558-14563.

(16) Beierle, J. M.; Ura, Y.; Ghadiri, M. R.; Leman, L. J. *Biochemistry* **2018**, *57*, 160-172.

(17) Draper, E. R.; Adams, D. J. *Langmuir* **2019**, DOI : 10.1021/acs.langmuir.9b00716.

(18) Miller, J. G.; Hughes, S. A.; Modlin, C.; Conticello, V. P. *Quarterly Reviews of Biophysics* **2022**, *55*, e2.

(19) Nakane, T. et al. *Nature* **2020**, *587*, 152-156.

(20) Xu, J.; Dayan, N.; Goldbourt, A.; Xiang, Y. *Proceedings of the National Academy of Sciences of the United States of America* **2019**, *116*, 5493-5498.

(21) Wang, F.; Gnewou, O.; Wang, S.; Osinski, T.; Zuo, X.; Egelman, E. H.; Conticello, V. P. *Matter* **2021**, *4*, 3217-3231.

(22) Feng, Z.; Wang, H.; Wang, F.; Oh, Y.; Berciu, C.; Cui, Q.; Egelman, E. H.; Xu, B. *Cell Reports Physical Science* **2020**, *1*, 100085.

(23) Görbitz, C. H. *Chemistry - A European Journal* **2001**, *7*, 5153-5159.

(24) Adams, D. J.; Morris, K.; Chen, L.; Serpell, L. C.; Bacsa, J.; Day, G. M. *Soft Matter* **2010**, *6*, 4144-4156.

(25) Reches, M.; Gazit, E. *Science* **2003**, *300*, 625-627.

(26) Reches, M.; Gazit, E. *Nature Nanotechnology* **2006**, *1*, 195-200.

(27) Wang, W.; Qian, J.; Tang, A.; An, L.; Zhong, K.; Liang, G. *Analytical Chemistry* **2014**, *86*, 5955-5961.

(28) Smith, A. M.; Williams, R. J.; Tang, C.; Coppo, P.; Collins, R. F.; Turner, M. L.; Saiani, A.; Ulijn, R. V. *Advanced Materials* **2008**, *20*, 37-41.

(29) Vigier-Carrière, C.; Garnier, T.; Wagner, D.; Lavalle, P.; Rabineau, M.; Hemmerlé, J.; Senger, B.; Schaaf, P.; Boulmedais, F.; Jierry, L. *Angewandte Chemie - International Edition* **2015**, *54*, 10198-10201.

(30) He, S.; Scheres, S. H. *Journal of Structural Biology* **2017**, *198*, 163-176.

(31) Scheres, S. H. *Journal of Structural Biology* **2012**, *180*, 519-530.

(32) Rohou, A.; Grigorieff, N. *Journal of Structural Biology* **2015**, *192*, 216-221.

(33) Wagner, T. et al. *Communications Biology* **2019**, *2*, 1-13.

(34) Wagner, T.; Lusnig, L.; Pospich, S.; Stabrin, M.; Schonfeld, F.; Raunser, S. *Acta Crystallographica Section D : Structural Biology* **2020**, *76*, 613-620.

(35) Estrozi Farias, L.; Schoehn, G.; Desfosses, A. HELIXPLORER, Grenoble, 2018.

(36) Scheres, S. H. *Acta Crystallographica Section D : Structural Biology* **2020**, *76*, 94-101.

(37) Henderson, R. et al. in *Structure*, 2012; t. 20, p. 205-214.

(38) Bera, S.; Mondal, S.; Xue, B.; Shimon, L. J.; Cao, Y.; Gazit, E. *Nature Materials* **2019**, *18*, 503-509.

(39) Christofferson, A. J.; Al-Garawi, Z. S.; Todorova, N.; Turner, J.; Del Borgo, M. P.; Serpell, L. C.; Aguilar, M. I.; Yarovsky, I. *ACS Nano* **2018**, *12*, 9101-9109.

(40) Jorgensen, W. L.; Chandrasekhar, J.; Madura, J. D.; Impey, R. W.; Klein, M. L. *The Journal of Chemical Physics* **1983**, *79*, 926-935.

(41) Usov, I.; Adamcik, J.; Mezzenga, R. *ACS Nano* **2013**, *7*, 10465-10474.

(42) Franke, D.; Petoukhov, M. V.; Konarev, P. V.; Panjkovich, A.; Tuukkanen, A.; Mertens, H. D.; Kikhney, A. G.; Hajizadeh, N. R.; Franklin, J. M.; Jeffries, C. M.; Svergun, D. I. *Journal of Applied Crystallography* **2017**, *50*, 1212-1225.

Supporting Information

Material and Methods

Part 1. Preparation of the sample

The hydrogelator Fmoc-FFY (1.6×10^{-4} mol/L) is dissolved in a fresh 25 mM of sodium tetraborate at pH = 9.3, then the solution is heated up to 80°C for 5 minutes to dissolve the peptide. Then the vial is brought down to room temperature (20°C). This sample is named "annealing". The second sample is the precursor Fmoc-FFpY (1.6^{-4}mol/L) dissolved in a fresh 25 mM sodium tetraborate at pH = 9.3 with addition of Alkaline Phosphatase (3.125^{-8} mol/L). This sample is named "EASA".

Part 2. Cryo-EM image acquisition

A 3.5 μL drop of each sample was deposited onto a Quantifoil holey carbon grid (R1.2/1.3, 300 mesh, copper) previously glow-discharged for 45 s at 25 mA. The grid was incubated for 5 s at 20 °C under 100% humidity using a Mark IV Vitrobot (ThermoFisher), blotted for 5.5 s using force 0, and plunge-frozen in liquid ethane for specimen vitrification.

The grids were transferred in a Talos Glacios 200 kV FEG microscope (ThermoFisher) equipped with a K2 summit direct electron detector camera (Gatan). Dataset of 3838x3710 movies of 40 frames were collected at 0.9 Å per pixel with a dose rate of 1 é/Å^2/s at a magnification of 45 k for annealed and EASA sample respectively using the SerialEM software : classical data collection (image taken in one hole, compustage movement and image of the next hole) for EASA sample and multihole data collection for sample annealed (3x3 holes).

Part 3. crYOLO autopicking

The training dataset of the filament model is trained with a previous dataset of the sample 1, not used in the further reconstruction, with a 0.59 Å/pix and binning factor of 2 after motion correction with an applied patch of 5x5 and 1 é/ Å^2 of dose per frame. The images have been then CTF corrected with CTFFIND 4.1 from Rohou[1] and only 355 micrographs are then furthered used for training. Particle picking has been done manually on the nanofibers in RELION resulting in 345 680 particles with an interbox distance of 14.65 Å. The model was trained with Phosphorus net an early stopping of 15 and a warmup of 5. The produced model is then used on the new dataset which parameters have been described in the above section and processing in the following one. The prediction has been processed on the new dataset of the sample annealed and resulting in 1,4 million extracted

particles with the parameters described below.

Part 4. RELION processing

All of the parameters and the processing section are described both in the article and in the Chapter 2 page 68.

Part 5. Map comparison and molecular fitting

The determination of the correlation between the two density maps have been done with ChimeraX and the tool “Fit in map”.[2] Correlation calculation between the maps was done with the correlation option in the toolbox along with the applying of a weight in the strongest densities in order to reduce the impact of residual noise in the calculation.

Molecular fitting have been done in ChimeraX 1.4 and with the use of “Fit in Map” tool. Initial PDB structures have been constructed with tLeap from AmberTools22.

Part 6. Molecular Dynamics simulations and analysis

This section have been described in the Material and Methods Chapter 2. The modifications from the standard presented procedure are listed below.

The cubic box has 143x112x112 Å dimensions and is filled with the nanofiber and 56,000 TIP3P water molecules. The fiber is placed in the center of the box. 3D Periodic Boundary Condition are applied during the full dynamic. A cutoff of 9 Å is used for non-bonded interactions, the long range electrostatic interactions is calculated through Particle Mesh Ewald method. The cartesian positions of the Fmoc are restrained with a 5 kcal.mol^{-1}Å^{-2} constant, the reference used for the position for each trajectory is from the starting structure. The production of the dynamic is done until 500 ns are generated.

Part 7. SAXS and WAXS measurement

Small- and Wide-Angle X-ray Scattering experiments (SAXS, WAXS) were performed on the X-ray scattering platform DiffériX of the Institut Charles Sadron (Strasbourg) using two diffractometers installed on the two ports of a Rigaku rotating anode generator (MicromaxTM- 007 HF, operating power 40 kV - 30 mA, wavelength $\lambda = 1.54$ Å). The beam was monochromatized and collimated with a confocal Max-Flux OpticsTM mirror (Osmics, Inc.) combined to a system of two (WAXS setup) or three (SAXS setup) pinholes. The scattered intensity was collected on a 2D multiwires

detector (Rigaku) located at 81 cm from the sample position (SAXS setup), or on a Pilatus 3R 300K detector (Dectris Ltd., Switzerland) with a sample - detector distance of 20 cm (WAXS setup). The combination of these two instruments allowed to explore a scattering vector range from q = 0.01 to 1.00 Å^{-1} ($q = \frac{4\pi}{\lambda} sin2\theta$, where 2θ is the scattering angle).

Data reduction was performed according to usual procedures for isotropic scattering (angular averaging, electronic background, sample transmission and thickness corrections). q vectors were calibrated with a silver behenate powder diffractogram. Intensities were converted into absolute scale using a calibrated Lupolen standard. All experiments were performed at room temperature. Liquid samples and gels were introduced in sample holders made of two thin calibrated mica windows 1 mm apart. Samples measurements were finally corrected from the solvent contribution (Borax) according to their volume fraction, yielding the scattering cross section per unit volume of the solute I(q).

Part 8. CRYSOL fitting

The module CRYSOL from ATSAS 2.8.3[3] has been used for simulating the SAXS spectra. All of the PDB files have been generated from ChimeraX 1.4. The PDB simulated consist in 500 propeller turns of the motif which correspond to 11.77 full turns of one strand.

$ crysol Fibre.pdb –ns=200 –lm=15

Figure S1

Representation of the phenylalanines in the crossed section of the density map. Each color represents a different strand. The scale is a length of 10 Å.

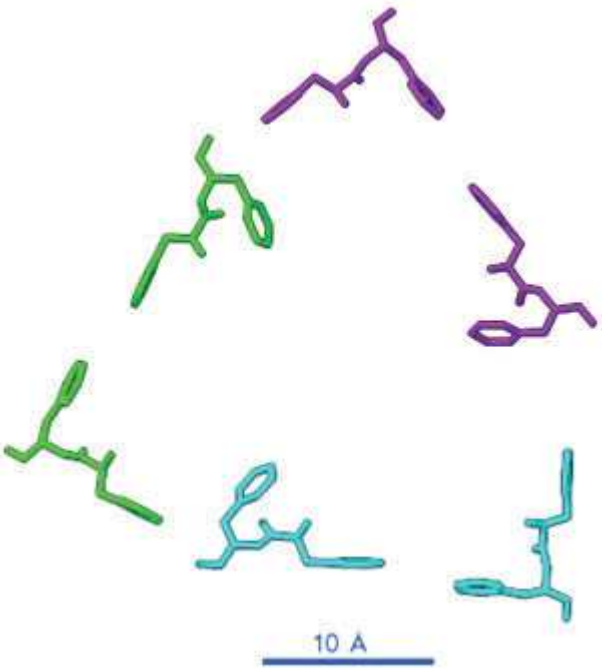

Figure S2

Normalized correlation maps between the tyrosines obtained from restrained MD simulations of the nanofiber. Higher values mean higher observed situations.

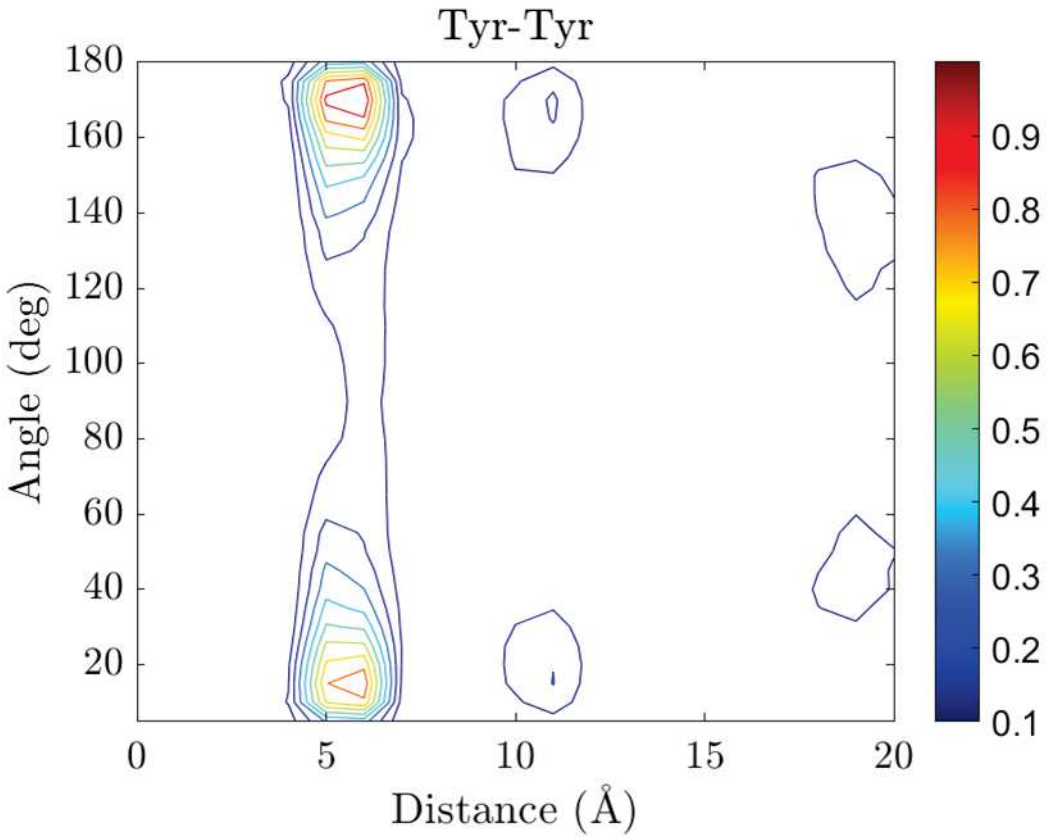

Figure S3

Map densities and molecular model of the Fmoc for the annealing systems. The density map is displayed at 2.5 Å of distance of the molecular model.

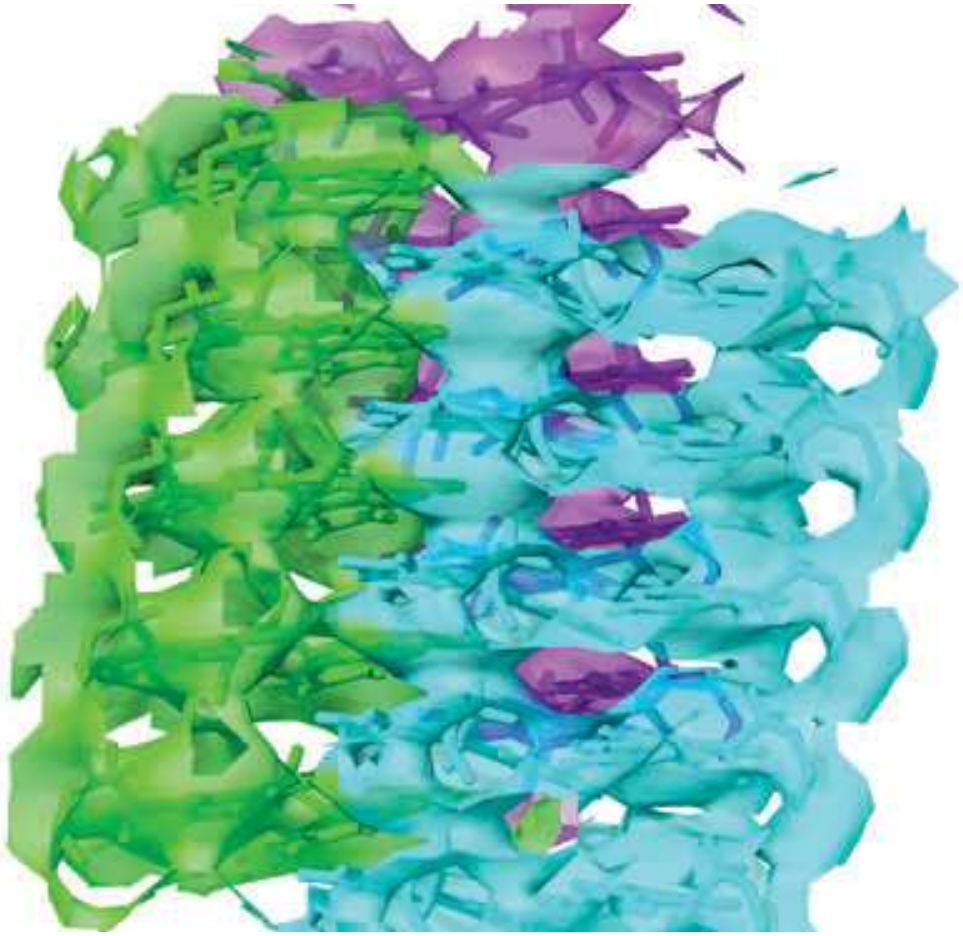

Figure S4

SAXS and WAXS curves of the EASA (Fmoc-FFpY 20 mg/mL + AP 0.8 mg/mL) in red and annealed (Fmoc-FFY 18 mg/mL) systems in orange. The simulated spectra from reconstruction process is in blue.

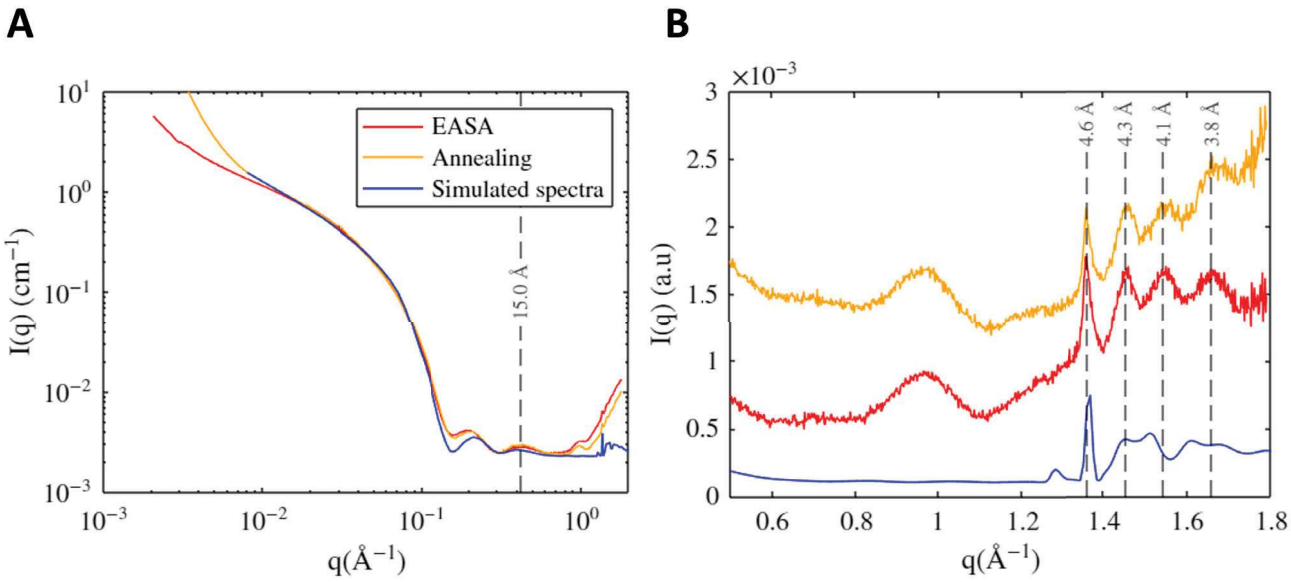

Figure S5

The FSC is the comparison of the Fourier coefficient between the masked and unmasked half maps during post-processing. At high distances (low spatial frequency) all of the coefficients are correlated. Up to a point in the high frequency domain(low distance) coefficients start to diverge and the value is dropping. The criteria to determine the resolution have been chosen to be 0.143 as described by Rosenthal & Henderson in 2003.[4] More the value of FSC stay close to 1 longer more the density map present a high order of resolution. In this case EASA the FSC drop if a little after the annealing but still gives the same resolution of the density map at the criteria. This is in accordance with a higher order of the density of EASA system. In our case the spatial frequency is in $Å^{-1}$.

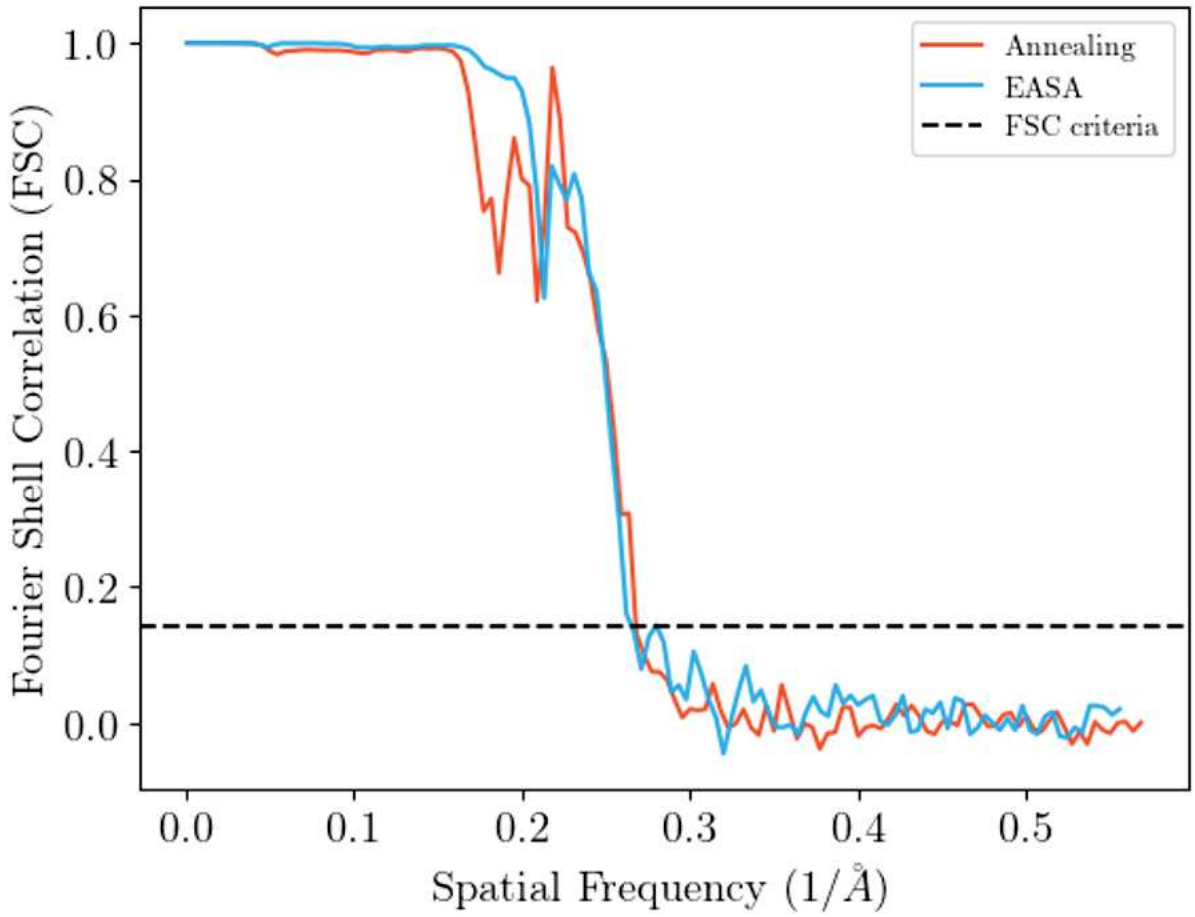

References

(1) Rohou, A.; Grigorieff, N. *Journal of Structural Biology* **2015**, *192*, 216-221.

(2) Goddard, T. D.; Huang, C. C.; Meng, E. C.; Pettersen, E. F.; Couch, G. S.; Morris, J. H.; Ferrin, T. E. *Protein Science* **2018**, *27*, 14-25.

(3) Franke, D.; Petoukhov, M. V.; Konarev, P. V.; Panjkovich, A.; Tuukkanen, A.; Mertens, H. D.; Kikhney, A. G.; Hajizadeh, N. R.; Franklin, J. M.; Jeffries, C. M.; Svergun, D. I. *Journal of Applied Crystallography* **2017**, *50*, 1212-1225.

(4) Rosenthal, P. B.; Henderson, R. *Journal of Molecular Biology* **2003**, *333*, 721-745.

Chapitre 5 : Mechanistic Insights into Hyaluronic Acid Induced Peptide Nanofiber Organization in Supramolecular Hydrogels

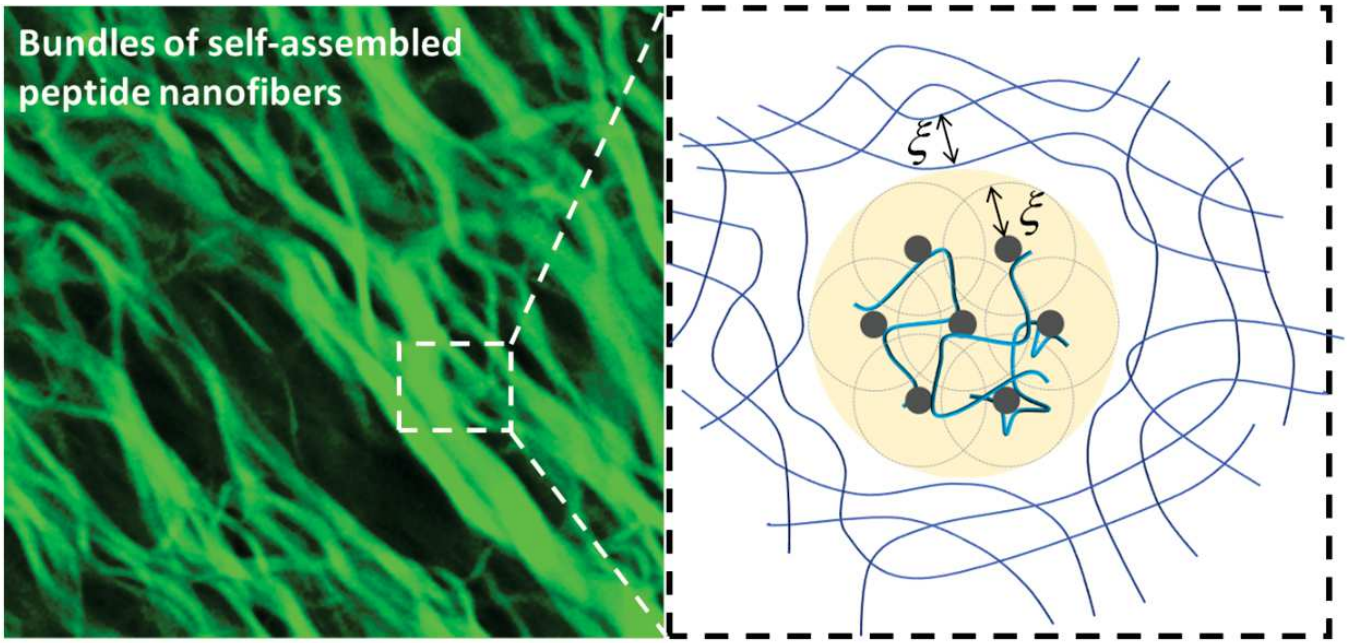

1 Contexte

Nous avons vu dans les précédents chapitres comment les peptides s'assemblent dans les premiers instants et que cet structuration de N- à C-terminale était également retrouvée dans les nanofibres de peptides reconstruites. Cependant, ces résultats sont à des concentrations de l'ordre de 10^{-1} mg/mL, alors qu'en est-il de la microstructure de l'hydrogel à des concentrations 100 fois plus importantes ?

Nous proposons ici d'étudier le changement de microstructure du gel de Fmoc-FFY initié par voie enzymatique avec la présence d'acide hyaluronique, un biopolymère biocompatible souvent étudié dans le domaine des applications biomédicales.

Dans ce dernier chapitre de résultats nous investiguons comment la microstructure varie avec l'augmentation croissante d'acide hyaluronique grâce à des mesures de diffusion de rayons X, de dichroïsme circulaire, dynamique moléculaire et de la microscopie confocale.

Ce chapitre est un article qui a été publié dans le journal Biomacromolecules de l'éditeur American Chemical Society (ACS). Copyright ACS - Biomacromolecules, 2014.

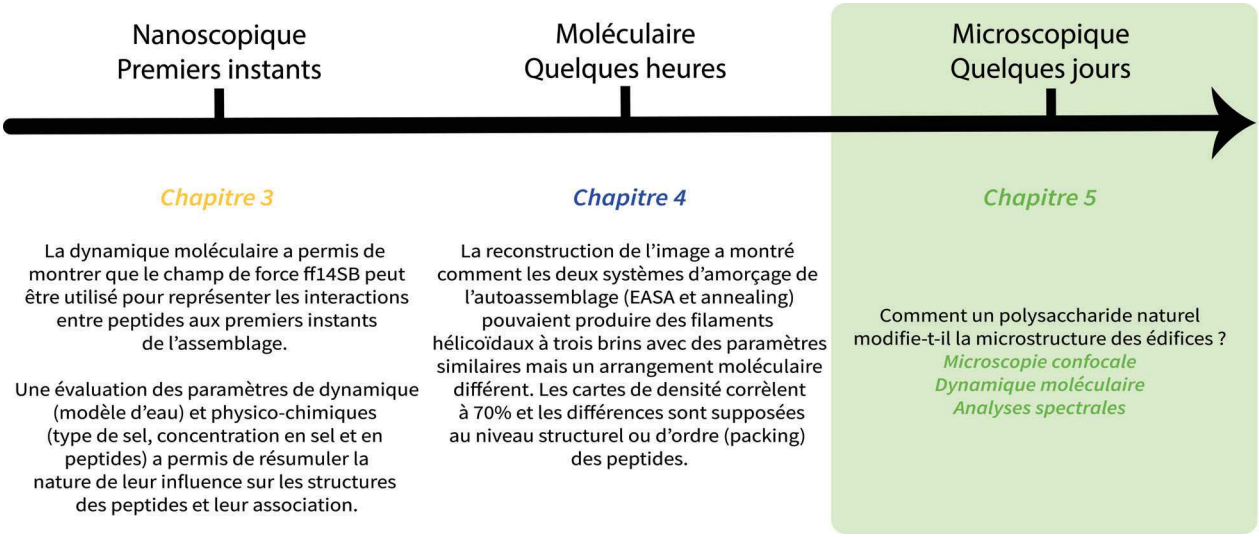

List of authors :

Alexis Bigo−−Simon, Jennifer Rodon Fores, Miryam Criado-Gonzalez, Lucille Blandin, Jean-Yves Runser, Bernard Senger, Guillaume Fleith, Marc Schmutz, Rachel Schurhammer, Alain Chaumont, Pierre Schaaf, Jérôme Combet and Loïc Jierry

2 Abstract

Composite hydrogels composed of low-molecular weight peptide self-assemblies and polysaccharides are gaining great interest as new types of biomaterials. Interactions between polysaccharides and peptide self-assemblies are well reported but a molecular picture of their impact on the resulting material is still missing. Using the phosphorylated tripeptide precursor Fmoc-FFpY (Fmoc : Fluorenylmethyloxycarbonyl ; F : phenylalanine ; Y : tyrosine ; p : phosphate group) we investigated how hyaluronic acid (HA) influences the enzyme-assisted self-assembly of Fmoc-FFY generated in situ in presence of alkaline phosphatase (AP). In the absence of HA, Fmoc-FFY peptides are known to self-assemble in nanometer thick and micrometer long fibers. The presence of HA leads to the spontaneous formation of bundles of several micrometers thickness. Using fluorescence recovery after photobleaching (FRAP) we find that in the bundles both (i) HA co-localizes with the peptide self-assemblies and (ii) its presence in the bundles is highly dynamic. The attractive interaction between negatively charged peptide fibers and negatively charged HA chains is explained through molecular dynamic simulations which show the existence of hydrogen bonds. Whereas the Fmoc-FFY peptide self-assembly itself is not affected by the presence of HA, this polysaccharide organizes the peptide nanofibers in a nematic phase visible by small angle X-ray scattering (SAXS). The mean distance d between the nanofibers decreases by increasing the HA concentration c as $d \sim c^{(-1/4)}$ but remains always larger than the diameter of the peptide nanofibers indicating that they do not interact directly one with each other. At high enough HA concentration, the nematic organization transforms into an ordered 2D hexagonal columnar phase with a nanofiber distance of 117 Å. The power law $d \sim c^{(-1/4)}$ is expected when depletion forces generated by the polysaccharides act between the nanofibers and are responsible for the bundle formation. Such behavior is thus suggested for the first time on nano-objects using polymers partially adsorbing on self-assembled peptide nanofibers.

3 Introduction

Low molecular weight hydrogelators (LMWH) are receiving great attention both for their fundamental interest and for their widespread potential applications in the biomedical field[1]. Since the landmark article from Reches and Gazit showing that Fmoc-FF dipeptides can form self-assembled nanotubes,[2] numerous studies investigating self-assembly processes of Ar-FF or Ar-FF-X peptides, where Ar represents a large aromatic group and X an additional short amino acid sequence, have

been reported. Under certain conditions, when the self-assembly of such peptides occurs in water, it leads to supramolecular hydrogels[3]. The formation of this material can be triggered by a large panel of stimuli such as a change in pH or temperature, the irradiation by light or the addition of metallic ions, for instance[1, 3]. In 2004, Xu and coworkers introduced the concept of enzyme-assisted self-assembly (EASA) illustrated by the enzymatic dephosphorylation by AP of a phosphorylated precursor compound, i.e. Fmoc-pY, providing *in situ* the LMWH Fmoc-Y which self-assembles in a nanofibrous network[4].

As already mentioned above and illustrated by a huge number of contributions in this field, supramolecular hydrogel based on Fmoc-FF-X peptide sequences or other kinds of LMWH, constitute a class of materials particularly appealing for biomedical applications mainly because of their high water content, their very soft mechanical features and the reversibility of the constitutive building block interactions which ensures adaptability and self-healing properties[5-10]. To design the most suitable material for biomedical purposes, additional components are often introduced before the hydrogelation step, i.e. at the sol state. This approach has been investigated with success and among the various components involved, polysaccharides are compounds of choice[11, 12]. Indeed, polysaccharides are biocompatible natural polymers which can contain ligands for specific cell receptor interactions. This is the case for HA, a polysaccharide constituted by the alternation of 1,4-D-glucuronic acid and β-1,3-N-acetyl-D-glucosamine, which is abundantly present in the extracellular matrix of all tissues. The interest of the presence of HA in biomaterials also lies in its implication in the internal self-assembled architecture underpinning the material which changes both the resulting biochemical and mechanical properties of the biomaterial[13, 14]. Stupps and co-workers have highlighted the strong ability of HA to interact with positively charged amphiphilic peptide self-assemblies leading to an ordered and hierarchical organization at the micro- and macro meter scale[15]. The groups of Nevo, Sitt and Adler-Abramovich investigated rheological features of HA gels mixed with Fmoc-FF self-assemblies, as well as their drug release properties and their cellular response[14, 16-18]. They have revealed the potential of HA to control the stiffness of the resulting hydrogel through the HA content and its beneficial influence on the biodegradability of the material. The tunability of the supramolecular mechanical features have also been recently reported by the Palmans and Meijer groups on HA-doped supramolecular hydrogels based on non-peptide hydrogelators[19]. Very recently, our group has demonstrated that HA can be introduced during the formation of supramolecular hydrogel coatings through localized EASA strategy[20]. In addition to the mechanical influence of HA on the hydrogel, we showed that the presence of HA also promotes the adhesion and the viability of

NIH 3T3 fibroblasts. The changes of the mechanical and chemical features of peptide-based hydrogels supplemented by HA are thus widely reported but a clear molecular picture of its origin is still lacking. Here, using the phosphorylated tripeptide precursor Fmoc-FFpY[21, 22], we investigate how HA influences the EASA of Fmoc-FFY generated in situ in presence of AP (Fig. 1a). The molecular-scale assembly of Fmoc-FFY and the enzymatic activity of AP are studied through circular dichroism (CD) and high performance liquid chromatography (HPLC) at various concentrations of HA. The role of HA in the self-assembled peptides organization is investigated by confocal laser scanning microscopy (CLSM), small- and wide-range X-ray scattering (SAXS-WAXS) and molecular dynamics (MD) simulations.

4 Materials and Methods

4.1 Materials

Fmoc-FFpY (purity > 98 %) was purchased from Pepmic company or prepared according to literature[20]. HA (PrimaHyal® from Givaudan Mw 406 000 g.mol^{-1}, Polydispersity 1.574) is sold by Givaudan. Its full ^{1}H NMR and size exclusion chromatography characterization have been given previsously[20]. Rhodaminated HA (HA^{RHO}) was prepared from HA following a reported procedure[23]. Sodium tetraborate decahydrate, 99% (Borax) was purchased from Alfa Aesar. AP from bovine intestinal mucosa (Mw 160 000 g.mol^{-1}) and thioflavine T (ThT) were from Sigma-Aldrich.

4.2 Circular Dichroism

The measurements were performed on a JASCO CD spectrometer (Model J-1700) at 20°C with a Peltier regulator. The scan speed was set to 20 nm/min, the resolution to 200 mdeg, the digital integration time was settled at 2 s, the data pitch was fixed at 0.05 nm and the band width at 2 nm. The voltage from the photomultiplier tube was monitored as below 500V for all measurements, to ensure the absence of artefacts coming from the gain (Fig. S1). The baseline was carried out with a 25 mM Borax solution. An adapted 1.5 mL CD UV-visible quartz-vial of 1 cm optic path length was carefully washed and dried before each measurement. Each solution was freshly prepared from a fresh 25 mM Borax solution in a 4 mL glass vial. Then the same volume of each solution (0.4 mL if there were three solutions, 0.6 mL if there were two) was harvested and placed into the cuvette. For the sample preparation, HA came first and was mixed to the Fmoc-FFpY solution, and then the AP

was added, at the end, just before starting the measurement. A constant agitation of 100 rpm on a magnetic stirrer inside the CD vial was applied. Concentrations into the quartz-vial were : 0.10, 0.25, 0.50, 1.00, 2.00, 2.50, 5.00, 10.00 mg/mL for HA, along with a constant 0.125 mg/mL concentration of Fmoc-FFpY and 0.01 mg/mL of AP.

4.3 Cryo-TEM

In cryo-TEM analysis, a 5 μL drop solution of Fmoc-FFpY and AP was deposited on a copper grid covered with a holey carbon film which was rendered hydrophilic using an ELMO glow discharge unit (Cordouan Technologies, France). The grid was placed in a home-made freezing chamber maintained at 22°C and a relative humidity of 80% before plunging into liquid ethane held at -190°C by liquid nitrogen. The grid was mounted onto a cryo holder (Gatan 626, Pleasanton, CA, USA) and observed under low dose conditions using a Tecnai G2 microscope (FEI, Eindhoven, the Netherlands) at 200 kV. Images were acquired using an Eagle slow scan CCD camera (FEI).

4.4 Confocal laser scanning microscopy

Observations on the confocal microscope were performed on a Zeiss LSM700 microscope from NIKON. A sample was prepared in a circular Teflon mould of 0.2 mL, fixed on an optical microscopy coverslip (DiaPaths, 24 × 60 × 0,16 mm, code 061061) with a silicon watertight seal. Each solution was freshly prepared with a fresh 25 mM Borax solution. The concentrations were : 0, 4, 10 and 20 mg/mL HA (respectively 8.95×10^{-6} mol/L, 22.38×10^{-6} mol/L and 44.76×10^{-6} mol/L), 10 mg/mL Fmoc-FFpY (12.86×10^{-3} mol/L) and 0,4 mg/mL AP (2.5×10^{-6} mol/L). HA^{RHO} used for CLSM was a mixture of 90% w/w of HA and 10% w/w of rhodamine-labelled HA, prepared as described in the literature.. 0.05 mL of Thioflavin T at 0.5 mg/mL (1.57×10^{-3} mol/L) was added to the 0.2 mL of hydrogel formed, 2 h before the observation. Measurements started with the rhodamine with a 514 nm laser and then with the Thioflavin T observation with a 455 nm laser. The lasers were used at 15% of their power. Image sizes were 2048 × 2048 pixels. Pictures are opened and handled with ImageJ software.

4.5 Classical molecular dynamics

MD were performed using the AMBER18 software suite in which the potential energy U is described by a sum of bond, angle and dihedral deformation energies and a pair wise additive 1-6-12

potential (electrostatic + van der Waals) between non-bonded atoms (Eq 1)[24].

$$U = \sum_{bonds} k_b(r-r_0)^2 + \sum_{angles} k_\theta(\theta-\theta_0)^2 + \sum_{dihedrals}\sum_{n} V_n(1+cos(n\varphi-\gamma)) + \sum_{i<j}[\frac{q_i q_j}{R_{ij}} - 2\epsilon_{ij}(\frac{R^*_{ij}}{R_{ij}})^6 + \epsilon_{ij}(\frac{R^*_{ij}}{R_{ij}})^{12}] \quad (6.1)$$

Two systems were simulated, each composed of 16 Fmoc-FFY peptides and 19851 water molecules. Additionally, 2 HA chains each composed by 8 units of 1,4-D-glucuronic acid and β-1,3-N-acetyl-D-glucosamine to one of the systems were introduced in one of these systems. The system without HA was neutralized by the addition of 416 Na^+ and 400 Cl^- ions, whereas the system with HA received 432 Na^+ and 400 Cl^- ions. Force field parameters for the different amino acids were taken from the AMBER ff14SB15[25] force field, those for Na^+ cations and Cl^- stem from the work of Cheatham and colleagues.[26] and those for HA were taken from GLYCAM06[27]. Water molecules were represented using the TIP3P model[28]. Atomic charges of the Fmoc fragment were obtained using the RESP procedure[29]. Cross terms in van der Waals interactions were constructed using the Lorentz-Berthelot rules. 1-4 van der Waals and 1-4 electrostatic interactions were scaled by a factor of 2 and 1.2, respectively. Simulations were performed using a cubic box and 3D periodic conditions were applied. An atom-based cutoff of 12 Å for electrostatic and van der Waals interactions was applied, while long-range electrostatic interactions were calculated using the particle mesh Ewald method. After equilibration an MD simulation of a total of 1.25 μs in the NVT ensemble was performed. The temperature of the system was maintained at 298.15 K using a Berendsen thermostat with a relaxation time of 1.0 ps[30]. A time step of 1 fs was used to integrate the equations of motion via the Verlet leapfrog algorithm. Snapshots along the trajectory were taken using the VMD software[31].

4.6 Small- and Wide-Angle X-ray Scattering

SAXS and WAXS experiments were performed on the X-ray scattering platform DiffériX of the Institut Charles Sadron (Strasbourg, France) using two diffractometers installed on the two ports of a Rigaku rotating anode generator (MicromaxTM-007 HF, operating power 40 kV - 30 mA, wavelength $\lambda = 1.54$ Å). The beam was monochromatized and collimated with a confocal Max-Flux OpticsTM mirror (Osmics, Inc.) combined to a system of two (WAXS setup) or three (SAXS setup) pinholes. The scattered intensity was collected on a 2D multiwires detector (Rigaku) located at 81 cm from the sample position (SAXS setup), or on a Pilatus 3R 300K detector (Dectris Ltd., Switzerland) with a sample - detector distance of 20 cm (WAXS setup). The combination of these two instruments

allowed to explore a scattering vector range from q = 0.01 to 1.00 Å^{-1} ($q = \frac{4\pi}{\lambda} sin2\theta$, where 2θ is the scattering angle). Additional information is given in the SI, Section 1, Part 1.

5 Results and discussion

5.1 Influence of HA on the EASA process

To elucidate the role of HA in the EASA of peptides, we should consider the whole mechanism pathway of this approach, as it is known[32, 33]. First, the precursor compound exists in a pre-assembled/pre-aggregated state before its enzymatic conversion in LMWH[34-37]. Then, the enzymatic production rate of the hydrogelator from this precursor impacts directly the morphology of the resulting self-assembled structures and even the obtaining of a hydrogel as well[38]. Finally, the self-assembly is not instantaneous : a lag time between the enzymatic production of LMWH and the initiation of the self-assembly process has been reported[22, 39-41]. Thus, we can expect that HA could influence the enzyme-assisted peptide self-assembly process in one or several of these steps. CD provides information on the chiral organization of supramolecular assemblies. Measurements performed on a solution of the precursor Fmoc-FFpY (0.125 mg/mL in Borax buffer pH 9.3) shows a negative ellipticity over the absorption bands of tyrosine and Fmoc between 200 and 300 nm (Fig. 1b and Fig. S1a). The bands at about 240 nm come from the arrangement of tyrosine and phenylalanine residues whereas those between 250-300 nm are attributed to helical arrangements of the fluorenyl moieties[42]. This strong CD band intensity for Fmoc-FFpY must originate from a pre-assembled state[32-37]. The influence of HA on the enzymatic action of AP has been studied through HPLC monitoring. When Fmoc-FFpY (0.25 mg/mL) is mixed with AP (0.01 mg/mL) in presence of HA of distinct concentrations (0.10, 0.25 and 0.50 mg/mL), the formation of Fmoc-FFY over time is quasi-identical in all cases, leading to an almost full conversion in 1 h (Fig. S2). Since HA has no effect on the catalytic action of AP, we investigated the influence of HA on the self-assembly of Fmoc-FFY when produced in situ from AP and the precursor Fmoc-FFpY. First, Fig. 1b shows a typical CD spectrum of this Fmoc-FFY self-assembly generated from Fmoc-FFpY brought in contact with AP in absence of HA. Compared to the CD spectra of Fmoc-FFpY, one observes significant changes between 240 and 300 nm originating from the Fmoc arrangement. In particular, the band at 299 nm disappears and a new band at 303 nm appears which is assigned to a super-helical arrangement of the fluorenyl groups, as already reported for other kinds of Fmoc-derivatives used as LMWH[42, 43]. In the following, the intensity

evolution of this band at 303 nm will be used as a probe to monitor the self-assembly of Fmoc-FFY since this band is not shifting over the 60 minutes time period studied (Fig. S1c). When this process takes place in the presence of HA, the whole CD spectrum of the Fmoc-FFY is identical to the one obtained in the absence of HA but the ellipticity intensity decreases when the HA concentration increases from 1.0 to 10.0 mg/mL (Fig. 1c and Fig. S1b). This difference can be interpreted by a similar molecular organization of the Fmoc-FFY peptides in the resulting self-assembled structures in presence or absence of HA. The decrease of the CD signal intensity when the HA concentration increases could eventually be due to diffusion rising when the HA concentration in increased in the sample analysed. This is in accordance with two recent reported observations[16-18, 20] : (i) the presence of HA changes the Young modulus of the resulting supramolecular hydrogels ; (ii) HA does not change the geometrical features of the Fmoc-FFY self-assembled nanofibers. In addition, the time evolution of this band intensity at 303 nm (Fig. 1c) is characterized by an initial time-lag which is of the order of 3-5 min quasi-independent of the HA concentration (from 1.0 to 10.0 mg/mL). The Fmoc-FFY self-assembly rate is not significantly affected by the presence of HA with a self-assembly time which is of the order of 4-5 min (Fig. S3).

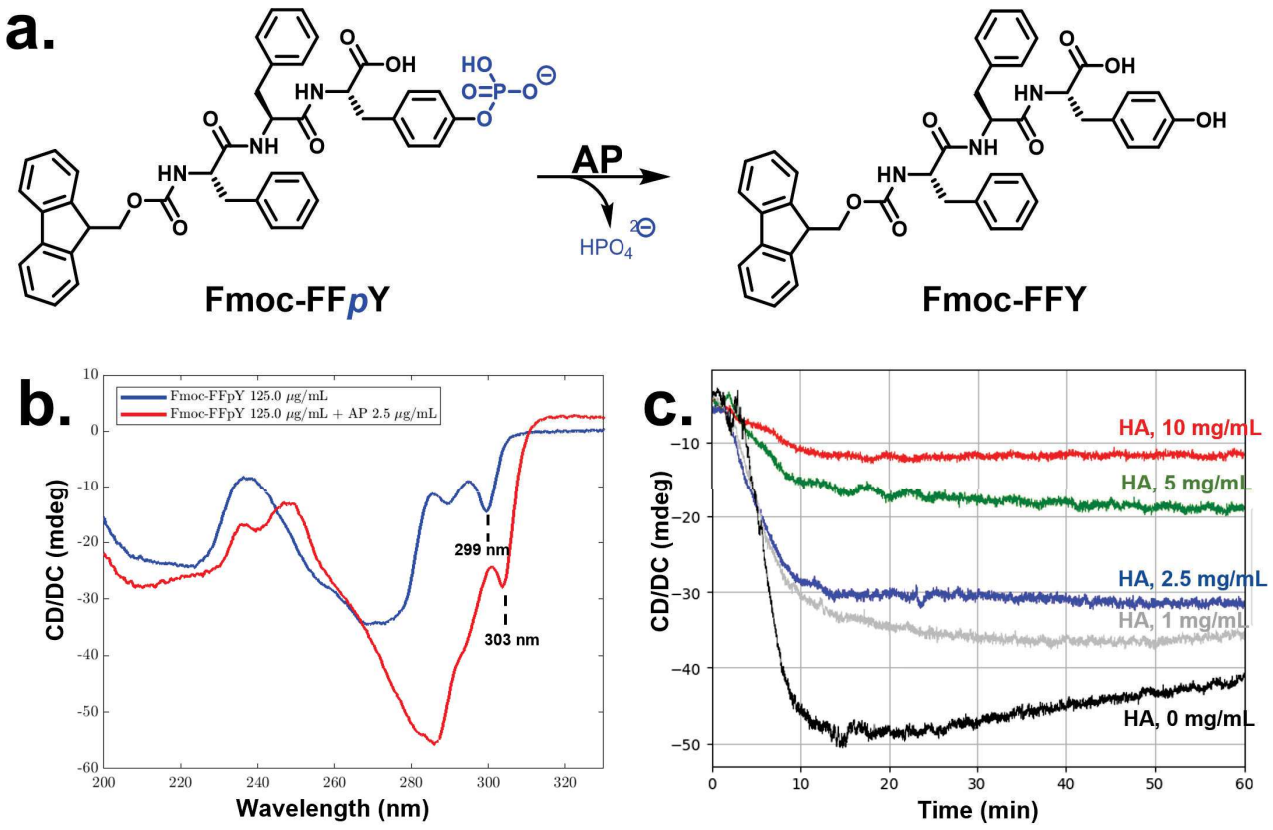

FIGURE 1 – (a) Enzymatic hydrolysis of Fmoc-FFpY to Fmoc-FFY. (b) CD spectra of Fmoc-FFpY (blue) and Fmoc-FFY (red) generated in situ from Fmoc-FFpY in presence of AP. (c) Evolution of the 303 nm band intensity in presence of Fmoc-FFpY (0.125 mg/mL), AP (0.01 mg/mL) and various HA concentrations (0, 1, 2.5, 5 and 10 mg/mL).

5.2 HA interaction with Fmoc-FFY self-assembly

In previous studies, CLSM has proven to be useful in studying the nanofibrous network of peptide self-assemblies[20]. We used HA labelled by rhodamine[23] (HA^{RHO}) and the Fmoc-FFY self-assembly was visualized by the presence of thioflavine T (ThT, $\lambda_{ex} = 350$ nm ; $\lambda_{em} = 438$ nm) which fluoresces in the green region of the visible spectrum when interacting with hydrophobic β-sheet structures. Contact between a solution of HA^{RHO} (4, 10 or 20 mg/mL) containing AP with a Fmoc-FFpY solution containing ThT leads to the formation of large bundles (Fig. 2a). This contrasts with the homogenous green appearance in the absence of HA (Fig. 2b). Taking into account the CD investigations described above, this CLSM observation shows that despite the fact that HA does not affect the molecular arrangement of the Fmoc-FFY peptides (as demonstrated by CD), it strongly influences the overall organization of the self-assembled Fmoc-FFY nanofibers at the microscopic level, leading to a few micrometers thick bundles at least, up to roughly 10 μm, whatever the HA concentration used, i.e. 4, 10 or 20 mg/mL. It must be noted that HA^{RHO} used herein for our fluorescent confocal investigations is only composed of 10 % w/w of rhodamine-labelled HA and the remaining major part is unlabelled HA. This ratio has been optimized in order to highlight the visualization of the bundles. Thus, the black area observed between the bundles does not mean that HA is absent in this space. Fluorescence intensity is still measured in the space between the bundles showing thus the presence of HA (Fig. S4).The involvement of HA is confirmed by the co-localization of HA (red color, Fig. 2a) and the peptide self-assembly (green color, Fig. 2a). A correlation image analysis between the red and the green colours removes any doubts about the full colocalization of HA and Fmoc-FFY self-assembly (Fig. S5). It is important to note that when HA is not labelled, similar bundles are observed by confocal microscopy.[20] In addition, using HA^{RHO} in absence of ThT results in the observation of typical red-coloured bundles (Figure S6). These two control experiments show that the presence of the dyes, i.e. ThT or HA^{RHO}, are not at the origin of the bundle formation. Next, we bleached rhodamine linked to the HA (i.e. HA^{RHO})[23] and determined the fluorescence recovery (Fig. 3). The photobleaching method consists of a mild photochemical transformation of fluorophores leading to a locally controlled fluorescence extinction of the bundles. In addition, the intensity of the laser applied is low enough to avoid both the polymer structure degradation of the HA and the disassembly of peptide Fmoc-FFY. A full recovery of the fluorescence at exactly the location the HA^{RHO} had before bleaching is observed. When a circular surface area (diameter : 14 μm) of a bundle of nanofibers is bleached, this recovery takes place typically over 130 s whatever the HA concentration used (Fig.

S7). These bundles seem thus to be highly dynamic entities even though the polymer diffusion seems relatively slow. This corresponds to a diffusion coefficient that is roughly 1 $\mu m^2/s$ for each HA concentration used (Fig. S3). The recovery of the bundle fluorescence can take place either through an exchange process between HA^{RHO} from the bundles and HA^{RHO} from the surrounding solution, or through the diffusion of HA^{RHO} along the bundles. If this would be the case, the fluorescence recovery should take place gradually from the two edges of the bleached bundles. Despite of a careful analysis of the images provided by FRAP experiments, it seems difficult to conclude unambiguously about the process involved in this fluorescence recovery (Fig. 3 and Fig. S7). Finally, a z-stack analysis has shown that hyaluronic acid is also homogeneously distributed within the bundle (Fig. S8).

As mentioned above, HA and self-assembled nanofibers are negatively charged but an attractive interaction still exists. Negatively charged polysaccharides, such as fucoidan, adsorbing on negatively charged peptide-based nanofibers has already been observed[44]. To elucidate how HA is interacting with self-assembled Fmoc-FFY, MD simulations have been performed. Simulations of 16 hydrogelators Fmoc-FFY in water in presence or in absence of two octamers of HA led to an equilibrated state after ≈ 1 μs. Thus, first steps of the Fmoc-FFY self-assembly are studied. The assembly of the 16 Fmoc-FFY shows a packed aggregate whose structure is mainly ensured by hydrogel bonds involved in β-sheet structures (Fig. 4a). In presence of HA, the two oligomers do not modify significantly the Fmoc-FFY organization despite interacting with the peptide assembly. Indeed, the two HA oligomer chains enlace the assembly (Fig. 4b). The nature of this interaction between HA and the self-assembly of Fmoc-FFY is based on hydrogen bonds between phenol group of the tyrosine residue in Fmoc-FFY sequence and the carboxylate groups of HA (Fig. 4c). In addition, hydrogen bonds between the carboxylate group of Fmoc-FFY in C-terminal position and hydroxyl groups of HA are also observed. One can thus assume that during the process, a small peptide self-assembly forms and part of the HA chain is surrounding it, leaving other parts of the HA chain free to encircle other small peptides self-assemblies. As HA interacts with these peptide self-assemblies through non-covalent bonds, the whole bundle results in a dynamic object as it comes out from FRAP experiments.

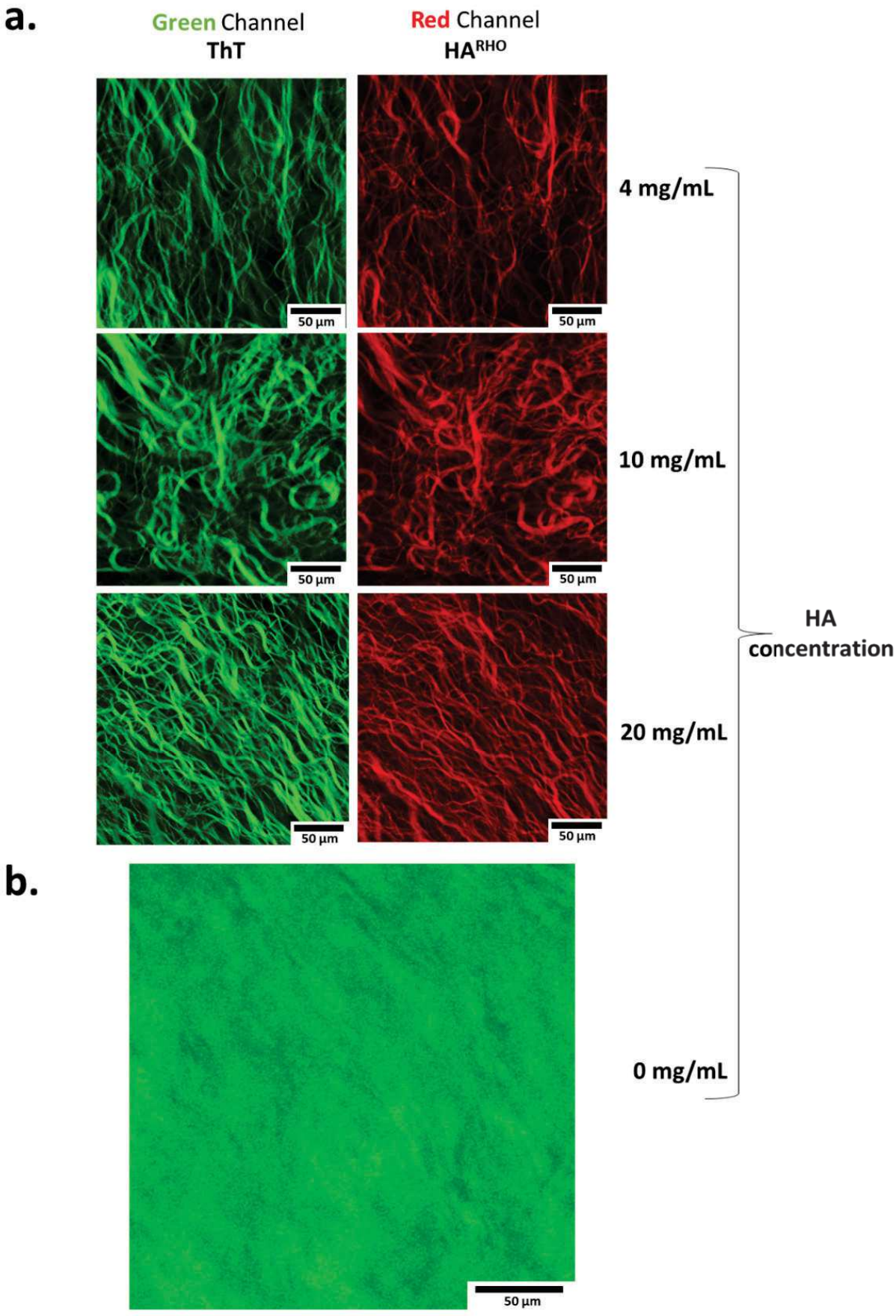

FIGURE 2 – CLSM images of Fmoc-FFY self-assembly revealed by ThT green emission (λ_{ex} = 350 nm ; λ_{em} = 438 nm) observed through the green channel in (a) presence of HA^{RHO} or in (b) absence of HA^{RHO}. Dashed square areas are magnified in the left column of CLSM images. The localization of HA is highlighted by the rhodamine red emission from HA^{RHO} (λ_{ex} = 570 nm ; λ_{em} = 595 nm).observed through the red channel. HA concentrations are mentioned on the right side.

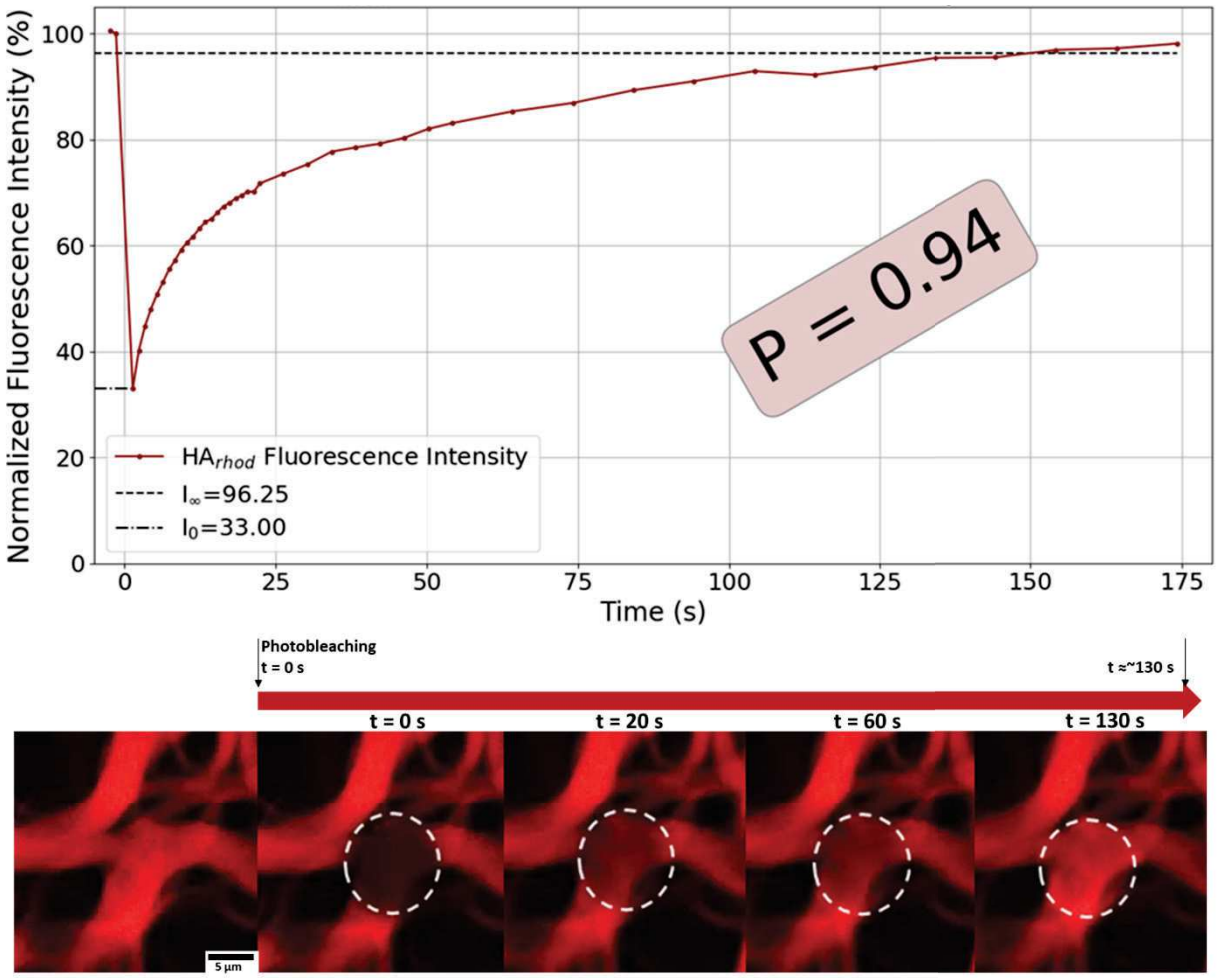

FIGURE 3 – Typical fluorescence recovery after photobleaching (FRAP) over time on HA^{RHO} (20 mg/mL) localized on the Fmoc-FFY bundles of peptide nanofibers. P means the % of fluorescence recovery.

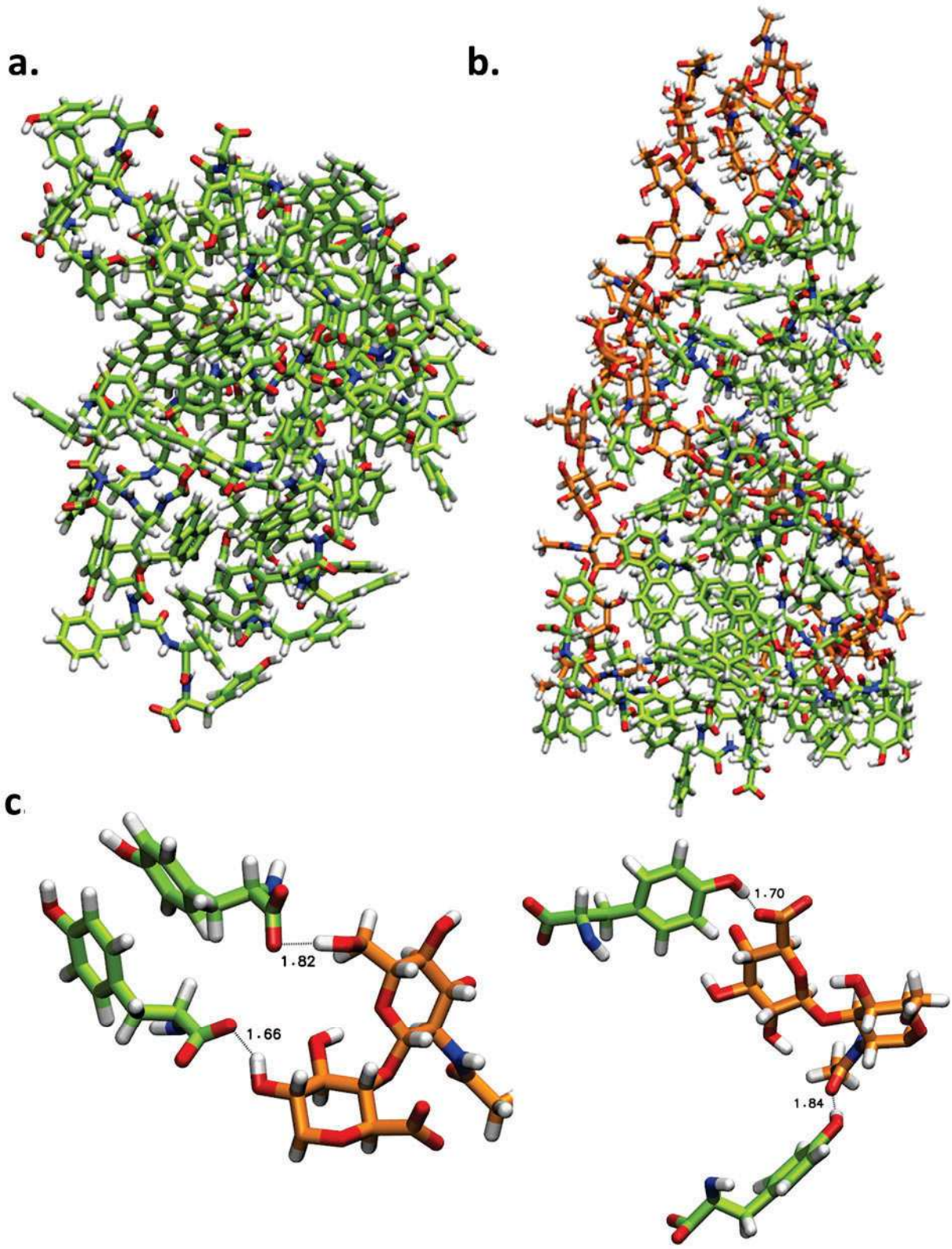

FIGURE 4 – Snapshot taken after 1.25 μs of MD representing the equilibrated self-assembly of 16 Fmoc-FFY in absence (a) and in presence of two oligomers of HA (b). (c) Magnification of a typical hydrogen bonds between (top) the C-terminal carboxylate group of Fmoc-FFY and hydroxyl groups of HA and (bottom) between phenol group of a tyrosine residue and the carboxylate group of the D-glucuronic acid unit of HA. For the sake of clarity, only the tyrosine residue of Fmoc-FFY and a dimer of HA are shown.

5.3 Formation of bundle nanofibers in presence of HA investigated by X-ray scattering

As observed by cryo-TEM in dilute conditions (Fig. 5a), Fmoc-FFY nanofibers are several hundred micrometers long, ≈ 5 nm in diameter and do not change in presence of HA[20]. To get some molecular clues about the self-assembly process and the bundle formation in presence of HA, we performed small- and wide-angle X-ray scattering experiments (SI, Section 1). It is important to note that all our X-ray investigations have been done in the gel state.

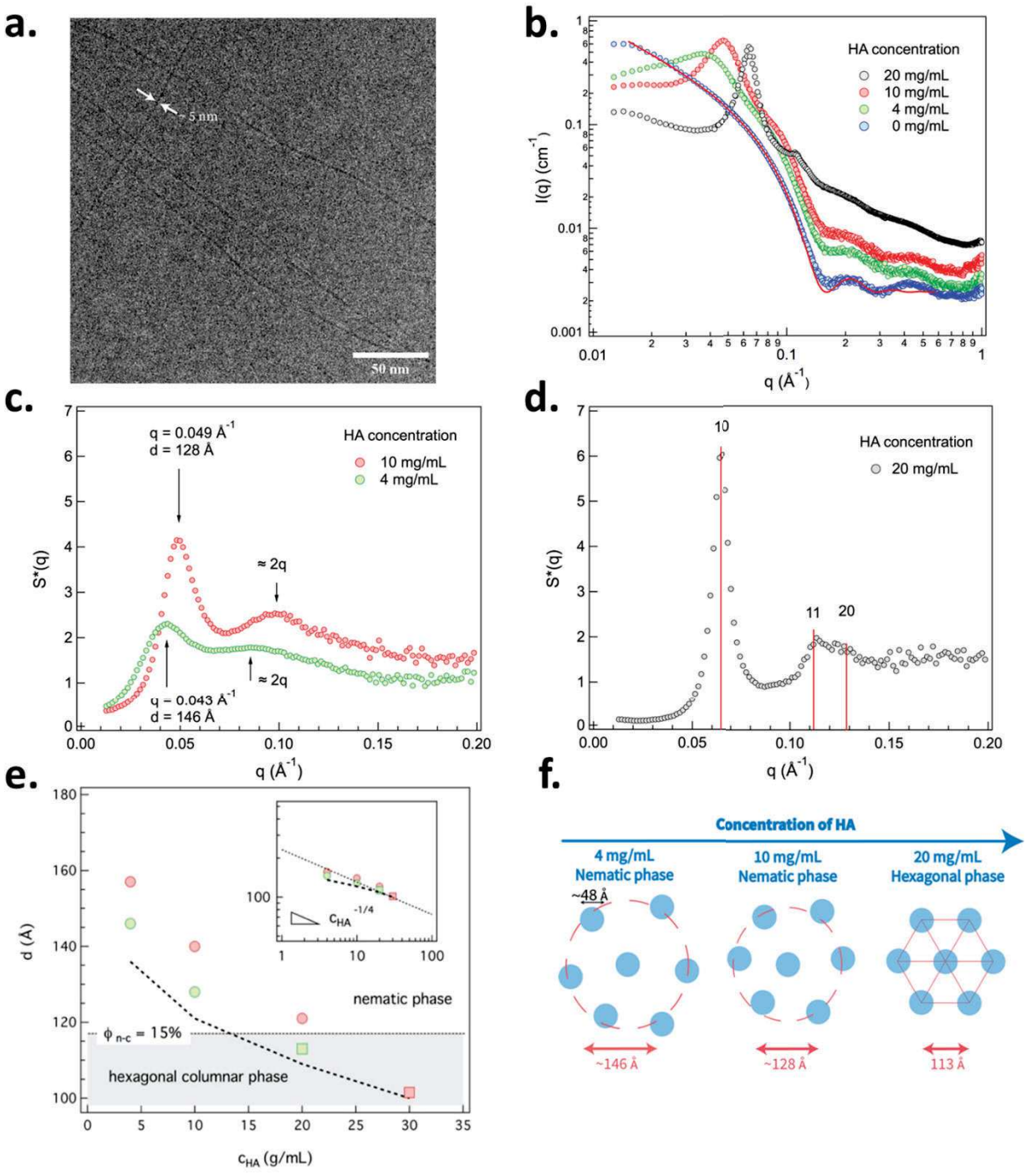

Figure 5 *(previous page)* – (a) Typical cryo-TEM image of self-assembled Fmoc-FFY nanofibers in diluted conditions in absence of HA. (b) X-ray scattering patterns of Fmoc-FFY self-assembly induced by AP (blue) and Fmoc-FFpY in presence of various concentrations of HA (green : 4 mg/mL, red : 10 mg/mL, black : 20 mg/mL) for sample stored at 4°C before measurements. Red line : fit with a model of infinite homogenous cylinder. Radius 23.9 ± 0.2 Å. (c) Effective structure factor S*(q) for hydrogels prepared from Fmoc-FFpY (10 mg/mL) and AP (0.4 mg/mL) and various concentration of HA stored at 4°C before measurements : (c) Nematic phase observed in presence of 4 mg/mL (green circles) or 10 mg/mL of HA (red circles) ; (d) Hexagonal columnar phase in presence of 20 mg/mL of HA (black circles). The vertical red lines correspond to the positions of the diffraction peaks of indices hk (10, 11 and 20). (e) Average distance d between nanofibers in the bundles with respect to HA concentration cHA. Green symbols : samples stored at 4°C for 8 days before measurements. Red symbols : samples kept at room temperature for 1 day before measurements. Discs : nematic phase. Square : hexagonal columnar phase. Long dash line : theoretical d values from pair potentials analysis. The short dash line corresponds to the critical distance delimiting the nematic and hexagonal phases ($d_{d\text{-}c} \approx 117$ Å). It corresponds to a peptide volume fraction $f_{f\text{-}c} \approx 15\%$ in the bundles. Insert : Log-Log variation of d with respect to cHA. Long dash line : theoretical d values. Dash line : power law variation d. (f) Schematic illustration of the local organization in a bundle cross-section according to the HA concentration for samples kept at 4°C. The discs represent the sections of the nanofibers.

Supramolecular hydrogels prepared from Fmoc-FFpY (10 mg/mL) mixed with AP (0.4 mg/mL) were studied with distinct HA contents, i.e. 0, 4, 10, 20 and 30 mg/mL. Two series of experiments were performed on samples stored at different temperatures after the hydrogelation step. Part of these hydrogels were kept at 4°C for 8 days before measurements, others were left at room temperature (≈ 21°C) and measured 24 h later. For both series, samples do not evolve in time. The storage temperature does not affect the formation of the large fibers in presence of HA, but slightly changes their internal ordering. The systems therefore appear roughly frozen, at least over the duration of the measurements. Only samples kept at 4°C are presented hereafter and a more detailed comparison of the two series can be found in the SI (Section 1, Part 2). The discovery of the impact of temperature on the organisation of peptide nanofibers was made by serendipity. Indeed, the choice of the 4°C and 20°C temperature was simply guided by the fact that some samples were prepared and stored at room temperature, and others were kept in the fridge at 4°C before SAXS measurements at room temperature due to experimental constraints.

For Fmoc-FFpY in presence of AP (and in absence of HA), we observe the formation of nanofibers homogeneously distributed in the hydrogel (Fig. 5b and Fig. S9). SAXS measurements ($0.010 < q < 0.30$ Å^{-1}) allow the determination of the form factor of these self-assemblies. The intensity can be fitted with a model of infinite cylinder of radius R ≈ 24 Å (Fig. 5b, red line and SI, Section 2, Part 2) that clearly reproduces the maximum at 0.2 Å^{-1} (first oscillation of the form factor). For larger q values ($0.30 < q < 1.00$ Å^{-1}), smaller distances are probed. A broad maximum is found around 0.43 Å^{-1}. It is related to the internal structure of the self-assembly and reveals a particular molecular

packing of the peptides in the nanofibers (characteristic distance ≈ 14.6 Å).

In presence of HA, the intensities at large scattering vectors (q > 0.12 Å^{-1}) are very similar to that of solely Fmoc-FFY generated from Fmoc-FFpY and AP (SI, Section 1, Part 3). The first oscillation of the form factor and the broad maximum are still visible ; only the background level, mainly originating from free polysaccharide segments in the hydrogels, is modified. The signature of the nanofibers is therefore unchanged indicating that the peptide self-assembly is unaltered by the polymer addition, a feature in full agreement with the previously described investigations. However, if the nanofibers remain identical in presence of HA, their dispersion state is clearly affected as revealed by the variation of the intensity below 0.12 Å^{-1}. The effective structure factor S*(q) (Fig. 5c and SI, Section 2, Part 4) related to their mutual arrangement shows distinct behaviors depending on the HA concentration (but also, on the storage temperature just after the sample preparation). For the lowest HA concentrations (4 mg/mL and 10 mg/mL), structure factor S*(q) shows two broad maxima around 0.043 - 0.08 Å^{-1} and 0.049 - 0.10 Å^{-1} respectively. These peaks are linked to the formation of bundles (large fibers) in which nanofibers align along a common direction and present a liquid-like order in the plane perpendicular to their main axis (nematic phase). The average distance d between the nanofibers can be estimated from the positions of the first maxima (d= $\frac{2\pi}{q}$) and clearly depends on the HA content. It decreases from d = 146 Å (HA : 4 mg/mL), i.e., about three times their diameter (2R ≈ 48 Å, R is the cylinder radius), to 128 Å (HA : 10 mg/mL). Peptide nanofibers are therefore not in contact in the bundles which consequently contain a large amount of water and HA according to previous CLSM experiments. For the highest HA concentration (20 mg/mL), the SAXS region is different and shows a series of three diffraction peaks that can be indexed with a two-dimensional hexagonal lattice (Fig. 5d). The addition of HA therefore leads to a 2D crystallization of the nanofibers in the plane perpendicular to the bundle direction (hexagonal columnar phase, lattice parameter a = 113 Å). Their separating distance d (d = a, Fig. 5e) is further reduced but keeps larger than their diameter (≈ 48 Å) : nanofibers are getting closer but are still not in contact. The width of the first diffraction peak can be used to estimate the diameter of the crystalline domains (SI Section 2, Part 4). A typical size of 4 μm is found in agreement with CLSM observations.

Composite supramolecular hydrogels stored at room temperature (instead of 4°C) show a similar behavior (SI, Section 1, Part 3 and Part 4). However, the average distance d is systematically larger, while the appearance of the hexagonal columnar phase is shifted to higher HA concentrations (Fig. 5e). Furthermore, the first maximum of the structure factor in the nematic phase is less pronounced and broader, indicating that the local order is reduced in the bundles.

The onset of the nematic and columnar organizations is very similar to the phase behavior found in lyotropic liquid crystals with rodlike nanoparticles. In these systems, the mesophase emerges from the shape anisotropy of the objects and their interactions of entropic (i.e. excluded volume) and/or electrostatic origin[45-49], leading to a rich phase diagram in concentration. In the present situation, the peptide concentration is constant and quite low (10 mg/mL, i.e. 1% w/v), no particular orientation of the nanofibers is expected in the absence of added polymer (isotropic phase). The observed structural ordering is triggered by the presence of HA which brings nanofibers together, increasing their local concentration, and leading to the formation of liquid crystalline bundles (Fig. 5f). Since polymer addition directly impacts the distance between nanofibers (and therefore their local concentration), it is possible to tune the nature of the mesophase and induce structural transition by changing the HA content. The peptide volume fraction Φ in the large fibers can be evaluated from the separation distance d (SI, Section 2, Part 4). The nanofibers volume fraction Φ in the hexagonal crystalline bundles can be deduced from geometrical arguments with the expression $\phi = \frac{2\pi}{\sqrt{3}} \times (\frac{R}{a})^2$, with R, the radius of the self-assemblies (R = 23.9 Å) and a, the lattice parameter. This expression can be generalized (with some approximation) to the nematic bundles (replacing a by d in the formula) if we assume a local 2D short range hexagonal organization in the bundle cross section. The global variation of the peptide volume fraction in the bundles is given in Fig. S11. It varies between 8% (lowest HA concentration) and 14% in the nematic phase (assuming a 2D short range hexagonal order) and increases to 16 - 20 % in the hexagonal crystalline phase. A peptide volume fraction Φ_{n-c} of about 15% ($d_{n-c} \approx 117$ Å) in the bundle is therefore required to induce the nematic to columnar phase transition, regardless of the thermal history of the samples.

5.4 Discussion about the mechanism responsible of the hyaluronic acid induced Fmoc-FFY peptide nanofibers organization

The process leading to the bundle formation and the ordering process is complex and depends on the nature of the polymer-nanofiber interaction. If the driving force is obviously related to the presence of HA, its strength is fixed by its concentration. These results are very similar to the depletion driven transitions observed in model rodlike particles suspensions such as tobacco mosaic virus (TMV)[50-52] or virus particles[53] in presence of non-adsorbing polymers (polysaccharide and polyethylene glycol). An attractive depletion interaction can indeed be observed when a depletant (HA) is added to a suspension of nanoparticles or nanofibers[54]. Since colloids are not penetrable objects, they create an

excluded shell in which the center of mass of the polymers cannot penetrate. When particles approach each other, their excluded volumes overlap and expel the macromolecules resulting in an imbalance osmotic pressure and a final net attraction. For charged particles, this attractive interaction may be balanced by repulsive electrostatic forces avoiding the formation of close packed aggregates. As observed with charged virus suspensions, this depletion interaction is responsible for the formation of liquid crystalline bundles composed of aligned particles, with an equilibrium spacing d that varies with the polymer concentration similarly to our system[50-53]. In addition, the power law variation $d \sim c^{-1/4}$ observed with TMV[50, 51] is very close to our experimental findings (Fig. 5e, insert). The diameter of these viruses (TMV : 18 nm, filamentous viruses infecting bacteria, such as fd type : 7 nm) are however larger than that of the Fmoc-FFY peptide self-assembled fibers (4.8 nm) while their contour lengths are extremely well defined (TMV : 300 nm, fd : 880 nm) leading to other possible morphologies[53] (platelets, smectic fibrils). Peptide nanofibers are much longer objects (several hundreds of micrometers long) with a persistence length of a few hundred nanometers. This results in different cluster sizes and shapes with possible interconnections as observed with particular DNA nanotubes[55]. To go further in the analysis, we determined the separating distance d between nanofibers in the bundles and its variation with polymer concentration by a theoretical approach based on pair potential interaction including a repulsive electrostatic and an attractive depletion contributions (SI, Section 1, Part 5)[50, 51]. The theoretical d values and their variation with polymer concentration are in close agreement with SAXS measurements (Fig. 5e) validating the role of the depletion interaction in the structural organization of peptide nanofibers / HA suspensions.

If the depletion acts as a key process for the bundle formation and the nanofiber ordering, it does not explain the presence of polysaccharides in the large fibers (CLSM experiments) and how their presence in the bundles is compatible with depletion forces. Free HA chains diffusing between the nanofibers is very unlikely since their exclusion from this region is precisely at the origin of the observed depletion effect. Another attractive interaction balancing the electrostatic repulsion between HA and peptide self-assemblies (both negatively charged) is required. MD simulations have suggested that hydrogen bonds between the Fmoc-FFY self-assembly and HA might be these forces. One can thus assume that the peptide nanofibers are decorated by adsorbed HA chains that might even form bridgind between fibers. It is then this entity that are pushed one to each other through depletion forces. This is schematically shown in Figure 6. This model could explain the larger radius of nanofibers determined through the calculation of the equilibrium distance between the nanofibers (SI, Section 2, Part 5). Using this model, the thickness could be of the order of 1-2 nm. It must be

reminded that most of the HA chains are free chains outside of the bundles. This is suggested by the high background level observed in the scattering curves when increasing HA concentration (SI, Section 2, Part 3) which is the signature of polysaccharide chains in solution : most of the polymer segments do not adsorb on the nanofibers and remain free in the surrounding environment. Second, if HA binds to peptides, they do not alter their self-assembly, neither form a dense homogeneous adsorbed layer on the surface of the nanofibers (core-shell structure). These situations would lead to new organizations with distinct measurable form factors[56]. Moreover polymers adsorbed on surfaces are known to exchange with those free in solution.[57, 58] This is exactly what we observe by FRAP experiments on our bundles.

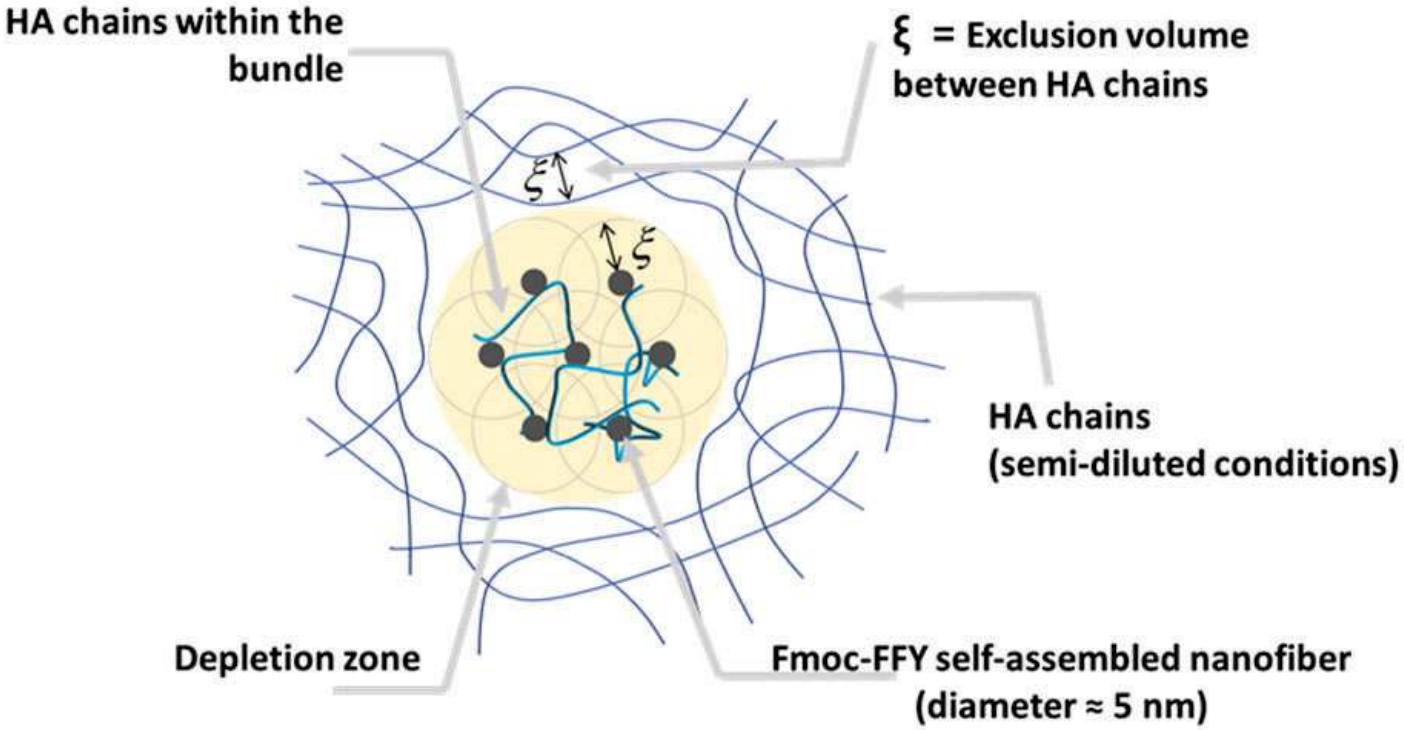

FIGURE 6 – Schematic of a perpendicular view of Fmoc-FFY peptide nanofibers (blue circles) in presence of HA chains (blue strings) which induces the bundle formation through an internal nanofiber organization thanks to both a depletion zone (yellow area) around the bundle and a shell-like layer of HA all along the self-assembled Fmoc-FFY nanofibers (light blue rings).

To the best of our knowledge, the mechanism behind this high structural ordering driven by polymer addition revealed with scattering techniques has never been highlighted so far with organic nanorods of self-assembled peptides. However, two recent contributions have reported this effect. First, Nisbet and Williams have investigated a similar chemical system composed of the pentapeptide Fmoc-FRGDF (R, arginine ; G, glycine ; D, aspartic acid) mixed with a negatively charged polysaccharide (fucoidan)[44]. If the microscale network, composed of fibrillar structures (i.e. small bundles of

nanofibers) became larger and aligned with addition of fucoidan, only a limited ordering of the nanofibers was observed by neutron scattering at high polymer content. No dependence of the separating distance on the polymer concentration was revealed. The underlying mechanism was rather attributed to molecular interaction between peptides and polysaccharides driving from nanofibrils to larger bundles. In a second study from Hudalla and coworkers, the authors show that glycosylated peptides mixed with different polymers formed bundles with well oriented nanofibers[59]. A nematic order parameter related to fiber orientation was determined from SAXS measurements, but no local structure factor or local organization was discussed. The lateral association between glycosylate nanofibers was promoted by specific attractive interactions tailored by complementary amino acids sequences.

6 Summary

We have studied the impact of HA on both the enzyme-assisted self-assembly of Fmoc-FFY and the spatial organization of the resulting self-assembled Fmoc-FFY nanofibers. The Fmoc-FFY self-assembly takes place by bringing a solution of phosphorylated precursor Fmoc-FFpY peptides in contact with AP in the presence of HA. Using CD, we found that HA does not modify the CD spectrum of the self-assembled Fmoc-FFY but that the different bands become weaker when the HA concentration is increased. In addition, the kinetics of self-assembly is not significantly affected by the presence of HA and by its concentration. Based on CLSM investigations, we observed the formation of micrometer thick bundles of nanofibers in the presence of HA with a co-localization of HA and the peptide self-assembly. These bundles are dynamic objects with constant exchange of HA. Molecular dynamic simulations of Fmoc-FFY peptides in the presence of oligosaccharide mimicking HA reveals that hydrogen bonds between the Fmoc-FFY self-assembly and HA are at the origin of their attractive interaction. Thus, HA does not affect the packing of the peptides at a molecular scale rising from the enzyme-assisted self-assembly process. Building on X-ray scattering analyses, we have highlighted the bundle organization constituted of peptide nanofibers alignment along a common direction leading to a nematic order. Induced by HA and controlled by the value of its concentration, this liquid-like order can switch to a 2D crystallization of nanofibers when HA concentration is still increased. However, these so-oriented nanofibers are never “sticked” one to the others since HA is interacting with the nanofibers even within the bundles. This transition of peptide nanofibers organization driven by the HA concentration can be explained by depletion effects, as

described in living systems such as protein or virus particle assemblies[50-53].

HA is highly used for cosmetic formulations, biomaterial designs or developments in the tissue engineering field for instance. In addition to its intrinsic features such as its biocompatibility, the presence of this natural polysaccharide also strongly impacts the microstructure organization and thus the mechanical properties of the resulting material. Even if it has been clearly established that the interaction between polysaccharide and self-assembled peptides is at the origin of this effect, the mechanism leading to this organization has been little explored so far. Herein, explanations based on depletion forces between the HA and peptide nanofibers are suggested for the first time on nano-objects using polymers partially adsorbing on self-assembled peptide nanofibers.

In the framework of future developments, it would be of great interest to investigate the effect of lower molar masses of HA, the nature of the polysaccharide involved and more generally, the impact of different polyelectrolytes and uncharged polymers such as polyethylene glycols. SAXS measurements at various temperatures will be also studied. Finally, since peptide self-assembly can also be generated by annealing, the role of the enzyme, i.e. AP, should also be investigated.

References

(1) Du, X.; Zhou, J.; Shi, J.; Xu, B. *Chemical Reviews* **2015**, *115*, 13165-13307.

(2) Reches, M.; Gazit, E. *Nature Nanotechnology* **2006**, *1*, 195-200.

(3) Draper, E. R.; Adams, D. J. *Langmuir* **2019**, DOI : 10.1021/acs.langmuir.9b00716.

(4) Yang, Z.; Gu, H.; Fu, D.; Gao, P.; Lam, J. K.; Xu, B. *Advanced Materials* **2004**, *16*, 1440-1444.

(5) Jayawarna, V.; Ali, M.; Jowitt, T. A.; Miller, A. F.; Saiani, A.; Gough, J. E.; Ulijn, R. V. *Advanced Materials* **2006**, *18*, 611-614.

(6) Jayawarna, V.; Smith, A.; Gough, J. E.; Ulijn, R. V. *Biochemical Society Transactions* **2007**, *35*, 535-537.

(7) Jayawarna, V.; Richardson, S. M.; Hirst, A. R.; Hodson, N. W.; Saiani, A.; Gough, J. E.; Ulijn, R. V. *Acta Biomaterialia* **2009**, *5*, 934-943.

(8) Yang, Z.; Liang, G.; Xu, B. *Soft Matter* **2007**, *3*, 515-520.

(9) Liebmann, T.; Rydholm, S.; Akpe, V.; Brismar, H. *BMC Biotechnology* **2007**, *7*, 1-11.

(10) Zhang, Y.; Kuang, Y.; Gao, Y.; Xu, B. *Langmuir* **2011**, *27*, 529-537.

(11) Huang, R.; Qi, W.; Feng, L.; Su, R.; He, Z. *Soft Matter* **2011**, *7*, 6222-6230.

(12) Cornwell, D. J.; Smith, D. K. Expanding the scope of gels - Combining polymers with low-molecular-weight gelators to yield modified self-assembling smart materials with high-tech applications, 2015.

(13) Shmidov, Y.; Zhou, M.; Yosefi, G.; Bitton, R.; Matson, J. B. *Soft Matter* **2019**, *15*, 917-925.

(14) Nadernezhad, A.; Forster, L.; Netti, F.; Adler-Abramovich, L.; Tessmar, J.; Groll, J. *Polymer Journal* **2020**, *52*, 1007-1012.

(15) Capito, R. M.; Azevedo, H. S.; Velichko, Y. S.; Mata, A.; Stupp, S. I. *Science* **2008**, 1812-1816.

(16) Aviv, M.; Halperin-Sternfeld, M.; Grigoriants, I.; Buzhansky, L.; Mironi-Harpaz, I.; Seliktar, D.; Einav, S.; Nevo, Z.; Adler-Abramovich, L. *ACS Applied Materials & Interfaces* **2018**, *10*, 41883-41891.

(17) Halperin-Sternfeld, M.; Ghosh, M.; Sevostianov, R.; Grigoriants, I.; Adler-Abramovich, L. *Chemical Communications* **2017**, *53*, 9586-9589.

(18) López-Moreno, A.; Torres-Sánchez, A.; Acuña, I.; Suárez, A.; Aguilera, M. *International Journal of Molecular Sciences* **2021**, *22*, 1-12.

(19) Varela-Aramburu, S.; Su, L.; Mosquera, J.; Morgese, G.; Schoenmakers, S. M.; Cardinaels, R.; Palmans, A. R.; Meijer, E. W. *Biomacromolecules* **2021**, *22*, 4633-4641.

(20) Fores, J. R.; Bigo-Simon, A.; Wagner, D.; Payrastre, M.; Damestoy, C.; Blandin, L.; Boulmedais, F.; Kelber, J.; Schmutz, M.; Rabineau, M.; Criado-Gonzalez, M.; Schaaf, P.; Jierry, L. *Polymers* **2021**, *13*, 1793.

(21) Wang, W.; Qian, J.; Tang, A.; An, L.; Zhong, K.; Liang, G. *Analytical Chemistry* **2014**, *86*, 5955-5961.

(22) Vigier-Carrière, C.; Garnier, T.; Wagner, D.; Lavalle, P.; Rabineau, M.; Hemmerlé, J.; Senger, B.; Schaaf, P.; Boulmedais, F.; Jierry, L. *Angewandte Chemie - International Edition* **2015**, *54*, 10198-10201.

(23) Mertz, D.; Vogt, C.; Hemmerlé, J.; Mutterer, J.; Ball, V.; Voegel, J. C.; Schaaf, P.; Lavalle, P. *Nature Materials* **2009**, *8*, 731-735.

(24) Pearlman, D. A.; Case, D. A.; Caldwell, J. W.; Ross, W. S.; Cheatham, T. E.; DeBolt, S.; Ferguson, D.; Seibel, G.; Kollman, P. *Computer Physics Communications* **1995**, *91*, 1-41.

(25) Maier, J. A.; Martinez, C.; Kasavajhala, K.; Wickstrom, L.; Hauser, K. E.; Simmerling, C. *Journal of Chemical Theory and Computation* **2015**, *11*, 3696-3713.

(26) Joung, I. S.; Cheatham, T. E. *Journal of Physical Chemistry B* **2008**, *112*, 9020-9041.

(27) Kirschner, K.; Yongye, A.; Tschampel, S. *J Comput Chem2* **2008**, *29*, 622-655.

(28) Jorgensen, W. L.; Chandrasekhar, J.; Madura, J. D.; Impey, R. W.; Klein, M. L. *The Journal of Chemical Physics* **1983**, *79*, 926-935.

(29) Bayly, C. I.; Cieplak, P.; Cornell, W. D.; Kollman, P. A. *Journal of Physical Chemistry* **1993**, *97*, 10269-10280.

(30) Berendsen, H. J.; Postma, J. P.; Van Gunsteren, W. F.; Dinola, A.; Haak, J. R. *The Journal of Chemical Physics* **1984**, *81*, 3684-3690.

(31) Tocci, G.; Joly, L.; Michaelides, A. *Nano Letters* **2014**, *14*, 6872-6877.

(32) Thornton, K.; Abul-Haija, Y. M.; Hodson, N.; Ulijn, R. V. *Soft Matter* **2013**, *9*, 9430-9439.

(33) Muller, C.; Ontani, A.; Bigo-Simon, A.; Schaaf, P.; Jierry, L. *Advances in Colloid and Interface Science* **2022**, *304*, 102660.

(34) Zhou, J.; Du, X.; Li, J.; Yamagata, N.; Xu, B. *Journal of the American Chemical Society* **2015**, *137*, 10040-10043.

(35) Baillet, J.; Gaubert, A.; Verget, J.; Latxague, L.; Barthélémy, P. *Soft Matter* **2020**, *16*, 7648-7651.

(36) Martin, A. D.; Wojciechowski, J. P.; Robinson, A. B.; Heu, C.; Garvey, C. J.; Ratcliffe, J.; Waddington, L. J.; Gardiner, J.; Thordarson, P. *Scientific Reports* **2017**, *7*, 1-6.

(37) Wang, Z.; Liang, C.; Shang, Y.; He, S.; Wang, L.; Yang, Z. *Chemical Communications* **2018**, *54*, 2751-2754.

(38) Yi, M.; Guo, J.; He, H.; Tan, W.; Harmon, N.; Ghebreyessus, K.; Xu, B. *Soft Matter* **2021**, *17*, 8590-8594.

(39) Qin, X.; Wenchun, X.; Tian, S.; Cai, J.; Yuan, H.; Zheng, Y.; Butterfoss, G. L.; Khuong, A. C.; Gross, R. A. *Chemical Communications* **2013**, *49*, 4839-4841.

(40) Williams, R. J.; Gardiner, J.; Sorensen, A. B.; Marchesan, S.; Mulder, R. J.; McLean, K. M.; Hartley, P. G. *Australian Journal of Chemistry* **2013**, *66*, 572.

(41) Yang, Z.; Xu, B. *Chemical Communications* **2004**, *1*, 2424-2425.

(42) Adhikari, B.; Nanda, J.; Banerjee, A. *Soft Matter* **2011**, *7*, 8913-8922.

(43) Yang, Z.; Gu, H.; Fu, D.; Gao, P.; Lam, J. K.; Xu, B. *Advanced Materials* **2004**, *16*, 1440-1444.

(44) Li, R.; Boyd-Moss, M.; Long, B.; Martel, A.; Parnell, A.; Dennison, A. J.; Barrow, C. J.; Nisbet, D. R.; Williams, R. J. *Scientific Reports* **2017**, *7*, 1-8.

(45) Vroege, G. J.; Lekkerkerker, H. N. *Reports on Progress in Physics* **1992**, *55*, 1241-1309.

(46) Grelet, E. *Physical Review Letters* **2008**, *100*, 1-4.

(47) Grelet, E. *Physical Review X* **2014**, *4*, 1-8.

(48) Grelet, E.; Rana, R. *Soft Matter* **2016**, *12*, 4621-4627.

(49) Paineau, E.; Krapf, M. E. M.; Amara, M. S.; Matskova, N. V.; Dozov, I.; Rouzière, S.; Thill, A.; Launois, P.; Davidson, P. *Nature Communications* **2016**, *7*, 1-8.

(50) Imai, M.; Urakami, N.; Nakamura, A.; Takada, R.; Oikawa, R.; Sano, Y. *Langmuir* **2002**, *18*, 9918-9923.

(51) Li, T.; Zan, X.; Winans, R. E.; Wang, Q.; Lee, B. *Angewandte Chemie - International Edition* **2013**, *52*, 6638-6642.

(52) Li, T.; Zan, X.; Sun, Y.; Zuo, X.; Li, X.; Senesi, A.; Winans, R. E.; Wang, Q.; Lee, B. *Langmuir* **2013**, *29*, 12777-12784.

(53) Sung, B.; Wensink, H. H.; Grelet, E. *Soft Matter* **2019**, *15*, 9520-9527.

(54) Asakura, S.; Oosawa, F. Interaction between particles suspended in solutions of macromolecules, 1958.

(55) Glaser, M.; Schnauss, J.; Tschirner, T.; Schmidt, B. U.; Moebius-Winkler, M.; Käs, J. A.; Smith, D. M. *New Journal of Physics* **2016**, *18*, DOI : 10.1088/1367-2630/18/5/055001.

(56) Criado-Gonzalez, M.; Wagner, D.; Rodon Fores, J.; Blanck, C.; Schmutz, M.; Chaumont, A.; Rabineau, M.; Schlenoff, J. B.; Fleith, G.; Combet, J.; Schaaf, P.; Jierry, L.; Boulmedais, F. *Chemistry of Materials* **2020**, *32*, 1946-1956.

(57) Sukhishvili, S. A.; Granick, S. *Journal of Chemical Physics* **1998**, *109*, 6869-6878.

(58) Pefferkorn, E.; Haouam, A.; Varoqui, R. *Macromolecules* **1989**, *22*, 2677-2682.

(59) Restuccia, A.; Seroski, D. T.; Kelley, K. L.; O'Bryan, C. S.; Kurian, J. J.; Knox, K. R.; Farhadi, S. A.; Angelini, T. E.; Hudalla, G. A. *Communications Chemistry* **2019**, *2*, DOI : 10.1038/s42004-019-0154-z.

Supporting Information

Figure S1

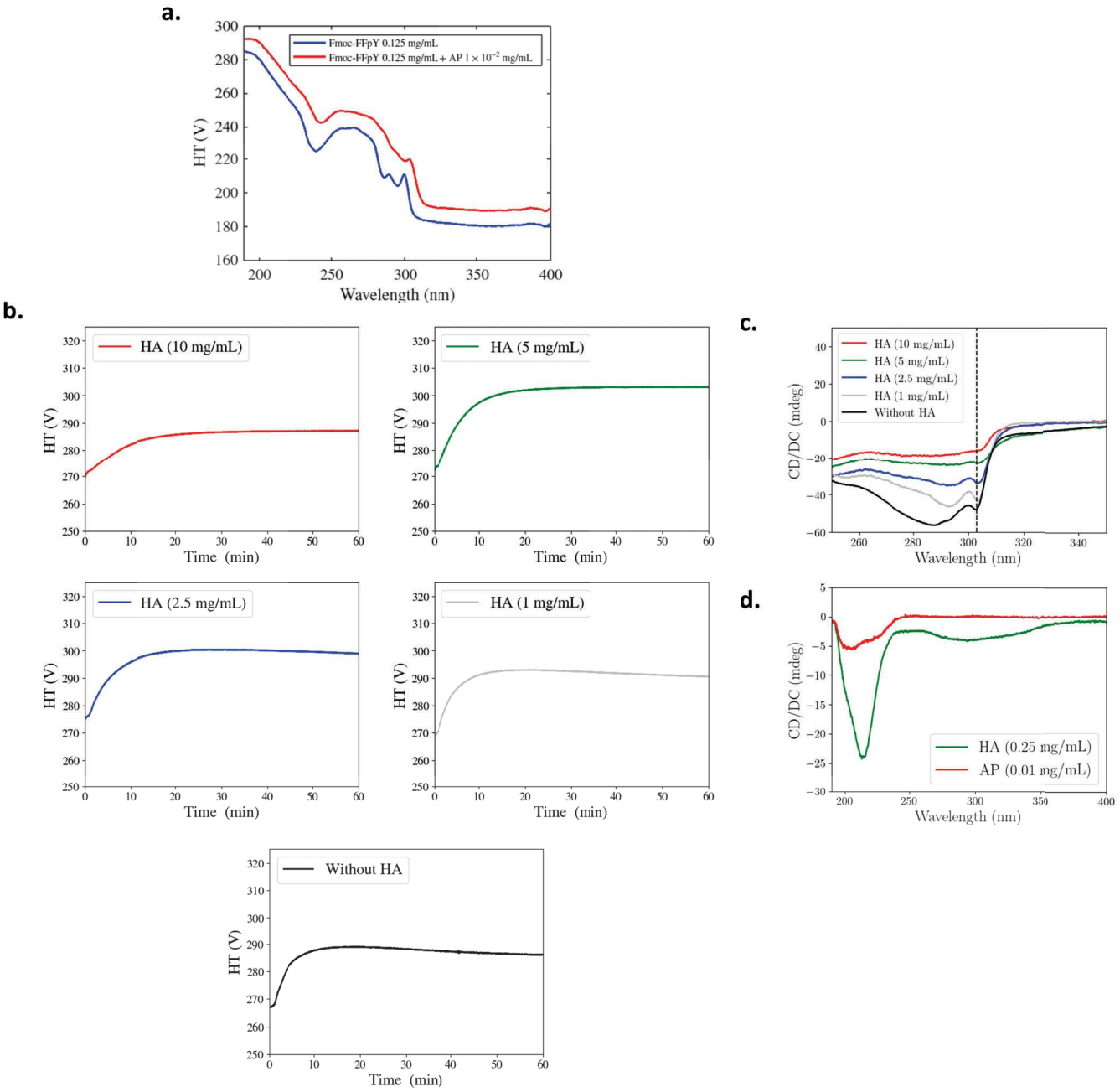

High voltage values corresponding to the circular dichroism (CD) measurements shown in Figures (a) 1b and (b) 1c in the manuscript. The photomultiplier tube voltage was measured concomitantly as the CD spectra to ensure reliable results providing the voltage kept below 500 V [1]. (c) CD spectra between 250 and 350 nm showing the position of the band at 303 nm after 60 min from a mixture of Fmoc-FFpY (0.125 mg/mL), AP (0.01 mg/mL) and various concentrations of HA (0, 1, 2.5, 5 and 10 mg/mL). (d) Control CD spectra of HA and AP.

Figure S2

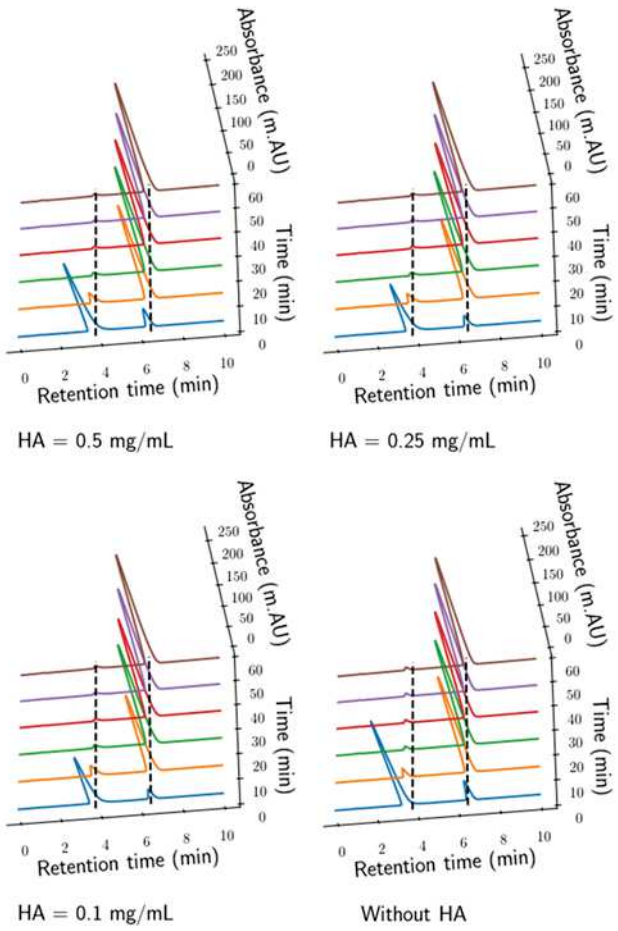

Conversion of Fmoc-FFY from Fmoc-FFpY (0.125 mg/mL) in presence of AP (0.01 mg/mL) and various concentrations of HA (0.1, 0.25 and 0.5 mg/mL). This monitoring overtime has been performed through HPLC analyses (UV lamp detection system, absorbances measured at 280 nm). Retention time of Fmoc-FFpY 3.9 min ; Retention time of Fmoc-FFY : 6.2 min..

HPLC was carried out with an Agilent 1100 Series system equipped with a UV-lamp detector system. The column was an Interchim Serie 191911 C18-HQSUM reversed-phase column (US5C18HQ-100/046, 100 x 4,6 mm, pore size 20 Å). The mobile phase contains 55% of ultrapure water purified with the MilliQ system from Merck (which contains 0,1% of TFA) and 45% of HPLC grade acetonitrile and is kept in that ratio during all the elution. Each measurement lasted 1h with 6 injections each separated by 10 min. The Fmoc-FFpY and Fmoc-FFY were detected by absorbance measurements at 280 nm. Each solution was freshly prepared with a fresh 25 mM Borax solution in a 0.25 mL HPLC glass insert placed in a 1 mL HPLC vial. Identical CD's concentrations are used, but only 0 mg/mL, 0.1 mg/mL (0.224×10^{-6} mol/L), 0.25 mg/mL (0.560×10^{-6} mol/L) and 0.5 mg/mL (1.12×10^{-6} mol/L) for the HA.

Figure S3

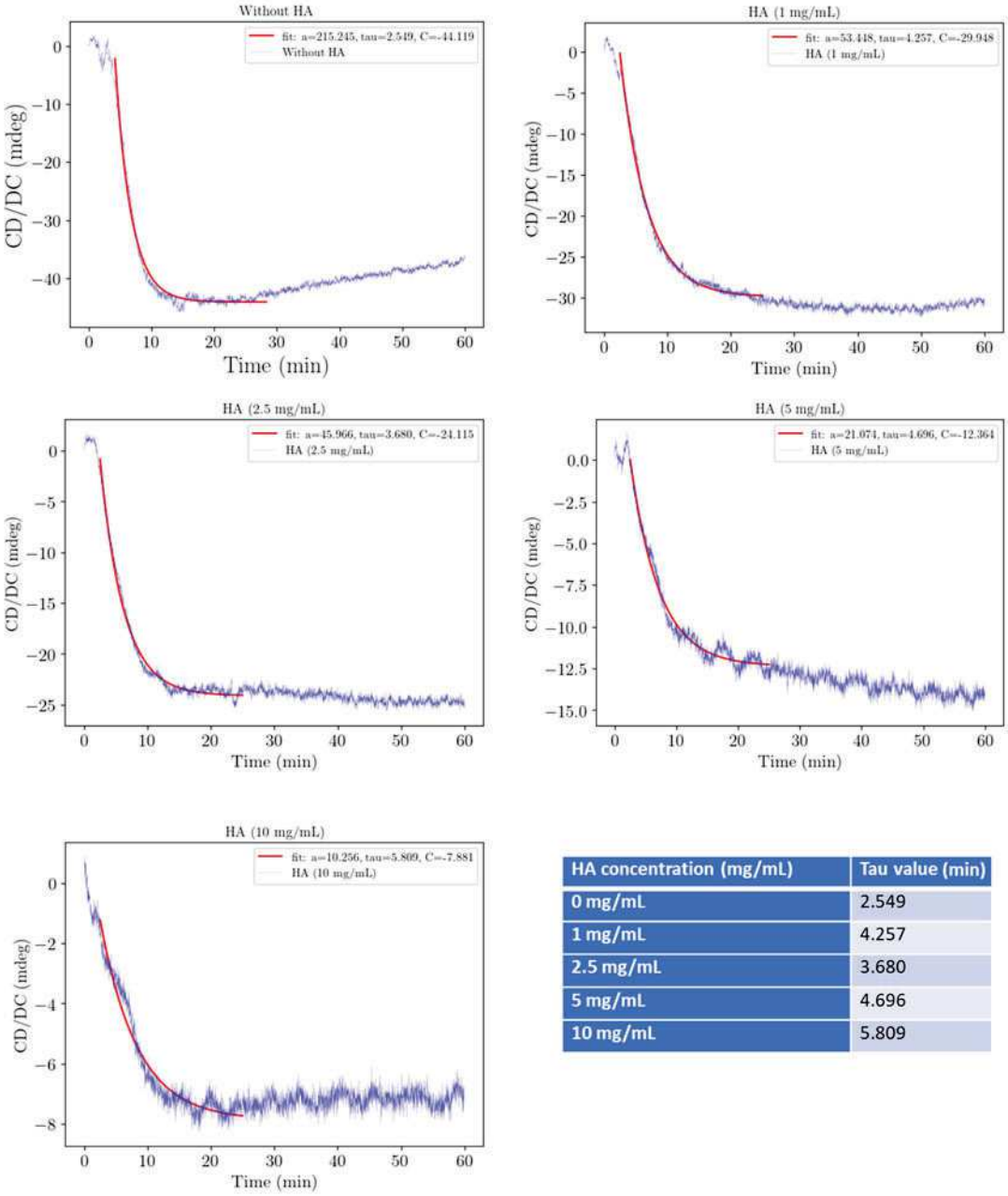

HA concentration (mg/mL)	Tau value (min)
0 mg/mL	2.549
1 mg/mL	4.257
2.5 mg/mL	3.680
5 mg/mL	4.696
10 mg/mL	5.809

We have fitted the ellipticity evolution over time of the different curves which correspond to different concentrations of HA (from 1, 2.5, 5 to 10 mg/mL, and without HA). In first approximation, each curve can be modelized by $\theta(t) = \theta_0 exp(-t/\tau)$ *where* τ *represents the characteristic time over which the Fmoc group superhelical arrangement takes place (used as an internal probe of the self-assembly). All graphs and their fits are shown below and all* τ *values are summarized in the table.*

Figure S4

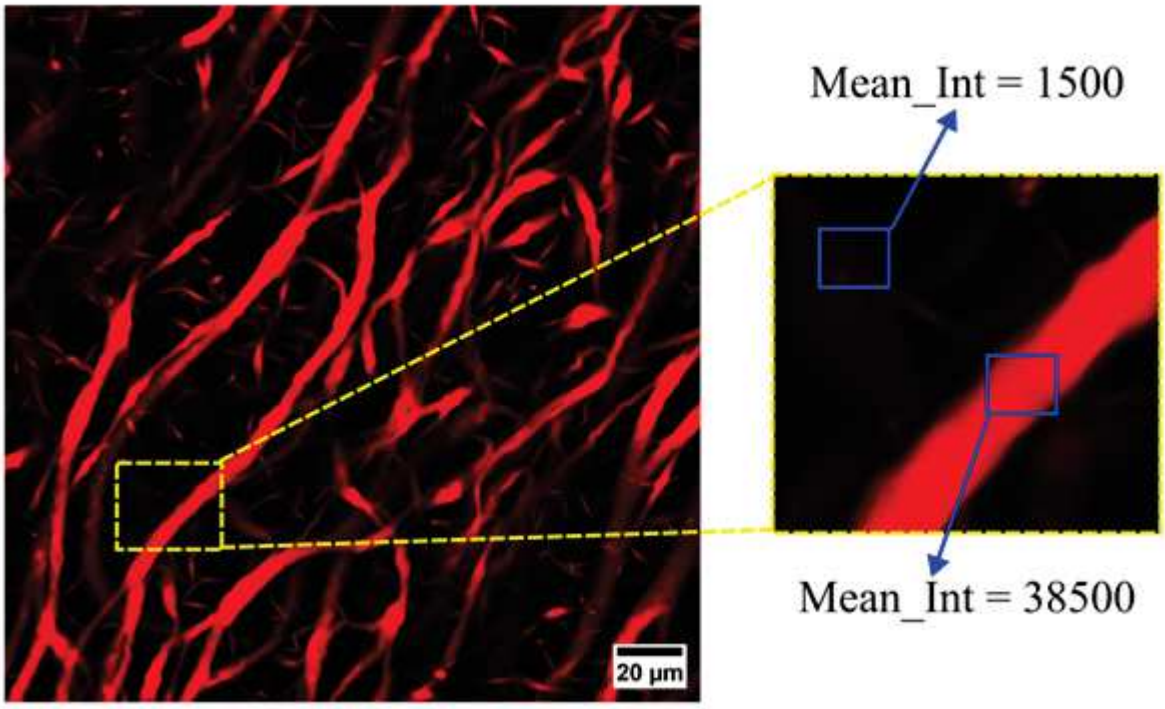

Quantification of the fluorescence intensity (arbitrary units) in the space between the bundles and from the bundle, realized by CLSM.

Figure S5

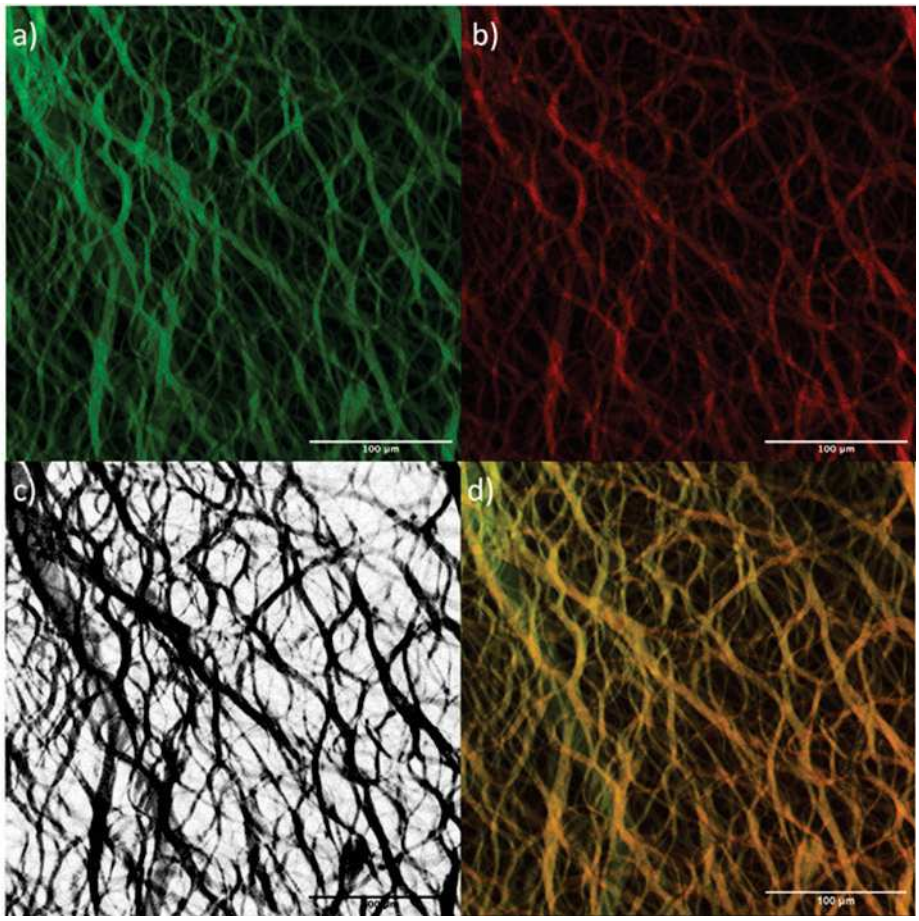

Colocalization analysis of CLSM images obtained from a mixture constituted of HA^{RHO} (10 mg/mL), Fmoc-FFpY (10 mg/mL) and AP 0.4 mg/mL in presence of ThT (0.5 mg/mL). In the images given below, the localization of hyaluronic acid is realized through the red coulour emission of rhodamine-labelled HA^{RHO} (b) and the peptide Fmoc-FFY self-assembly is revealed by ThT green colour emission (a). A correlation image is realized in (c) : when an overlap between the red and green colour occurs, it results in a black coulour. Otherwise, white colour appears. We thus observe a black pattern (c) fully similar to the red (b) and to the green (b) one. An overlap of the red image (b) and the green one (a) leads to the yellow one (d), identical to the correlation image (c).

Figure S6 *CLSM control experiments to evaluate the impact of the dyes on the bundle's formation.* HA^{RHO} (10 mg/mL) was mixed with AP (0.4 mg/mL) and Fmoc-FFpY (10 mg/mL) in absence of ThT, and immediately analyzed by confocal microscopy. As observed in the typical image shown below, bundles are formed as well in absence of ThT. These bundles look very much like those obtained in presence of ThT (see Figure 2 in the manuscript).

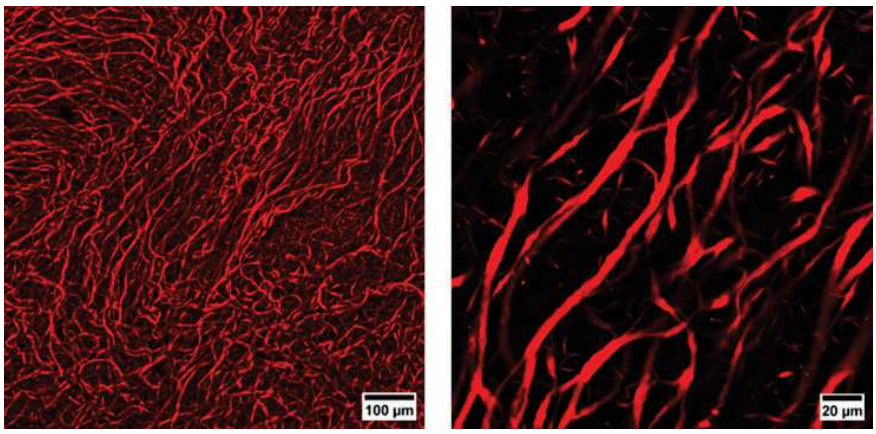

HA^{RHO}(10 mg/mL) was mixed with AP (0.4 mg/mL) and ThT (0.5 mg/mL) in absence of Fmoc-FFpY. Except the presence of some black bubbles, a homogeneous red colour is observed as shown in the typical image below, high-lighting that HA^{RHO} are not forming bundles alone (without peptides). Moreover, ThT is not fluorescing in absence of peptides.

Figure S7

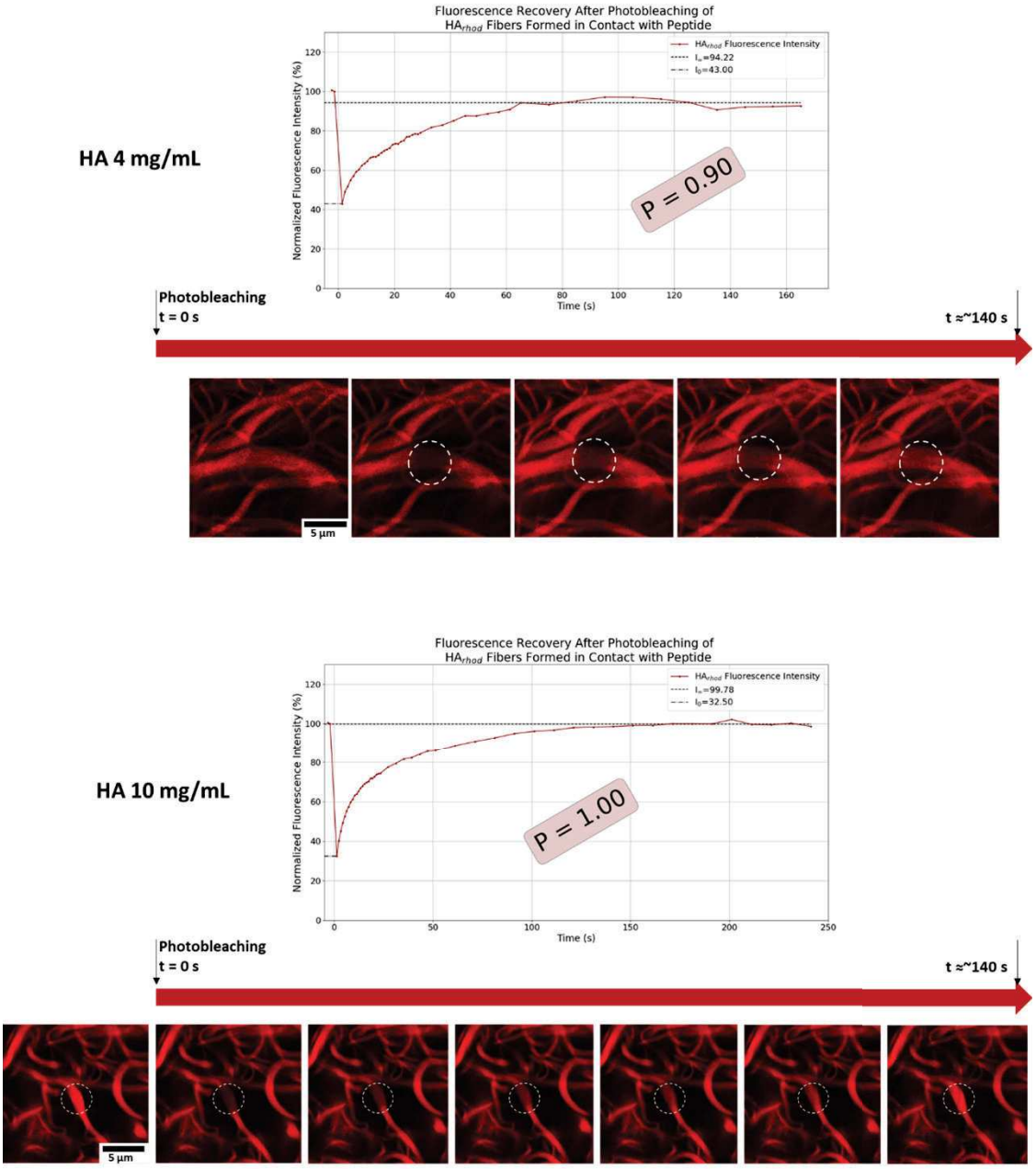

Typical fluorescence recovery after photobleaching (FRAP) over time of HA^{RHO} *(4 or 10 mg/mL) localized on the Fmoc-FFY bundles of peptide nanofibers. P means the relative amount of fluorescence recovery. The coefficient diffusion measured is 1.03 and 1.07* $\mu m^2.S^{-1}$ *for 4 and 10 mg/mL of HA concentration respectively.*

Figure S8

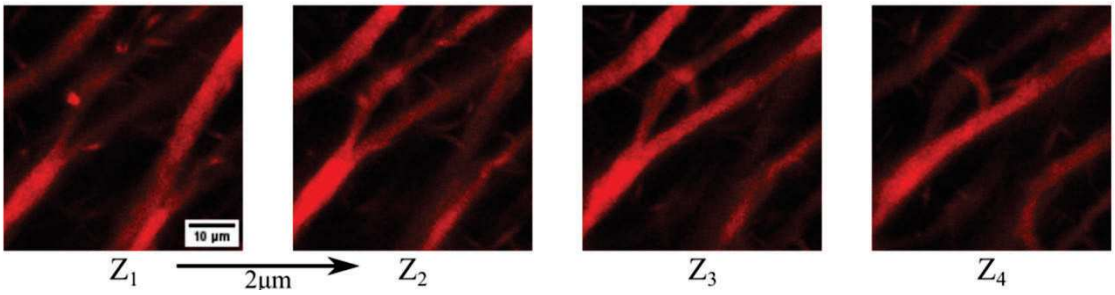

A typical z-stack series is given below and shows that the red colour of HA^{RHO} is homogeneously distributed inside the bundle for each image separated one from the other by 2 µm. This experiment demonstrates that hyaluronic acid is not only adsorbed on the exterior surface of the bundles but present all inside the bundles.

SECTION 1 : SAXS-WAXS investigations

Part 1 - X-ray scattering experiments

Small- and Wide-Angle X-ray Scattering experiments (SAXS, WAXS) were performed on the X-ray scattering platform DiffériX of the Institut Charles Sadron (Strasbourg) using two diffractometers installed on the two ports of a Rigaku rotating anode generator (MicromaxTM- 007 HF, operating power 40 kV - 30 mA, wavelength λ = 1.54 Å). The beam was monochromatized and collimated with a confocal Max-Flux OpticsTM mirror (Osmics, Inc.) combined to a system of two (WAXS setup) or three (SAXS setup) pinholes. The scattered intensity was collected on a 2D multiwires detector (Rigaku) located at 81 cm from the sample position (SAXS setup), or on a Pilatus 3R 300K detector (Dectris Ltd., Switzerland) with a sample - detector distance of 20 cm (WAXS setup). The combination of these two instruments allowed to explore a scattering vector range from q = 0.01 to 1.00 $Å^{-1}$ ($q = \frac{4\pi}{\lambda} sin\theta$, where 2θ is the scattering angle).

Data reduction was performed according to usual procedures for isotropic scattering (angular averaging, electronic background, sample transmission and thickness corrections). q vectors were calibrated with a silver behenate powder diffractogram. Intensities were converted into absolute scale using a calibrated Lupolen standard. All experiments were performed at room temperature. Liquid samples and gels were introduced in sample holders made of two thin calibrated mica windows 1 mm apart. Samples measurements were finally corrected from the solvent contribution (Borax) according to their volume fraction, yielding the scattering cross section per unit volume of the solute I(q).

Experiments were carried out on two series of samples stored at two different temperatures after

preparation. The first set of solutions and gels was kept at 4°C for one week before measurements. The second set of samples was left at room temperature and measured 24 h later. For both series, all gels were kept in their sample holder at room temperature and regularly measured over a period of 7 days to ensure the absence of intensity variation (equilibrium state).

Complementary measurements were conducted on the SWING beamline of the SOLEIL Synchrotron (Saint-Aubin, France) on samples requiring higher resolution. Measurements were carried out at an X-ray beam energy E = 12 keV (λ = 1.03 Å) with two sample-to-detector distances of 6.481 m and 0.783 m (0.0016 < q < 1 $Å^{-1}$). The scattered intensity was recorded at room temperature on a Eiger 4M detector (Dectris Ltd., Switzerland) using borosilicate capillaries (diameter 1.8 mm) as sample containers. Data correction was done as mentioned just above using the software Foxtrot developed at the beamline.

Part 2 - Nanofibers characterization

Note : A hydrogel sample prepared from Fmoc-FFpY, AP and HA at various concentrations, has to be unambiguously identified. For instance, a hydrogel prepared from the mixture of 10 6 mg/mL of Fmoc-FFpY, 0.4 mg/mL of AP and 10 mg/mL of HA is labelled "P 10 AP 0.4 HA 10".

Small angle X-rays scattering allows to reveal the shape and the dispersion state of the nanofibers in solution (or gel). For an isotropic suspension of monodisperse elongated particles in a solvent, the scattered intensity I(q) writes (in first approximation)

$$I(q) = \Phi_v V_p \Delta\rho^2 P(q) S(q) \tag{6.2}$$

where V_p is the volume of the particles, Φ_v their volume fraction, $P(q)$ their normalized form factor (related to their shape and size), and $S(q)$ their structure factor (associated to their dispersion state). $\Delta\rho$ is the difference of scattering length densities between the particles and the solvent.

When interactions between scattering objects are negligible (highly diluted systems, screened interactions...), S(q) = 1 and the intensity only reflects the shape and size of the particles through their form factor P(q). This situation applies for nanofibers in absence of added polymer. Since the self-assemblies are several micrometers long, their global shape is not accessible with SAXS (limited q range) and only their cross section can be evaluated. The scattered intensity for an isotropic dispersion of infinite cylinders of radius R and homogeneous scattering length density in a solvent

can be written :

$$I(q) = 4\pi^2 \Phi_v R^2 \Delta\rho^2 \frac{(\frac{J_1(qR)}{qR})^2}{q} \propto J_1 \frac{qR^2}{q^3} \tag{6.3}$$

where J1 is the cylindrical Bessel function of order one.

The fit of the data (without HA) was performed with this theoretical expression to determine the diameter of the nanofibers (P 10 AP 0.4) in Borax buffer. Modeling was done in Igor Pro 6.0 using the NCNR SANS package[2] on a restricted q-range (0.01 - 0.3 $Å^{-1}$). Scattered intensities from samples kept at 4°C (8 days) and at room temperature (1 days) are very similar and lead to identical results (Fig. S4).

A radius of 23.9 ± 0.2 Å is found in accordance with cryo-TEM measurements (diameter ≈ 5 nm, Fig. 4a in the manuscript). The maximum at 0.2 $Å^{-1}$ corresponds to the first oscillation of P(q) while the minima at 0.15 and 0.3 $Å^{-1}$, to the first zeros of the scattering function. These characteristics are thus strong indicators for the shape of the particles.

Figure S9

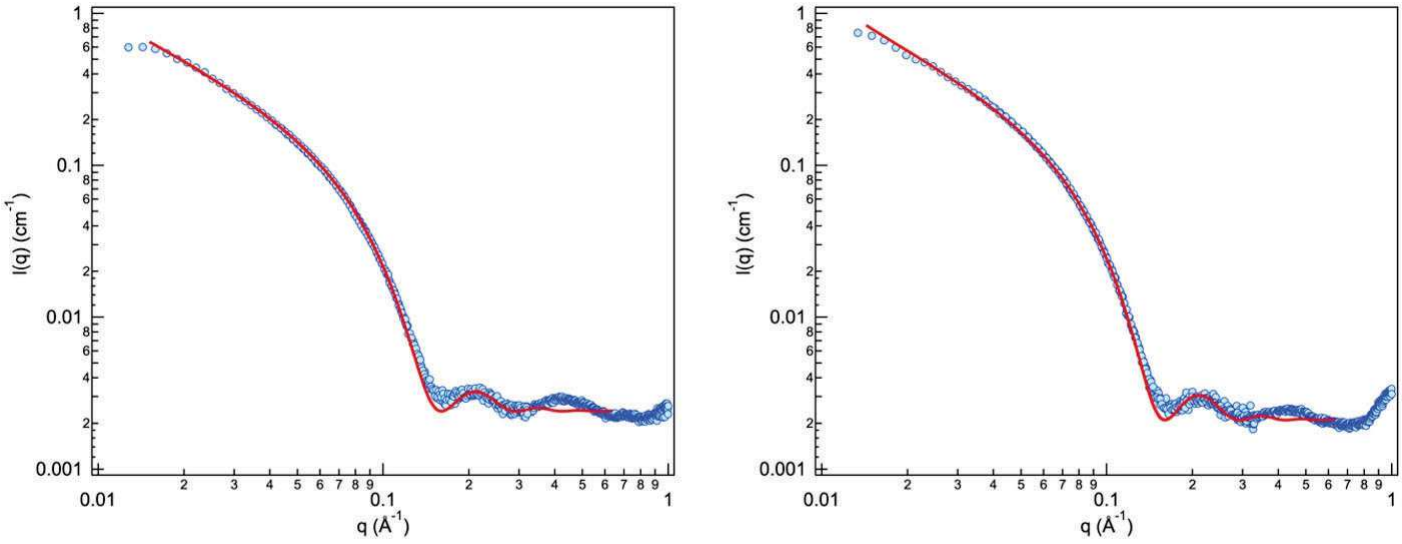

SAXS intensity for Fmoc-FFY self-assembly (Fmoc-FFpY 10 mg/mL, AP 0.4 mg/mL). Red line : fit using a model of infinite homogenous cylinder. The nanofibers have a radius of 23.9 ± 0.2 Å. (a) Sample kept at 4°C for 8 days before measurement. (b) Sample kept at room temperature for 1 day before measurement.

Part 3 - Nanofibers with addition of HA

In presence of HA, the interpretation of the scattering curves is more complex. The respective contributions of the peptides and the polysaccharides to the total scattering (partial structure functions) cannot be determined separately. Furthermore, a cross-term can also contribute depending on the interaction between the two species and their mutual organization.

Samples with HA show similar behaviors regardless of their thermal history before measurements.

The scattering curves (Fig. S5a and Fig. S6a) roughly show the signature of the nanofibers already observed on pure Fmoc-FFY self-assembly above 0.12 $Å^{-1}$ (Fig. S4), i.e., an oscillation at 0.2 $Å^{-1}$ (form factor) and a maximum around 0.43 $Å^{-1}$ (internal structure). These features are however less pronounced with higher polysaccharide content due to a larger background contribution. The slope of this background (log-log scale representation) reproduces that observed for pure HA solutions (color lines) probably revealing the presence of numerous free polysaccharide segments in the gels. To highlight the contribution of the nanofibers alone (neglecting the cross-term), a fraction of the intensity of pure HA solutions was subtracted from the peptide-HA measurements. The corresponding

intensity I*(q) (Fig. S5b and Fig. S6b) clearly evidences the same high q characteristics as those observed for pure Fmoc-FFY selfassembly above 0.12 $Å^{-1}$ (blue curve) and related to the geometrical properties of the nanofibers and their internal structure. The shape of the nanofibers as well as the internal peptide organization are therefore not really impacted by the addition of HA (regardless of the storage temperature of the sample). Only their dispersion state (visible below 0.12 $Å^{-1}$) is significantly changed.

Figure S10

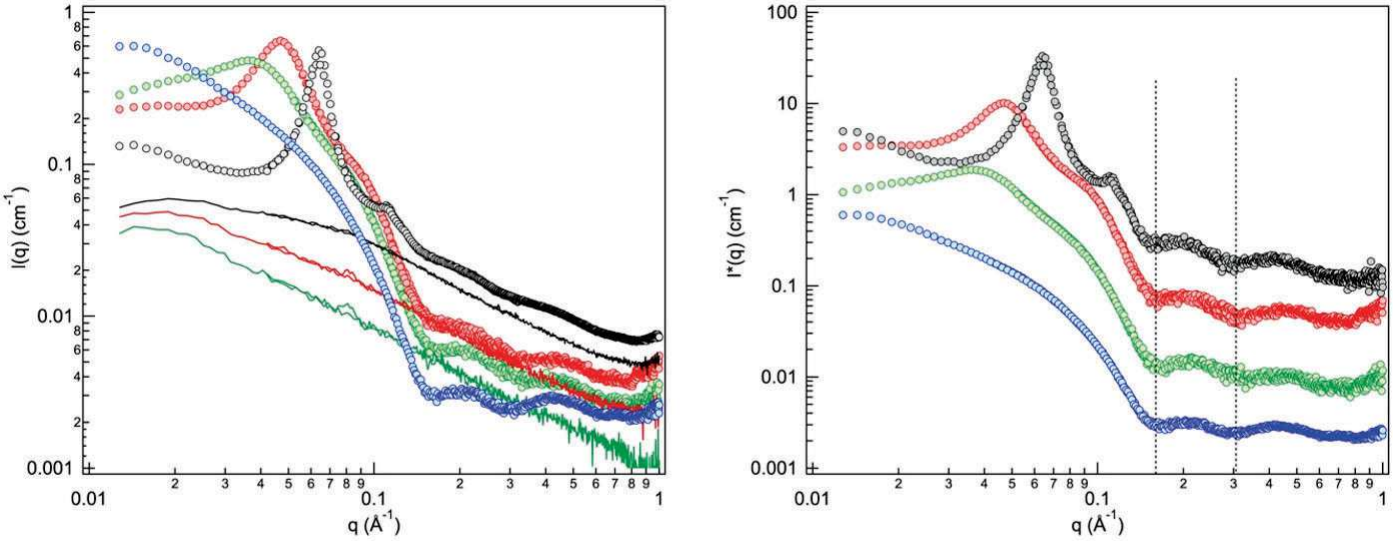

a) *b)*

Samples kept at 4°C for 8 days before measurements. (a) Scattered intensity I(q) : P10 AP0.4 (blue circles), P10 AP0.4 HA4 (green circles), P10 AP0.4 HA10 (red circle), AP0,4 HA20 (black circles), HA4 (green line), HA10 (red line), HA20 (black line). (b) I(q) P10 AP0.4 (blue circles) and I(q) : P10 AP0.4 HA4 (green circles), P10 AP0.4 HA10 (red circle), P10 AP0.4 HA20 (black circles). A multiplicative coefficient is applied for a better visibility (P10 AP0.4 HA4 : ×4, P10 AP0,4 HA10 : ×16, P10 AP0.4 HA20 : ×64). The two vertical dotted lines are guide for the eye to visualize the position of the two first minima of the nanofibers form factor.*

Figure S11

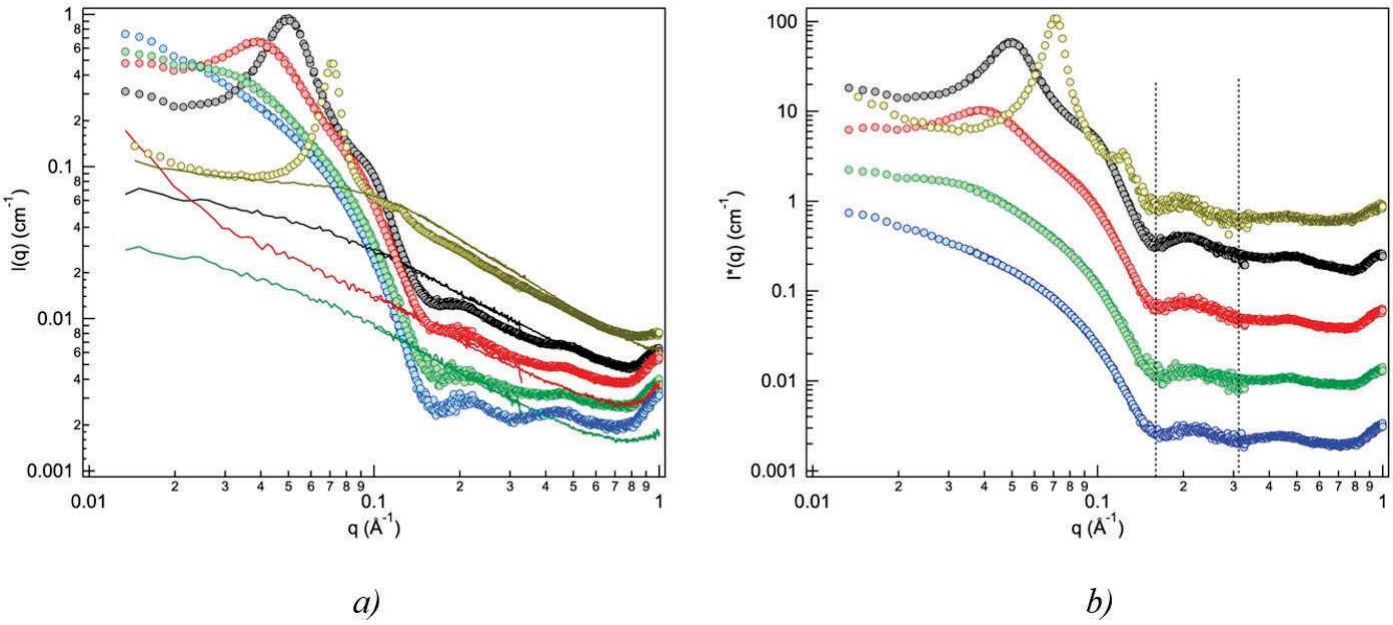

Samples kept at room temperature for 1 day before measurements. (a) Scattered intensity I(q) : P10 AP0.4 (blue circles), P10 AP0.4 HA4 (green circles), P10 AP0.4 HA10 (red circles), AP0.4 HA20 (black circle), HA4 (green line), HA10 (red line), HA20 (black line), HA30 (yellow line). (b) I(q) P10 AP0.4 (blue circles) and I(q) : P10 AP0.4 HA4 (green circles), P10 AP0.4 HA10 (red circle), P10 AP0.4 HA20 (black circle), P10 AP0.4 HA30 (yellow circle). A multiplicative coefficient is applied for a better visibility (P10 AP0.4 HA4 : ×5, P10 AP0.4 HA10 : ×25, P10 AP0.4 HA20 : ×125). The two vertical dotted lines are guide for the eye to visualize the position of the two first minima of the nanofiber form factor.*

Part 4 - Structure factor with addition of HA

The dispersion state of the nanofibers (q < 0.12 Å^{-1}) in the gel can be discussed directly from the scattering curves I(q), but also, for more accurate conclusions, from the structure factor S(q). Considering that the previous intensity I*(q) is dominated by the scattering of the nanofibers, it is possible to derive an effective structure factor S*(q) by a simple normalization to the common form factor P(q), $S^*(q) \propto I^*(q)/P(q)$, or more directly $S^*(q) = I^*(q)/I(q)_{P10AP0.4}$. The derived structure factors S*(q) show distinct behaviors depending on the HA concentration but also, on the storage temperature after sample preparation (Fig. S7 and S9).

Samples kept at 4°C for one week before measurements

For low HA concentrations (4 and 10 mg/mL), S*(q) exhibits two broad maxima at 0.043 - 0.08

$Å^{-1}$ and 0.049 - 0.10 $Å^{-1}$ respectively (Fig. S7a). They are characteristic of a nematic phase and correspond to the first and second order maxima of a liquid-like structure factor between rodlike particles in a plane perpendicular to their mean axis. In the present situation, due to the low volume fraction of peptide ($\approx$ 1 wt %), this liquid-like organization can only be observed if nanofibers are not homogenously distributed and rather form bundles or "large fibers" in the gels. The position of the first maximum (q) directly yields the average distance d between peptide nanorods in the bundles ($d = 2\pi/q$) : d = 146 Å for 4 mg/mL and 128 Å for 10 mg/mL (Fig. S9). This distance decreases with the HA concentration and is in between 3 and 2.7 times larger than the diameter of a single nanofiber ($\approx$ 48 Å) : nanofibers are not in contact and solvent widely penetrates into the bundles.

For high HA concentration (20 mg/mL, Fig. S7b), a structural rearrangement occurs. We observe thin diffraction peaks and a third shoulder that can be indexed with a two-dimensional hexagonal lattice (hk indices : 10, 11, 20, Fig. S7b). This diffraction pattern indicates a new structure with hexagonally packed nanofibers in a plane perpendicular to the bundle axis (2D order). The lattice parameter a (or the distance d) can be deduced from the position of the first diffraction peak q_{10} using $a = d = (4\pi/\sqrt{3})/q_{10}$.

To confirm this hexagonal structure, and more precisely, the presence of a third peak (of very weak intensity), complementary high resolution SAXS-WAXS measurements were also performed using synchrotron radiation (Fig. S8). The presence of this later contribution (more visible with the WAXS setup) definitively validates our 2D hexagonal description. Increasing the HA concentration to 20 mg/mL is therefore responsible for a transition from a nematic to a hexagonal columnar organization in the bundles with a lattice parameter a = 113 Å (Fig. S9). The typical distance between nanofibers a is always larger than their diameter ($\approx$ 48 Å). It follows that they are still not in contact. A schematic illustration of the local organization in a bundle cross-section according to the HA concentration for samples kept at 4°C is given in Fig. S9b.

The high resolution of the synchrotron measurements (SAXS setup) also allows to carefully estimate the size D of the crystalline domains from the half-width at half maximum w of the first diffraction peak ($D \cong \frac{2\pi}{w} = 4.2\ \mu$m). This value is in good agreement with the size of the large bundles observed by CLSM investigations.

Figure S12

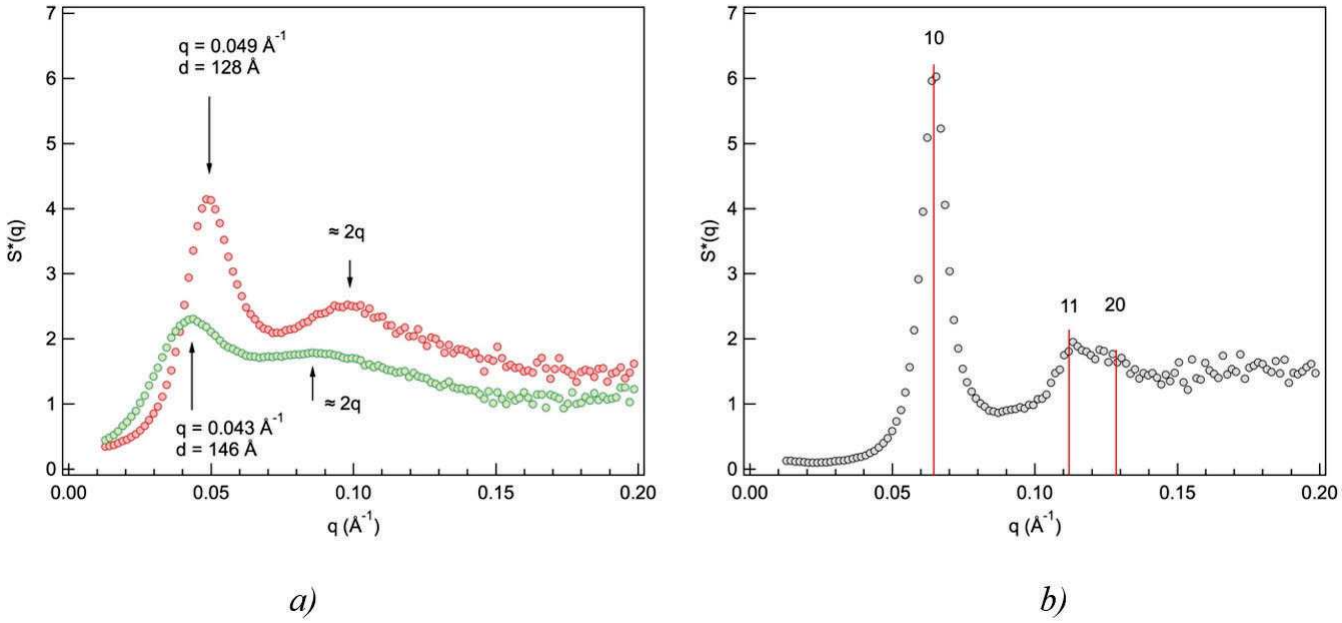

Samples kept at 4°C for 8 days before measurements. (a) Nematic phase : effective structure factor S(q) for P10 AP0.4 HA4 (green circles) and P10 AP0.4 HA10 (red circles). (b) Hexagonal columnar phase : effective structure factor S*(q) for P10 AP0.4 HA20 (black circles). The vertical red lines correspond to the position of the diffraction peaks. hk indices of the three reflections are indicated.*

Figure S13

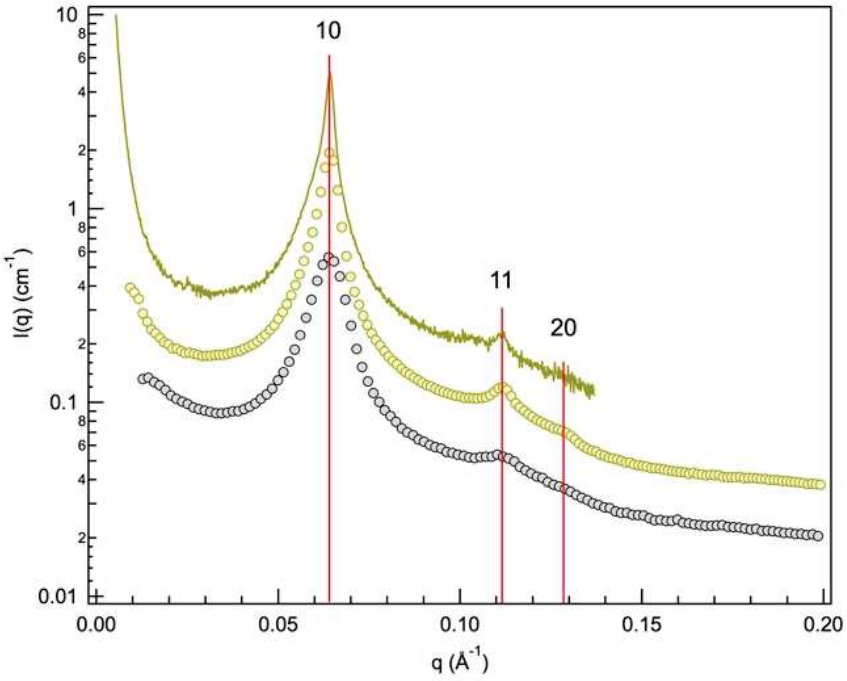

Samples kept at 4°C for 8 days before measurements. I(q) for P10 AP0.4 HA20 measured on the DiffériX platform (SAXS data, black circles) and on the SWING beamline of the SOLEIL Synchrotron (SAXS : yellow line, WAXS : yellow circles). Multiplicative coefficients are applied along the vertical axis for a better visualization (yellow circles : ×2, yellow line : ×4). The vertical red lines correspond to the position of the diffraction peaks. hk indices of the three diffraction peaks are indicated.

Figure S14

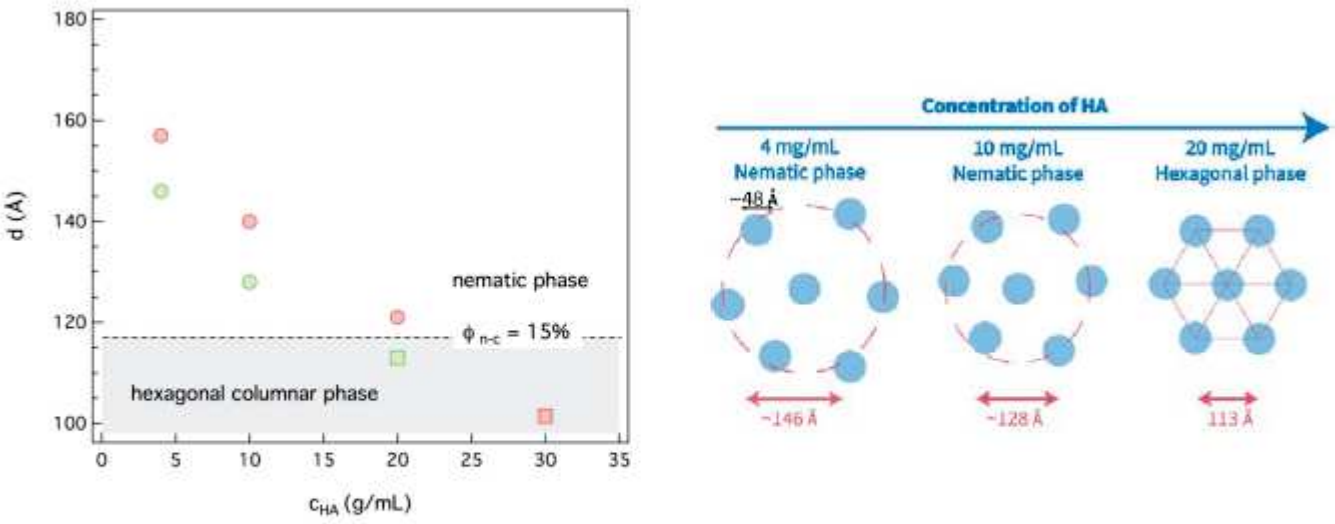

a) *b)*

(a) Average distance d between nanofibers in the bundles. The dash line corresponds to the critical distance delimiting the nematic and hexagonal phases (d_{n-c} = 117 Å). (b) Schematic illustration of the local organization in a bundle cross-section according to the HA concentration for samples kept at 4 °C. The discs represent the sections of the nanofibers.

Samples kept at room temperature for 24 h before measurements

Samples kept at room temperature before measurements show a rather similar behavior (Fig. S10). However, compared to gels stored at 4°C, the average distance between nanofibers d is systematically larger (d = 157 Å for 4 mg/mL, 140 Å for 10 mg/mL and 121 Å for 20 mg/mL, Fig. S10a and the first maximum of the structure factor in the nematic phase is less pronounced and broader ; the local order in the bundles is reduced. Furthermore, the transition to the hexagonal phase is displaced to higher HA concentration and only visible at 30 mg/mL (Fig. S10b).

Figure S15

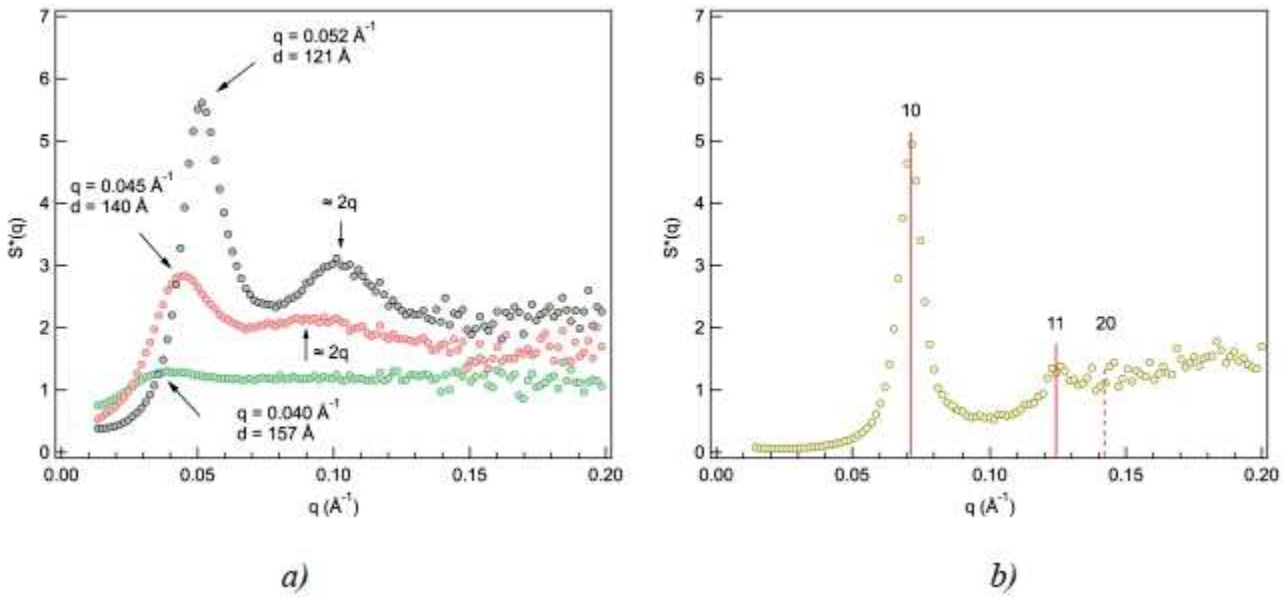

Samples kept at room temperature for 1 day before measurements. (a) Nematic phase : effective structure factor $S^*(q)$ for P10 AP0.4 HA4 (green circles), P10 AP0.4 HA10 (red circles) and P10 AP0.4 HA20 (black circles). (b) Hexagonal columnar phase : effective structure factor $S^*(q)$ for 12 P10 AP0,4 HA30 (yellow circle). The vertical red lines correspond to the position of the diffraction peaks. hk indices of the three reflections are indicated.

Nanofibers volume fraction Φ in the bundles

The volume fraction of the nanofibers regularly increases with the HA concentration. A volume fraction of $\Phi_{n-c} \approx 15\%$ is found for the nematic to columnar phase transition regardless of the thermal history of the samples (Fig. S16).

Figure S16

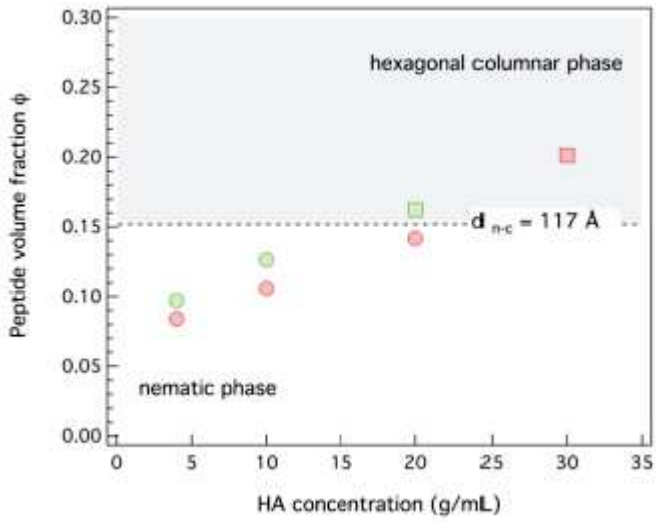

Peptide volume fraction in the bundles Φ*. Green symbols : Samples kept at 4°C for 8 days before measurements. Red symbols : samples kept at room temperature for 1 day before measurements. Discs : nematic phase. Square : hexagonal columnar phase. The dash line corresponds to the peptide volume fraction* Φ *delimiting the nematic and hexagonal phases (*$\Phi_{n-c} \approx 15\%$*).*

Part 5 - Pair potential calculation

The average distance between nanofibers in the bundles and its variation with polymer concentration can be modelled theoretically by considering pair potential interactions (Imai, 2002, Li, 2013). The total potential U_{tot} between parallel nanorods can be expressed as the sum of two contributions resulting from repulsive electrostatic (U_{elec}) and attractive depletion (U_{dep}) interactions.

$$U_{tot} = U_{elec} + U_{dep} \tag{6.4}$$

The equilibrium spacing can be derived from the position of the minimum of the total potential U_{tot} and directly compared to the inter-nanofiber distance measured in SAXS experiments.

Electrostatic contribution U_{elec}

The electrostatic potential between two charged parallel cylinders of radius R and length L can be written[3]

$$U_{elec}(d) = \frac{\sigma^2}{\epsilon\epsilon_0\sqrt{2\pi^3}} \frac{exp(-\kappa(d-2R))}{\kappa R\sqrt{\kappa d}} L \tag{6.5}$$

where d is the separation distance between the center of mass of the cylinders, σ, their linear

charge density (= ne with n the number of charges per unit length and e the elementary charge) and κ, the inverse Debye length. ϵ and ϵ_0 are the relative permittivity of water and the permittivity of vacuum, respectively. The inverse Debye length κ writes

$$\kappa^2 = 4\pi l_B I \tag{6.6}$$

with l_B the Bjerrum length (0.714 nm) and I the ionic strength of the solution defined as

$$I = \sum_i c_i Z_i^2 \tag{6.7}$$

with c_i and Z_i the concentration and the valency of ion i.

For the calculations, the radius R was set to the value determined by SAXS (2.39 nm). The inverse Debye length was determined assuming a homogeneous distribution of ions in the sample (inside and outside the bundles). The total ionic strength I contains a contribution from the Borax buffer I_{buf} (I_{buf} = 150 mM), the divalent phosphate ions I_P (for a total dephosphorylation, their concentration is that of the peptides $c_{peptide}$, $I_P = 4\ c_{peptide}$) and from the HA counterions I_{HA} that depends on the added polymer concentration c_{HA} (when all ionizable groups are dissociated and in absence of charge condensation, $I_{HA} = c_{HA}$). The total ionic strength I ($I = I_{buf} + I_P + I_{HA}$), the different contributions I_{buf}, I_P, and I_{HA} as well as the Debye length κ^{-1} used in the calculations, are given in Table S1.

Table S1

c_{HA} (mg/mL)	c_{HA} (mol/L)	I_{HA} (mol/L)	I_{buf} (mol/L)	I_P (mol/L)	I (mol/L)	κ^{-1} $DebyeLength(nm)$
4	0.010	0.010	0.150	0.052	0.212	0.93
10	0.025	0.025	0.150	0.052	0.227	0.90
20	0.050	0.050	0.150	0.052	0.251	0.86
30	0.075	0.075	0.150	0.052	0.276	0.82

Total Ionic strength I (mol/L) for different HA concentrations c_{HA}. I_{buf}, I_P, and I_{HA} are the contributions from the Borax buffer, the phosphate ions, and the HA counterions. κ^{-1} is the Debye length.

The length L was arbitrary fixed to a 100 nm which is somewhat shorter than the persistence length of the nanofibers. This value, although changing the depth of the potential well in U_{tot}, does not modify its position, and therefore, the theoretical equilibrium spacing d.

The linear charge density σ is a key parameter difficult to evaluate without of a structural knowledge of the self-assembly at the molecular level. This value was varied and arbitrary set to n = 10 charges per nanometer along the nanofibers.

Depletion contribution U_{dep}

Depletion interaction in a suspension of cylinders (of radius R) may be observed in presence of added small colloids. For spherical particles, their radius Rs fixes the thickness of the depletion layers. When the distance between cylinders is such that their excluded layers overlap (d < 2(R+ R_s)), the volume accessible to the particles is larger. The entropy of the system is increased while the free energy is reduced : an attractive depletion interaction of entropic origin is observed.

The depletion potential between two parallel cylinders induced by hard spheres of radius RS can be written [4-6]

$$U_{dep}(d) = -\Delta\pi V_{OV}(d) \tag{6.8}$$

where $\Delta\pi$ is the osmotic pressure difference between inside and outside the bundles, which reduces to the non-ionic contribution of the polymer solution π. d is the separation distance and V_{OV} the overlap volume of the excluded layers.

In the semidilute regime, chains are entangled, the correlation volumes (of size ξ) act as the depletant[7, 8]. The thickness of the depletion layer corresponds to the correlation length ξ of the HA network. The polymer contribution to the osmotic pressure is therefore[9].

$$\pi = \frac{k_B T}{\xi^3} \tag{6.9}$$

The experimental correlation length ξ to use in the calculations is not easy to determine. If it can be extracted quite simply in binary salt free polyelectrolyte solutions (of ionic strength I_0) from the position of the scattering peak q^* ($\xi(I_0) = \frac{2\pi}{q^*}$)[10]), it is more complex in presence of salt since the maximum disappears. To estimate the proper correlation length $\xi(I)$ of the HA network at an ionic strength I in our systems, we first assume that it is identical to that of pure HA solutions at the same I value. The correlation length $\xi(I)$ can then be derived from the general scaling relation[11]

$$\xi(I) \approx \xi(I_0)(\frac{I}{I_0}^{0.25}) \tag{6.10}$$

The ionic strength in salt free HA solutions I_0 (or I_{0HA}) is only due to the polyelectolyte counterion, while I contains in addition a contribution from the buffer, i.e. from the phosphate ions ions, as previously discussed (Tab. S1). References values for $\xi(I_0)$ were extrapolated from SAXS measurements on salt free solutions on HA of comparable molar mass[12]. For the HA concentration range used in this work, q^* varies as $c^{0.5}$ ($q^* = 0.33c_{HA}^{0.5}$,$c_{HA} < 0.07mol/L$) and $c^{0.25}$ ($q^* = 0.173c_{HA}^{0.25}$,$c_{HA} > 0.07mol/L$) which are characteristic of semi-dilute entangled and concentrated regimes, respectively.

The knowledge of q^* and I_{0HA} in salt free HA solutions as well as the ionic strength I in our systems allows to determine the correlation length $\xi(I)$ for each HA concentration (Table S2).

Table S2

c_{HA} (mg/mL)	c_{HA} (mol/L)	$I_{HA} = I_0$ (mol/L)	q^* (Å)	$\xi(I_0)$ (nm)	I (mol/L)	$\xi(I)$ (nm)
4	0.010	0.010	0.033	19.1	0.212	40.9
10	0.025	0.025	0.052	12.1	0.227	20.9
20	0.050	0.050	0.074	8.5	0.251	12.7
30	0.075	0.075	0.090	6.9	0.276	9.1

HA correlation length in salt free solutions and with peptide in Borax. q^* values are extrapolated from experimental measurements on HA of comparable molar mass[12].

The overlap volume V_{OV} of depletion layers between two parallel cylinders varies with their separating distance d and can write :

$$V_{OV}(d) = (\pi a^2 - d\sqrt{a^2 - (d/2)^2} - 2a^2 \tan^{-1}(d/2\sqrt{a^2 - (d/2)^2}))L \tag{6.11}$$

where $a = R + \xi$. When d is larger than $2(R + \xi)$, no overlap is found, the depletion interaction disappears.

The total interaction potential U_{tot} was calculated using the previous expressions for U_{elec} and U_{dep} . It presents a clear minimum for all HA concentrations that allows to determine the theoretical equilibrium distance d between nanofibers (Fig. S17).

Figure S17

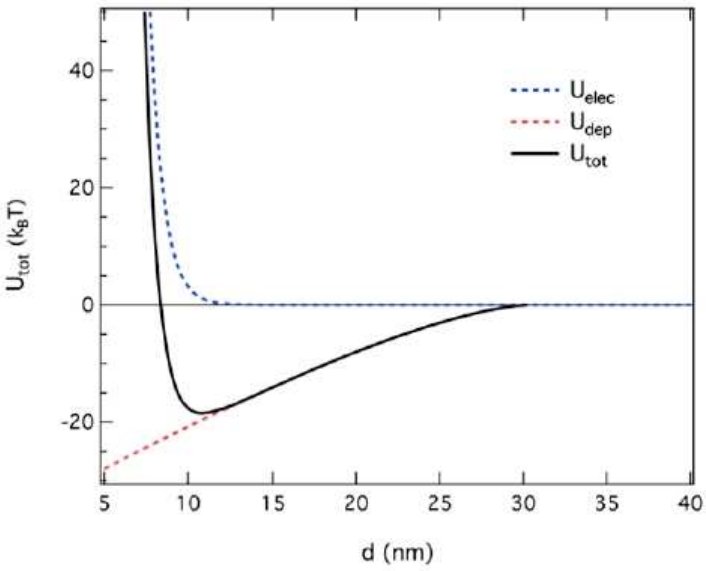

Pair potential analysis for c_{HA} = 20 mg/mL. Electrostatic (U_{elec}) and depletion (U_{dep}) contributions to the total potential (U_{tot}). Equilibrium distance d = 10.9 nm.

References

(1) Greenfield, N. J. *Nature Protocols* **2007**, *1*, 2876-2890.

(2) Kline, S. R. *Journal of Applied Crystallography* **2006**, *39*, 895-900.

(3) Smith, D. A. *Journal of Theoretical Biology* **2011**, *276*, 8-15.

(4) Asakura, S.; Oosawa, F. Interaction between particles suspended in solutions of macromolecules, 1958.

(5) Imai, M.; Urakami, N.; Nakamura, A.; Takada, R.; Oikawa, R.; Sano, Y. *Langmuir* **2002**, *18*, 9918-9923.

(6) Li, T.; Zan, X.; Sun, Y.; Zuo, X.; Li, X.; Senesi, A.; Winans, R. E.; Wang, Q.; Lee, B. *Langmuir* **2013**, *29*, 12777-12784.

(7) Joanny, J. F.; Leibler, L.; De Gennes, P. G. *J Polym Sci Polym Phys Ed* **1979**, *17*, 1073-1084.

(8) Verma, R.; Crocker, J. C.; Lubensky, T. C.; Yodh, A. G. *Physical Review Letters* **1998**, *81*, 4004-4007.

(9) Dobrynin, A. V.; Rubinstein, M. *Progress in Polymer Science (Oxford)* **2005**, *30*, 1049-1118.

(10) Combet, J.; Lorchat, P.; Rawiso, M. *European Physical Journal : Special Topics* **2012**, *213*, 243-265.

(11) Carrillo, J. M. Y.; Dobrynin, A. V. *Macromolecules* **2011**, *44*, 5798-5816.

(12) Lorchat, P.; Konko, I.; Combet, J.; Jestin, J.; Johner, A.; Laschewski, A.; Obukhov, S.; Rawiso, M. *Epl* **2014**, *106*, DOI : 10.1209/0295-5075/106/28003.

Conclusion

Il s'agit dans cette partie de réunir tous les chapitres et d'apporter une réponse structurée sur les questions que nous nous sommes posées (Figure 1).

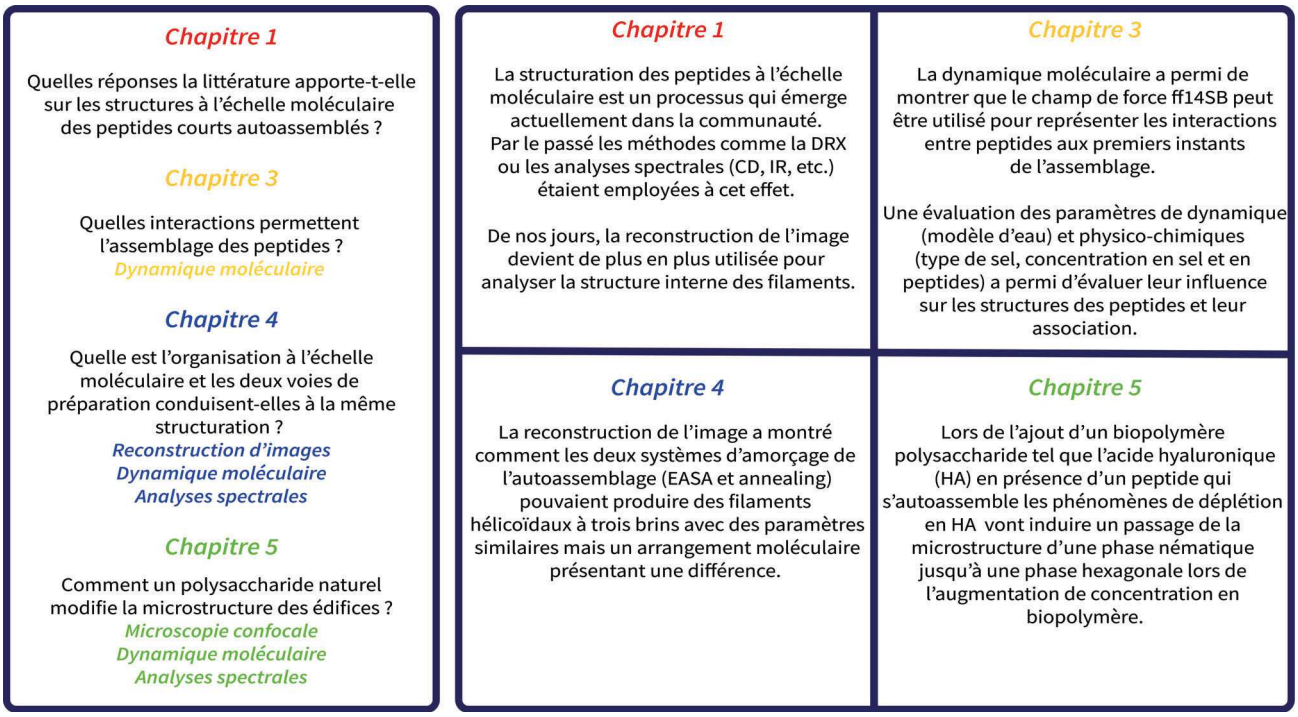

FIGURE 1 – Description des objectifs de la thèse (à gauche) avec les questions qui se sont posées dans chaque chapitre et la réponse aux problématiques, par chapitre (à droite).

Dans le chapitre 1 d'état de l'art nous avons vu que certaines équipes de recherches avaient déjà utilisé la méthode de reconstruction de l'image de cryo-MET. Les structures élucidées ont été : un octapeptide (KFE8) et un quadrapeptide (1-KMe_3). La reconstruction donne effectivement toutes les informations attendues et permet même de proposer un modèle initial pour la dynamique moléculaire. Cet avènement de la résolution quasi atomique est une forme de révolution dans le domaine de la chimie qui, depuis le début du siècle, s'appuyait sur la diffraction des rayons X de

cristaux 2D de peptides assemblés dont la structure à l'état solvaté n'était pas atteignable. Cependant, les auteurs qui se focalisent principalement sur l'obtention de la structure sont majoritairement des chimistes intéressés par des applications en biologie alors que cette thèse porte principalement sur la comprenhésion du phénomène d'auto-assemblage.

Dans le chapitre 3 de dynamique moléculaire les interactions supramoléculaires aux premiers instants de l'auto-assemblage ont été identifiées : empilement $\pi - \pi$ et liaisons hydrogène. Les paramètres de dynamique moléculaire tel que le modèle d'eau et les paramètres physico-chimiques comme le type et la concentration en sel ainsi que la concentration en peptides ont été analysés. Il a été montré que le champ de force employé (ff14SB) permettait de reproduire les structures des peptides observées dans la littérature en adéquation avec le filament obtenu en reconstruction d'images. Les dynamiques réalisées avec les trois modèles d'eau (TIP3P, SPC/E et TIP4P-Ewald) montrent que la structuration est dépendante du choix de ce dernier. Ainsi, les résultats des dynamiques de futurs articles ou projets pourraient être fortement impactés par la décision du modèle à employer. L'étude en fonction du type de sel a montré que les sels chaotropes (NaI, CsI et CsCl) peuvent influencer la dynamique de l'auto-assemblage de peptides. L'augmentation du nombre de peptides en peptides (passant de 2 à 5 peptides) montre des interactions et structures similaires. Ainsi, la diminution des degrés de liberté lors de l'assemblage ne semble pas affecter la structuration de l'édifice. La majorité des systèmes simulés ont une structuration de N- à C-terminal. Cependant, ces résultats devraient être confirmés avec d'autres dynamiques comme du REMD (Replica Exchange Molecular Dynamics) ou des simulations $\Delta\mu$VT où un apport en peptides dans la boîte est constant au cours du temps. Cela augmenterait l'échantillonnage des systèmes et permettrait peut être de se rapprocher de la formation de la nanofibre observée en cryo-MET.

Le chapitre 4 montre comment il est possible de reconstruire les filaments de peptides auto-assemblés à partir d'un très grand nombre d'images de cryo-MET. Deux méthodes d'hydrogélation ont été comparées : par amorçage enzymatique (EASA) et par amorçage thermique (annealing). Deux cartes de projection du potentiel électrostatique des filaments ont été obtenues à une résolution de 3,8 Å. Les cartes possèdent des paramètres hélicoïdaux identiques et sont corrélées à 70% en terme de densité. Après introduction de modèles moléculaires nous avons montré que la nanofibre présente une structuration en trois brins identiques composés chacun d'un dimère de Fmoc-FFY. L'organisation des peptides dans le filament est constitué d'un coeur hydrophobe comprenant des Fmoc et phénylalanines et une écorce, plus hydrophile, composée des tyrosines. Les interactions principales entre les peptides dans un brin sont de l'empilement $\pi - \pi$ entre les cycles aromatiques d'un peptide l'un au dessus de

l'autre ainsi que des liaisons hydrogène. Il apparait que la carte issue du Fmoc-FFpY + PA présente un ordre plus grand que celle obtenue lors de la préparation de l'auto-assemblage par annealing. En effet, les densités sont moins diffus et plus concentrées sur le potentiel électrostatique des peptides. Cependant, dans la totalité des jeux de données il n'a pas été possible de résoudre la chiralité de l'hélice (hélice gauche ou droite) car il faudrait arriver à une résolution de 2,8 Å. Pour se faire, une acquisition future sur un Titan Krios G4, un microscope de meilleure résolution, est prévue.

Le chapitre 5 traite des modifications de microstructure lors de l'ajout d'acide hyaluronique avant l'auto-assemblage. La microstructure passe d'une phase nématique à une maille hexagonale 2D avec l'augmentation croissante en concentration d'HA. Il a été montré que ce sont les forces de déplétion en HA qui induisent cette structuration. Il est important de noter également que le HA n'a pas d'influence sur la cinétique d'auto-assemblage observée en dichroïsme circulaire. Grâce à une analyse de co-localisation du HA et de l'auto-assemblage en microscopie confocale il a été observé que le biopolymère et le réseau de l'hydrogel se recouvrent. L'origine de cette interaction, étudiée en dynamique moléculaire, repose sur la formation de liaisons hydrogène entre les tyrosines et le biopolymère ce qui favorise la formation du réseau. Des investigations supplémentaires pourraient être réalisées avec d'autres polymères (PolyEther Glycol, PEG) avec d'autres conditions physico-chimiques (concentration en sel, type de sel, température, etc.). Une investigation supplémentaire pourra être portée sur le rôle de la phosphatase alcaline qui permet d'initier la formation de l'hydrogélateur afin de comprendre si l'enzyme a un rôle supplémentaire dans la formation de l'auto-assemblage

Glossaire

Nom	Contexte d'utilisation	Définition
Image	Reconstruction	Signal bidimensionnel (2D) composés de pixels pouvant prendre une valeur unitaire de 0 à 255
Micrographie	Reconstruction	Image obtenue à partir d'un bombardement d'électrons sur l'échantillon
Tube	Reconstruction	Portion d'une fibre qui contient les coordonnées de départ et de fin. Le tube pourra ensuite être segmenté et donner des particules.
Particule	Reconstruction	Portion d'une image comprenant l'objet d'intérêt avec une portion de glace amorphe entourant l'objet
Hélice	Reconstruction	Objet tridimensionnel constitués de trois paramètres : rise, pitch, twist
Élévation de l'hélice (rise)	Reconstruction	Distance entre deux unités répétitives dans une hélice, distance donnée régulièrement en angstrom (Å)
Tour d'hélice (pitch)	Reconstruction	Distance lorsqu'une unité a réalisé un tour complet, distance donnée régulièrement en angstrom (Å)
Pas angulaire (twist)	Reconstruction	Angle formé entre deux unités répétitives, angle régulièrement donné en degrés (°)

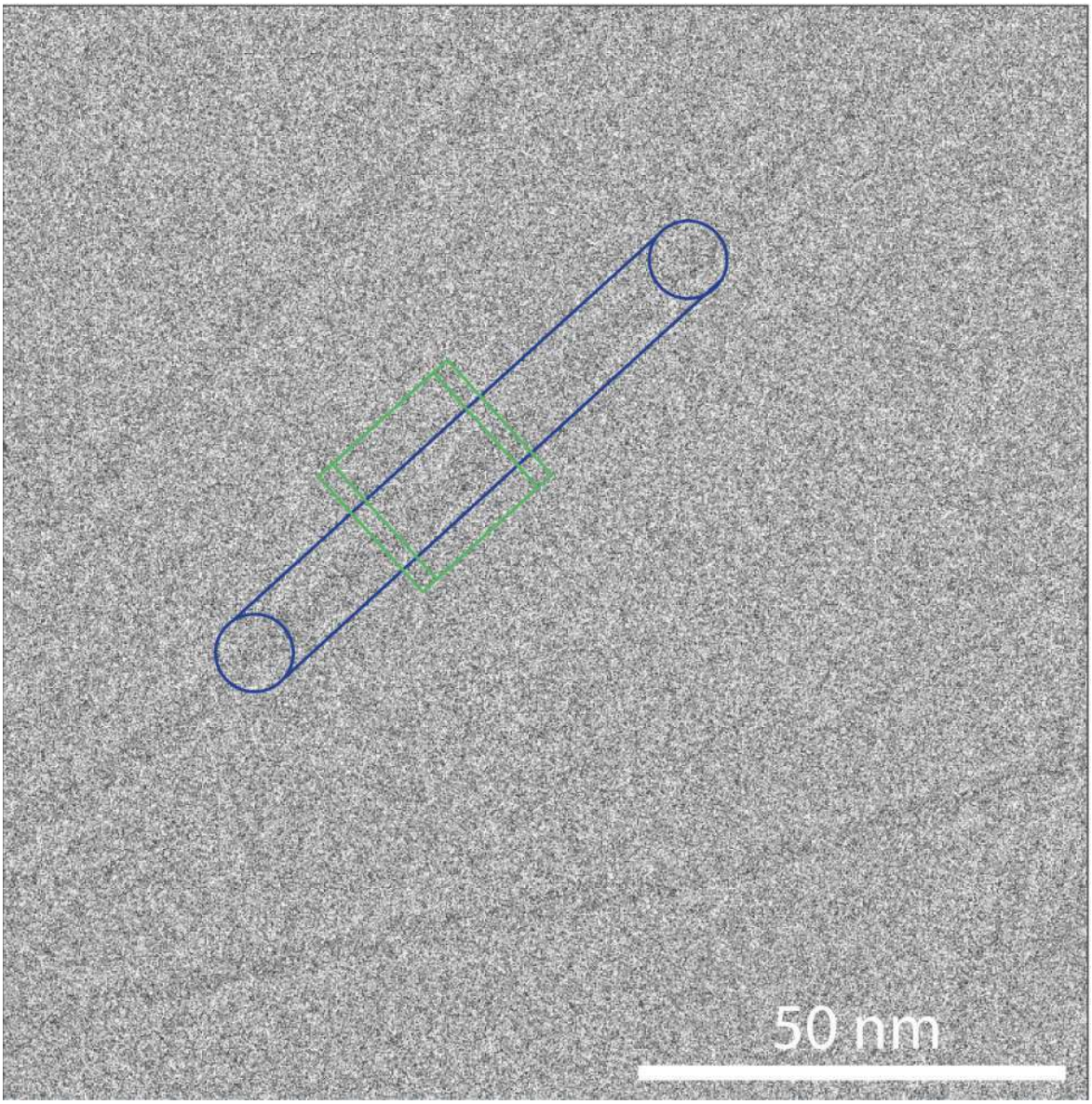

Illustration de la définition du tube, en bleu, les deux cercles représentent le début et la fin du tube. En vert, schéma d'une taille de boîte comprenant une partie de fibre et de la glace entourant l'objet. La distance interboîte est calculée à partir du nombre d'unités asymétriques choisies multiplié par l'élévation de l'hélice (en Å).

Annexes

polymers

MDPI

Communication

Localized Enzyme-Assisted Self-Assembly in the Presence of Hyaluronic Acid for Hybrid Supramolecular Hydrogel Coating

Jennifer Rodon Fores [1], Alexis Bigo-Simon [1], Déborah Wagner [1], Mathilde Payrastre [1], Camille Damestoy [1], Lucille Blandin [1], Fouzia Boulmedais [1], Julien Kelber [1], Marc Schmutz [1], Morgane Rabineau [2,3], Miryam Criado-Gonzalez [1,2,3,*], Pierre Schaaf [1,2,3,*] and Loïc Jierry [1,*]

1 Institut Charles Sadron (UPR22), Université de Strasbourg, CNRS, 23 rue du Loess, CEDEX 2, BP 84047, 67034 Strasbourg, France; jennifer.rodon-fores@tum.de (J.R.F.); abigosimon@unistra.fr (A.B.-S.); wagner.deborah1@gmail.com (D.W.); mathilde.payrastre@gmail.com (M.P.); camille.damestoy@gmail.com (C.D.); lucille.blandin@gmail.com (L.B.); boulmedais@unistra.fr (F.B.); kelber@unistra.fr (J.K.); marc.schmutz@ics-cnrs.unistra.fr (M.S.)

2 Institut National de la Santé et de la Recherche Médicale, INSERM Unité 1121, CRBS, 1 rue Eugène Boeckel, CEDEX, 67085 Strasbourg, France; morgane.rabineau@inserm.fr

3 Faculté de Chirurgie Dentaire, Université de Strasbourg, 8 rue Sainte Elisabeth, 67000 Strasbourg, France

* Correspondence: mcriado@ictp.csic.es (M.C.-G.); schaaf@unistra.fr (P.S.); ljierry@unistra.fr (L.J.); Tel.: +91-25-8-74-97 (M.C.-G.); +33-3-68-85-33-87 (P.S.); +33-3-68-41-41-47(L.J.)

Abstract: Hydrogel coating is highly suitable in biomaterial design. It provides biocompatibility and avoids protein adsorption leading to inflammation and rejection of implants. Moreover, hydrogels can be loaded with biologically active compounds. In this field, hyaluronic acid has been largely studied as an additional component since this polysaccharide is naturally present in extracellular matrix. Strategies to direct hydrogelation processes exclusively from the surface using a fully biocompatible approach are rare. Herein we have applied the concept of localized enzyme-assisted self-assembly to direct supramolecular hydrogels in the presence of HA. Based on electronic and fluorescent confocal microscopy, rheological measurements and cell culture investigations, this work highlights the following aspects: (*i*) the possibility to control the thickness of peptide-based hydrogels at the micrometer scale (18–41 µm) through the proportion of HA (2, 5 or 10 mg/mL); (*ii*) the structure of the self-assembled peptide nanofibrous network is affected by the growing amount of HA which induces the collapse of nanofibers leading to large assembled microstructures underpinning the supramolecular hydrogel matrix; (*iii*) this changing internal architecture induces a decrease of the elastic modulus from 2 to 0.2 kPa when concentration of HA is increasing; (*iv*) concomitantly, the presence of HA in supramolecular hydrogel coatings is suitable for cell viability and adhesion of NIH 3T3 fibroblasts.

Keywords: supramolecular hydrogel; enzyme-assisted self-assembly; hyaluronic acid; peptide; coating

Citation: Rodon Fores, J.; Bigo-Simon, A.; Wagner, D.; Payrastre, M.; Damestoy, C.; Blandin, L.; Boulmedais, F.; Kelber, J.; Schmutz, M.; Rabineau, M.; et al. Localized Enzyme-Assisted Self-Assembly in the Presence of Hyaluronic Acid for Hybrid Supramolecular Hydrogel Coating. *Polymers* **2021**, *13*, 1793. https://doi.org/10.3390/polym13111793

Academic Editor: Luminita Marin

Received: 14 May 2021
Accepted: 25 May 2021
Published: 29 May 2021

1. Introduction

Supramolecular hydrogels resulting from the self-assembly of low molecular weight hydrogelators (LMWH) in water [1] give rise to self-assembled nanostructures, mainly nanofibers, following the same mechanisms as those governing classical polymerizations. That is why this self-assembly process is sometimes called supramolecular polymerization [2]. The non-covalent nature of the interactions between LMWH can ensure both a reversibility between the "sol" and the "gel" state, and self-healing features of the resulting material [3]. In addition, the very low amount of hydrogelator used (from 0.01 to 1 wt% in general) leads to a particular class of highly hydrated and thus very soft materials. Peptides-saccharide derivatives have been intensively reported as efficient LMWH for biomedical applications such as wound healing, antibacterial coating, biosensing, 3D cell culture, immunological modulation, drug delivery or tissue engineering [4–8]. Many physical or chemical stimuli were reported to trigger the hydrogelation process. Among them,

we can distinguish the use of enzymes since this way involves the chemical transformation of molecular precursors in hydrogelators. These latter are thus produced in situ. In 2004, the group of Bing Xu (Brandeis University, Waltham, MA, USA) introduced the first self-assembly triggered by an enzyme leading to a supramolecular hydrogel [9]. This opened the route to the precise localization of peptide self-assemblies, and a step that was taken in 2009 when Williams and Ulijn groups showed that peptide self-assembly can be initiated from covalently immobilized enzyme on a surface [10]. Our group further developed the localized enzyme-assisted self-assembly (LEASA approach by introducing seed-layers in addition to an enzyme-adsorbed layer to trigger the localized self-assembly growth [11,12], for catalytic and auto-catalytic self-assembled hydrogels [13–15] or self-assemblies initiated from nanoparticles surface [16] and in host materials [17,18]. This bottom-up approach is efficient in water and once the surface coated with an adequate enzyme, the localized self-assembled structure growth proceeds in an autonomous way [19].

Peptide supramolecular hydrogels have exhibited excellent biological properties. Based on the exceptional ability of the FF moiety to self-assemble in various nanostructures [20], the dipeptide Fmoc-FF hydrogel was investigated for 2D and 3D cell cultures (Fmoc = Fluorenylmethyloxycarbonyl; F = phenylalanine) [21–24]. The analogous morphological features of the nanofibrous self-assembled network of Fmoc-FF with the natural components of the extracellular matrix (ECM) has led to extensive research targeting the design of several peptide hydrogels for specific cell culture lines or biological applications [23–26]. One interesting aspect of peptide-based hydrogels is the possibility to easily tune both the chemistry and the mechanical features of the resulting material through the co-assembly of different peptide sequences [21,22]. Because the RGD amino acid sequence is a natural endogenous ligand of integrins, a protein receptor involved in the adhesion mechanism of cells, the Fmoc-RGD tripeptide has been largely investigated (R = arginine; G = glycine; D = aspartic acid) [27,28]. Once included in the self-assembled nanostructured of several peptides, Fmoc-RGD is exhibited at the surface of interwoven cylindrical nanofibers and thus promotes adhesion, spreading and proliferation of cells [27]. Longer peptides such as RGDS-Q_{11} and IKVAV-Q_{11} have been also co-assembled leading to β-sheet organization in nanofibers (S = serine; Q = glutamic acid; I = isoleucine; K = lysine; V = valine; A = alanine) [29,30] and showing excellent properties for cell culture support applications [31–37]. Apart from pure peptide based hydrogels, obtained through different peptide mixtures to modify the properties of the co-assembled structures, hybrid hydrogels can be achieved by combination of peptides and polysaccharides. Among them, hyaluronic acid (HA), a natural negatively charged polysaccharide constituted of repeated disaccharide units, i.e., D-glucuronic acid and N-acetyl-D-glucosamine, attracts great attention in the biomedical field. This polymer is involved in cell signaling, wound reparation, tissue regeneration, morphogenesis and extracellular matrix (ECM) organization in humans. Stupp and coworkers highlighted the interaction of HA with positively charged peptide self-assemblies through the preparation of stable membranes [38,39]. Thin self-supporting bioactive membranes combining positively charged multi-domain self-assembling peptides and HA prepared by varying time and temperature, lead to membranes with finely controlled morphology, which improves the stem cell adhesion and spreading, [40] for tissue regeneration applications. [41] Recently, Nevo and Adler-Abramovich have studied the hybrid supramolecular matrix designed from HA and the dipeptide Fmoc-FF, prepared in a mixture of dimethyl sulfoxide (DMSO) and water [42,43]. The ratio between HA and Fmoc-FF present in the resulting bulk material determined its mechanical features and its biodegradability. However, toxicological properties of DMSO make it an undesirable candidate for the design of many biocompatible hydrogels. For such purpose, herein we use a water-soluble tripeptide, Fmoc-FF*p*Y (Y = tyrosine; *p* = phosphate group), by incorporation of the phosphorylated tyrosine amino-acid to the peptide sequence. Then, this water soluble Fmoc-FF*p*Y precursor is dephosphorylated in presence of alkaline phosphatase (AP) forming the hydrogelator Fmoc-FFY (Figure 1a). We have applied the LEASA concept to direct the hydrogelation process exclusively from the surface of polymer multilayer

films, and evaluated the compatibility of this enzyme-assisted self-assembly process with the presence of HA to get hybrid peptide/polymer supramolecular hydrogels with tunable mechanical and biological properties. When adsorbed on a surface through an adequate multilayer film, AP initiates the self-assembly process leading to a micrometer thick hydrogel layer. The influence of HA proportion both on the resulting thickness and on the internal architecture of the peptide self-assembled network was observed by scanning electronic microscopy (SEM and cryo-SEM) and by atomic force microscopy (AFM). The impact of HA on the peptide-based nanofibers organization was studied by transmission electronic microscopy (TEM) and fluorescence confocal microscopy. Since the modification of the internal architecture of hydrogels, the variation of the mechanical properties according to the HA concentration was measured by dynamic oscillatory rheology. Finally, the cell adhesion and cell viability properties of these supramolecular peptide/polymer hydrogels were determined.

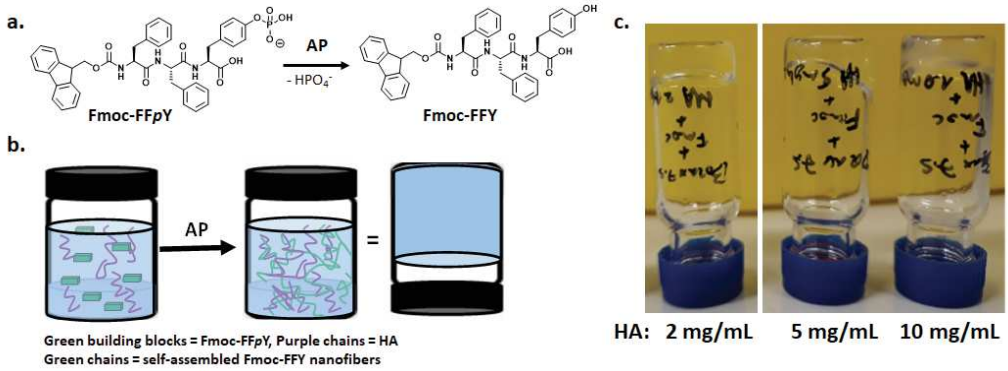

Figure 1. (**a**) Chemical structure of the precursor peptide Fmoc-FF*p*Y transformed in hydrogelator Fmoc-FFY in presence of an enzyme, i.e., AP; (**b**) Scheme of inverted tube test of a Fmoc-FFY hydrogel formed from Fmoc-FF*p*Y precursor and AP in presence of HA; (**c**) Inverted tube tests of self-assembled Fmoc-FFY hydrogels formed in Borax buffer solution (pH 9.5) in presence of various HA concentrations.

2. Materials and Methods

2.1. Materials

A table indicating the commercial sources of all chemicals used in this work is given in the Supplementary Materials (SM). Materials used: confocal microscope from Zeiss (Oberkochen, Germany), rheometer from Malvern (Malvern, United-Kingdom), the scanning electronic microscope from Hitachi (Tokyo, Japan), the transmission electronic microscope from FEI (Oregon, USA), the atomic force microscope from BioScope Catalyst (Bruker corp., Santa Barbara, CA, USA).

2.1.1. Precursor Peptide Fmoc-FF*p*Y and HA

The precursor peptide Fmoc-FF*p*Y has been prepared through solid support chemistry using a "fmoc" strategy. The synthetic pathway of Fmoc-FF*p*Y is shown in Scheme S1 in the SM. All details about the synthetic procedure and characterization of Fmoc-FF*p*Y (^{1}H, ^{13}C, ^{31}P NMR, HPLC analysis given as Figures S1–S4 respectively in the SM) are given in supporting information, HA characterization (^{1}H NMR and size exclusion chromatogram shown as Figures S5 and S6 respectively in the EM) as well.

2.1.2. Buffers and Substrates

All polyelectrolytes and alkaline phosphatase solutions were freshly prepared before being used using a buffer or cell culture medium (RPMI). Borax buffer (25 mM, pH 9.5): 1 g of sodium tetraborate anhydrous was solved in 200 mL of ultrapure water (Milli-Q Plus System, Millipore, Billerica, MA, USA) and pH was adjusted using HCl 0.1 M or NaOH 0.05 M. PBS buffer (pH 7.4): 1 tablet was solved in 200 mL of ultrapure water (Milli-Q

Plus System, Millipore, Billerica, MA, USA) and pH was adjusted as described previously. RPMI Cell culture medium was commercially available and used without further steps. Glass slides or silica wafers used for cryo-SEM, confocal, AFM, SAFAS and biological assays, were previously cleaned with an aqueous Hellmanex solution (2% *v/v*) and rinsed extensively with Milli-Q water

2.2. Methods

2.2.1. Upside down Test Vials

All tests were performed in glass vials of 1.5 mL capacity. First, four different stock solutions were prepared: a solution of AP at 3 mg/mL (solution 1), a solution of Fmoc-FF*p*Y at 15 mg/mL (solution 2), a solution of HA, three times the desired concentration (solution 3), and finally the borax buffer solution or RPMI (solution 4). All solutions 1, 2 and 3 were prepared in borax buffer. Then, 50 µL of each solution 1, and 2 are mixed together in the glass vial. Then, 50 µL of solution 3 or 4 are added to the previous vial containing solutions 1 and 2 and mixed together with the vortex for 5 s. Then, samples were kept without stirring at room temperature.

2.2.2. Confocal Microscopy

Observations were carried out with a Zeiss LSM 710 microscope using ×10, ×20 and ×40 objectives. To observe the self-assembly, a fluorescent compound, the Thioflavin T (TF), was added to the samples. TF fluorescence was detected between 505 and 530 nm (green emission) after excitation at λ = 488 nm (argon laser). Images were analyzed with Zen black software from Zeiss and "Image J" software. Samples are prepared on a glass surface, by the protocol described in the part 4.3.2, and on solution. Final concentrations in solution are the following: Fmoc-FF*p*Y (5 mg/mL), HA (10 mg/mL), AP (1 mg/mL) and TF (0.15 mg/mL), which is solubilized in the peptide solution. Then, on the glass cover slip 50 µL of each solution (Fmoc-FF*p*Y, TF, AP and HA, or not) are mixed together for the analysis.

2.2.3. Rheological Measurements

Rheological properties were measured on a Kinexus Malvern rheometer using a sand-blasted plate geometry of 1 cm diameter and a gap of 0.5 mm. Firstly, 380 µL of Fmoc-FF*p*Y solution in RPMI were mixed with 20 µL of AP solution (in RPMI as well) within a homemade teflon mold of 1 cm of diameter. The resulting solution was gently shaken for some seconds and left to gelate at room temperature for 24 h. Then, the hydrogel was removed from the mold to perform the measurements. Strain measurements were carried out from 0.01% to 100% at 0.3 Hz and frequency sweeps were performed from 0.01 to 10 Hz at a fixed strain of 0.06%.

2.2.4. Multilayer Film Buildup and Directed Hydrogelation

After deposition of the PEI (1 mg/mL) layer on the chosen substrate by dipping, the multilayer film was performed by alternately exposing the surface to PSS (1 mg/mL in borax buffer) and PAH (1 mg/mL in borax buffer) solutions for 10 min with an intermediate rinsing step with borax buffer for 5 min. Then, AP (1 mg/mL in borax buffer) is adsorbed for 20 min followed by 5 min of rinsing step with borax. Finally, the Fmoc-FF*p*Y solution with or without HA (in borax buffer or in RPMI) was brought in contact with the multilayer polymer film coated substrate for 24 h.

2.2.5. Electronic Microscopy Analyses (TEM, SEM and cryo-SEM)

SEM and cryo-SEM: to get cross-sectioned gels, the glass slide (or silica wafer) covered by the supramolecular hydrogel studied, was inserted vertically in the jaws of a homemade vise. The holder with the sample was dipped into the liquid nitrogen slush and then transferred in the chamber of the Quorum PT 3010 machine. High vacuum was applied, and the sample was fractured with an adapted razor blade. After a slight etching at −80 °C

the sample was then transferred in the FEG-cryo-SEM (Hitachi SU8010) and observed at 1 kV at −170 °C. *TEM:* hydrogels studied were prepared as described above and then vortexed to get a solution, diluted with borax buffer up to 500 times. 20 µL of a diluted solution was dropped off on a shelf and observed using a TEM Technai G2 machine in negative staining. To make the observations, 5 µL of each solution was deposited onto a freshly glow discharged carbon-covered grid (400 mesh). The solution was left for 2 min and the grid was negatively stained with 5 µL of uranyl acetate (2% in water) for another minute and finally dried using a filter paper. The grids were observed at 200 kV with a Tecnai G2 (FEI) microscope. Images were acquired with a camera Eagle 2 k (FEI) ssCD camera.

2.2.6. Atomic Force Microscopy (AFM)

AFM investigations were carried out with a BioScope Catalyst (Bruker corp., Santa Barbara, CA, USA). Micrographs from different supramolecular hydrogels were recorded in contact mode by using silicon tips mounted on nitride levers. All samples were observed in dry state with triangular cantilevers having a spring constant of 0.4 N/m and a nominal tip radius of 2 nm. Selected AFM images were treated with the nanoscope analysis software (Bruker corp., Santa Barbara, CA, USA). All samples analyzed by AFM were prepared on gold-coated quartz crystal and they were air dried before analysis.

2.2.7. Cell Viability Test

Glass slides of 12 mm of diameter were cleaned up by UV-Ozone for 15 min, and then dropped off at the bottom of a 24-well plate (CORNING brand) for cell culture. Then, the polyelectrolyte multilayer was buildup by filling the 24-wells plate with 1 mL of polyelectrolyte solutions as following. After the deposition of a PEI (1 mg/mL in borax buffer) precursor layer for 10 min, the multilayer film was performed by alternately exposing the surface to PSS (1 mg/mL in borax buffer) and PAH (1 mg/mL in borax buffer) solutions for 10 min with an intermediate rinsing step with borax buffer for 5 min. Then, AP (1 mg/mL in borax buffer) was adsorbed for 20 min followed by 5 min of rinsing step with borax or RPMI medium. Finally, the Fmoc-FFpY solution with or without HA (in borax buffer or RPMI medium) was added and brought in contact for 24 h. Finally, two rinsing steps with the cell culture medium were performed (RPMI + 10% FBS) and then the solution containing the cells were dropped off on the samples. Samples were freshly prepared for the assay and sterilized with UV exposure for 30 min. Then, 5×10^4 NIH 3T3 mouse fibroblasts cells were seeded in each well. The cell culture was done at 37 °C in an incubator for 4 h, in DMEM containing glucose, 10% fetal bovine serum and 1% penicillin-streptomycin. After 4 h, samples were observed using an optical microscope.

3. Results

Enzyme-Assisted Self-Assembly (EASA) leads to supramolecular hydrogels differently than with all other methods since the LMWH is generated in situ in water thanks to an enzymatic transformation of a molecular precursor [19]. Many enzymes have proven to be useful on a large variety of precursor compounds. Among them, peptide derivatives are probably the main class of precursors investigated, and thus hydrogelators as well [3]. The precursor is a molecule well soluble in water and the enzymatic action will disturb the balance between its hydrophilicity and its hydrophobicity in favor to this later, driving thus the self-assembly of the hydrogelator [9]. In our study, we have investigated the tripeptide Fmoc-FF*p*Y as precursor and Fmoc-FFY as hydrogelator. This is a model system well studied by our group over the last years [8,11,16–18]. When Fmoc-FF*p*Y (5 mg/mL, 6.44 mM) is dissolved in buffer solution at room temperature (Borax buffer 25 mM, pH 9.5, 20 °C), the addition of AP (1 mg/mL, 6.67 µM) induces the self-assembly of Fmoc-FFY in β-sheet organization and then the supramolecular hydrogel is obtained in 20 min. As expected, without the addition of AP, the Fmoc-FF*p*Y solution does not lead to a gel even after two days. To ensure that HA does not prevent the action of AP and/or the

gelation process, simple tube test experiments were carried out (Figure 1b). In several vials containing borax buffered solution of Fmoc-FF*p*Y (5 mg/mL), HA (Mw = 406,000 g/mol) was introduced in various proportions to get final 2, 5 and 10 mg/mL concentration of the polysaccharide. After the addition of AP (1 mg/mL), hydrogels were obtained in each vial (Figure 1c) confirming the innocuity of HA toward the hydrogel formation. However, the time required to form the gel is different in each case: ~20, ~40 and ~50 min for the vial corresponding to 2, 5 and 10 mg/mL of HA, respectively. The highest concentration of HA leads to slightly cloudy hydrogels while all others are entirely translucent. This slowdown of the hydrogelation time can be due either to the increase of the viscosity at higher HA concentration or to the fact that HA perturbs the Fmoc-FFY self-assembly and thus the gelation process.

To observe the effect of HA on the self-assembled peptide architecture, we have used fluorescent confocal microscopy which allows observations in hydrogels formed in bulk conditions (vials) and at room temperature. Peptide self-assembly can be revealed by using Thioflavine T (TF), a compound that becomes fluorescent in presence of β-sheet organizations when excited at 450 nm [17]. When Fmoc-FF*p*Y and TF are mixed together (Borax buffer 25 mM, pH 9.5), no fluorescence is measured. The addition of AP solution leads spontaneously to a highly dense-packed tiny microfiber-network emitting a green fluorescence at 482 nm when excited (Figure 2a). When the same experiment is carried out with HA (10 mg/mL) initially present in the precursor Fmoc-FF*p*Y solution, the addition of AP provides a completely different self-assembled microstructure: very long and curvy microfibers are entangled together (Figure 2b). These structures are more than several hundred micrometers long and have diameters ranging from 2 to 15 µm. These experiments support the assessment that the presence of HA considerably impacts the resulting peptide assembly in an EASA process: larger micro-organization occurs in presence of this polysaccharide.

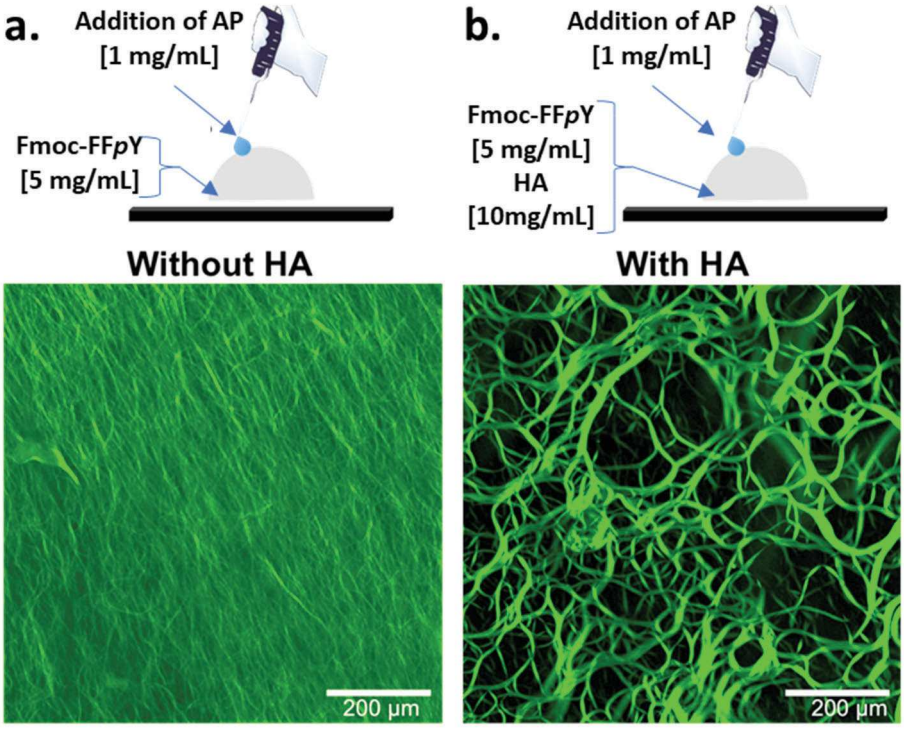

Figure 2. Fluorescence confocal microscopy images taken after the addition of AP (1 mg/mL) in Fmoc-FF*p*Y (5 mg/mL) borax buffered solution (25 mM, pH 9.5) containing Thioflavine T in (**a**) absence or in (**b**) presence of HA (10 mg/mL).

To get insight into the way HA induces the generation of these microstructures, we examined by TEM the fiber morphology of self-assembled Fmoc-FFY hydrogels in absence or in presence of HA at 2, 5 and 10 mg/mL, in bulk conditions ([AP] = 1 mg/mL, [Fmoc-FF*p*Y] = 5 mg/mL). We focused our attention on the diameter values of the self-assembled single fibers, called elementary fibers (EF). In order to observe them properly, hydrogels were vortexed and diluted with borax buffer before observation. All calculated values result from the mean of thirty measurements at least, randomly selected on several TEM images. Without HA, the self-assembly of Fmoc-FFY leads to elementary nanofibers with 5.8 ± 0.9 nm diameter. When 2, 5 and 10 mg/mL of HA is present with Fmoc-FF*p*Y, the addition of AP leads to EF of 5.9 ± 1.0 nm, 5.8 ± 0.8 nm and 6.0 ± 1.1 nm respectively (Figure 3a,b). Thus, the diameter of EF does not vary when HA is present, even at the highest concentration. Therefore, we can presume that the polysaccharide does not take part in the mechanism of peptide self-assembly initiated by AP but rather interacts with the EF once formed. This seems to indicate that the slow-down of the gel formation observed when the HA concentration is increased is not due to the self-assembly kinetics of Fmoc-FFY, but rather to the interaction of the self-assembled Fmoc-FFY fibers with HA, so that fiber entanglements are less effective.

The change of the peptide self-assembled structure when various concentrations of HA are used can tune the mechanical properties of the resulting hybrid hydrogel as already reported [42,43]. This aspect is particularly important for biological applications since mechanical features of the substrate are directly involved in cell viability, motility and differentiation. Therefore, rheological analyses were carried out using plate-plate geometry. Hydrogels were prepared in home-made Teflon molds providing the right shape and diameter. Anticipating the cell culture study, all hydrogels were prepared in Roswell Park Memorial Institute (RPMI) medium at pH 7.6. The elastic (G′) and loss moduli (G″) were measured at 1 Hz with a shear stress applied of 0.06% (see Figure S7 in SM). The values of both G′ and G″ are given in Figure 3c for each hybrid hydrogel prepared in presence of 0, 2, 5 and 10 mg/mL of HA. When HA is not involved in the hydrogel preparation, the resulting material has a G′ value of roughly 2 kPa. This is an expected order of magnitude for supramolecular hydrogels. By increasing the HA concentration used to get the hydrogel from 2, 5 to 10 mg/mL, the G′ value measured of each hybrid hydrogel decreases to 1.15, 0.47 and 0.20 kPa respectively. G″ values are very low (<0.4 kPa) but follow the same trend. The role of HA proportion on the mechanical features of supramolecular hydrogel agrees with previous and recent contributions based on dipeptide supramolecular hydrogels [42,43].

Circular Dichroism (CD) is a tool to get information related to the chirality at the molecular and supramolecular scale. In particular, it allows for identifying patterns in self-assembled architectures. Thus, when AP is added to a Fmoc-FF*p*Y solution, CD measurements show superhelicoidal structures due to the π-π stacking of the "Fmoc" groups, highlighted by a typical band located at 303 nm [9,44]. In presence of HA (0.5 mg/mL), the whole CD spectra is quasi similar to the one in absence of HA (see Figures S8 and S9 in SM). It appears that the self-assembled Fmoc-FFY organization at the molecular scale is unaffected by HA.

Localized enzyme-assisted self-assembly is performed when the enzyme is spatially located at a specific area [19,45]. The production of hydrogelators takes place in close vicinity of the enzymes and therefore the hydrogel grows from them. One easy and universal way to get surfaces modified with enzymes is to use multilayer films. This approach is based on the alternation of oppositely charged polyelectrolytes leading to a multilayer film [46]. Enzymes being charged according to the pH value of their environment are able to be adsorbed on top of a film being oppositely charged. AP has an isoelectric point around 5, which means that this enzyme is mainly negatively charged at pH 7.6, i.e., the pH used to build up the thin film. Thus, the following multilayer film has been deposited on silica wafers or glass slides through a dipping process: PEI/$(PSS/PAH)_2$ (PEI = poly(ethylene imine); PSS = poly(styrene sulfonate); PAH = poly(allylamine hydrochloride). This mul-

tilayer is capped with a polycationic layer due to PAH, allowing the adsorption of AP, and leading to the enzymatically active thin film PEI/$(PSS/PAH)_2$/AP. This multilayer architecture ensures to be independent of the substrate's nature. Then, these polymer multilayer films were dipped in borax buffered solution (pH 9.5) of Fmoc-FF*p*Y (5 mg/mL) containing 0, 2, 5 or 10 mg/mL of HA, during 12 h before analysis by cryo-SEM. To observe both the thickness of each hydrogel formed and its internal architecture, each sample was frozen in liquid ethane, then broken and finally freeze-dried. No metallization has been done. In all studied conditions, cryo-SEM images show a full covering of the substrate by the hydrogel layer (Figure 4a).

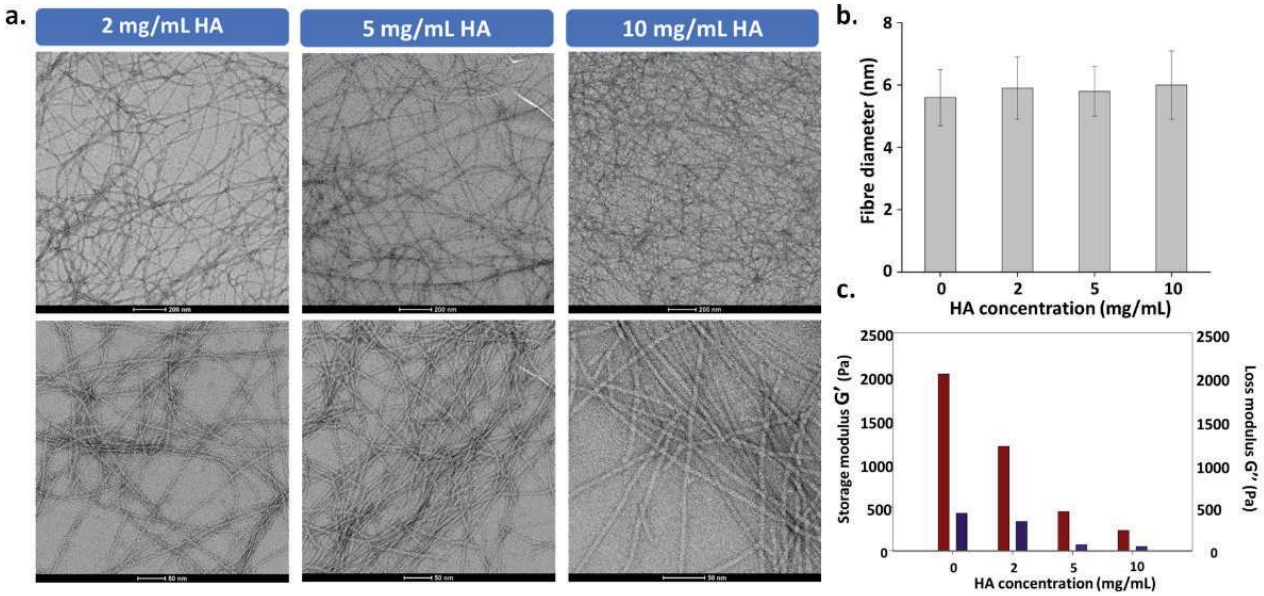

Figure 3. (**a**) The diagram provides the mean diameter of elementary fibers (ca. 30 fibers/image) determined after analysis of several TEM images (ca 10 images); (**b**) TEM images of self-assembled Fmoc-FFY nanofibers formed in presence of different HA concentrations ranging from 2, 5 and 10 mg/mL; (**c**) Elastic modulus (G′) and loss modulus (G″) values measured on hydrogels prepared in presence of 0, 2, 5 and 10 mg/mL of HA.

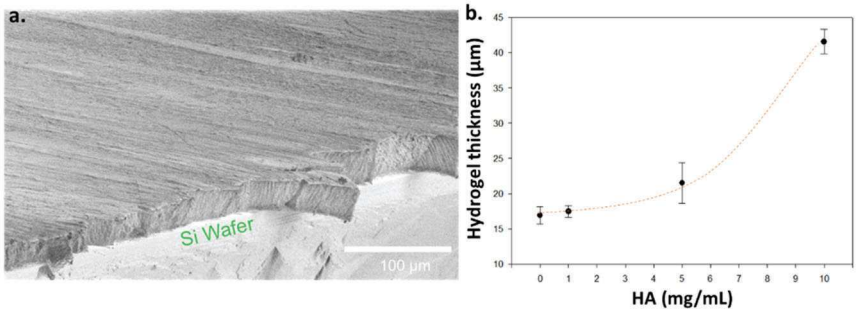

Figure 4. *Cont.*

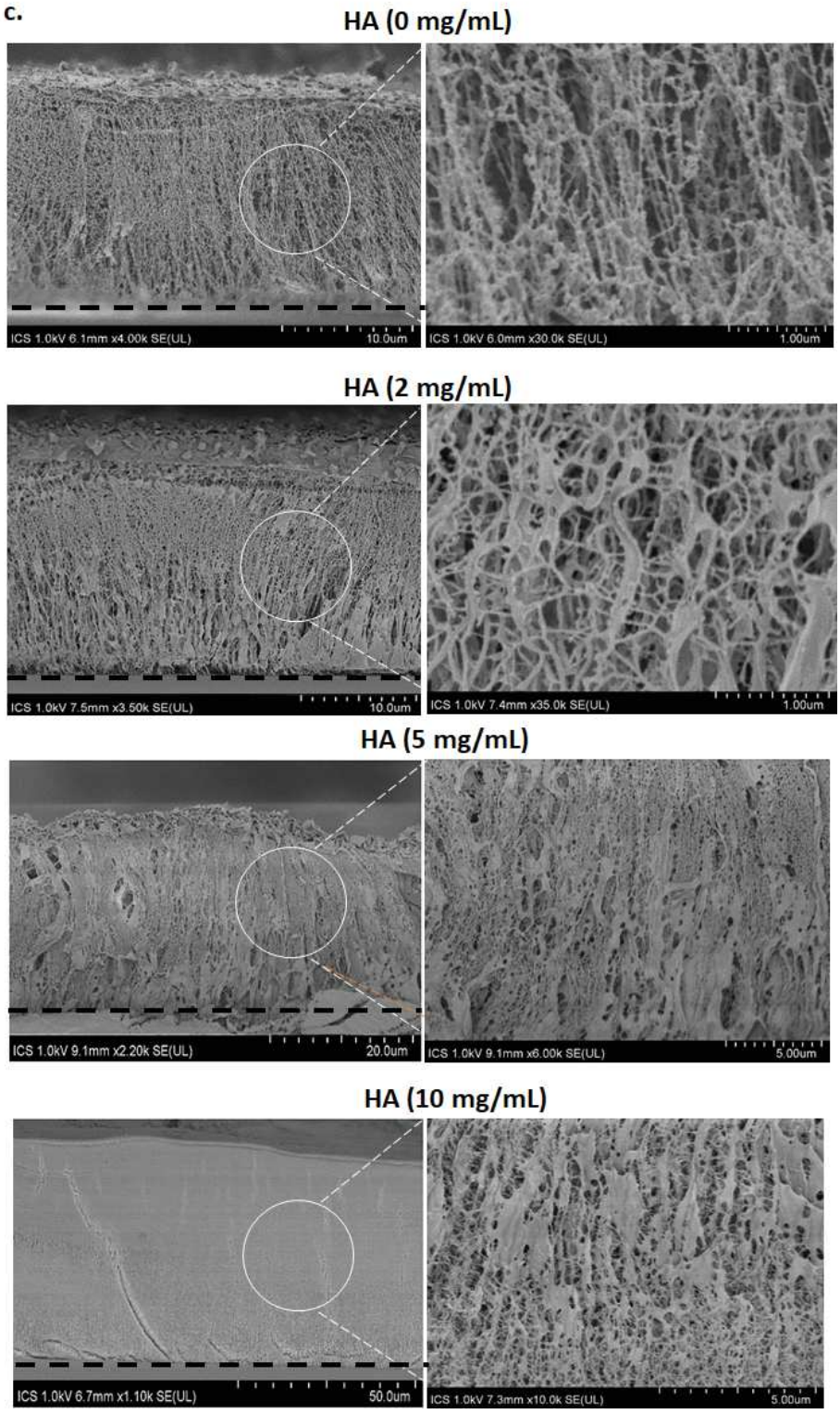

Figure 4. (**a**) Sectional cryo-SEM image of supramolecular hydrogel (dark grey part) formed from silica wafer (light grey part) from Fmoc-FFY self-assembled from PEI/$(PSS/PAH)_2$/AP multilayer; (**b**) Hydrogel thickness evolution according to the HA concentration present initially in solution with the precursor peptide Fmoc-FF*p*Y and AP; (**c**) Cryo-SEM images of hydrogels formed from AP-modified multilayer film in presence of various HA concentrations: 0, 2, 5 and 10 mg/mL. Dashed black lines indicate the separation between the glass substrate and the hydrogel.

Cross-section of the supported self-assembled hydrogels was measured at three different areas at least allowing to represent error bars for each thickness value, highlighting the low roughness of the hydrogel coating all along the substrate through the low standard deviations (Figure 4b). An increase of the thickness is measured from 18 ± 1 µm, 19 ± 0.5 µm, and 22 ± 3 µm to 41 ± 2 µm when the proportion of HA is increased from 0 to 2, 5 and 10 mg/mL respectively. When no HA is present, a fibrillar architecture constituted by nanofibers having a "string of pearls" shape is observed. These fibers are perpendicularly orientated to the substrate, as already reported for others surface-mediated self-assembly of LMWH [11,12,47,48]. When HA is added, the film still displays an internal fibrous organization that remains, at a larger scale, perpendicularly oriented with respect to the substrate. With an increase of the HA concentration, one observes that the fibers are increasingly associated in entities having the shape of veils. These must be certainly constituted both from the Fmoc-FFY self-assembled fibers and HA. As the HA concentration increases, these veils increase in size and fiber network becomes denser. We also performed AFM microscopy on such films. The resulting images were obtained at the dry state. Figure 5a represents typical images obtained in deflection mode. First of all, one observes that PEI/$(PSS/PAH)_2$/AP multilayer exhibits aggregates corresponding to clusters of enzymes as already reported by Ulijn and coworkers [10]. In absence of the AP layer over the resulting multilayer film PEI/$(PSS/PAH)_2$, no nanofibers are formed once brought in contact with Fmoc-FF*p*Y solution (5 mg/mL), as expected. However, it appears some small globules distributed everywhere on the surface. This could be due to Fmoc-FFpY aggregates as already reported for other Fmoc-peptides hydrogelators. When the enzymatically-active multilayer film PEI/$(PSS/PAH)_2$/AP is brought in contact with Fmoc-FF*p*Y solution (5 mg/mL), a dense fibrous network is observed. The presence of HA (2 mg/mL) leads to larger structures that could be formed from the assembly of thin nanofibers in presence of HA. This influence of HA on the internal peptide self-assembled architecture grew up from the surface is confirmed by SEM images taken from surface: kind of veil structures are observed when HA is present (2 or 5 mg/mL) whereas only thinner nanofibers constitute the supramolecular hydrogel in absence of the polysaccharide, as described previously through cryo-SEM studies (Figure 5b).

Finally, biological properties of the developed hybrid peptide/polymer supramolecular hydrogel coatings were assessed. Direct cell adhesion tests were performed by seeding NIH 3T3 fibroblasts on top of the peptide/polymer hydrogel coatings. Fibroblasts (in DMEM + 10% FBS) were brought in contact with the hydrogels for 4 h at 37 °C. Then, a life/dead fluorescent test was performed to obtain the cell viability values for each hydrogel (Figure 6). In comparison with naked glass slides used as control (96.9 ± 1.9% cell viability), cell viability values are excellent for all hydrogels under study with values ≥ 95%, except in the case of the hydrogel containing the highest HA content (10 mg/mL) which is a bit lower (88.4 ± 2.0% cell viability) but suitable for the development of biomaterials. Moreover, cellular spreading was also analyzed through optical image monitoring (Figure 6). When no HA is present, or the concentration is low (2 mg/mL), most of adhered cells shows a round morphology and only few of them have started to spread. When 5 or 10 mg/mL HA are employed, it is possible to distinguish that almost all cells are clearly spread on the hydrogel displaying an elongated shape and philopodes. These results allow us to prove that HA promotes cell adhesion and cell spreading of NIH 3T3 fibroblasts despite the decrease of the mechanical properties of such materials when HA concentration is increased. This achievement is particularly important since previous works showed that NIH 3T3 fibroblasts growth was favored on substrates with high storage modulus.

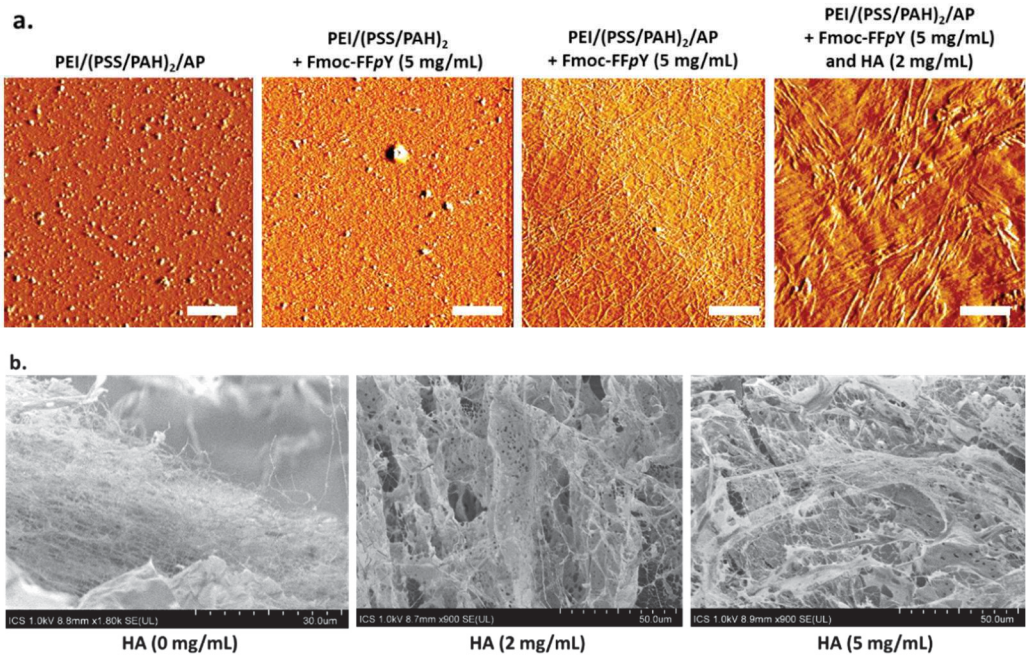

Figure 5. (**a**) AFM images (deflection mode, dry state) of the multilayer film PEI/$(PSS/PAH)_2$ in the following conditions (from left to right): after the adsorption of AP on the top of the film, when the multilayer is brought in contact with Fmoc-FF*p*Y solution (5 mg/mL), after the buildup of the peptide self-assembled architecture from a precursor peptide solution [Fmoc-FF*p*Y] = 5 mg/mL in absence or in presence of HA (2 mg/mL). Scale bar = 2 μm; (**b**) SEM images of supramolecular hydrogels formed from PEI/$(PSS/PAH)_2$/AP in presence of Fmoc-FFpY (5 mg/mL) and HA at 0, 2 and 5 mg/mL.

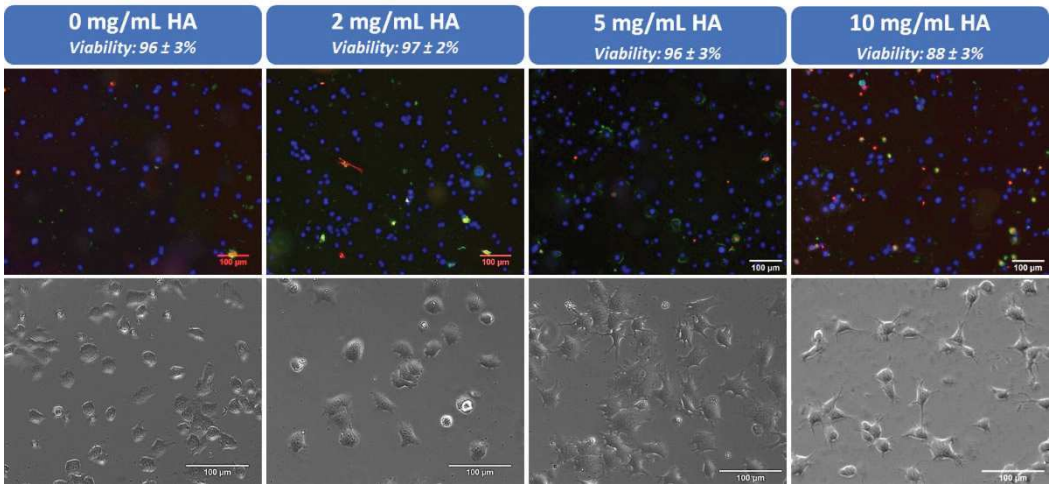

Figure 6. Apoptotic/necrotic/healthy cells detection kit was used to determine the cell viability of NIH 3T3 fibroblasts after 4 h in contact with different hydrogel coatings containing 0, 2, 5 and 10 mg/mL HA. Live cells are stained in blue and death cells in red. Phase contrast microscopy images showing NIH 3T3 fibroblasts cell spreading on the hydrogel coatings.

4. Conclusions

The spatial localization of enzymes on polymer multilayer films allows us to direct the peptide self-assembly exclusively where enzymes are located. This LEASA approach is a powerful tool to design micrometer thick supramolecular hydrogel coatings from any kind of substrate using the multilayer film method. Herein, we have used the tripeptide hydrogelator Fmoc-FFY generated in situ from the system AP/Fmoc-FF*p*Y and we have

shown that additional polymer components such as HA can be incorporated during the spatially localized hydrogel growth to get hybrid peptide/polymer coatings displaying good cell adhesion and spreading. Thus, HA does not prevent the hydrogelation process and the variation of its proportion allows to modulate the resulting hydrogel thickness. Furthermore, as the HA proportion increased, the storage modulus of the resulting hydrogel decreased, a balance that can be useful to get very soft hydrogels to be employed as essential substrates for nerve cell cultures, for instance. Based on electron and fluorescence microcopy investigations, the incorporation of HA does not change the shape of the peptide-based nanofibers, but it has a strong impact on their ability to collapse together, generating large microstructures. The study of the origin of this interaction between HA and EASA is currently under investigation by our group.

Supplementary Materials: The following are available online at https://www.mdpi.com/article/10.3390/polym13111793/s1: Scheme S1. Synthetic pathway to prepare Fmoc-FF*p*Y through solid support chemistry; Figure S1. ^{1}H NMR spectra of Fmoc-FF*p*Y (400 MHz, $CDCl_3$+10%MeOD); Figure S2. ^{31}P NMR spectra of Fmoc-FF*p*Y (161.92 MHz, $CDCl_3$+10% MeOD); Figure S3. ^{13}C NMR spectra of Fmoc-FF*p*Y (100 MHz, DMSO-d_6+10% MeOD) and magnifications; Figure S4. Chromatogram of the purified Fmoc-FF*p*Y; Figure S5. Size exclusion chromatogram of HA; Figure S6. 1H NMR (400 MHz) spectra of HA in D_2O at 25 °C; Figure S7. Evolution of the elastic modulus (G′) and loss modulus (G″) as a function of the strain (a) or the frequency (b) for Fmoc-FF*p*Y and AP hydrogels in absence or in presence of HA; Figure S8. CD spectra of Fmoc-FF*p*Y and AP in absence (blue line) or in presence (red line) of HA; Figure S9. HT evolution corresponding to the CD spectra of Fmoc-FF*p*Y and AP in absence (blue line) or in presence (red line) of HA.

Author Contributions: Conceptualization, M.C.-G.; P.S. and L.J.; methodology, P.S. and L.J.; validation, M.C.-G.; M.S.; P.S. and L.J.; formal analysis, J.R.F.; D.W.; A.B.-S.; M.P.; C.D.; L.B.; J.K.; M.R.; F.B.; M.C.-G. and M.S.; writing—original draft preparation, J.R.F.; writing—review and editing, J.R.F.; M.C.-G.; P.S. and L.J.; supervision, P.S and L.J.; project administration, L.J.; funding acquisition, P.S. and L.J. All authors have read and agreed to the published version of the manuscript.

Funding: This research was funded by *Agence Nationale de la Recherche*, EASA project grant number ANR-18-CE06-0025-03 and by *Labex Chimie des Systèmes Complexes*, grant number CSC-PSC-016.

Institutional Review Board Statement: Not applicable.

Informed Consent Statement: Not applicable.

Data Availability Statement: Data are contained within the article and its Supplementary Materials. Additional data may be provided upon request.

Acknowledgments: L.J. acknowledges his membership to the CNRS GDR2088 BIOMIM research network. J.R.F. acknowledges *the International Center for Frontier Research in Chemistry* for her PhD fellowship (CSC-PSC-016). Alain Carvalho and Christian Blanck are acknowledged for their technical support in electronic microscopy analyses. The analytical and the microscopy platforms of Charles Sadron Institute are acknowledged.

Conflicts of Interest: The authors declare no conflict of interest.

References

1. Draper, E.R.; Adams, D.J. Controlling the assembly and properties of low-molecular-waight-hydrogelators. *Langmuir* **2019**, *35*, 6506–6521.
2. Roy, S.; Ulijn, R.V. Exploiting biocatalysis in the synthesis of supramolecular polymers. In *Enzymatic Polymerization*; Palmans, A.R.A., Heise, A., Eds.; Springer: Berlin/Heidelberg, Germany, 2010; pp. 127–145.
3. Du, X.; Zhou, J.; Shi, J.; Xu, B. Supramolecular hydrogelators and hydrogels: From soft matter to molecular biomaterials. *Chem. Rev.* **2015**, *115*, 13165–13307. [CrossRef] [PubMed]
4. Baillet, J.; Gaubert, A.; Bassani, D.M.; Verget, J.; Latxague, L.; Barthelemy, P. Supramolecular gels derived from nucleoside based bolaamphiphiles as a light-sensitive soft material. *Chem. Commun.* **2020**, *56*, 3397–3400. [CrossRef]
5. Clemente, M.J.; Romero, P.; Serrano, J.L.; Fitremann, J.; Oriol, L. Supramolecular hydrogels based on glycoamphiphiles: Effect of the disaccharide polar head. *Chem. Mater.* **2012**, *24*, 3847–3858. [CrossRef]

6. McCloskey, A.P.; Gilmore, S.M.; Zhou, J.; Draper, E.R.; Porter, S.; Gilmore, B.F.; Xu, B.; Laverty, G. Self-assembling ultrashort NSAID-peptide nanosponges: Multifunctional antimicrobial and anti-inflammatory materials. *RSC Adv.* **2016**, *6*, 114738–114749. [CrossRef]
7. Webber, M.J.; Appel, E.A.; Meijer, E.W.; Langer, R. Supramolecular biomaterials. *Nat. Mater.* **2016**, *15*, 13–26. [CrossRef]
8. Criado-Gonzalez, M.; Iqbal, M.H.; Carvalho, A.; Schmutz, M.; Jierry, L.; Schaaf, P.; Boulmedais, F. Surface triggered self-assembly of Fmoc-tripeptide as an antibacterial coating. *Front. Bioeng. Biotechnol.* **2020**, *8*, 938. [CrossRef]
9. Yang, Z.M.; Gu, H.W.; Fu, D.G.; Gao, P.; Lam, J.K.; Xu, B. Enzymatic formation of supramolecular hydrogels. *Adv. Mater.* **2004**, *16*, 1440–1444. [CrossRef]
10. Williams, R.J.; Smith, A.M.; Collins, R.; Hodson, N.; Das, A.K.; Ulijn, R.V. Enzyme-assisted self-assembly under thermodynamic control. *Nat. Nanotechnol.* **2009**, *4*, 19–24. [CrossRef] [PubMed]
11. Vigier-Carriere, C.; Garnier, T.; Wagner, D.; Lavalle, P.; Rabineau, M.; Hemmerle, J.; Senger, B.; Schaaf, P.; Boulmedais, F.; Jierry, L. Bioactive seed layer for surface-confined self-assembly of peptides. *Angew. Chem. Int. Ed.* **2015**, *54*, 10198–10201. [CrossRef]
12. Vigier-Carriere, C.; Wagner, D.; Chaumont, A.; Durr, B.; Lupattelli, P.; Lambour, C.; Schmutz, M.; Hemmerle, J.; Senger, B.; Schaaf, P.; et al. Control of surface-localized enzyme-assisted self-assembly of peptides through catalyzed oligomerization. *Langmuir* **2017**, *33*, 8267–8276. [CrossRef]
13. Rodon Fores, J.; Mendez, M.L.M.; Mao, X.Y.; Wagner, D.; Schmutz, M.; Rabineau, M.; Lavalle, P.; Schaaf, P.; Boulmedais, F.; Jierry, L. Localized supramolecular peptide self-assembly directed by enzyme-induced proton gradients. *Angew. Chem. Int. Ed.* **2017**, *56*, 15984–15988. [CrossRef] [PubMed]
14. Rodon Fores, J.; Criado-Gonzalez, M.; Chaumont, A.; Carvalho, A.; Blanck, C.; Schmutz, M.; Serra, C.A.; Boulmedais, F.; Schaaf, P.; Jierry, L. Supported catalytically active supramolecular hydrogels for continuous flow chemistry. *Angew. Chem. Int. Ed.* **2019**, *58*, 18817–18822. [CrossRef]
15. Rodon Fores, J.; Criado-Gonzalez, M.; Chaumont, A.; Carvalho, A.; Blanck, C.; Schmutz, M.; Boulmedais, F.; Schaaf, P.; Jierry, L. Autonomous growth of a spatially localized supramolecular hydrogel with autocatalytic ability. *Angew. Chem. Int. Ed.* **2020**, *59*, 14558–14563. [CrossRef]
16. Criado-Gonzalez, M.; Rodon Fores, J.; Carvalho, A.; Blanck, C.; Schmutz, M.; Kocgozlu, L.; Schaaf, P.; Jierry, L.; Boulmedais, F. Phase separation in supramolecular hydrogels based on peptide self-Assembly from enzyme-coated nanoparticles. *Langmuir* **2019**, *35*, 10838–10845. [CrossRef]
17. Criado-Gonzalez, M.; Rodon Fores, J.; Wagner, D.; Schroder, A.P.; Carvalho, A.; Schmutz, M.; Harth, E.; Schaaf, P.; Jierry, L.; Boulmedais, F. Enzyme-assisted self-assembly within a hydrogel induced by peptide diffusion. *Chem. Commun.* **2019**, *55*, 1156–1159. [CrossRef] [PubMed]
18. Criado-Gonzalez, M.; Loftin, B.; Rodon Fores, J.; Vautier, D.; Kocgozlu, L.; Jierry, L.; Schaaf, P.; Boulmedais, F.; Harth, E. Enzyme assisted peptide self-assemblies trigger cell adhesion in high density oxime based host gels. *J. Mater. Chem. B* **2020**, *8*, 4419–4427. [CrossRef] [PubMed]
19. Vigier-Carriere, C.; Boulmedais, F.; Schaaf, P.; Jierry, L. Surface-assisted self-assembly strategies leading to supramolecular hydrogels. *Angew. Chem. Int. Ed.* **2018**, *57*, 1448–1456. [CrossRef]
20. Reches, M.; Gazit, E. Controlled patterning of aligned self-assembled peptide nanotubes. *Nat. Nanotechnol.* **2006**, *1*, 195–200. [CrossRef]
21. Jayawarna, V.; Ali, M.; Jowitt, T.A.; Miller, A.E.; Saiani, A.; Gough, J.E.; Ulijn, R.V. Nanostructured hydrogels for three-dimensional cell culture through self-assembly of fluorenylmethoxycarbonyl-dipeptides. *Adv. Mater.* **2006**, *18*, 611–614. [CrossRef]
22. Yang, Z.M.; Liang, G.L.; Xu, B. Enzymatic control of the self-assembly of small molecules: A new way to generate supramolecular hydrogels. *Soft Matter* **2007**, *3*, 515–520. [CrossRef]
23. Liebmann, T.; Rydholm, S.; Akpe, V.; Brismar, H. Self-assembling Fmoc dipeptide hydrogel for in situ 3D cell culturing. *BMC Biotechnol.* **2007**, *7*, 88. [CrossRef] [PubMed]
24. Jayawarna, V.; Richardson, S.M.; Hirst, A.R.; Hodson, N.W.; Saiani, A.; Gough, J.E.; Ulijn, R.V. Introducing chemical functionality in Fmoc-peptide gels for cell culture. *Acta Biomater.* **2009**, *5*, 934–943. [CrossRef] [PubMed]
25. Jayawarna, V.; Smith, A.; Gough, J.E.; Ulijn, R.V. Three-dimensional cell culture of chondrocytes on modified di-phenylalanine scaffolds. *Biochem. Soc. Trans.* **2007**, *35*, 535–577. [CrossRef]
26. Zhang, Y.; Kuang, Y.; Gao, Y.A.; Xu, B. Versatile small-molecule motifs for self-assembly in water and the formation of biofunctional supramolecular hydrogels. *Langmuir* **2011**, *27*, 529–537. [CrossRef]
27. Zhou, M.; Smith, A.M.; Das, A.K.; Hodson, N.W.; Collins, R.F.; Ulijn, R.V.; Gough, J.E. Self-assembled peptide-based hydrogels as scaffolds for anchorage-dependent cells. *Biomaterials* **2009**, *30*, 2523–2530. [CrossRef]
28. Cheng, G.; Castelletto, V.; Jones, R.R.; Connon, C.J.; Hamley, I.W. Hydrogelation of self-assembling RGD-based peptides. *Soft Matter* **2011**, *7*, 1326–1333. [CrossRef]
29. Jung, J.P.; Nagaraj, A.K.; Fox, E.K.; Rudra, J.S.; Devgun, J.M.; Collier, J.H. Co-assembling peptides as defined matrices for endothelial cells. *Biomaterials* **2009**, *30*, 2400–2410. [CrossRef]
30. Tian, Y.F.; Devgun, J.M.; Collier, J.H. Fibrillized peptide microgels for cell encapsulation and 3D cell culture. *Soft Matter* **2011**, *7*, 6005–6011. [CrossRef] [PubMed]
31. Silva, G.A.; Czeisler, C.; Niece, K.L.; Beniash, E.; Harrington, D.A.; Kessler, J.A.; Stupp, S.I. Selective differentiation of neural progenitor cells by high-epitope density nanofibers. *Science* **2004**, *303*, 1352–1355. [CrossRef]

32. Matson, J.B.; Stupp, S.I. Self-assembling peptide scaffolds for regenerative medicine. *Chem. Commun.* **2012**, *48*, 26–33. [CrossRef]
33. Song, Y.L.; Zheng, Q.X.; Guo, X.D.; Zheng, J.F. Cytocompatibility of self-assembled hydrogel from IKVAV-containing peptide amphiphile with neural stem cells. *J. Wuhan Univ. Technol. Mater. Sci. Ed.* **2009**, *24*, 753–756. [CrossRef]
34. Song, Y.L.; Zheng, Q.X.; Wu, Y.C.; Guo, X.D. Two-dimensional effectsof hydrogel self-organizedfrom IKVAV-containing peptides on growth and differentiation NSCs. *J. Wuhan Univ. Technol. Mater. Sci. Ed.* **2009**, *24*, 186–192. [CrossRef]
35. Song, Y.L.; Li, Y.X.; Zheng, Q.X.; Wu, K.; Guo, X.D.; Wu, Y.C.; Yin, M.; Wu, Q.; Fu, X.L. Neural progenitor cells survival and neuronal differentiation in peptide-based hydrogels. *J. Biomater. Sci. Polym. Ed.* **2011**, *22*, 475–487. [CrossRef]
36. Sur, S.; Matson, J.B.; Webber, M.J.; Newcomb, C.J.; Stupp, S.I. Photodynamic control of bioactivity in a nanofiber matrix. *ACS Nano* **2012**, *6*, 10776–10785. [CrossRef] [PubMed]
37. Muraoka, T.; Koh, C.Y.; Cui, H.G.; Stupp, S.I. Light-triggered bioactivity in three dimensions. *Angew. Chem. Int. Ed.* **2009**, *48*, 5946–5949. [CrossRef]
38. Capito, R.M.; Azevedo, H.S.; Velichko, Y.S.; Mata, A.; Stupp, S.I. Self-assembly of large and small molecules into hierarchically ordered sacs and membranes. *Science* **2008**, *319*, 1812–1816. [CrossRef] [PubMed]
39. Mata, A.; Geng, Y.B.; Henrikson, K.J.; Aparicio, C.; Stock, S.R.; Satcher, R.L.; Stupp, S.I. Bone regeneration mediated by biomimetic mineralization of a nanofiber matrix. *Biomaterials* **2010**, *31*, 6004–6012. [CrossRef]
40. Mendes, A.C.; Smith, K.H.; Tejeda-Montes, E.; Engel, E.; Reis, R.L.; Azevedo, H.S.; Mata, A. Co-assembled and microfabricated bioactive membranes. *Adv. Funct. Mater.* **2013**, *23*, 430–438. [CrossRef]
41. Ribeiro, S.; Radvar, E.; Shi, Y.; Borges, J.; Pirraco, R.P.; Leonor, I.B.; Mano, J.F.; Reis, R.L.; Mata, A.; Azevedo, H.S. Nanostructured interfacial self-assembled peptide-polymer membranes for enhanced mineralization and cell adhesion. *Nanoscale* **2017**, *9*, 13670–13682. [CrossRef]
42. Aviv, M.; Halperin-Sternfeld, M.; Grigoriants, I.; Buzhansky, L.; Mironi-Harpaz, I.; Seliktar, D.; Einav, S.; Nevo, Z.; Adler-Abramovich, L. Improving the mechanical rigidity of hyaluronic acid by integration of a supramolecular peptide matrix. *ACS Appl. Mater. Interfaces* **2018**, *10*, 41883–41891. [CrossRef] [PubMed]
43. Nadernezhad, A.; Forster, L.; Netti, F.; Adler-Abramovich, L.; Tessmar, J.; Groll, J. Rheological analysis of the interplay between the molecular weight and concentration of hyaluronic acid in formulations of supramolecular HA/FmocFF hybrid hydrogels. *Polym. J.* **2020**, *52*, 1007–1012. [CrossRef]
44. Adhikari, B.; Nanda, J.; Banerjee, A. Multicomponent hydrogels from enantiomeric amino acid derivatives: Helical nanofibers, handedness and self-sorting. *Soft Matter* **2011**, *7*, 8913–8922. [CrossRef]
45. Yang, B.; Adams, D.J.; Marlow, M.; Zelzer, M. Surface-mediated supramolecular self-assembly of protein, peptide, and nucleoside derivatives: From surface design to the underlying mechanism and tailored functions. *Langmuir* **2018**, *34*, 15109–15125. [CrossRef]
46. Decher, G. Fuzzy nanoassemblies: Toward layered polymeric multicomposites. *Science* **1977**, *277*, 1232–1237. [CrossRef]
47. Olive, A.G.L.; Abdullah, N.H.; Ziemecka, I.; Mendes, E.; Eelkema, R.; van Esh, J.H. Spatial and directional control over self-assembly using catalytic micropatterned surfaces. *Angew. Chem. Int. Ed.* **2014**, *53*, 4132–4136. [CrossRef]
48. Rodon Fores, J.; Criado-Gonzalez, M.; Schmutz, M.; Blanck, C.; Schaaf, P.; Boulmedais, F.; Jierry, L. Protein-induced low-molecular weight hydrogelator self-assembly through a self-sustaining process. *Chem. Sci.* **2019**, *10*, 4761–4766. [CrossRef]

Alexis BIGO--SIMON

Résolution à l'échelle moléculaire de la structure de nanofibres de peptides courts par reconstruction d'images de cryo-microscopie électronique, analyse spectrale et dynamique moléculaire

Résumé

Les hydrogels de peptides auto-assemblés sont des matériaux mous utilisés principalement dans le domaine des matériaux, de la catalyse et du domaine biomédicale. Pour pouvoir designer ces matériaux il est nécessaire de connaître l'organisation à l'échelle moléculaire. Dans cette thèse nous nous sommes focalisés sur un tripeptide modifié le Fmoc-FFY. Ce dernier a la capacité de s'auto-assembler dans l'eau via deux modes d'initiation : le premier est la voie enzymatique (Enzyme Assisted Self-Assembly) par l'ajout de phosphatase alcaline avec le Fmoc-FFpY, un précurseur du Fmoc-FFY. Le second mode d'initiation est une voie de chauffage puis refroidissement du Fmoc-FFY (annealing). Durant cette thèse nous avons investigué la structuration du Fmoc-FFY à différentes échelles temporelles et spatiales : (i) dans les premiers instants de l'assemblage grâce à la dynamique moléculaire, (ii) la structure moléculaire dans la nanofibre grâce à la reconstruction d'images et (iii) la variation de la microstructure d'amas de fibres via l'ajout d'acide hyaluronique identifié principalement via la diffusion des rayons X.

Mots-clefs : auto-assemblage, microstructure, édifice moléculaire, filaments synthétiques, reconstruction d'images, dynamique moléculaire

Résumé en anglais

Self-assembled peptides' hydrogels are soft materials currently used in the material, catalytical and biomedical domains. In order to design these materials it is imperative to know the molecular organization of peptides. In this thesis we focused on a modified tri-peptide : Fmoc-FFY. The later have the capability to self-assemble in water via two triggers : the first one is the enzymatic way (Enzymatic Assisted Self-Assembly) with the addition of alkaline phosphatase and Fmoc-FFpY, a precursor to Fmoc-FFY. The second way is the annealing of Fmoc-FFY. In this work we have investigated the structuration of Fmoc-FFY at different spatial and time scales : (i) in the early instants of self-assembly thanks to a molecular dynamics study, (ii) the molecular structure in the nanofiber by the use of image reconstruction and (iii) the microstructure modification of bundles of nanofibers upon the addition of hyaluronic acids identified via X-ray diffusion.

Keywords : self-assembly, microstructure, molecular structure, artificial filaments, image reconstruction, molecular dynamics